CRANFIELD UNIVERSITY

SONIA ANDREIA MARTINS MECO

Joining of steel to aluminium alloys for advanced structural applications

SCHOOL OF AEROSPACE, TRANSPORT AND MANUFACTURING
Welding Engineering and Laser Processing Centre

PhD
Academic Year: 2015-2016

Supervisor: Doctor Supriyo Ganguly and Professor Stewart Williams
March 2016

CRANFIELD UNIVERSITY

SCHOOL OF AEROSPACE, TRANSPORT AND MANUFACTURING
Welding Engineering and Laser Processing Centre

PhD Thesis

Academic Year 2015-2016

SONIA ANDREIA MARTINS MECO

Joining of steel to aluminium alloys for advanced structural applications

Supervisor: Doctor Supriyo Ganguly and Professor Stewart Williams
March 2016

This thesis is submitted in partial fulfilment of the requirements for the degree of PhD

Declaration of authorship

I, Sónia Andreia Martins Meco, declare that this thesis and the work presented in it, with the exception of section 5.2.4, are my own and have been generated by me as the result of my own original research.

Section 5.2.4 was produced by Dr. Daniel Cozzolino who is an expert in finite element analysis. Dr. Daniel Cozzolino developed a thermal model to predict the thermal field during laser welding of steel to aluminium at the joint interface based on my instructions. I was responsible for the experimental design, calibration and validation of the model and also the analysis of the data resultant from the model.

Abstract

When joining steel to aluminium there is a reaction between iron and aluminium which results in the formation of brittle intermetallic compounds (IMC). These compounds are usually the reason for the poor mechanical strength of the dissimilar metallic joints. The research on dissimilar metal joining is vast but is mainly focused on the automotive industry and therefore, the material in use is very thin, usually less than 1 mm. For materials with thicker sections the present solution is a transition joint made by explosion welding which permits joining of steel to aluminium and avoids the formation of IMCs. However, this solution brings additional costs and extra processing time to join the materials.

The main goals of this project are to understand the mechanism of formation of the IMCs, control the formation of the IMCs, and understand their effects on the mechanical properties of the dissimilar Fe-Al joints during laser welding. Laser welding permits accurate and precise control of the welding thermal cycle and thereby the underpinning mechanism of IMC formation can be easily understood along with the factors which control the strength of the joints. The further goal of this project is to find an appropriate interlayer to restrict the Fe-Al reaction.

The first stage of the work was focused on the formation and growth of the Fe-Al IMCs during laser welding. The understanding of how the processing conditions affect the IMC growth provides an opportunity to act and avoid its formation and thereby, to optimize the strength of the dissimilar metal joints. The results showed that even with a negligible amount of energy it was not possible to prevent the IMC formation which was composed of both Fe_2Al_5 and $FeAl_3$ phases. The IMC growth increases exponentially with the applied specific point energy. However, for higher power densities the growth is more accentuated. The strength of the Fe-Al lap-joints was found to be not only dependent on the IMC layer thickness but also on the bonding area. In order to obtain sound joints it is necessary to achieve a balance between these two factors. The thermal model developed for the laser welding process in this joint configuration showed that for the same level of energy it is more efficient to use higher power densities than longer interaction

times. Even though a thicker IMC layer is formed under this condition due to higher temperature there is also more melting of aluminium which creates a larger bonding area between the steel and the aluminium. The joint strength is thus improved.

In the second stage of the work the study was focused on the use of copper as interlayer between steel and aluminium to suppress the reaction between Fe and Al. Different welding processes were used and the interaction between the Fe, Cu and Al was investigated. The application of copper interlayer in laser welding between the steel and the aluminium plates in a lap-joint configuration was found to be not very effective in preventing the reaction between Fe and Al. The thermal gradient required to melt the aluminium without melting the steel was not possible to achieve and for this reason ternary Fe-Cu-Al IMCs were found in the majority of the experiments.

The Al-Cu IMCs formed during the deposition of copper interlayer by Cold Metal Transfer (CMT) arc welding, either with copper onto aluminium or aluminium onto copper, were analysed. It was found that by controlling the energy of the welding process the ductility of the joints was improved by reducing the amount of copper-rich IMCs. The maximum hardness found on the Al-Cu-Fe samples was much lower than that on the Fe-Al joints, 450 HV against 1100 HV, respectively. The effect of the alloying elements, Si, Mg and Cu, of the welding wire on the Al-Cu IMCs growth was also studied. It was found that Cu and higher Si content enhances the formation of the IMCs and that Mg and lower Si content minimize the IMC growth.

As a part of this project the joint design was also studied and, by changing the joint design, the joining principle used in the investigation of laser welding of steel to aluminium in a lap-joint configuration was successfully transferred to a T-joint configuration. By combining the joint design and the control of the process energy it was possible to create crack free joints with superior strength due to the mechanical lock effect caused by the small distortion resultant from the welding

process. For lower levels of energy the IMC layer was less than 5 μm and showed similar characteristics to those observed in the lap-joint.

Keywords

Laser welding; steel; aluminium; intermetallic compounds; conduction welding; cold metal transfer; copper; interlayer; lap joint; T-joint, thermal model.

List of publications

- S. Meco, G. Pardal, S. Ganguly, S. Williams, and N. McPherson, “Application of laser in seam welding of dissimilar steel to aluminium joints for thick structural components,” *Opt. Lasers Eng.*, 2014
- S. Meco, S. Ganguly, S. Williams, and N. McPherson, “Effect of Laser Processing Parameters on the Formation of Intermetallic Compounds in Fe-Al Dissimilar Welding,” *J. Mater. Eng. Perform.*, vol. 23, no. 9, pp. 3361–3370, Jun. 2014

List of conferences

- Euromat 2013 conference presentation
- ILAS 2015 conference presentation

Acknowledgements

I would like to thank Cranfield University and in particular the Welding Engineering and Laser Processing Centre for giving me the opportunity to work in this very interesting project and for providing me with all the conditions to develop new skills, knowledge and experience during the PhD research.

I am sincerely grateful to BAE System Naval Ships, more specifically Doctor Norman McPherson, and EPSRC (through grant number EP/J017086/1) for the financial support given to this project.

I would like to express my sincere gratitude to my supervisors, Doctor Supriyo Ganguly and Professor Stewart Williams, for the guidance, sharing the technical and scientific knowledge and all the support given during the entire length of the PhD research.

To my colleagues and friends who are or were in the welding department during my stay in Cranfield I would like to say thank you. Daniel Cozzolino, Eurico Assuncao, Pedro Almeida, Elisabete Costa, Wojciech Suder, Filomeno Martina, Jibrin Sule, Anthony McAndrew, Wasiu Ayoola, Sergio Rios, Adrian Adison, Jialuo Ding and other colleagues, their friendship helped creating a good working environment. Good moments were spent with them in the tea room talking not only about science and technical subjects but also about every-day life subjects. These moments were important to decompress and relax.

I would like to acknowledge Brian Brooks and Flemming Nielson for the technical support given during the laboratorial work and for sharing their experience with me. Andrew Dyer was always very helpful in the metallographic laboratory.

Finally, I would like to thank my beloved colleague, friend and now husband, Goncalo Pardal, for sharing his live with me. He has given me not only emotional strength but he has also given me support in my career through technical and scientific discussions. I would like to acknowledge my family, in particular my mother, Filomena Meco and my father, Leopoldino Meco who has already passed away, for all the motivation, strength and unconditional support given during my whole life.

Table of contents

List of figures

List of tables

List of abbreviations

Symbol	Description	Units
FLMIP	Fundamental laser material interaction parameters	-
E_{sp}	Specific point energy	kJ
PD	Power density	$MW.m^{-2}$
t_i	Interaction time	S
A_{beam}	Area of the laser beam	mm^2
D_{beam}	Diameter of the laser beam	mm
P	Laser power	W
TS	Travel speed	$m.min^{-1}$
IMC	Intermetallic compound	-
CMT	Cold Metal Transfer	-
PF	Power factor	$MW.m^{-1}$
X	Intermetallic layer thickness	µm
K	Diffusion constant	-
K_0	Constant	-
t	Time	s
Q	Activation energy for growth of the layer	$kJ.mol^{-1}$
R	Gas constant	$J.K^{-1}.mol^{-1}$
T	Temperature	°K
Q	Heat input	$J.mm^{-1}$
U	Voltage	V
I	Current	A
k	Efficiency of the welding process	%

1.0 Review of the dissimilar metal joining

1.1 Introduction

The investigation of dissimilar metal joining started more than five decades ago. Since then, many studies have been done using different materials or metallic combinations, applying different strategies and joining processes. Innovative material efficient structures are built with multiple materials which are selected based on their properties, either physical, chemical or mechanical, and on the requirements of the structure, viz. mechanical strength, weight or corrosion resistance. The combination of dissimilar materials offers many advantages at economical, performance or environmental level. The principal driving force for the investigation on dissimilar metal joining has been the transportation industry. The maritime, automotive and aerospace industries aim to reduce the body weight without compromising structural integrity. In the automotive industry one of the motivations to develop lightweight vehicles was the European regulation established in 2009 (EC Regulation No. 443/2009 (Mock, 2014)(Kastensson, 2014)) which imposes a reduction in CO_2 emissions on newly manufactured cars. The weight reduction leads to a better performance of the car in terms of fuel consumption and consequently, this is reflected on the levels of CO_2 emitted. By replacing partially or completely traditional structural metals with high strength steel, aluminium, magnesium or composites a significant reduction of the total weight of the vehicle has been observed. However, this has only been applied to luxury brand cars due to the high cost associated with the lightweight vehicle manufacturing. For instance, the application of carbon fibre and aluminium in the new generation of the Range Rover Sport resulted in a total structural weight reduction of about 420 kg. The development of lighter structures in shipping and aviation permits not only fuel savings but also the ability to use the equivalent weight to transport passengers or cargo.

Aluminum (Al) is often the material of choice because it is abundant, cost effective, has high specific modulus and corrosion resistance. The new design solutions are aimed at using more proportion of Al as a structural material. Steel is the most used structural alloy due to its high strength properties, low cost and recyclability. The problem is that these two metals have different physical properties and they lack solid

solubility. Different melting temperatures, thermal expansion and conductivity may lead to defects during the joining process and the formation of brittle intermetallic compounds (IMC) reduces the strength of the welded joints.

1.2 Intermetallic compound formation and growth between Fe and Al

The formation of intermetallic compounds (IMC) is almost certain when joining steel to aluminium. These compounds have a non-metallic covalent bond which gives them a brittle behaviour. According to the binary Fe-Al phase diagram, Al has about 20 at.% solid solubility in Fe but Fe has zero solid solubility in Al at room temperature (see Figure 1-1). Different IMCs are formed depending on the temperature of the reaction and the chemical composition of the mixture, as indicated in Table 1-1. The IMCs are organized into two groups, the iron-rich IMCs which include the Fe_3Al and FeAl phases and the aluminium-rich IMCs which include the $FeAl_2$, Fe_2Al_5 and $FeAl_3$. The hardest and thus more brittle IMCs are found in the Al-rich group, as indicated in Table 1-2.

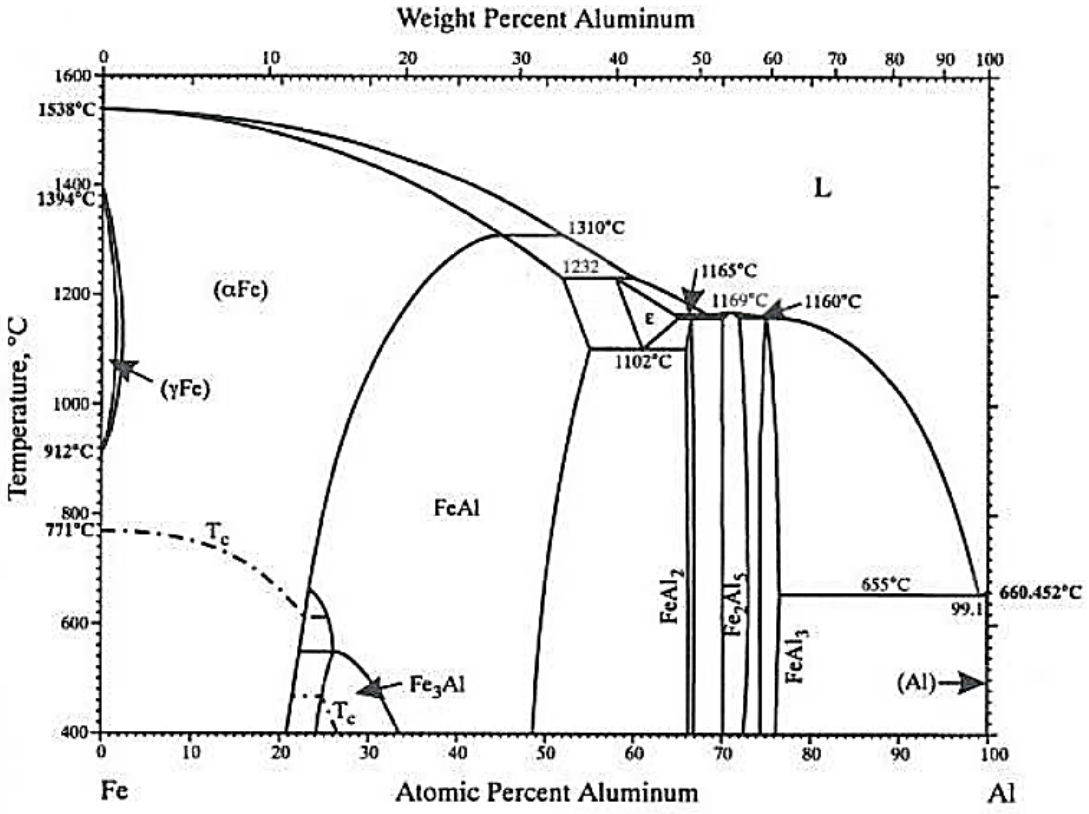

Figure 1-1: Binary Fe-Al phase diagram (Massalski, 1986).

Table 1-1: Phase reactions in Fe-Al phase diagram (*A.S.M American Society for Metals, Bulletin of binary phase diagrams*, 1994).

Reaction	Reaction composition (at.% Al)	Reaction temperature (°C)	Reaction type
$\alpha Fe \leftrightarrow FeAl$	45	1310	Critical
$L + FeAl \leftrightarrow Fe_2Al_3$	52	1232	Peritectic
$L \leftrightarrow Fe_2Al_3 + Fe_2Al_5$	70.5	1165	Eutectic
$L \leftrightarrow Fe_2Al_5 + FeAl_3$	72	1160	Unknown
$L \leftrightarrow FeAl_3 + Al$	76.6	655	Eutectic
$Fe_2Al_3 + Fe_2Al_5 \leftrightarrow FeAl_2$	70	1156	Peritectoid
$Fe_2Al_3 \leftrightarrow FeAl + FeAl_2$	55	1102	Eutectoid
$L \leftrightarrow Fe_2Al_5$	71	1169	Congruent
$\alpha Fe \leftrightarrow FeAl$	23.9	662	Tricritical
$FeAl \leftrightarrow Fe_3Al$	26.5	552	Critical
$L \leftrightarrow \delta Fe$	0	1538	Melting
$L \leftrightarrow Al$	100	660	Melting
$\delta Fe \leftrightarrow \gamma Fe$	0	1394	Allotropic
$\gamma Fe \leftrightarrow \alpha Fe$	0	912	Allotropic
Metastable phase, $L\ kFeAl_6 + Al$	85.7	653	Eutectic

Table 1-2: Fe-Al phases and Vickers microhardness (Massalski, 1986) (Olsen, 2009).

	Phase	Al [at%]	HV
	Fe (solid solution)	0-45	-
	Fe (γ)	0-1.3	-
Iron-rich IMCs	Fe_3Al (β_1)	23-34	250-350
	FeAl (β_2)	23-55	400-520
Aluminium-rich IMCs	Fe_2Al_3 (ε)	58-65	-
	$FeAl_2$ (ζ)	66-66.9	1000-1050
	Fe_2Al_5 (η)	70-73	1000-1100
	$FeAl_3$ (ɵ)	74.5-76.5	820-980
	Al (solid solution)	99.998-100	-

There are two main lines of research with regard to Fe-Al IMC formation and growth. The iron-rich IMCs have been investigated with the main goal of their production whereas the studies involving aluminium-rich IMCs have been focused on finding ways to avoid their formation.

There are many applications for the iron-rich IMCs due to their thermal-mechanical properties. When compared to the aluminium-rich IMCs, the iron-rich IMCs have good high temperature corrosion resistance (Liu et al., 1998) and they also have relatively high ductility. They are used in a form of coatings to increase the wear resistance of

structural parts or in a form of full structural parts as it is the case of Fe_3Al-based iron aluminide structures produced by Wire plus Arc Additive Manufacturing (WAAM) with simultaneous feeding of wires of aluminium and iron for in situ alloying (Shen et al., 2015). Figure 1-2 shows a wall built with this technology.

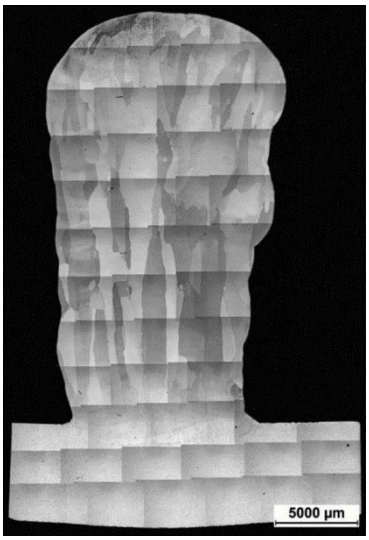

Figure 1-2: Cross section of the additive manufactured wall which is mainly composed of iron-rich Fe–Al IMCs (Shen et al., 2015).

The formation and growth of Fe-Al IMCs have been investigated by many researchers over recent decades (Shahverdi et al., 2002) (Fan et al., 2011) (Springer et al., 2011). Time and temperature were found to be the main factors responsible for the formation and growth of the IMCs. Some researchers studied IMC formation by using a technique named “aluminize hot dipping” which permitted independent control of the temperature and time. In the study a solid steel bar was dipped in a molten aluminium bath for different periods of time and at constant temperature and then the composition and thickness of the IMCs formed were analysed (Kobayashi and Yakou, 2002). Fe_2Al_5 was the main IMC formed on the steel surface in the temperature range of 700-900 °C. However, for the same range of temperatures other researchers have also identified the presence of $FeAl_3$ at the interface between the Fe_2Al_5 and aluminium (Bouche et al., 1998).

Diffusion specimens of Fe-Al were also prepared in order to study the formation of Fe-Al IMCs. It was found that at 600 °C with heat treatment longer than one hour, only $FeAl_3$ was formed by diffusion of Al into Fe, as represented in Figure 1-3 (Wang et al., 1998). At this temperature, both Fe and Al were in the solid state and the diffusivity of

Al into Fe was higher than that of Fe into Al. However, for temperatures higher than 700 °C and for the same heat treatment duration, Fe_2Al_5 was formed instead of $FeAl_3$. At this temperature Al is in the liquid state and Fe remains in the solid state and thus, the diffusivity of Fe into Al is higher. Based on the results, the authors (Wang et al., 1998) have proposed the following sequence of events for the formation for the Fe_2Al_5 IMCs at temperatures higher than 700 °C:

(1) Eutectic reaction of $FeAl_3$ with Al (during heating, still with metals in solid phase);
(2) Eutectic liquid;
(3) Fe and Al interdiffusion;
(4) Intermetallic reaction;
(5) Fe_2Al_5.

It was also found that the composition of the IMCs did not change with the heat treatment duration. The only difference found was that the IMC layer became thicker for a longer heat treatment time which shows the thermodynamic stability of the different phases at different processing temperatures.

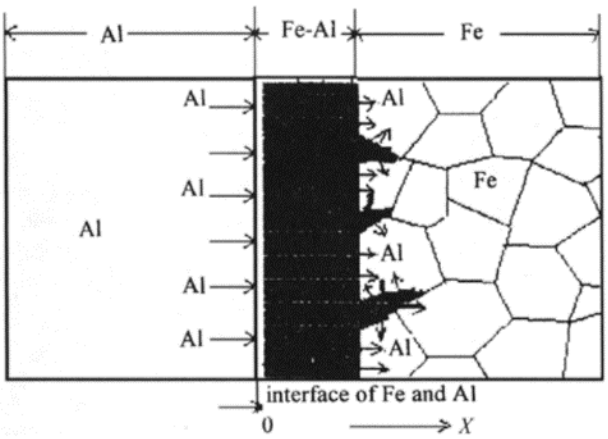

Figure 1-3: Schematic representation of the diffusion of Al into Fe and $FeAl_3$ formation at the Fe side during diffusion heat treatment at 600 °C for 1 hour (Wang et al., 1998).

Other researchers found that the Fe-rich IMCs, such as FeAl and Fe_3Al, were only formed when the aluminium bath was at temperatures higher than 1000 °C. FeAl is believed to be formed due to diffusion of Fe into Fe_2Al_5, whereas Fe_3Al if formed due to the diffusion of Fe into FeAl (Kobayashi and Yakou, 2002). However, FeAl has been found at lower temperatures in Fe-Al joints produced by inertia friction welding (Taban

et al., 2010). One possible reason indicated by the authors was the close contact of the metals and the heavy working on the aluminium side during the welding process. Thereby, easier atomic diffusion was enabled which possibly overcame the activation energy barrier.

There are two main mechanisms of formation of the IMCs. One mechanism is controlled by a chemical reaction at the interfaces and the growth of the IMCs follows linear kinetics. The second mechanism is controlled by interdiffusion of the atoms through the different phases and follows parabolic kinetics. In the literature it was mentioned that in the range between 700 and 900 °C the IMC growth is mainly controlled by diffusion (Bouche et al., 1998). However, in a short transient period, between 30 s up to 30 min and just before the parabolic growth of the IMC layer, there is linear growth which is characteristic of a chemical reaction.

The thickness of the IMC layer following parabolic growth and controlled by diffusion can be calculated by the following equation: $X = K\sqrt{t}$ (Kobayashi and Yakou, 2002). X [µm] represents the thickness of the IMC layer, K is the diffusion constant and t [s] is the time for diffusion. K can be determined by $K = K_0 exp\left(-\frac{Q}{RT}\right)$ where K_0 is constant, Q [kJ.mol^{-1}] is the activation energy for growth of the IMC layer, R is the universal gas constant and T [K] corresponds to the absolute temperature of the process.

Diffusion is defined as the “phenomenon of material transport by atomic motion” (Callister, 2006). When two metals are in close contact, as shown in Figure 1-4a, and heat is applied to them for a certain amount of time, the atoms start moving from the side with higher concentration to the other side where the concentration is lower by diffusing into each other. The result of the atomic diffusion is the formation of a new alloy (alloy C) which grows from the surface of contact between metal A and B towards the edges of the metals, as represented in Figure 1-4b. The concentrations of the metals A and B within the alloy change with the position. The extent or length of diffusion depends on many factors, for example, heat treatment temperature, diffusion time and diffusivity of one element into another or diffusion coefficient.

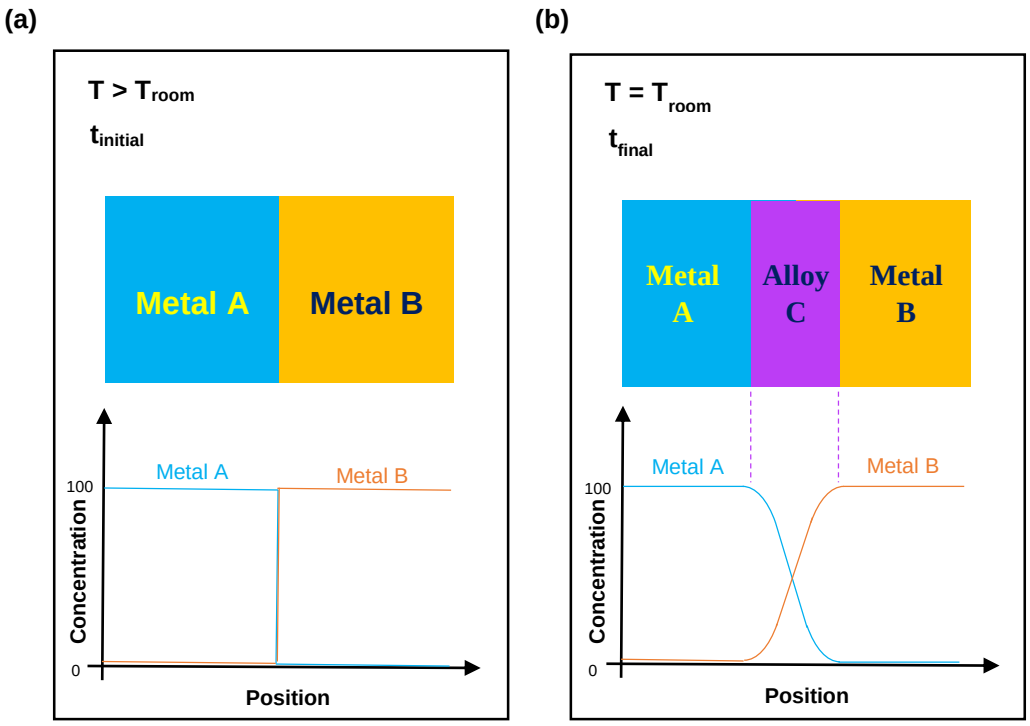

Figure 1-4: Schematic representation of the diffusion process showing the diffusion sample and the concentration of both metals across the sample (a) before and (b) after heat treatment.

Fick's first law of diffusion (equation 1-1) is an equation which permits the calculation of the diffusion flux (kg.m^{-2}.s^{-1}), or the number of particles which pass through a plane of unit area in unit time, in one direction for steady state condition (Cottrell, 1995). The steady state condition means that the flux of atoms passing through a surface perpendicular to the gradient does not change with time.

$$J = -D\frac{dC}{dx} \qquad (1\text{-}1)$$

In this equation, D corresponds to the diffusion coefficient (m^2.s^{-1}), C is the concentration of the element (kg.m^{-3}) at the position x (m). The term *dC/dx* represents the concentration gradient.

The diffusion distance (*dx*) can be calculated using Fick's law if all the other terms are known. If the diffusion process is nonsteady-state then an alternative equation needs to be used; Fick's second law is a partial differential equation as written in equation 1-2.

$$\frac{\partial C}{\partial t} = \frac{\partial}{\partial x}\left(D\frac{dC}{dx}\right) \qquad (1\text{-}2)$$

The simplified version of the equation 1-2 is written below and is based on the boundary conditions for a semi-infinite solid in which the surface concentration is kept constant:

$$\frac{C_x - C_0}{C_s - C_0} = 1 - erf\left(\frac{x}{2\sqrt{Dt}}\right) \quad (1\text{-}3)$$

In this equation C_x corresponds to the concentration at position x after time t, C_0 is the initial concentration of the element in the solid, C_s is the concentration at the surface perpendicular to the gradient during time t. The term erf(x/(2/$\sqrt{Dt}$) is the Gaussian error function which can be found in mathematical tables for different vlues of 2/$\sqrt{Dt}$.

The diffusion coefficient can be calculated based on equation 1-4, where D_0 is a constant for temperature independent pre-exponential ($m^2.s^{-1}$), Q_d is the activation energy for diffusion ($J.mol^{-1}$), R is the gas constant (8.31 $J.mol^{-1}.K^{-1}$) and T is the absolute temperature (K).

$$D = D_0\, exp\left(-\frac{Q_d}{RT}\right) \quad (1\text{-}4)$$

This equation shows that the temperature is the factor which most influences the diffusion coefficient and consequently, the diffusion rate.

When joining steel to aluminium using a thermal process, there is also diffusion due to the close contact of the metals and the heat applied to them (see Figure 1-4). The diffusion of Fe and Al occurs perpendicularly to the surface where the metals are in contact each other. At the joint interface the composition will change and a new zone containing both Fe and Al will be produced. Due to the lack of solubility of Fe into Al and vice versa, this diffusion causes the formation of IMCs. Fick's law could be used to estimate the extent of the diffusion and thus, predict the thickness of the IMC layer. However, this approach is only valid when the joining process occurs under equilibrium conditions. In this thesis the most accurate method to determine the IMC layer thickness was by metallographic analysis because the welding processes used in this work do not result in equilibrium conditions.

The thermal cycle resulting from a fusion joining process is different to that of the examples previously mentioned. The fusion processes occur in transient conditions, with high heating and cooling rates and for this reason, the formation of the IMCs is mainly controlled by chemical reactions. In fact, it has been referred that when the

heating time is short, as is the case in fusion joining processes or the beginning of a hot-dipping process, the growth of the IMCs occur by chemical reaction in opposition to atomic diffusion (Bouche et al., 1998).

There are two main types of IMCs, Fe_2Al_5 and $FeAl_3$, which are formed during welding of steel to aluminium and are frequently found at the joint interface, as represented in Figure 1-5. Even though $FeAl_3$ is the first IMC to grow due to the lower activation energy (Shahverdi et al., 2002), the sub-layer formed with this IMC is never thicker than that of the Fe_2Al_5 due to the fast growth of the latter IMC.

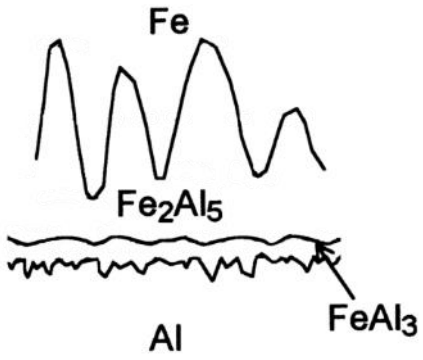

Figure 1-5: Schematic representation of the IMC layers formed in Fe-Al welded joints (Bouche et al., 1998).

The process starts with the formation of islands of $FeAl_3$, which has a monoclinic structure, at the border line between the steel and aluminium, as represented in Figure 1-6. Afterwards, these islands spread along the interface and form a continuous layer of needle shape compounds (Rathod and Kutsuna, 2004). The Fe_2Al_5 forms a second layer between the already existent $FeAl_3$ sub-layer and the steel. The Fe_2Al_5 sub-layer is easily identified by the tong shape grains growing towards the steel (Ranfeng Qiu et al., 2009a)(Kobayashi and Yakou, 2002).

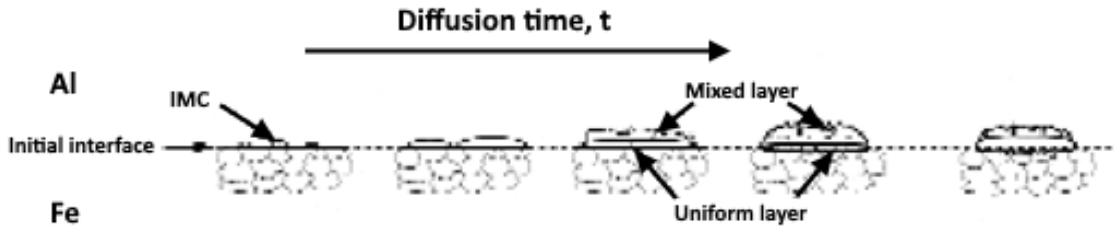

Figure 1-6: Stages of IMC layer formation during diffusion bonding with variable time and constant temperature (reproduced from original) (Rathod and Kutsuna, 2004).

The tongue-like morphology of the Fe_2Al_5 phase is believed to be resultant from the preferential growth along the [001] direction of the crystal structure, the c-axis, the longest crystallographic axis (Cheng and Wang, 2009). It was also reported that along the c-axis of the Fe_2Al_5 phase there is about 30% vacancies and this defect allows a rapid diffusion path along the [001] direction (Heumann and Dittrich, 1959). This explains the almost equiaxial morphology of the Fe_2Al_5 in the early stages of the IMC formation.

1.3 Joining processes used in direct joining of steel to aluminium

Joints can be produced in solid-solid, solid-liquid and liquid-liquid phases between steel and aluminium, depending on the joining process and joint configuration. The physical state of the alloys (solid or liquid) at the joint interface during the joining process is one of the determining factors for the formation of IMCs because it directly controls the activity and mobility of the atoms of the participating alloys. Broad research has been carried out aiming to produce sound dissimilar metal joints between steel and aluminium. The analysis of the IMCs and the mechanical strength of the welded joints were part of the majority of studies.

1.3.1 Mechanical joining

Non-permanent joining, such as fastening or riveting, are successful alternatives to join metallurgically incompatible metals. These processes are used at room temperature and thus, the formation of brittle IMCs is avoided. However, these solutions have a few drawbacks.

With bolts or screws, additional weight is added to the structure, uneven stress is induced in the structure and when in service the bolts can work loose and the gaps may lead to the initiation of corrosion. In contrast, a joint produced by thermal processes results in an integrated structure and it is water sealed. The use of bolts and screws restrict the joint configuration to a lap joint and have low specific strength. Having said that, Audi GmbH has used a fastening process with flow drill screws to join steel to aluminium that only requires access from one side of the joint (Graham, 2014).

Clinching (Abe et al., 2011) and self-piercing riveting (Abe et al., 2009) can only applied to a maximum thickness and strength of material and also require access from both sides of the joint.

Apart from the mechanical joining techniques referred to in this section there are others covered in a review paper written by Martinsen *et al*. (Martinsen et al., 2015).

1.3.2 Chemical joining

Similar to mechanical joining processes, adhesive bonding is also widely used in industry and it is an alternative solution for dissimilar material joining (Avt et al., 2002). This process creates continuous and sealed joints, there is minimal additional adhesive weight and no deformation induced in the joint. On the other hand, the integrity of the joints is dependent on the surface condition prior to the application of the adhesive, the joints have low thermal resistance and they are susceptible to environmental conditions. When compared to mechanical and thermal joining processes, adhesive bonding has relatively lower strength and is very much dependent on the temperature of the application.

1.3.3 Thermal process - Solid state joining

The formation of Fe-Al IMC is usually minimized when solid state joining processes are used. Processes such as friction stir welding (Lee et al., 2006), linear friction welding (Taban et al., 2010) and ultrasonic spot welding (Haddadi and Prangnell, 2013)(Prangnell et al., 2011) are operated at temperatures lower than the melting temperature of any of the intervenient materials. Under this condition, one of the materials in a fluid-like plastic state flows and adheres to the other forming the bond. For these two reasons the formation of the brittle IMCs is minimized or even avoided.

Successful results have been obtained by friction stir welding, either using a linear (Lee et al., 2006) (Uzun et al., 2005) (Watanabe et al., 2006) or circular weld pattern (Yasui et al., 2014). The low heat input is controlled by the travel speed and rotating speed and it is transferred from the periphery of the tool to the surrounding material. The thickness of the IMC layer found at the joint interface can be in the order of a few nanometers, which is much lower than that formed by conventional fusion welding processes. The mechanical strength of the joints is identical to that of the weakest metal of the joint, which is usually the aluminium.

The solid state joining processes have also some limitations. All the previous examples have restrictions in terms of joint configuration and material dimensions or thickness. In friction stir welding there is tool wear due to its permanent contact with the material. In friction welding the heat generation is not at an uniform rate at the interface which may result in the growth of the IMCs (Martinsen et al., 2015). In ultrasonic spot welding the surface of the material may be heavily deformed due to the pressure applied by the sonotrode. However, one of the greatest drawbacks of friction processes is the energy requirement exponentially increases with the thickness of the component. Therefore, to join a dissimilar metal structure where the section is thicker than 5 mm the energy required is very high and the formation of IMCs is expected.

There are three types of resistance spot welding: solid state, fusion and braze, depending if the materials are melted or not at the joint interface. This process has also been investigated to join steel to aluminium (Qiu et al., 2010; R Qiu et al., 2009; Ranfeng Qiu et al., 2009a, 2009b) but the researchers couldn’t prevent formation of the IMCs and the specimens failed from the joint interface when tested under tensile-shear loading.

Explosion welding is also a solid state joining process. Initially this process was mainly used to clad large areas of one metal with another (see Figure 1-7a). The different material combinations is represented in Figure 1-7b. Nowadays this process has many industrial applications, such as in nuclear fuel reprocessing plants where joining of titanium to stainless steel is required, or in shipbuilding, to successfully join steel to aluminium via an explosion bonded hybrid transition joint, which is made of half aluminium and other half steel. As the process is very fast there is almost no time for the reaction between Fe and Al and so the IMC layer is usually very thin, as demonstrated in (Acarer and Demir, 2008; Findik, 2011; Pl, 1989). With regards to the limitations of this process it can only be applied to large structures with simple geometries and there are often restrictions to the use of explosives in industrial areas due to noise and ground vibrations caused by the explosion.

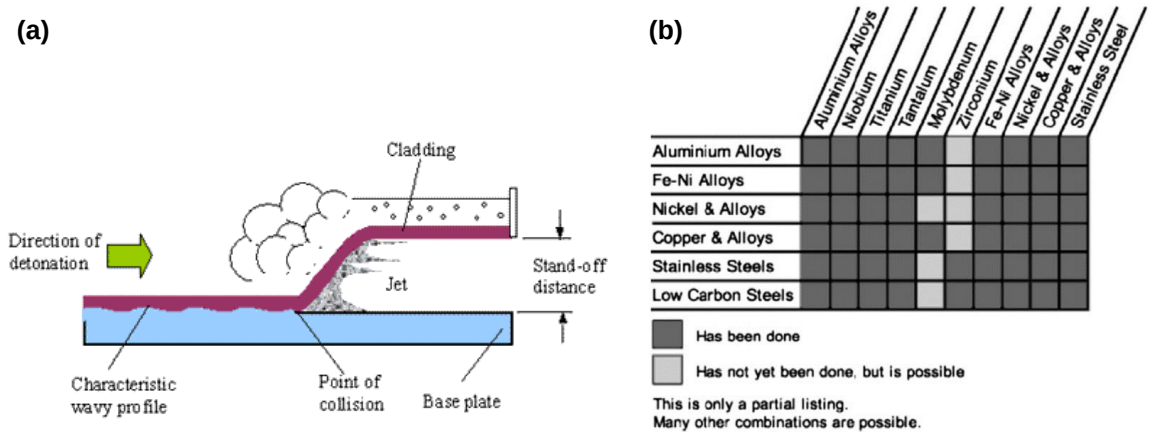

Figure 1-7: (a) Schematic representation of explosive cladding (TWI, n.d.) and (b) list of materials that are commonly clad (Findik, 2011).

It is also important to note that the joints produced with the transition joint might not be free of IMCs. During the joining process, when the transition joint is being welded to the other metals, the heat produced by the welding process may lead to the formation and growth of Fe-Al IMCs (Tricarico et al., 2009)(Tricarico and Spina, 2010).

1.3.4 Thermal process - Fusion joining

There is a significant research focus on dissimilar metal joining of steel to aluminium using fusion joining processes, despite of the perception that these processes cannot be used in dissimilar metal joining due to the strong reaction and interdiffusion of the intervenient elements during the joining process leading to poor mechanical properties of the joints. This is a wrong perspective and the evidences that prove the feasibility of using fusion joining processes to create sound joints between steel to aluminium are presented in this section.

In fusion joining, as the name suggests, at least one of the metals is melted during the joining process and thus, the processing temperature is higher than the melting temperature of one of the metals. There are two main sub-categories in this group: welding and brazing. By definition, welding refers to the joining process which results in the melting of the parent metals. Brazing refers to the joining process which uses and melts a third metal, usually a filler wire, and the parent metals are not melted. There is also a third category named welding-brazing which has not been standardized yet but it has been applied to dissimilar metal joining. Welding-brazing is the best terminology to describe the process where the metal with the lowest melting

temperature melts and wets the surface of the metal with higher melting temperature. During this process, at the joint interface, the bonding occurs between the liquid and solid metals and no filler material is used.

In terms of temperatures involved in each joining process, one may say that brazing is the coldest, welding is the hottest and welding-brazing fits in the middle. This is important to have in mind in dissimilar metal joining because of the high sensitivity of IMC growth to the temperature and time.

A few examples of the fusion joining processes applied to dissimilar metal joining of steel to aluminium are shown in Table 1-3.

Table 1-3: Examples of fusion joining processes investigated in joining of steel to aluminium.

Joining process	Category	Reference
TIG	Welding-brazing	(G Sierra et al., 2008)
Autogenous laser	Welding	(Sierra et al., 2007) (Yan et al., 2010) (Torkamany et al., 2010)
Autogenous laser	Welding-brazing	(Peyre et al., 2007)
Laser + wire	Brazing	(Dharmendra et al., 2011) (G. Sierra et al., 2008) (Mathieu et al., 2007) (Korte et al., 2005)
Laser roll welding and bonding	Welding-brazing	(Rathod and Kutsuna, 2004) (Kreimeyer et al., 2004) (Ozaki and Kutsuna, 2009)
Hybrid laser-MIG	Welding	(Olsen, 2009)
Cold metal transfer (CMT)	Brazing	(Zhang et al., 2009) (Padmanabham et al., 2013) (Transfer, 2012)

The majority of the references in this table are laser based due the numerous advantages that lasers have to offer. Some of the reasons to use lasers in dissimilar metal joining are:

(1) During laser processing there is a minimal zone affected by the heat surrounding the spot where the energy is applied;
(2) Good control of the energy transferred to the substrate (related to the previous point);
(3) By controlling the position of the laser beam in relation to the joint interface it is possible to control the composition of the fusion zone;

(4) In comparison to other fusion joining processes, this process has high cooling and solidification rates;

(5) Laser processing can be applied to any material type and dimension and in any joint configuration;

(6) Lasers can be integrated with other equipment (ex. laser roll bonding and hybrid laser-MIG).

Laser joining also covers many of the limitations of the processes referred in the previous sections. Depending on the joint configuration, the spatial location of laser irradiation, the level of energy level applied and the welding mode, it is possible to cover the three joining categories, viz. welding, brazing or welding-brazing. In summary, lasers are versatile and give extra flexibility to the joining process.

Different lasers have been used to join steel to aluminium by autogenous laser welding (without welding wire and with a liquid-liquid joint interface). For instance, a high power and continuous wave (CW) laser (Sierra et al., 2007), a tandem system composed by a CW and a pulsed mode lasers (Yan et al., 2010) and a pulsed laser (Torkamany et al., 2010). All lasers were operated in keyhole mode and for this reason both metals were melted and mixed in liquid state during the joining process (see Figure 1-8). For this reason, the reaction between Fe and Al was enhanced, very thick IMCs were formed, ranging from the Al-rich to the Fe-rich IMCs.

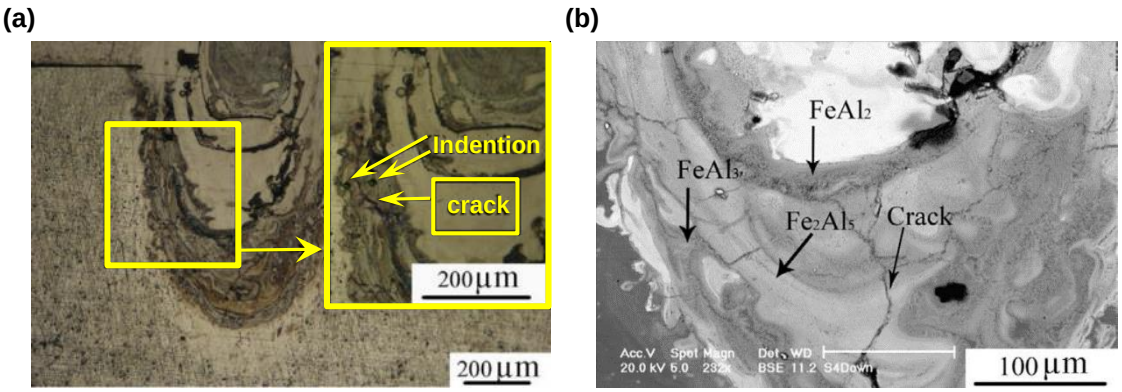

Figure 1-8: Pulsed laser welding of 0.8 mm thick steel to 2.0 mm thick aluminium in a lap-joint configuration and with steel on the top. (a) Micrograph of the cross-section of the keyhole weld (b) SEM micrograph of the weld-joint interface (Torkamany et al., 2010).

The mechanical strength of the joints was found to be dependent on the energy of the process, either via peak power, pulse duration or overlapping factor. However, even with the process optimized the strength of the joint could not surpass that of the weakest parent metal and thus, the failure of the joints usually occurred along the IMC layer or in the weld metal.

Autogenous laser welding-brazing was also investigated (Peyre et al., 2007). The laser beam was positioned onto the aluminium in order to only melt the edge of the sheet metal. The joints were formed by reactive wetting of the molten aluminium on the steel surface, as shown in Figure 1-9.

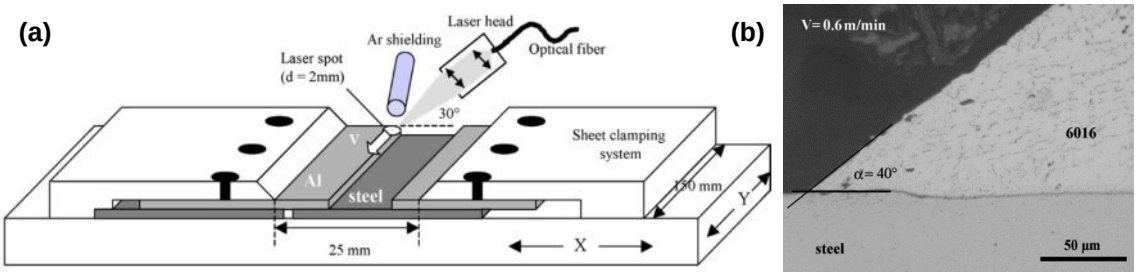

Figure 1-9: Laser welding-brazing (a) Schematic representation of the experimental setup and (b) micrograph of the fusion zone of the joint (Peyre et al., 2007).

The IMCs formed a thin layer along the steel-aluminium interface as opposed to laser keyhole welding, where the IMCs could be found in the entire fusion zone. The IMCs were mainly $FeAl_3$ and Fe_2Al_5 and the mechanical tensile-shear strength of the joints was low and the specimens had interfacial shear failure.

Laser plus welding wire was used to braze aluminium to steel (Dharmendra et al., 2011; Korte et al., 2005; Mathieu et al., 2007; G. Sierra et al., 2008). The interaction between both metals using this technique was minimal and consequently, sound dissimilar joints were produced with mechanical strength either identical or near to that of the weaker of the two metals (steel or aluminium, depending on the cross-sectional area of the coupon). An alternative technique was assessed in which a rolling system was combined with the laser (Kreimeyer et al., 2004; Ozaki and Kutsuna, 2009; Rathod and Kutsuna, 2004). The principle of this technique is to heat the substrate with the laser and immediately apply pressure on the soft metal with a roller to improve the contact between the metals and thus the bonding. This way sound joints could be produced with an IMC layer thickness of less than 10 µm (many researchers have

considered 10 µm as a reference maximum value of IMC layer thickness for an acceptable steel to Al joint (Schubert et al., 1997)).

The cold metal transfer process, or CMT, is a variant of gas metal arc welding (GMAW). It is claimed to be “colder” than the conventional GMAW processes due to the innovative way of droplet detachment and process control. The effect of the lower heat input is observed in the thickness of the IMC layer when producing Fe-Al lap joints using a brazing technique with an Al-Si welding wire (Padmanabham et al., 2013). These researchers found that the IMC layer thickness was halved when using CMT in comparison to pulsed MIG. After over 20 years Fronius has claimed to have produced successful joints between galvanized steel and aluminium sheets with the patented $AlSi_3Mn_1$ welding wire (Transfer, 2012). The failure of the joints always occurred at the aluminium sheet.

Most of the research so far has been oriented towards the automotive industry. Thus, only small gauge sheets (~1 mm thick) of steel and aluminium have been used. For naval applications, where thick plates are used, only a few studies were found, with a special focus on the laser-GMAW hybrid process, where 3 mm plates of steel and Al were joined in a butt joint configuration (Thomy et al., 2007). Thomy *et al*. combined two welding processes, laser and GMAW as represented in Figure 1-10, and by this way they managed to decrease the IMC layer thickness to a minimum value of 1 µm and thus, increase the joint strength to a maximum value of 140 MPa. The leading laser beam and the MIG torch were positioned on the aluminium plate, close to the Fe-Al interface, with a fixed gap between them. The filler wire supplied by the GMAW torch provides the material necessary for the bonding of the two plates. The advantages of this process are good gap tolerance, the possible addition of alloying elements in the weld seam (by changing the composition of the filler material) and lower temperatures in the joining process, both inducing a thin IMC layer (in this work the thickest IMC layer observed was 3 µm). Compared to the laser welding process, the hybrid laser-MIG process is more complex because the latter requires not only the control of the laser parameters but also the GMAW parameters and the relative position between the laser beam and the GMAW torch.

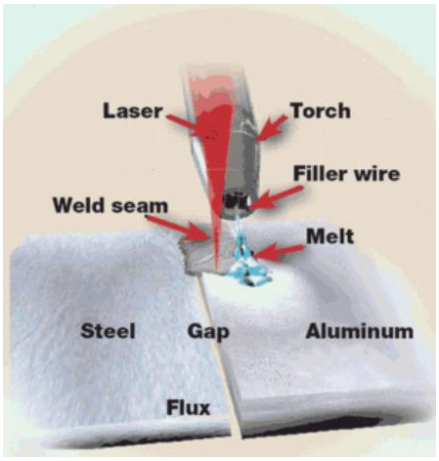

Figure 1-10: Hybrid laser-GMAW welding of steel to aluminium (Thomy et al., 2007).

1.4 Weld metal engineering to create a bridge between Fe and Al

An alternative approach to create sound joints between steel and aluminium is by preventing the reaction between Fe and Al during the joining process. By introducing a transition metal, so called interlayer, a diffusion barrier is created between both metals. Ideally the interlayer needs to be metallurgically compatible with both Al and Fe to avoid the formation of brittle IMCs. However, the elements compatible with both Fe and Al are not suitable for the majority of the applications either due to their low melting temperature or due to their poor mechanical properties. There are five elements which do not form any IMCs neither with Al nor Fe, viz. mercury (Hg), potassium (K), sodium (Na), indium (In) and lead (Pb). The melting temperature of Hg, K, Na and In is lower than 150 °C. Pb has higher melting temperature (327 °C) than the previous elements but it has poor mechanical strength when compared to that of aluminium (UTS_{Pb} = 12 MPa and UTS_{Al} = 45 MPa). Therefore, an alternative solution is to choose elements that only form IMCs with one of the elements, either Al or Fe. There are only a few elements which are compatible with Al, viz. zinc (Zn), tin (Sn) and silicon (Si), and compatible with Fe there are copper (Cu), silver (Ag), gold (Au) and manganese (Mn). Considering the cost, the melting temperature and the mechanical properties of the elements, Cu seems to be the most suitable element to create a bridge between the Fe and Al.

There is only limited information about the application of interlayers in Fe-Al joints to prevent the diffusion between Al and Fe. For instance, a 0.2 mm thick foil of tantalum (Ta) was used between steel and aluminium in a butt joint configuration (Mukherjee et

al., 2010). The researchers used laser welding to join the metals. Ta is a refractory material and thus, it has a very high melting temperature compared to that of steel or aluminium. The results were successful and the authors showed that even with partial dissolution of Ta into Al and into Fe during the joining process, there were no signs of IMCs (Fe-Ta, Al-Ta or Fe-Al). Instead, in the fusion zone there was only solid solution of Ta into Al and Ta into Fe. The strength of the joints was not measured.

1.5 Effect of alloying elements on Fe-Al reaction

Even though time and temperature are the main parameters in the reaction between Fe and Al, it is also known that the addition of alloying elements may affect the rate of interdiffusion and thus, the thickness of the IMC layer.

A study was done to determine the values of activity coefficients of Al atoms in α-$Fe_{0.95}(Al_{1-n}X_n)_{0.05}$ alloys in which X represents the alloying element added to the dissimilar metal mixture (Akdeniz, 1998). The results showed the existence of two main groups of alloying elements, the ones which reduce the diffusion of Al into α-Fe and therefore, minimize the thickness of the IMC layer, and the other group which enhances the diffusion of Al into α-Fe and the growth of the IMC layer. Table 1-4 shows the two groups with the respective alloying elements.

Table 1-4: List of alloying elements with regard to their effect on the diffusion of Al in the reaction layer and consequently, in the IMC layer growth (Akdeniz, 1998).

Alloying elements which minimize the Fe-Al IMC layer growth	Alloying elements which enhance the Fe-Al IMC layer growth
Si, Ti, Ge, Sb, Mg, Cu, Ca, Ag, Cd, Cr	Co, Zn, Mn, Ni, Pb, Bi

Shih *et al*. also studied the effect of the alloying elements on the IMC growth (Shih and Tu, 2007). The authors used the hot dipping process with a steel bar dipped in different molten Al alloys (pure, Si, Mg and Si-Mg based) during different time intervals (between 3 and 60 minutes) at constant temperature of 700 °C. They found that Si diffuses to the reaction layer reducing the Al diffusion and thus, acting as a diffusion barrier which restricts the growth of Fe-Al IMCs. This theory is supported by other workers who found that instead of the formation of $FeAl_3$ initially, there is a new layer formed $Fe_xSi_yAl_z$ which acts as a barrier to diffusion (Akdeniz, 1998). In another study

using a similar approach, a ternary phase ($Fe_xSi_yAl_z$) was also found in a form of fine particles distributed inside the Fe_2Al_5 layer (Yin et al., 2013). This author suggested that the reduction in IMC layer thickness with the increase in Si content in the aluminium bath was due to the penetration of Si atoms inside the vacancies of the Fe_2Al_5 structure. Thus, the Si atoms restrict the easy interdiffusion of Fe and Al in the Fe_2Al_5 phase.

The addition of Mg in the aluminium alloy also seems to reduce the Fe-Al reaction but only after a long dipping time (more than 10 minutes) (Shih and Tu, 2007). This work showed that Mg reacts with Al and forms a binary Al-Mg reaction layer between the Fe-Al layer and the molten aluminium which slows down the Fe-Al reaction. In comparison to Si, for a dipping time of three minutes, the addition of Mg formed a thicker IMC. A molten bath containing simultaneously Si and Mg formed the thinnest IMC layer. It seems that there is a combination of the effects previously described in this alloy which minimizes the Fe-Al IMC growth.

In another study, the IMC thickness could be reduced by increasing the Cu content in the aluminium alloy (Yousaf, 2011). However, after a certain concentration the IMC could not be further reduced, as indicated in Figure 1-11. A similar trend is observed when Si is added into the aluminium alloy (Figure 1-11b). The author suggested that the additional alloying elements fill the vacancies thought which the Al atoms flow to react with Fe and produce the IMC layer.

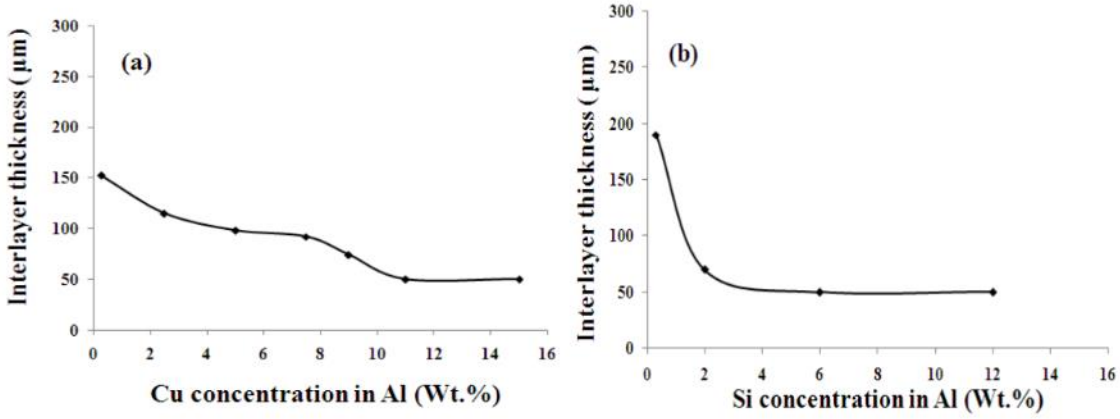

Figure 1-11 : Thickness of the IMC layer of specimens aluminized at 800 °C in (a) Al-Cu alloys for one minute and (b) Al-Si alloys for two minutes (Yousaf, 2011).

One may argue that the conclusions taken for the Fe-Al IMC formation and growth are not valid in fusion joining. The conclusions were based on hot-dip aluminizing and diffusion experiments which occur in isothermal conditions and for much longer periods of time than in fusion joining. However, the results obtained in the fusion joining processes are similar to the ones previously described. Agudo et. al analysed and compared the IMC phases formed in hot-dip aluminizing with those formed in CMT brazing of aluminium alloy to galvanized steel with a nearly pure aluminium welding wire (Agudo et al., 2007). The authors found similar IMC phases (Fe_2Al_5 and $FeAl_3$) in both processes but the IMC layer was much thinner when using CMT welding due to the short interaction time of the heat source with the material. They also found that the ratio of Fe_2Al_5 to $FeAl_3$ was nearly 1 to 1 in the welded joints whilst in hot-dip aluminizing the ratio was up to several orders of magnitude bigger. Many other studies were carried out to assess the effect of the alloying elements on the Fe-Al reaction by varying the chemical composition of the welding wires. Once again there are many similarities in the results obtained between the welding processes and the hot-dipping experiments.

A less investigated metallic joint combination is hot-dip aluminized (Al coated) steel to aluminium. Similar to Zn in galvanized steel, the Al coating also intends to improve the wettability of molten aluminium onto the steel surface. However, it was proved by using CMT brazing as a joining process that the Zn coating is more effective than an Al coating for the wetting of Al on the steel surface (Kang and Kim, 2015). Despite this result, it was found that by using aluminized steel instead of the galvanized steel the IMC layer was thinner and the mechanical strength was higher (Kan and Kim, 2013) (Kang and Kim, 2015). It was suggested by the authors that during hot-dip aluminizing of the steel sheet a thin $Fe_x(AlSi)_y$ IMC layer is formed and this layer creates a diffusion barrier against Al-Fe diffusion. Thus, the presence of the $Fe_x(AlSi)_y$ IMC layer suppressed the growth of the IMC layer.

The effect of the thickness of the pre-formed $Fe_x(AlSi)_y$ IMC layer on the Fe-Al reaction during the joining process was also assessed. The hot-dipped aluminized coupons were heat treated to induce further growth of the pre-formed IMC layer to about twice of its initial thickness. Then, the coupons were joined to aluminium with a AA5183 welding wire (Mg based). The results suggested that a thicker $Fe_x(AlSi)_y$ IMC layer also reduces the diffusion of Al and Fe atoms. There was no further growth of the IMC

layer and the layer was more uniform, similar to what was previously found when using the Si based welding wire. However, the morphology of the IMCs formed with the AA5183 was still tong-like, as opposed to the flat IMC layer formed when welding with Si based wire. Based on these results the authors thought that the suppression mechanism of the IMC layer growth when using AA5183 is different than with AA4047 welding wire (Si based). When a Si based wire is used, the Si occupies the vacancies in the Fe_2Al_5 crystal and suppresses the diffusion between Fe and Al, therefore forming a flat IMC layer instead of the tong-like morphology. If this is true, when using the Mg based wire and higher heat input the IMC layer may grow even further.

The effect of Si content on the IMC layer growth is shown in Figure 1-12 (Kang and Kim, 2015). As described before in hot-dip aluminizing experiments, in fusion welding a higher Si content in the welding wire also suppresses the formation of IMCs and the IMC layer loses the tong-like morphology. Moreover, the addition of Mg is not as effective as addition of Si to reduce the IMC layer thickness.

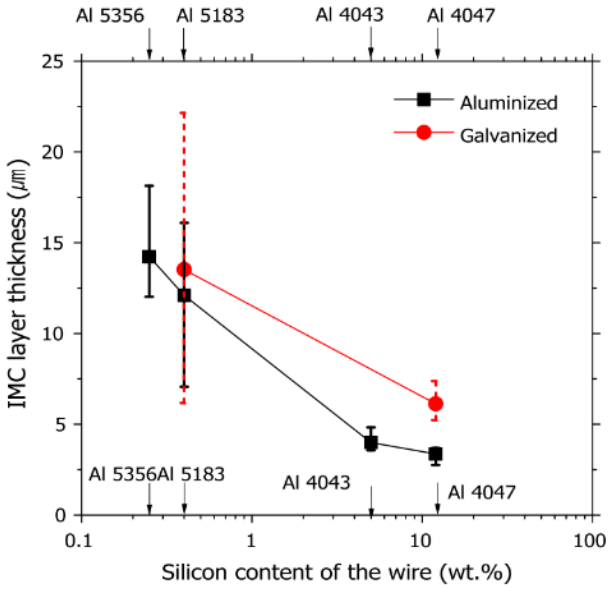

Figure 1-12: Effect of the Si content on the IMC layer thickness formed in joints of galvanized steel/AA5052 and aluminized steel/AA5052. CMT brazing was the joining process used (Kang and Kim, 2015).

In terms of the effect of the alloying elements on the mechanical properties of the joints, the joints brazed with a Si based wire were less strong than the joints brazed with a Mg based wire. Even though the IMC layer was thinner with a Si based wire, near the fusion zone there were defects such as micro-cracking which undermined the

joint strength. On the other hand, the authors suggested that the positive results obtained with the Mg based wire were due to the perpendicular orientation of the IMC grains in relation to the load applied during the mechanical test. They believe that there is a mechanical anchoring of the IMCs into the steel made which makes the joints stronger.

In arc welding experiments, more specifically using Gas Tungsten Arc Welding (GTAW) with welding wires of different compositions, it was also found that a higher content of Si (Al-12%Si instead of Al-5%Si) also seems to restrict the formation of Fe-Al IMCs (Dong et al., 2012). On the contrary, the addition of Zn to the fusion zone, by using a Zn-15%Al wire, enhanced the reaction between Fe and Al which led to the formation of a thicker IMC layer (10 µm compared to the 2 µm thick layer found in the joint welded with the Al-12%Si wire) and a premature failure of the lap welded joint when tested to failure (55% less strong than the joint welded with Si based wire). Compared to the Si-based welding wire, the addition of Cu reduced the joint strength by 23% and induced the formation of Al_2Cu IMCs.

1.6 Interaction of copper with aluminium and iron

Figure 1-13 and Figure 1-14 show the binary Al-Cu and Cu-Fe phase diagrams, respectively. The Al-Cu phase diagram shows many intermediate phases stable at room temperature such as phase θ (Al_2Cu), η phase (AlCu), ζ_2 phase, δ phase (Al_2Cu_3) and γ_2 phase ($AlCu_2$) (Rabkin et al., 1970). The hardness of the Al-Cu IMCs is lower than the ones formed during the Al-Fe reaction, where hardness can reach up to 1100 HV (Olsen, 2009) (see Table 1-5). Nevertheless, the Cu-rich IMCs are harder and more brittle than the Al-rich IMCs but it has been reported that these IMCs are less sensitive to cracking (Kouters et al., 2011). On the other hand, the Cu-Fe phase diagram doesn't show any intermediate phase formed between both elements, although there is solid solubility between Cu and Fe (Figure 1-14).

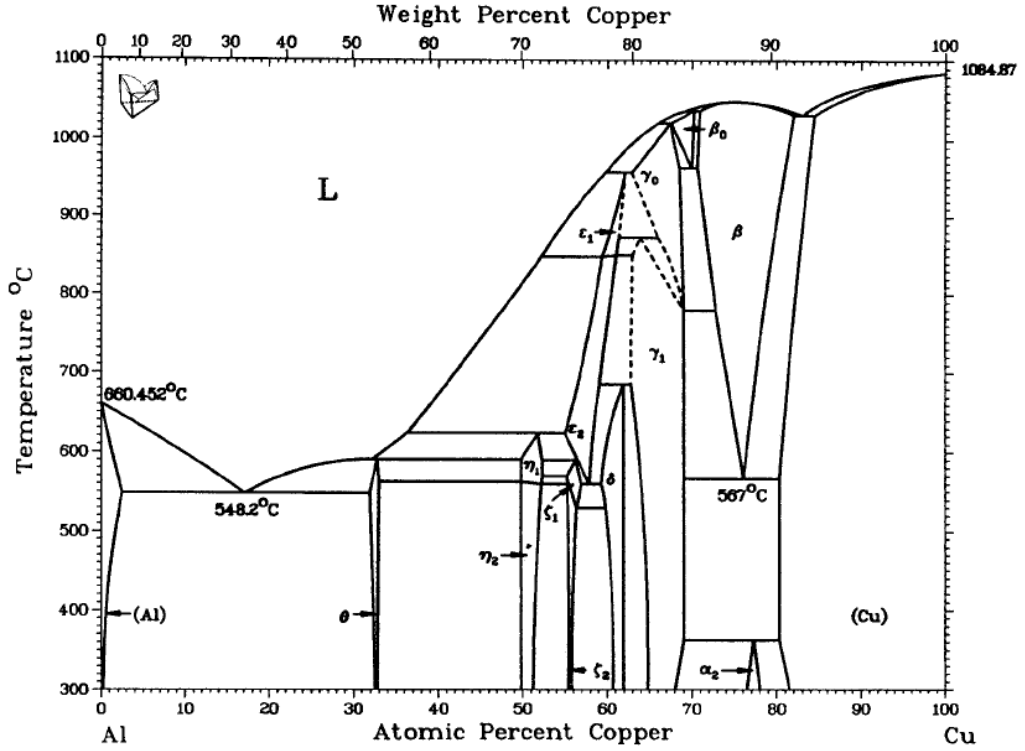

Figure 1-13: Binary Al-Cu phase diagram (Massalski, 1986).

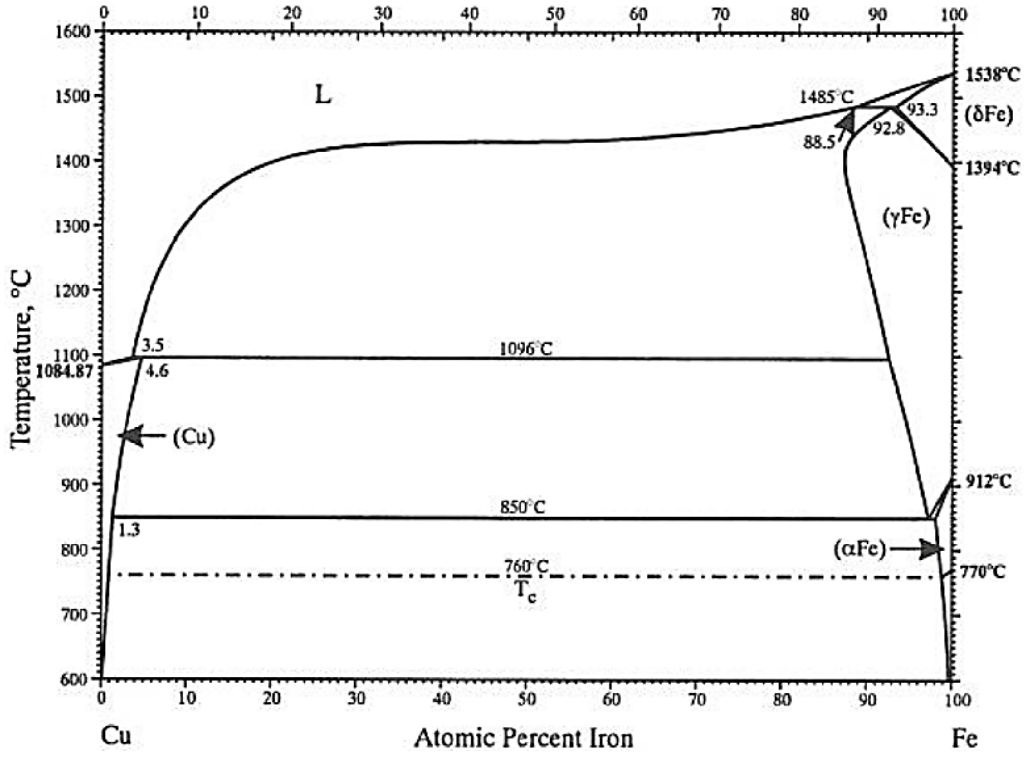

Figure 1-14: Binary Cu-Fe phase diagram (Okamoto, 2000).

Table 1-5: Physical properties of Al-Cu IMCs (Wulff et al., 2004).

Phase	Concentration (At. % Cu)	Crystal structure	Color	Hardness HV5	Resistivity ρ (μΩ cm)	CTE (ppm/°C)	Density (g/cm^2)
Al	0.0 – 2.84	cubic	silverish	20– 50	2.4	2.35	2.70
$CuAl_2$	31.9 – 33.0	tetragonal	white-yellow	324	7.0 – 8.0	1.61	4.36
CuAl	49.8 – 52.3	monoklin	gray	628	11.4	1.19	2.7
Cu_4Al_3	55.2 – 56.3	monoclinic	white-yellow	616	12.2	1.61	NA
Cu_3Al_2	59.3 – 61.9	trigonal	white-gray	558	13.4	1.51	NA
Cu_9Al_4	62.5 – 69	cubic	white-light yellow	549	14.2 – 17.3	1.76	6.85
Cu	80.3 - 100	cubic	red	60-100	2.0	1.73	8.93

Despite the Al-Cu IMCs formed during the reaction between Al and Cu, Cu is still an alternative element to create a bridge between Al and Fe. It can be easily used in the industry because it is commercially available and it is less expensive than the other elements compatible with Fe. Moreover, it is possible to have a solid solution between Al and Cu. It was found that the maximum solid solubility of copper in aluminium was 2.7 at.% and that of Al in Cu is 18 at.% (Okamoto, 2000)(Feng et al., 1991).

Ternary phases are expected to grow in joints produced between steel and aluminium when copper is used as an interlayer. Figure 1-15 shows a modified ternary Al-Cu-Fe phase diagram in which colours were used to ease the identification of the IMC.

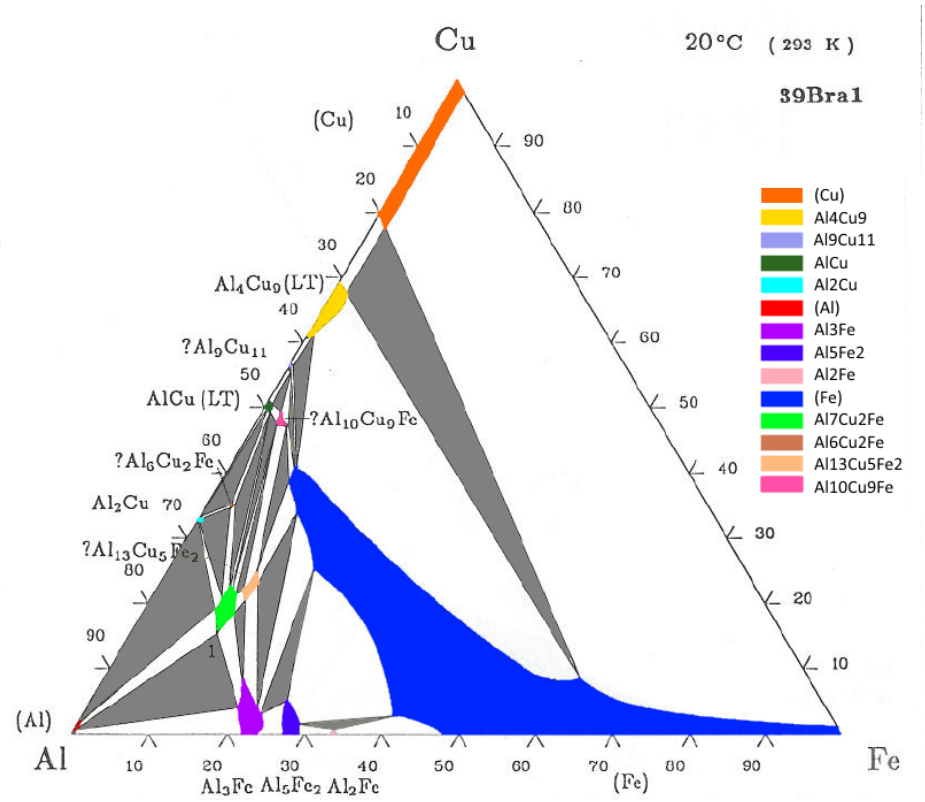

Figure 1-15: Ternary Al-Cu-Fe phase diagram (in at.%) (Villars et al., 1995).

The white areas represent the solution of two IMCs and the grey areas represent the solution of three IMCs.

The formation and growth of the Al-Cu IMCs are similar to what was previously described for Fe-Al IMCs. The reaction and interdiffusion of Al and Cu atoms at the joint interface is sensitive to temperature and because of the brittle behaviour of the IMCs formed, the joints may be susceptible to a premature failure. Joining of copper wires to aluminium pads was studied aiming at the electronics industry. Kim et.al reported that moderate IMC growth increases the joint strength by alloying between the copper wire and the aluminium pads (Kim et al., 2003).

The effect of the alloying elements on the mechanical strength of the Al-Cu joints was investigated during laser welding with $AlSi_{12}$ and $CuSi_3$ filler wires in a butt joint configuration (see Figure 1-16) (Weigl et al., 2011).

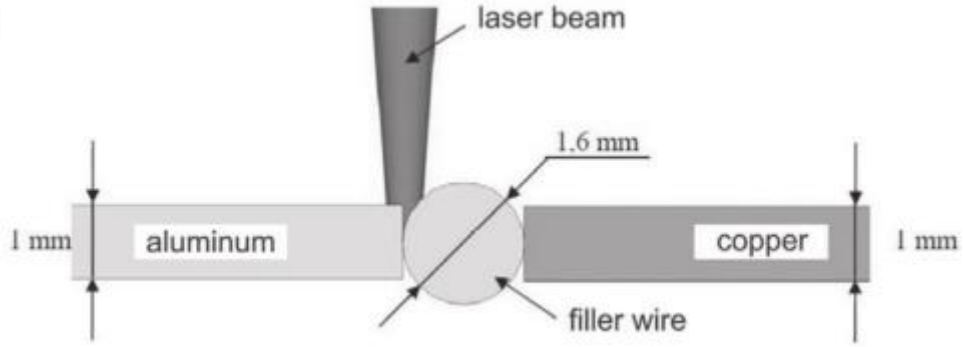

Figure 1-16: Schematic representation of laser welding of aluminium and copper sheets with $AlSi_{12}$ and $CuSi_3$ filler wires (Weigl et al., 2011).

The researchers found that the joints welded with $AlSi_{12}$ had higher mechanical strength than the ones welded with $CuSi_3$ wire. The fusion zone of the joints welded with $AlSi_{12}$ had lower hardness and the joints were more ductile. The authors proposed that the higher content of Si in the welding wire increases the turbulence in the fusion zone and this improves the stirring effect of the elements in the fusion zone and therefore, a reduction in local formation of IMC near the Cu substrate, where usually harder IMCs are formed due to higher Cu content.

One interesting result was observed by Abbasi et al. in a study where Al-Cu joints were produced by cold roll bonding and then heat treated at 250 °C for different periods of time (from 1 to 1000 h) (Abbasi et al., 2001). Five distinct sub-layers were visible on

the transition between Al and Cu. In a diffusion-controlled process and considering the Al-Cu binary phase diagram, one would expect to see a smooth variation from low to high Al-content across the IMC layers. In fact, a solid solution of Al in Cu was found in the middle of the IMC layers, as shown in Figure 1-17. The authors justified this result by the presence of Si and Fe in small quantities (0.12 and 0.22 at.%, respectively) in this region. The authors believe that the formation of the IMCs is suppressed by the presence of these impurities.

It was reported that a protective alumina coating is formed on the Cu solid solution when aluminium is in a concentration higher than 9 at.%. If Al is in lower concentration it acts as a contaminant and increases the susceptibility for oxidation of the copper solid solution (Plascencia et al., 2005). The increased oxidation of the copper solid solution when aluminium is less than 9 at.% is shown in Figure 1-18 (Kouters et al., 2011). The same figure shows the Kirkendall plane in ɣ-phase formed due to the presence of contamination at the interface which can mechanically weaken the joint strength.

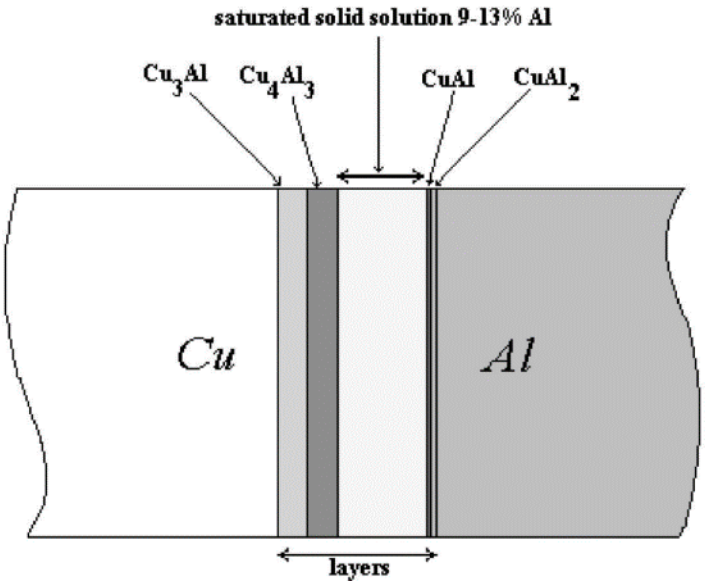

Figure 1-17: Schematic representation of the IMC layers formed during heat treatment at the Cu-Al joint interface (Abbasi et al., 2001).

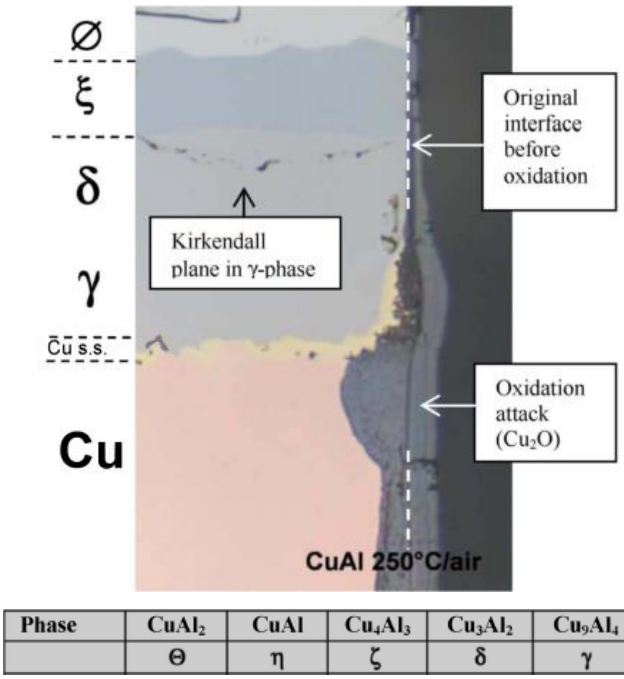

Phase	$CuAl_2$	CuAl	Cu_4Al_3	Cu_3Al_2	Cu_9Al_4
	Θ	η	ζ	δ	γ

Figure 1-18: Oxidation of the copper solid solution when aluminium is less than 9 at.% in a diffusion bonded sample (Kouters et al., 2011).

1.7 FEM of dissimilar joints

All fusion joining processes occur in transient conditions and it is not possible to control temperature and heating time independently. The IMC layer thickness and the weld geometry (in particular weld width which determines the bonding area) are resultant from the thermal cycle applied to the joint. Therefore, to control these two factors it is necessary to understand the thermal cycle and their dependency on it. FEA is a useful tool to estimate the thermal cycle under different welding conditions, i.e. different energy levels. In laser welding there are only a few research papers published where the IMC layer thickness is correlated with time and temperature. Fan et. al. measured the thermal cycle at the interface between steel and aluminium and correlated the peak temperature and cooling time with the laser power and IMC layer thickness (Fan et al., 2011). The results showed that the IMC layer thickness varies with those factors, viz. peak temperature and cooling time. It is important to note that in fusion joining processes as temperature and time are inter-dependent parameters, therefore, when temperature increases, the time the joint is above a certain temperature also increases. However, the authors have not considered the two other important laser processing parameters, travel speed and laser beam diameter. FEA was used by Borrisutthekul *et al*. to predict the transient thermal cycle at the interface of the lap

joints (Borrisutthekul et al., 2007). In this case the authors only assessed the influence of welding speed (or travel speed) and the material of the backing bars (heat sink) on the IMC layer growth. They showed that higher travel speeds and backing bars made of high thermal conductive materials minimise the IMC layer thickness. Once again, the authors have not considered the effect of laser power and laser beam diameter in the IMC layer growth.

1.8 Welding processes used in this work

1.8.1 Autogenous laser welding

Laser processing is getting very popular in manufacturing due to the numerous advantages that this process has to offer when compared to the traditional welding processes. Lasers have also been used for many years in the investigation of dissimilar metal joining with several metallic combinations (*Laser Materials Processing (Google eBook)*, 1983). Due to the high power density heat source, laser offers significant advantages in terms of low energy process and resulting lowering in component distortion. Laser beam can also be applied with high precision in positioning resulting controlled mixing of the participating alloys. The versatility of lasers permit them to be integrated with other systems such as arc welding processes (hybrid laser-arc welding) or rolling (laser-roll bonding). The process can be operated with or without filler material. If no filler material is used the process becomes autogenous.

Depending on the level of power density used lasers can be operated in conduction or keyhole mode (Assuncao, 2012). Laser welding in conduction mode brings many benefits to the welding process. Because of the larger beam diameter used, there are fewer problems with the fit up tolerance, the weld pool temperature is maintained below the vaporisation point which helps in achieving a stable and controlled welding process and fewer defects in welds produced under this mode. However, compared to keyhole mode laser welding, conduction mode results in significantly more total energy transferred to the material.

Keyhole mode is induced when high power densities are used and it is characterized by the high depth to width ratio of the fusion zone, metal vaporization and projection of molten metal. When joining steel to aluminium by laser keyhole welding mode

metals are melted and mixed together which enhances the reaction between the intervenient elements and thus, the formation and growth of the IMCs.

1.8.1.1 System parameters versus fundamental laser material interaction parameters (FLMIP)

In research and industrial applications of laser welding, the vast majority of results are presented in terms of the laser system parameters, such as laser power (*P*), travel speed (*TS*) and laser beam diameter (D_{beam}). However, these parameters alone are not sufficient to describe the interaction of the laser beam with the material. Welding experiments using the fundamental laser material interaction parameters (*FLMIP*), which include power density (*PD*), interaction time (t_i) and specific point energy (E_{sp}), have proven to be able to fully characterize the laser welding process (Suder and Williams, 2012).

Within the defined fundamental laser material interaction parameters, power density is defined as the ratio of the power to the applied area of the spot as shown in equation 1-5. This parameter is one of the chief determinant of welding mode (conduction and keyhole) (Ion, 2005). Interaction time is defined by the ratio of travel speed to the laser beam diameter and signifies the irradiation time of an infinitesimal element within a circular laser beam. Calculation of interaction time (t_i) is shown in equation 1-6. The total laser energy delivered within a spot designated here as specific point energy is shown in equation 1-7 which is the product of power density, interaction time and the total area of the laser beam (A_{beam}) (Hashemzadeh et al., 2014).

- Power density, MW.m^{-2} $$\mathrm{PD} = \mathrm{P}.\mathrm{A}_{\mathrm{beam}}^{-1} \quad (1\text{-}5)$$
- Interaction time, s $$\mathrm{t_i} = \mathrm{D_{beam}}.\mathrm{TS}^{-1} \quad (1\text{-}6)$$
- Specific point energy, kJ $$\mathrm{E_{sp}} = \mathrm{PD} \times \mathrm{t_i} \times \mathrm{A_{beam}} \quad (1\text{-}7)$$

The researchers who investigated the FLMIP emphasized that the results are transferrable between different laser systems if this set of parameters are used (Assuncao et al., 2012) (Suder and Williams, 2014) and showed direct correlation between FLMIP, thermal profile and weld metal geometric profile. It is known that each laser system is almost unique because it can have many combinations, viz. maximum power, beam diameter and processing speed. Thereby, it is difficult to replicate results in different laser systems. The power factor model is a tool that was developed by

Cranfield University to allow the transferability of the results from laser to laser. In keyhole welding, the weld profile is controlled by E_{sp} and PD. The power factor is a combination of these two parameters in a single equation and it is written as the ratio between laser power and beam diameter, as showed in equation 1-8.

- Power factor, W.m^{-1}

$$PF = P.D_{beam}^{-1} \quad (1\text{-}8)$$

It was proven that the depth of the penetration of the welds is independent of the laser beam diameter if the power factor and interaction time remain constant (see Figure 1-19b). Based on these two parameters, it is possible to create similar welds in different laser systems. The laser user only needs to follow the procedure that is represented in Figure 1-19a and described below:

(1) Identify the values of PF and t_i for the required weld geometry, based on the power factor model represented in Figure 1-19b;
(2) Identify the constrains of the laser system in use, i.e. beam diameter, maximum power or processing speed
(3) Calculate the system parameters to use based on equations 6 and 8.

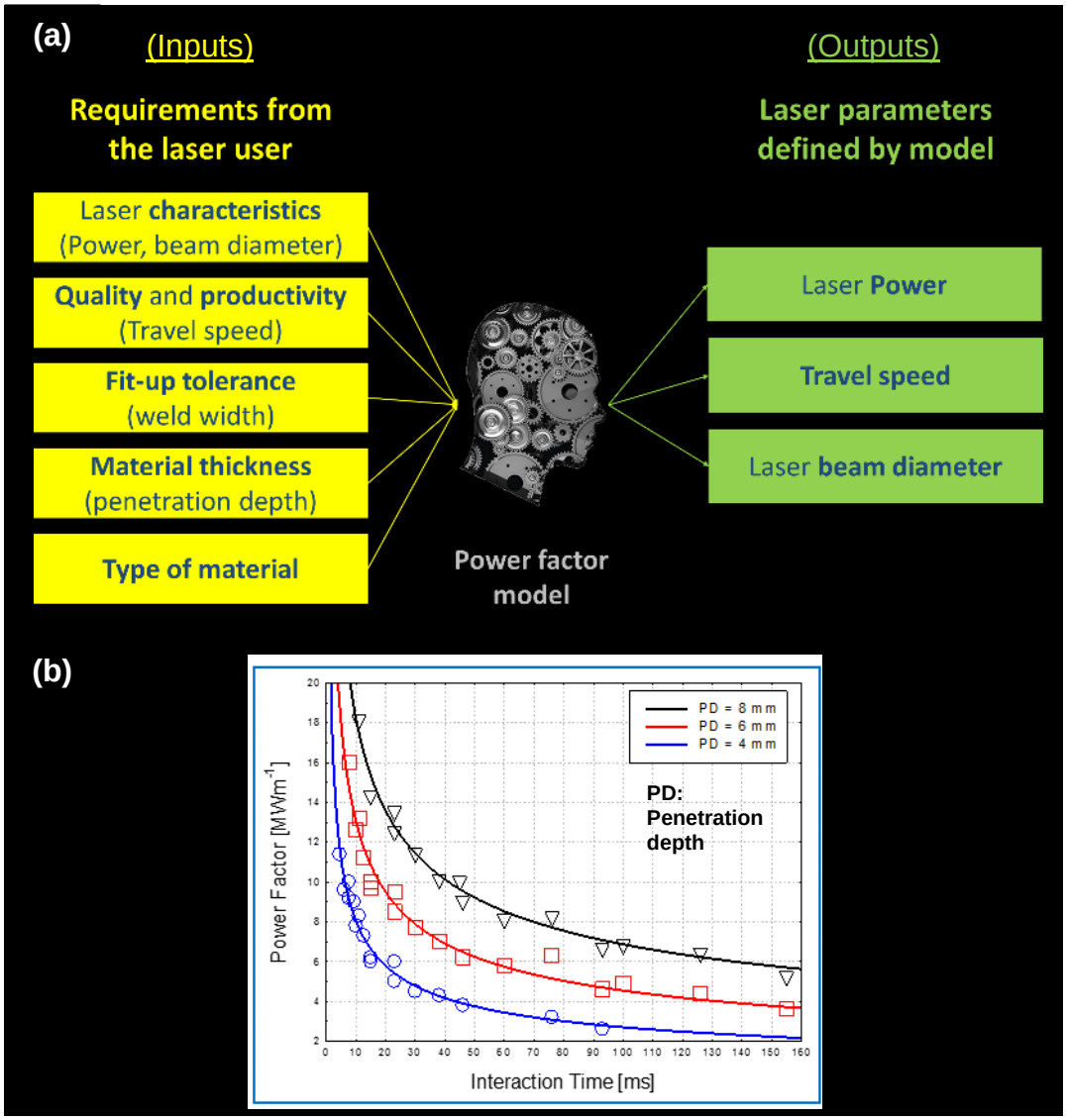

Figure 1-19: (a) Schematic representation of the mechanism to determine the system parameters and (b) power factor model.

1.8.2 CMT welding process

Cold Metal Transfer, or CMT, was launched in 2005 by Fronius and it is a variant of the gas metal arc welding (GMAW) process. Both processes have in common the way the energy is produced. An electric arc is established between the continuous filler metal electrode and the weld pool and the mode of metal transfer is by short circuiting (AWS, 1991). However, CMT differs from the conventional GMAW process in the way the material is transferred to the substrate. Instead of the droplets of molten wire being detached by electromagnetic forces generated by a peak on the welding current, in the CMT process when the power source detects a short circuit, the welding current drops to a lower level and the filler wire is retracted, causing the detachment of the

droplet to occur by inertia. CMT is then a low heat input process which permits welding of thin sheets with no distortion, with high speed rates. Clean and spatter-free metal deposition is possible due to highly controlled droplet detachment provided by the wire retraction.

This process has been applied in the automotive industry to weld thin panels made of steel but it has also been used in the investigation of dissimilar metal joining, more specifically steel and aluminium. Fronius International have reported successful joints between galvanized steel and aluminium using the CMT process. With low level of heat insertion, using CMT the filler wire is mixed with molten aluminium substrate and this mixture then wets the galvanized steel (Zhang et al., 2009)(Padmanabham et al., 2013).

CMT welding process is relatively easy to automate and easy to operate. There are several welding modes available in the power source and each contains several programs according to the material in use. The CMT Advanced power source has the following welding modes: CMT Standard, CMT Pulse, CMT Advanced and CMT Advanced Pulse. The differences between these welding modes are represented in Figure 1-20.

CMT Standard works with direct current electrode positive which means the electrode has positive polarity. The wire moves forward and when it touches the melt pool the arc is extinguished. At this time the welding current drops and the filler wire is retracted. The droplet detachment occurs by inertia. The filler wire then moves forward and the cycle is repeated. This process occurs at very high frequency, up to 90 droplets being deposited into the molten pool per second. The manufacturers also managed to boost the frequency up to 130 Hz (Fronius, 2013).

The CMT Pulse combines a pulsing cycle with a CMT cycle which results in a higher heat input. The transfer mode is known as spray mode (AWS, 1991) which means that during the pulsing cycle small droplets are transferred to the substrate at high energy levels.

- **CMT Standard – CMT cycles in single phase with welding wire in positive phase (DCEP phase)**

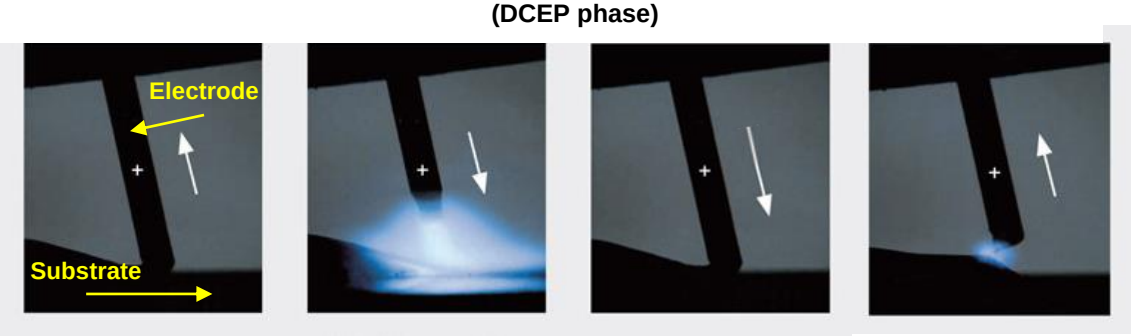

- **CMT Pulse – Combination of CMT and pulsing cycles, in single DCEP phase**

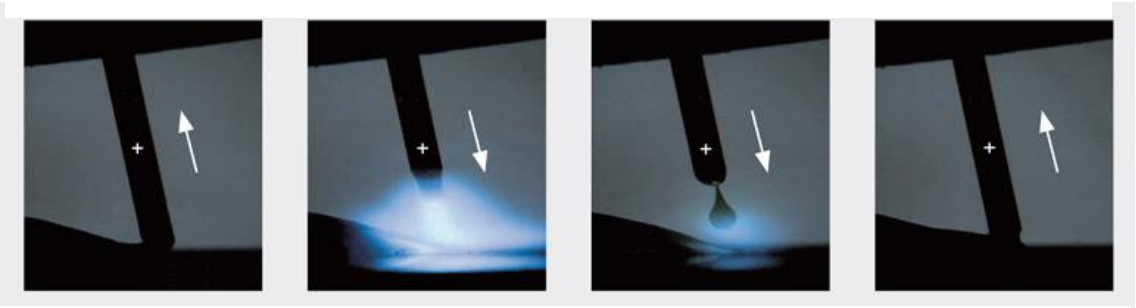

- **CMT Advanced – CMT cycles alternating between positive and negative phases (AC)**

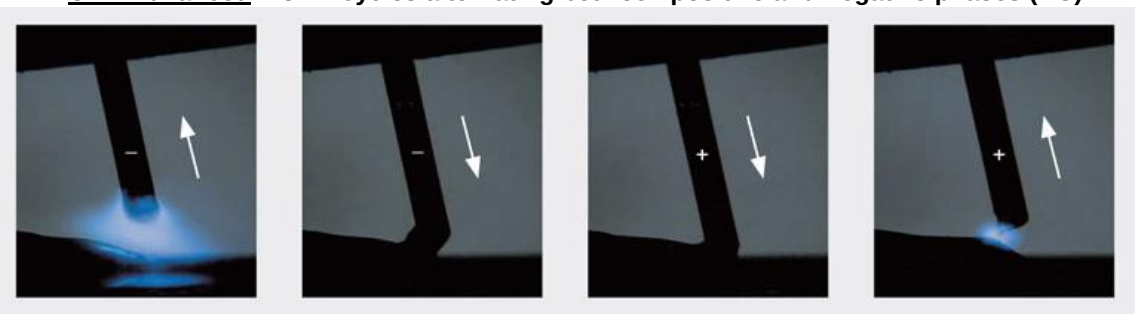

- **CMT Advanced Pulse – Combination of CMT negative and positive pulsing cycles (AC)**

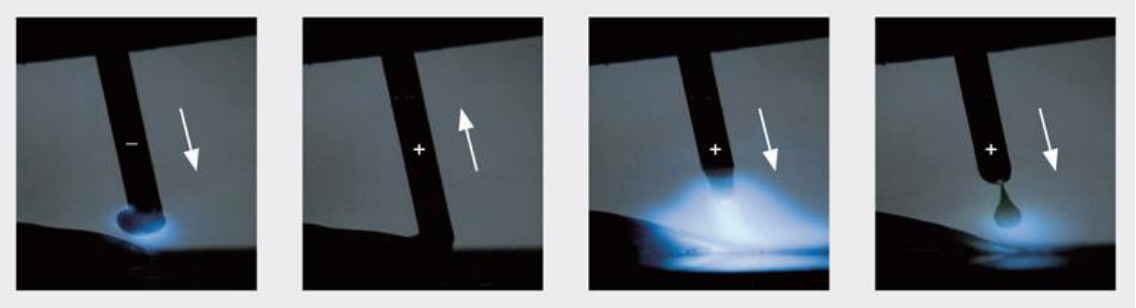

Figure 1-20: Images from a high-speed camera showing the differences of polarity and metal transfer mode of CMT Standard, Pulse, Advanced and Advanced Pulse (Fronius, 2014).

The CMT Advanced operates in alternate polarity of the welding current. The polarity inversion happens during the period of short circuit avoiding arc instability. The positive phase enhances penetration whereas the negative phase increases the deposition

rate with similar level of heat input. It is then possible to alternate between high deposition rate and low thermal input during the welding process.

CMT Advanced Pulse alternates between negative CMT phases with reversing wire movement and short-circuiting transfer mode and positive pulsed arc phases with continuous wire feed and spray transfer mode.

Maintaining the quality, the CMT Advanced and Advanced Pulse permit welding of thin and very thin sheets and bridging of larger and uneven gaps. Moreover, this technology permits to achieve the same deposition rate with a lower thermal input.

Each program has a specific synergic curve which facilitates the process operation. According to the wire feed speed defined by the user, the power source adjusts the welding voltage and current to attempt the stabilisation of the welding process.

CMT Advanced was mainly developed to applications which demand a low and adjustable heat input. For this reason in this project this mode was used.

1.8.2.1 Heat input calculation

Waveform-controlled welding enables an operator to establish the amount of energy used in the welding process and then correlate the process energy with the weld geometry, heat affected zone and microstructure of the weld. The heat input, or Q, can be calculated using equation 1-9, where k (non-dimensional) is the thermal efficiency of the welding process, V (Volt) and I (Ampere) are welding voltage and current, respectively, and v (millimetre per second) is the travel speed, or welding speed (E N British Standard, 2009).

Heat input, kJ.mm^{-1} $$Q = k\frac{V.I}{v}.10^3 \quad (1\text{-}9)$$

The process efficiency included in the equation enables comparison between different arc welding processes. According to the standard BS EN 1011-1:2009, the thermal efficiency for GMAW is 0.8. However, Pepe *et al*. used a liquid nitrogen calorimeter to determine the process efficiency for CMT and the authors found that the process efficiency was 0.85 (Pépe et al., 2011).

1.9 Summary

The literature review on dissimilar metal joining techniques showed that IMC formation is extremely sensitive to the thermal field produced by the joining process. For this reason it is important to consider a low energetic joining process which simultaneously allows control of the energy applied to the joint and gives flexibility to weld in different joint configurations to control the dilution of one metal into another. It was found that it is important to reduce the mixing of elements in the liquid state to supress the reaction between Fe and Al.

Even though the solid state joining processes minimize the Fe-Al IMC formation, the fusion processes offer more dimensional and joint configuration flexibility. Among the fusion joining processes, laser welding permits transfer of energy to a small spot on the material with a very fast heating and cooling rate and leaves a small heat affected zone. Because of the formation of brittle IMCs which are sensitive to temperature and time, it is important to control the processing energy and if possible, create a joint between solid steel and liquid aluminium. The use of interlayers can be also important to minimize or avoid the diffusion between Al and Fe. Copper is a possible candidate due to its availability and relatively low cost. It was shown that alloying elements play an important role on the formation of the IMCs. Si was found to be the most effective alloying elements to suppress the reaction between Fe and Al. On the other hand, Zn was found to improve the wetting by the molten aluminium on the steel surface but forming simultaneously a thick IMC layer. Mg was proven to be less effective than Si to suppress the IMC growth but the joints produced with Mg based wire had less defects (micro-cracking and porosity) and showed higher strength than the ones brazed with Si based wire.

1.10 Gaps found in science

The points indicated below correspond to the gaps found on the literature relating to dissimilar metal joining of thick sections of steel to aluminium. These gaps motivated the research presented in this manuscript.

- For applications requiring thick (> 6.0 mm) plates of steel and aluminium, for instance shipbuilding, the current solution is to use a transition bar between the steel and the aluminium, so called Triclad® bar (Figure 1-21) (Tricarico et al., 2009). The half steel and half aluminium Triclad bar is produced by explosion

bonding. This bar permits the direct joining of steel substrate to the steel side of the Triclad bar and similarly, to join the aluminium substrate to the aluminium side of the Triclad bar. Even though this solution overcomes the loss in strength caused by the presence of the intermetallic compounds, there are a few disadvantages in terms of and logistics and cost. The application of the transition bar is not cost effective, as it increases the cost of production via the cost of the bar (US $25 per kg (Aerodynamic metals PTE Ltd, 2009)) and complicated logistics of operation, for instance to purchase, storing and handling. In addition, as demonstrated in the example in Figure 1-21, four fillet welds are necessary when a transition joint is used, instead of two, if steel and aluminium were joined directly. The cost effectiveness and mass efficiency is thus reduced in such structures;

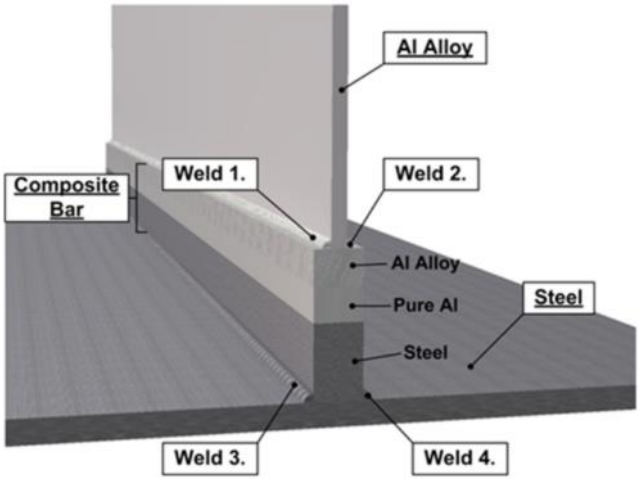

Figure 1-21: Schematic representation of a dissimilar metal joint of steel to aluminium using the Triclad ® bar.

- The majority of the research on dissimilar metal joining of steel to aluminium is focused on thin gauge materials which has application in the automotive industry. Therefore, the research done for thick sections is limited;
- The results found on the literature review for laser welding of steel to aluminium are based on the system parameters and thus, are dependent of the laser system. Using the FLMIP it would be possible to correlate the IMC formation and the weld geometry to the energy transferred to the material;
- The finite element analysis methods suitable to estimate the thermal cycle of the laser welding process of steel to aluminium which were available in the

literature was limited. The processing parameters were not fully investigated and the effect of the temperature and time were not independently analysed;

- The research on dissimilar metal joining of steel to aluminium with interlayers was limited.

1.11 Project aim and goals

The aim of the work is to develop a cost effective and energy efficient joining solution between steel and aluminium with appropriate mechanical strength and metallurgical characteristics suitable for the intended application. The final application requires a T-joint configuration of thick plates of aluminium and steel which will be used as a stiffener in shipbuilding as shown in Figure 1-21 but without the Triclad® bar.

One of the goals is to understand and, therefore be able to control the growth of the intermetallic compounds formed during the direct joining of steel to aluminium (see Figure 1-22). The development of a thermal model to predict the time and temperature during the formation and growth of the intermetallic compound layer was also part of the work.

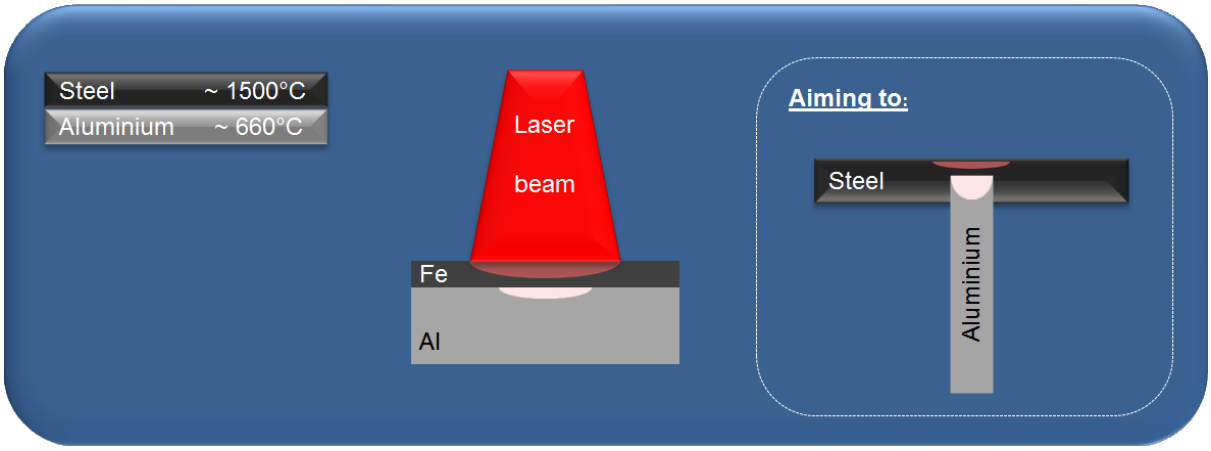

Figure 1-22: Direct joining of steel to aluminium using laser in conduction mode.

The second goal was to investigate the use of engineering metallic alloys to create a bridge between the steel and the aluminium to avoid the reaction between Fe and Al (see Figure 1-23). Copper is a good candidate for an interlayer because even though it reacts with aluminium and forms intermetallic compounds, it is still possible to have solid solution in certain joining conditions. The welding process used in this study was Cold Metal Transfer (CMT) with a $CuSi_3$ and different aluminium alloy welding wires in

a bead on plate configuration. Different joining configurations and energy levels were used to assess the viability of using copper as interlayer.

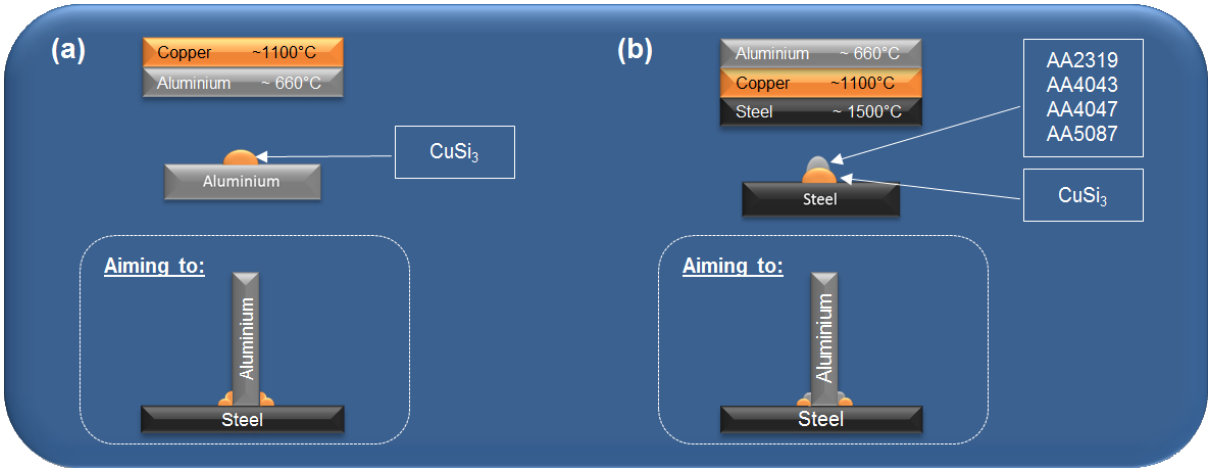

Figure 1-23: Strategies for metal deposition using CMT welding process to evaluate the reaction between copper and aluminium: (a) copper deposited onto aluminium and (b) aluminium deposited onto copper which previously has been deposited onto steel.

The third goal of this project was to transfer the knowledge acquired in the experiments obtained for the lap joint configuration to the intended T-joint. In this stage an innovative joint design was necessary.

1.12 Research objectives and thesis structure

1.12.1 Research objectives

- Use of laser welding in conduction mode, with heat conducted through the steel plate up to the aluminium plate to induce only melting on the aluminium;
- Development of the clamping system to ensure the reproducibility of the experiments and the contact between the two plates (no gap, no defect, good heat transference from steel to aluminium);
- Determine the window of welding parameters suitable to produce sound joints;
- Evaluate the influence of the laser welding parameters on the IMC layer type and thickness;
- Correlation between mechanical strength, IMC layer thickness, bonding area and laser welding conditions;

- Development of a thermal model to predict the thermal profile at the Fe-Al interface, where the IMC layer grows;
- Investigate use of copper interlayer to restrict the Fe-Al reaction and avoid the IMC layer formation;
- Investigate the Al-Cu IMCs formed during CMT welding with copper and different grades of aluminium welding wires
- Study different innovative joint designs and welding configurations to transfer the findings obtained for the lap-joint configuration to the intended T-joint configuration.

1.12.2 Thesis Structure

- Chapter 1 contains a brief introduction to the project, a review of the existing literature review necessary for this work, the motivation for the research, the aim, goal and objectives for the project;

- Chapter 2 has the description of the experimental procedures used either in direct joining of steel to aluminium by laser welding or joining of steel to aluminium with addition of copper in between using CMT welding process. This chapter also shows the methodology used for the metallographic analysis and mechanical strength analysis of the dissimilar metal joints. A description of a procedure developed to measure the intermetallic layer thickness is provided.

  The following five chapters correspond to the main outcome of the work produced in this project. Chapters 3 to 5 and 7 are formatted versions of papers submitted for publication:

- Chapter 3 is based on the paper (Meco et al., 2015) about the effect of different laser welding conditions on the intermetallic layer thickness and on the mechanical strength of lap welded joints. A detailed metallographic characterization of the intermetallic layer is done in this chapter with the identification of the intermetallic compounds formed during the laser welding process and the measurement of the intermetallic compound layer thickness for each welding condition. The power density and specific point energy are correlated with the intermetallic compound layer thickness and the mechanical strength of the joints;

- Chapter 4 is based on the paper (Meco et al., 2014) about a deeper study on the effect of the fundamental laser material interaction parameter. Here a matrix was created where only one parameter was changed individually in each welding condition. Once again the results shows how the strength and intermetallic compound layer thickness of steel-aluminium joints vary with the laser power density, interaction time and specific point energy;

- Chapter 5 is based on a paper about the development of a thermal model to predict the thermal cycle at the Fe-Al interface where the IMC layer grows. In this chapter the thermal cycle resulting from different values of fundamental laser material interaction parameters are correlated to the IMC layer thickness and bonding area (weld width) and these two factors are then correlated to the mechanical strength of the joints. This allows evaluation of how the mechanical strength is affected by the thermal conditions via IMC layer thickness and bonding area;

- In chapter 6, the reaction between copper and aluminium was investigated using Cold Metal Transfer MIG welding and $CuSi_3$ copper welding wire. This extensive study covered different metal deposition configurations and different levels of energy;

- Chapter 7, is based on a paper about a novel joint design to permit the transferability of the results achieved for laser welding of steel to aluminium in a lap-joint configuration to the required T-joint configuration aiming to shipbuilding;

- Chapter 8 summarises the findings of this project, a brief discussion about the outcome of the project and the main conclusions. The future work is also presented in this chapter and includes ideas for future projects worthy of further investigation;

- The last section includes the appendices and a list with the sources of the citations used in this thesis.

2.0 Experimental procedure

2.1 Introduction

This chapter has a brief description of the experimental principles and methodology used to investigate direct joining of steel to aluminium using laser welding.

2.2 Materials

The materials used in direct joining of steel to aluminium were 2 mm thick plates of XF350 high strength low alloy steel and 6 mm thick 5083 H22 aluminium. Copper welding wire and foils were also used as interlayers. The chemical composition and mechanical properties of these materials are shown in Table 2-1 and Table 2-2, respectively. The physical properties of these alloys are shown in Table 2-3.

Table 2-1: Chemical composition of the base materials and interlayers.

Material	Elements (wt. %)												
	Al	**Fe**	**C**	**Si**	**Mn**	**P+S**	**Ni**	**Ti**	**Cu**	**Mg**	**Zn**	**Cr**	**Other**
XF350	0.047	Bal.	0.059	0.021	0.610	0.025	0.020	0.001	0.03	-	-	0.030	0.255
5083-H22	Bal.	0.400	-	0.400	0.500	-	-	0.150	0.100	2.600-3.600	0.200	0.300	-
Cu foil	-	-	-	-	-	-	-	-	99.9	-	-	-	0.1
$CuSi_3$ wire	<0.01		0.017	2.9	0.84	0.009	-	-	Bal.	-	0.005	-	0.005

Table 2-2: Mechanical properties of the base materials and interlayers.

Material	**Yield strength, MPa**	**Ultimate tensile strength, MPa**	**Total elongation at failure, %**
XF350 (ASW, 1996)	350	430	23 (at 80mm of gauge length)
5083-H22 (Metalweb, 2013)	250	337	8 (at 50mm of gauge length)
Cu foil (Weigl et al., 2011)	-	290	-
$CuSi_3$ wire (Weigl et al., 2011)	-	350	-

Table 2-3: Thermal properties of the pure iron and aluminium and copper interlayers.

	Melting temperature, °C	Thermal conductivity at room temperature, $W.(m.K)^{-1}$	Thermal expansion, 10^{-6} $m.(m.K)^{-1}$ (0-100 °C)
Fe (Matweb, 1996)	1538	80	12.2
Al (Azom, 2000)	660	238	23.5
Cu foil (Weigl et al., 2011)	1083	400	17.7
$CuSi_3$ wire (Weigl et al., 2011)	965	35	18

The aluminium and steel plates were all cut with the same dimensions, i.e. 150 mm long and 138 mm wide.

2.3 Methodology and Experimental Setup

2.3.1 Joining principle

Laser welding was the joining process chosen to bond steel to aluminium, in a lap joint configuration with steel on top of the aluminium. The experimental arrangement is schematically explained in Figure 2-1. Since the gap between both plates is negligible and the thermal conductivity of the aluminium is much higher than the steel, forming a heat sink which helps the heat to be easily transferred from the steel plate to the aluminium. Laser welding in conduction mode was used because of the characteristic weld shape with low depth-to-width ratio which is necessary for the joint configuration used in this work. This welding mode also avoids any vapourisation effects which leads to poor quality welds. In this manner, the heat produced when the laser beam irradiates on the steel surface is conducted through the thickness of the steel plate and induces local melting of the aluminium (Figure 2-1b). A copper backing bar was positioned underneath the joint to remove part of the heat produced during welding. Due to the high thermal conductivity of the copper the heat is efficiently conducted away from the joint, reducing the temperature and thus the growth of the IMCs. The welding parameters must be controlled so that the temperature at the Fe-Al interface remains in the range between 570 °C ($T_{melting,\ AA5083}$) and 1500 °C ($T_{melting,\ XF350}$). Figure 2-1b-c indicates different areas resulting from the joining process. In these figures on the steel side there is a darker area correspondent to the fusion zone. The energy required to melt the aluminium at the Fe-Al interface is such that partial melting of the steel plate

is not avoided. The energy of the laser must be controlled to prevent melting of the whole thickness of the steel plate so that the steel and aluminium are not mixed in the molten state at the interface.

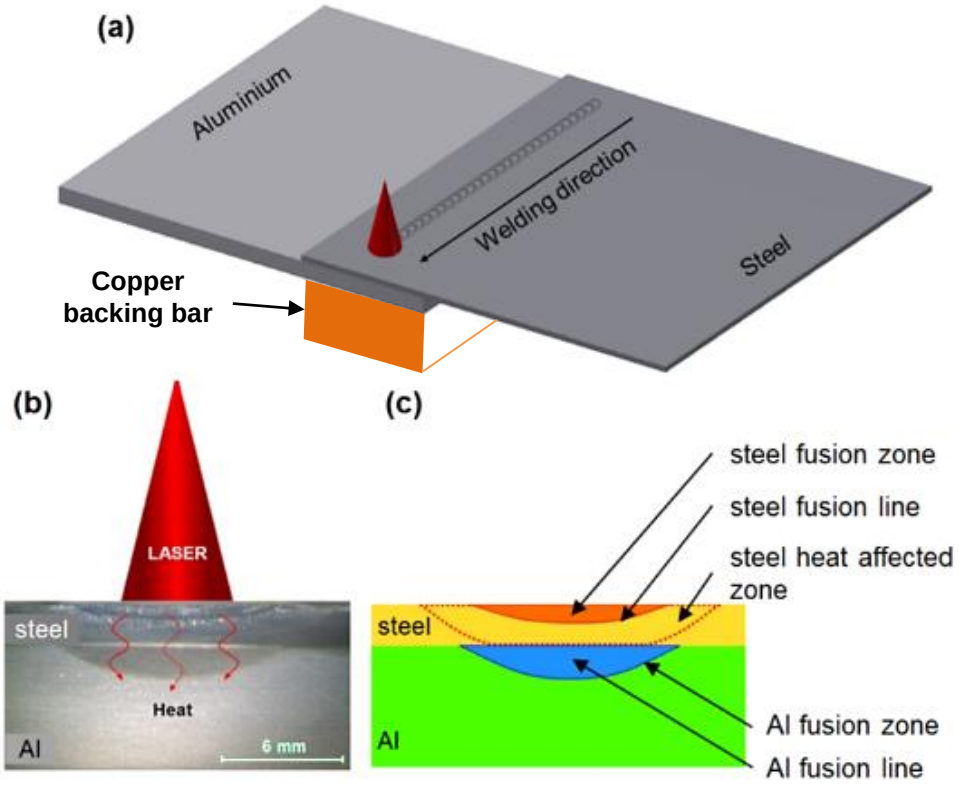

Figure 2-1: Schematic representation of the laser welding process: (a) perspective view, (b) macroscopic cross-sectional view and (c) identification of the fusion zone and the heat affected zone.

This technique allows relatively lower interaction between the alloys since the diffusion of elements in the solid state is lower than that in the liquid state and therefore, it is possible to minimize the reaction between both elements and the formation of IMCs (Ma et al., 2014).

A large and defocused laser beam is used to create a large bonding area between the aluminium and steel plates. The geometry of the fusion zone visible in Figure 2-1 is the characteristic of a weld produced in conduction mode. By definition, the aspect ratio (penetration depth by weld width) must be smaller than 0.5 (Nakamura et al., 2000) (Quintino and Assuncao, 2013) and the power density must be lower than 10^6 $W.cm^{-2}$ (J. M. Sánchez-Amaya et al., 2009) for a weld to be considered in conduction mode. In this work, both conditions were verified and all joints were produced in

conduction mode. Compared to laser keyhole welding, laser conduction welding is more stable, the weld geometry is favourable to create a large bond area and the slower processing speed allows appropriate temperature gradients to establish between the dissimilar alloys to ensure melting of the aluminium only. As can be understood, keyhole mode is not suitable for such a joining process as with the high depth to width ratio of the weld it would be impossible to control melting of the steel and thereby mixing of the two alloys. Another consequence of the keyhole mode is the number of defects formed during the welding process, such as porosities due to the gas entrapment during the solidification of the weld pool and undercuts due to metal projection (Assuncao et al., 2012; J.M. Sánchez-Amaya et al., 2009).

2.3.2 Development of the clamping system

The integrity of dissimilar joints in this particular joint configuration relies on good contact between the overlapped plates. Therefore, it is essential to have an effective clamping system to ensure the reproducibility of the experiments. The first stage of the work focused on the development of the clamping system for laser welding of steel to aluminium with the joint configuration previously described. The following characteristics of the device were considered:

- Good contact between both plates, ideally zero gap: Good contact between the upper and lower plates is essential so that the heat resulting from the interaction of the laser with the steel can be transferred to the aluminium to produce the joint. The presence of a gap at the Fe-Al interface would reduce the heat transfer and the success of the joining process would be compromised;
- Uniform pressure along the substrate: The weld seam becomes unstable if the pressure applied by the clamps on the substrate is not uniform. As a consequence, the mechanical strength of the joint might be compromised;
- Low setup time: Aiming to save time during the experimental work. The clamping should require a low setup time to clamp the substrate;
- Copper backing bar to increase the cooling rate of the welds: According to the literature it is beneficial to use a copper backing bar in the setup for dissimilar metal joining. Some researchers have pointed to the effect of the cooling conditions on the IMC layer growth (Borrisutthekul et al., 2007). They showed that the use of a copper backing bar, which has a very high thermal conductivity,

tends to form thinner IMC layers and they also associated this with an increase in the mechanical strength of the joints.

Figure 2-2 shows the different clamping systems developed for the experimental work. The identification of several issues during the initial experiments resulted in the progressive improvement of the clamping system.

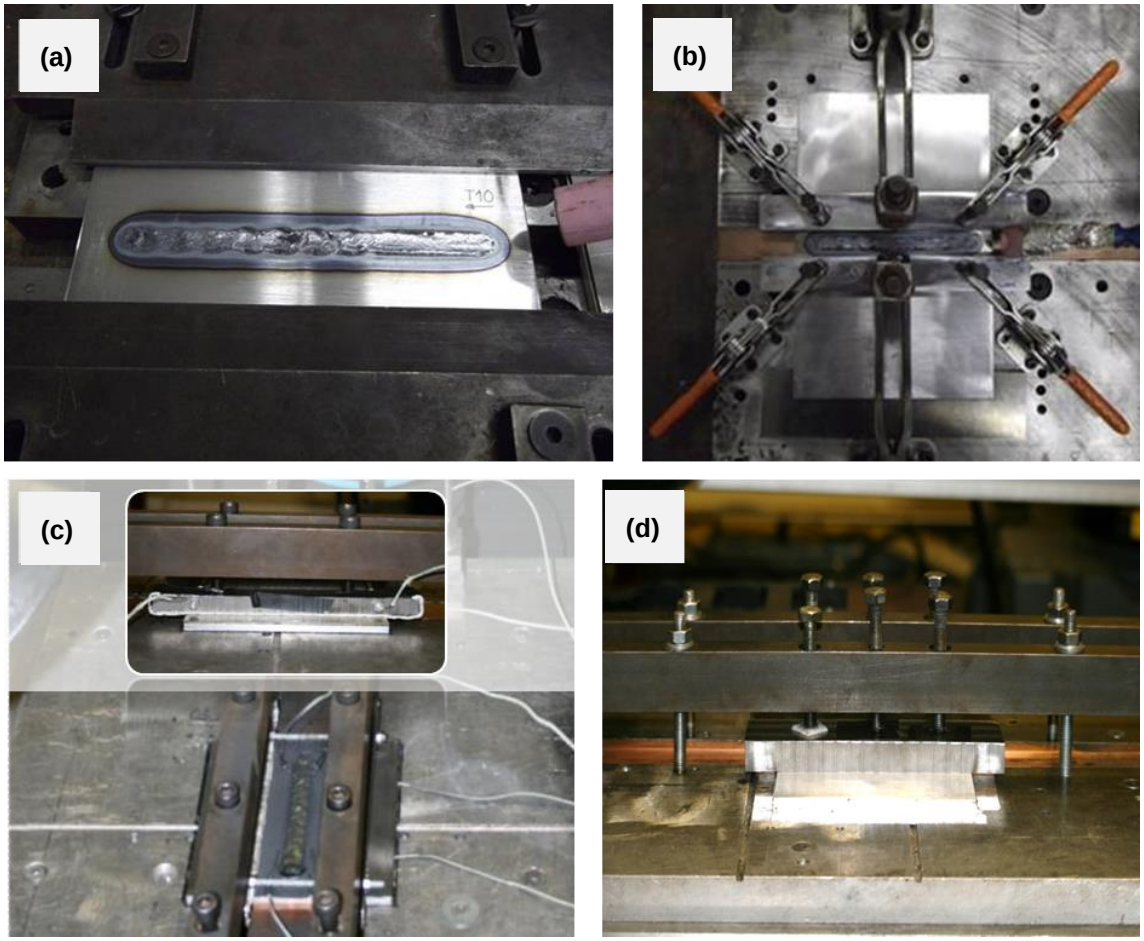

Figure 2-2: Evolution of the clamping system.

The first version of the clamping system proved not to be effective because it could not clamp uniformly. The welds produced using this device were unstable, as shown in Figure 2-2a. Since the substrate was not properly clamped at the centre, the increase in temperature during the welding process caused distortion of the material and the formation of a gap between the upper and lower plates.

On the second version of the clamping system three toggle clamps were added to improve the setting up time and to ensure a uniform pressure along the substrate (see Figure 2-2b). However, these clamps are prone to lose strength and therefore,

consecutive experiments might have different pressure applied on the substrate. This could lead to inconsistent results.

Figure 2-2c shows the next clamping generation with bolts applying load on two bars positioned on the plates. The use of the torque wrench keeps the same load applied in each bolt which ensures the same pressure on the plates in consecutive experiments. However, this clamping system also proved to be not effective due to the way that the upper bars were fastened to the base of the clamping system. The schematic representation in Figure 2-3 helps to understand the problem. When the bolts were tightened and the lower bar (represented in green) applies pressure on the substrate, there is a reaction force (represented by the white arrows in Figure 2-3a) which produces torque. The bigger the arm length between the point where the load is applied and the point where the bar is clamped to the base of the clamping system (represented in grey), the bigger the torque. As the distance between P1 (point where the top bar is clamped to the base of the clamping system) and P2 (the point where the bolt applies pressure on the substrate) in the original jig is too big and therefore, the top bar (represented in purple) bends due to the torque resultant from tightening the bolts. Therefore, the latest development of the clamping system consisted in adding two more bolts closer to the plates and thus reducing the arm length and the deformation of the upper bar. An extra bolt was also added between the existing two to ensure good contact between both plates.

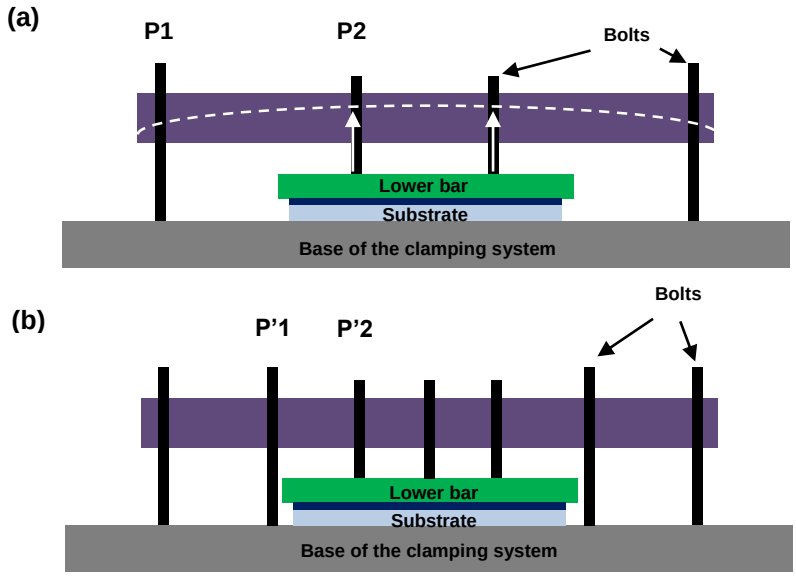

Figure 2-3: Schematic representation of the changes carried out on the clamping system to avoid bending of the top bar due to the reaction force from the substrate. (a) Original jig with 4 bolts and (b) modified jig with 7 bolts.

Further improvements were also made to the bars in contact with the work piece. To increase the pressure on the plates the bars were machined and the contact area was reduced. Figure 2-4 shows the 3D CAD model of the clamping with the respective bars created using Autodesk Inventor Professional 2013 software.

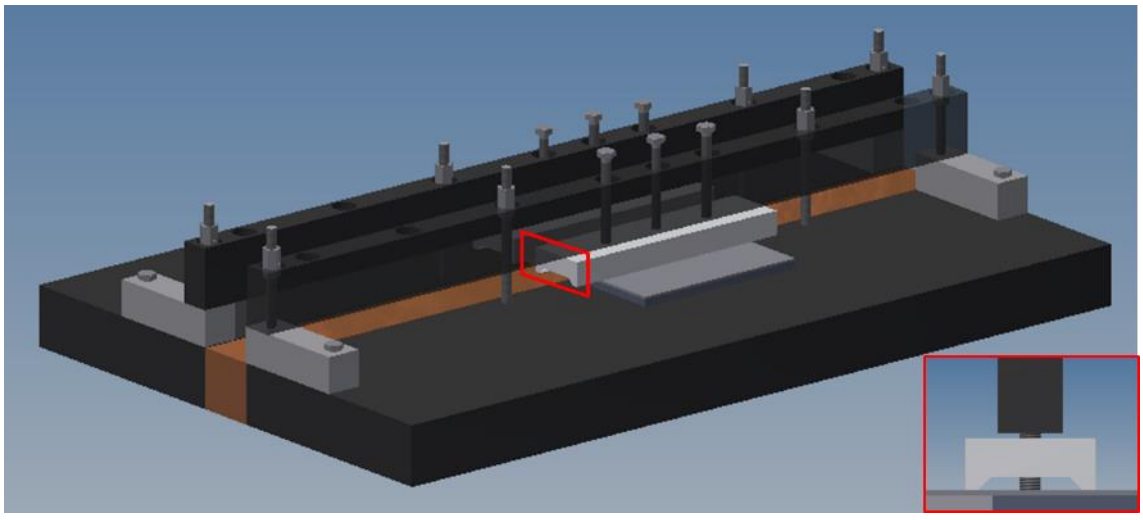

Figure 2-4: Model of the final clamping device with redesigned bars to increase the pressure on the plates designed with CAD 3D.

Minimum distortion of the upper bars when the plates were clamped and the new shape of the bars in contact with the plates minimized the gap between the plates to

be joined. Moreover, the torque wrench ensured the samples were clamped with similar force and therefore, the same clamping condition were always consistent. Finally, with the support from the 3D CAD model software it was possible to build the jig with the requirements needed to join steel to aluminium in a lap joint configuration.

2.3.3 Laser welding

The steel and aluminium plates were linished before welding to remove most of the oxides from the surface of the material, and then degreased with acetone. For each joint, the steel plate was positioned on the aluminium plate in a lap joint configuration (see Figure 2-5), with an overlap of 46 mm, as in agreement with the standard for seam welds in lap joint configuration (British Standard Institurion, 2001).

The laser head was fixed to a 6-axis Fanuc robot, which was kept stationary during the joining process. The linear movement to produce the weld seams was produced by the gantry, as shown in Figure 2-6.

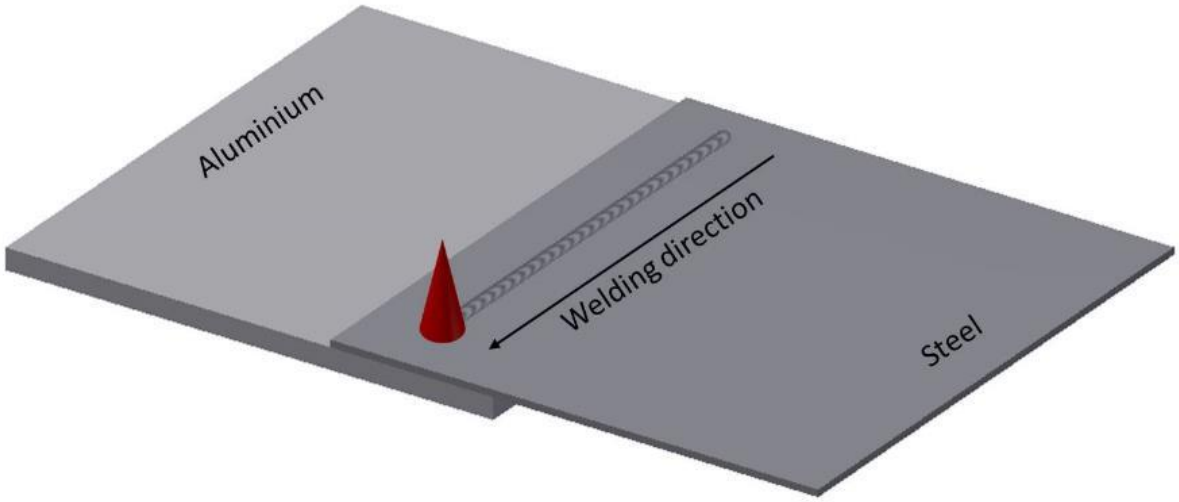

Figure 2-5: Schematic representation of the joint configuration.

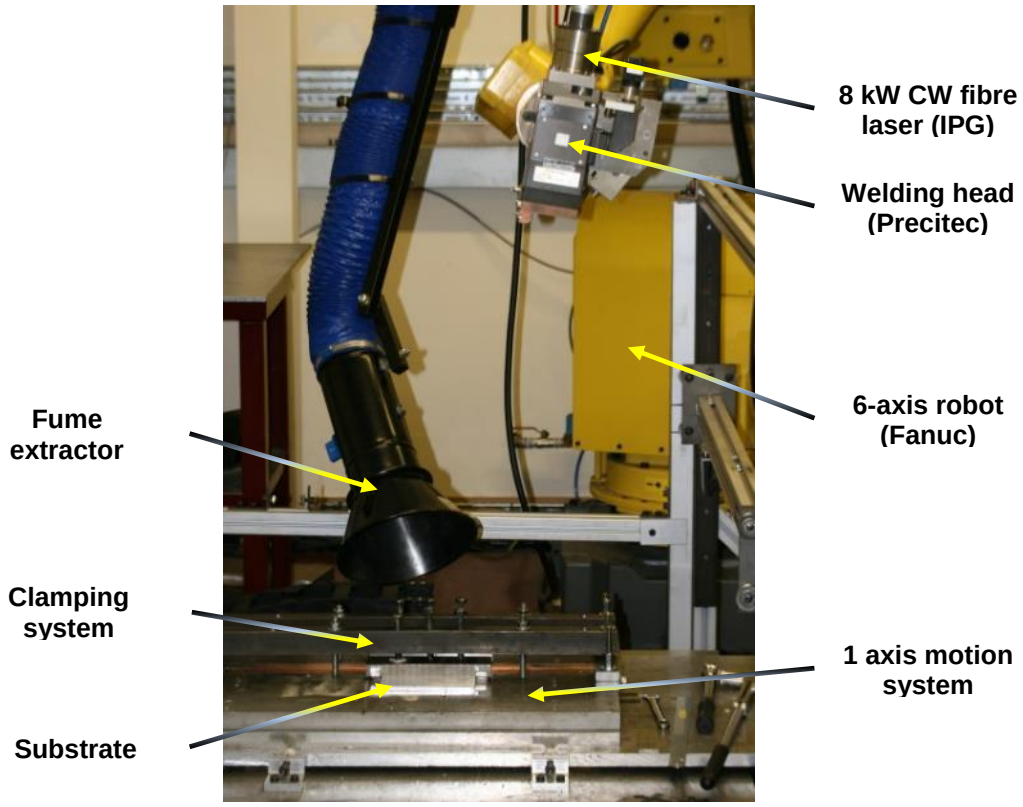

Figure 2-6: Experimental setup for laser welding of steel to aluminium.

At this stage of the work, neither filler material nor brazing flux was used. The joints were produced with an IPG continuous wave fibre laser with 8000 W maximum power and a wavelength of 1.07 µm. The delivery system consisted of a fibre with 300 µm of diameter, a 125 mm collimating lens and a 500 mm focal length lens. The laser beam was characterized using a Primes GmbH focus monitor system and the D4σ (second order moment) method (International Standard, 2005). The distance between the laser head and the substrate to have a particular laser beam diameter was determined based on the divergence of the laser beam and the focal position. As the laser beam was defocused, the beam profile was Gaussian instead of top hat (see Figure 2-7).

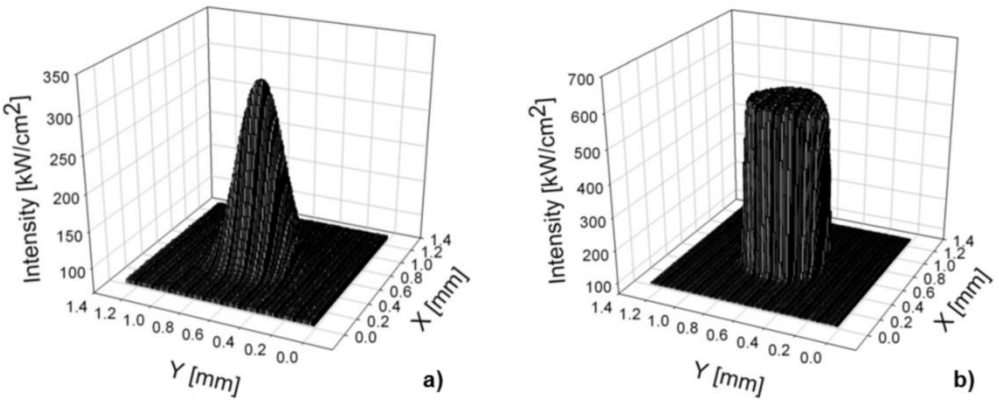

Figure 2-7: Laser beam profiles: (a) Gaussian and (b) top hat.

The initial part of the work consisted in determining the window of parameters which resulted in defect free welds, welds were done in conduction mode and with partial penetration of the steel plate to avoid mixing of the steel into aluminium. Afterwards, considering the best parameters, further tests were done to produce samples for metallographic analysis and mechanical tests.

The system parameters (laser power and travel speed) and the fundamental laser material interaction parameters (power density, interaction time and specific point energy) used in the welding experiments are provided in each subchapter. The latter parameters are calculated based on the system parameters as depicted in 1.8.1.1 (equations 1-5 to 1-7).

2.3.4 Metallographic analysis

Cross-sections were machined out from the welded joints for analysis of the weld geometry and the IMC layer thickness. Two samples, A and B, were cut from each welded joint, as represented in Figure 2-8. The cross-sections were mounted either in cold resin or in conductive resin and then polished using the standard metallographic procedure for 5xxx series of aluminium alloy (MetPrep Ltd, n.d.). The aluminium and steel microstructures were then etched using Keller and Nital 2% etchant solutions, respectively. Micrographs were taken with an Optiphot optical microscope with total magnification ranging from 25x up to 400x. Penetration depth and weld width were measured using the digital imaging software AxioVision (Ltd., 2009). The IMC layer thickness was measured according to the following procedure.

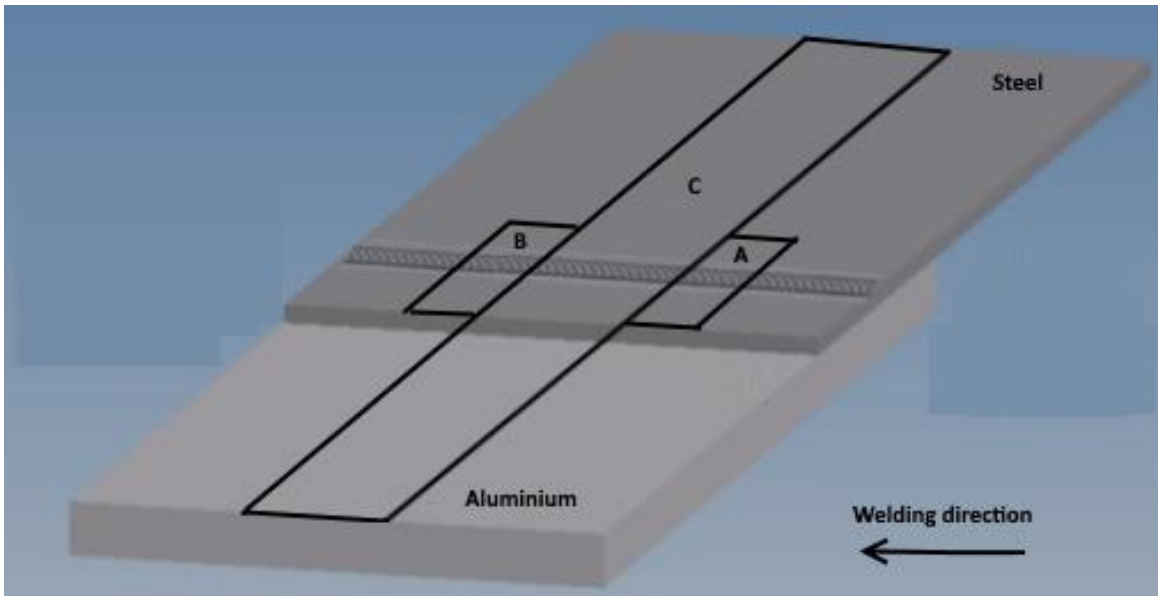

Figure 2-8: Schematic representation of the samples cut from the dissimilar metal joint; Samples A and B for metallography analysis and sample C for mechanical shear test.

A series of 10 micrographs were taken from each sample with the maximum magnification of the objective lens (40x magnification) to determine the thickness of the IMC layer formed at the joint interface. Then, the micrographs showing the thickest IMC layer were analysed by using the Axio Vision software, which is a digital image processing software, and the thickness of the IMC layer was measured. As the IMC layer is not uniform along the Fe-Al interface the micrograph, several measurements were taken in each micrograph along the IMC layer in order to provide a representative value. The values of the IMC layer thickness presented in this report correspond to the average of 20 measurements, equally spaced, with a gap of 10 µm between each other (see Figure 2-9). This procedure was reapeated for all samples.

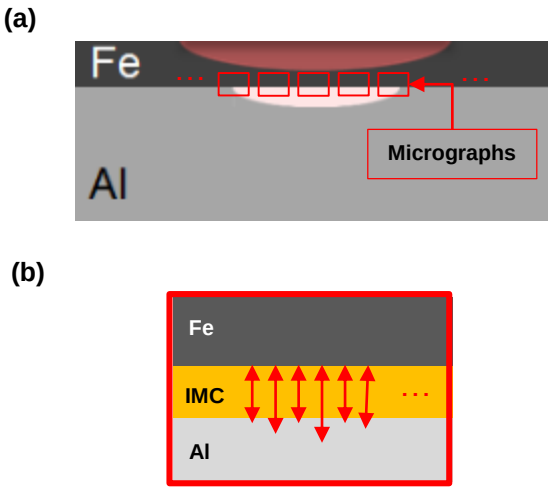

Figure 2-9: Schematic representation showing (a) the positions where the micrographs were taken and (b) the methodology how the IMC layer thickness was measured.

The semi-quantitative compositional analysis of the IMC layer was done using the scanning electron microscope (SEM) with an integrated energy-dispersive X-ray spectroscopy (EDS) using an accelerating voltage of 20 kV.

2.3.5 Microhardness test

Microhardness tests were carried out on the welded samples to determine the hardness in different areas of the joint, such as fusion and heat affected zones of steel and aluminium, and most importantly, the hardness of the IMC layer formed between both metals. The tests were performed with the Zwick/Roell type ZHV microhardness equipment, with a pyramidal diamond indenter using 25 g of load with loading duration of 10 s.

2.3.6 Mechanical Test

The geometry and dimensions of the cross weld lap tensile-shear test specimens were according to the standard for mechanical tensile-shear testing of seam welds (British Standard Instiurion, 2001). The specimens were straight-sided, 60 mm wide and 230 mm long (see Figure 2-8, sample C). An electro-mechanical equipment Instron 5500R was used for testing with a load cell of 100 kN. The tests were carried out at room temperature and with 1 $mm.min^{-1}$ crosshead speed. The elongation of the specimens was measured by the laser extensometer model LE-15. The specimens were coated

with graphite and two pieces of reflective tape were attached to the surface (see Figure 2-10, detail B). The distance between the strips, i.e. gauge length, was kept constant for all specimens, at 50 mm. It is important to highlight that the laser extensometer measured the total elongation of the specimen, i.e. the elongation of the parent metals, heat affected zones and fusion zones.

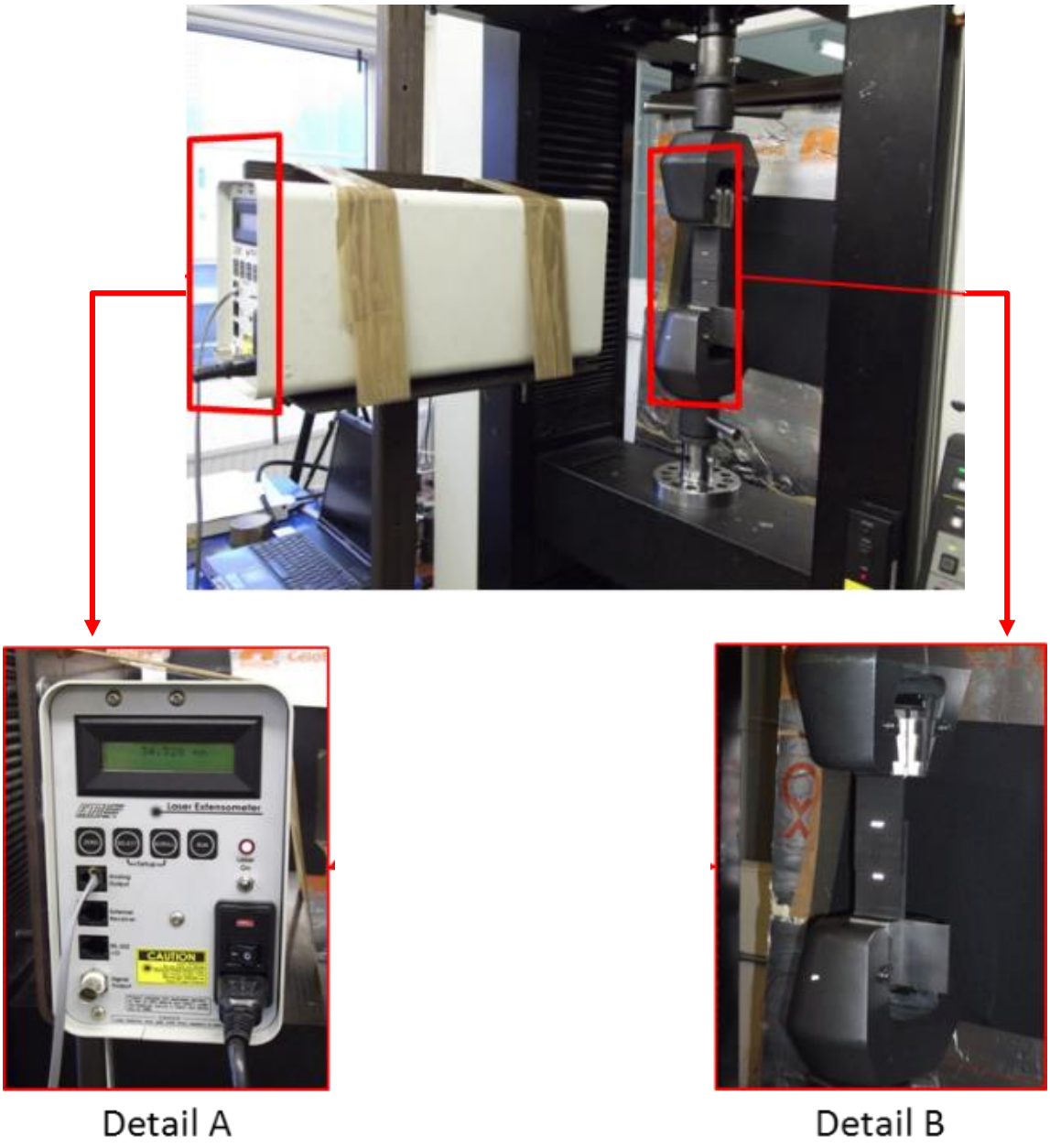

Figure 2-10: Picture from the experimental setup: Detail A – Laser extensometer (model LE-15) and detail B – sample coated with graphite and with two reflective tape strips attached on the surface, fastened on the grips of the Instron 5500R.

The high speed laser scanning measured the elongation, i.e. the distance between both reflective tape strips, and the information was transferred and saved to the

computer. The settings relative to the data acquisition were controlled by a Labview program which was running in the computer.

3.0 Characterization and analysis of the IMC layer growth with the fundamental laser material interaction parameters

3.1 Introduction

In the present section 2.0 mm thick plates of steel were joined directly to 6.0 mm thick aluminium by autogenous laser welding. In order to achieve viable joints it was necessary to understand the underpinning interaction between the laser source and the alloys and correlate the microstructural constituents of the interface with the interaction parameters and finally to the mechanical strength of the joint. In order to achieve this, an experimental matrix based on fundamental laser material interaction parameters was defined, the Fe-Al IMCs were characterized and the growth of IMC layer was correlated with the welding parameters and the mechanical strength of the joints was correlated to the thickness of the IMC layer.

3.2 Experimental procedure

3.2.1 Materials

The materials used in the experiments were 2 mm thick plates of XF350 high strength low alloy steel and 6 mm thick plates of 5083 H22 aluminium. The chemical composition and mechanical properties of the materials are indicated in Table 2-1 and Table 2-2, respectively, of section 2.2.

3.2.2 Methodology and Experimental Setup

The welds were produced in a lap-joint configuration with steel on the top. The joint dimensions and experimental setup are depicted in section 2.3.

The welded area was shielded with inert argon gas with a 20 $l.min^{-1}$ flow rate. The laser parameters, viz. system and fundamental material interaction parameters, used in the experiments are shown in Table 3-1. The latter parameters are calculated using the system parameters as shown in section 1.8.1.1 of this paper (equations 1-5 to 1-7).

Table 3-1: System and fundamental material interaction parameters used in the laser welding experiments.

System parameters			Fundamental laser material interaction parameters		
Beam diameter, D_{beam}, mm	**Power, P, kW**	**Travel speed, TS, m.min^{-1}**	**Power density, PD, MW.m^{-2}**	**Interaction time, t_i, s**	**Specific point energy, E_{sp}, kJ**
13	4	0.20	30.1	3.90	15.60
		0.25		3.12	12.48
		0.30		2.60	10.40
	5	0.30	37.7	2.60	13.00
		0.35		2.23	11.14
		0.40		1.95	9.75

The values of the parameters indicated in Table 3-1 result from a number of trial experiments produced prior to the main experiments to identify the laser parameters needed to produce the welds with the required characteristics, i.e. in conduction mode, free of defects and with partial melting of the steel near the top surface to prevent any interaction between the steel and aluminium in liquid state. A combination of two values of laser power and a single laser beam diameter was considered for laser conduction welding. The minimum travel speed for each laser power corresponds just before having the entire thickness of the steel plate melted, whereas the maximum travel speed corresponds to the limit from which no bonding is produced.

3.2.3 Metallurgical and mechanical characterization

The experimental error of the welding process was calculated based on two samples welded under similar conditions. Then, the welded specimens were machined to take three samples from each weld – one for mechanical testing and the other two for microanalysis, as described in section 2.3.4.

The microstructural analysis was based on optical microscopy and scanning electron microscopy. The important features of the joints were the fusion zone geometry, dimension of the steel and aluminium and the IMC layer thickness and composition. More details are presented in section 2.3.4

The micro-hardness was also measured on the steel, aluminium and IMC layer, as described in section 2.3.5.

The mechanical strength of the joints was quantified by tensile-shear testing according to the procedure described in section 2.3.6.

3.3 Results and Discussion

3.3.1 Macro and Microstructure

Figure 3-1a shows a cross section of a weld. It can be seen that the steel was partially melted near the top where it was irradiated by the laser, however, near the Fe-Al interface the steel remained in the solid state. This happened in all the experiments, even in the samples produced with 9.75 kJ the lowest specific point energy (E_{sp}) (see Table 3-1), since to ensure the temperature on the Fe-Al interface is higher than aluminum melting point, the temperature gradient across the steel plate thickness needs to be sufficiently high, melting occurs at the steel top surface.

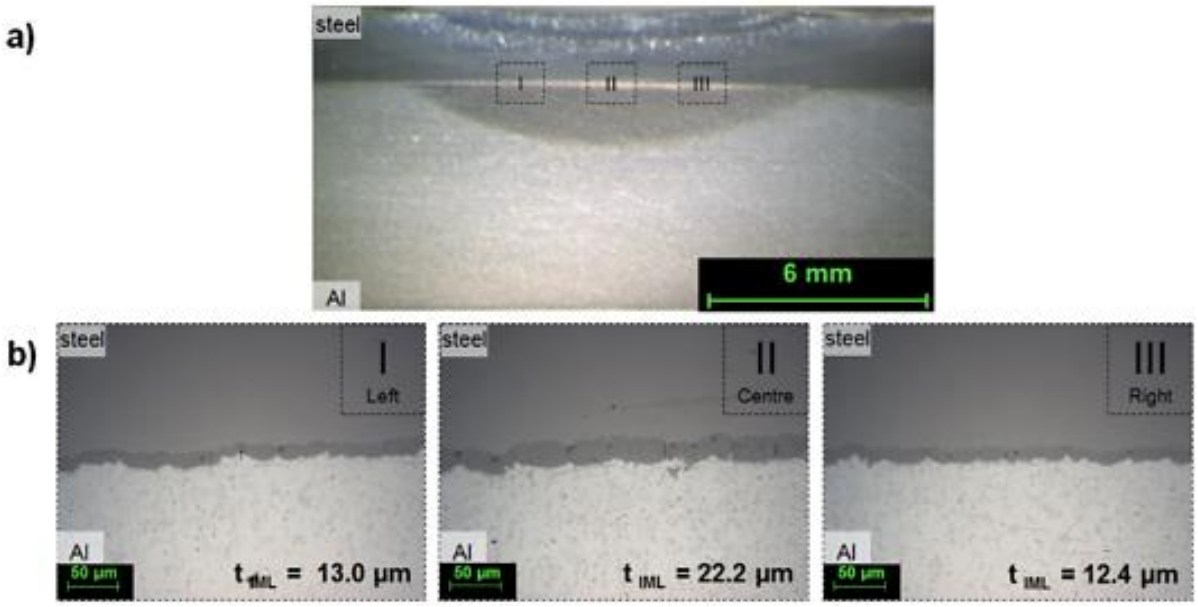

Figure 3-1: Evolution of IMC layer thickness along the cross section (*P* = 4.0 kW; *TS* = 0.20 m.min^{-1}; D_{beam} = 13 mm; *PD* = 0.301 W.m^{-2}; t_i = 3.9 s; E_{sp} = 15.6 kJ): (a) Macrosection; (b) Microsections.

Micrographs in Figure 3-1b show the presence of the IMC layer formed by the Fe-Al reaction. The IMC layer thickness is not uniform along the cross section. Micrograph I and III in Figure 3-1b correspond to the edges of the weld and show relatively thinner IMC layer as compared to the centre (micrograph II in Figure 3-1b) where the IMC layer is thicker. This can be attributed to the differential thermal cycle near the edge and the centre of the weld. Near the centre, the temperature is expected to be higher and the cooling rate lower whilst in the edges the temperature is expected to be lower

and the cooling rate higher. Three factors may be responsible for this: (1) the surrounding material that extracts the heat from the weld zone and (2) the Gaussian distribution of the applied laser power (intensity) which induced the highest temperature near the centre of the weld and (3) the fact that the interaction time is highest near the centre of the weld. According to the literature, the IMC formation is diffusion controlled and thereby dependent on the time and temperature characteristics of the process.

The IMC layer is composed of two distinct layers (Figure 3-2). The IMC present in these layers are $FeAl_3$ on the aluminium side and Fe_2Al_5 on the steel side. As found by (Ranfeng Qiu et al., 2009a), (Olsen, 2009) and (Kobayashi and Yakou, 2002), the $FeAl_3$ layer is usually thin and present as a needle shape morphology whilst the Fe_2Al_5 layer is usually thicker than the latter and tongue shape but strongly dependent on time-temperature. At the edges, where the temperature is lower as well as the interaction time, there is only the $FeAl_3$ layer. According to Qiu *et al*. (Qiu et al., 2010), $FeAl_3$ IMC has lower free energy of formation than other IMC and, thus its formation is easier in terms of thermodynamic principles. However, the kinetic aspect of the Fe_2Al_5 formation is more favorable. The nearly constant thickness of $FeAl_3$ could be due to the sluggish growth of this IMC in contrast to the irregular thickness of Fe_2Al_5 layer across the weld.

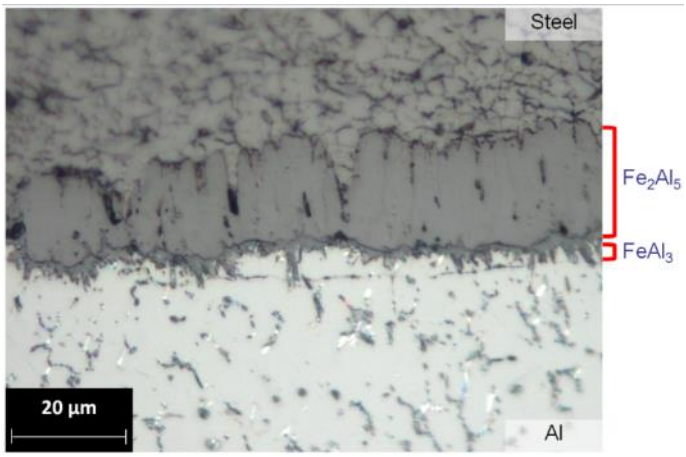

Figure 3-2: Optical micrograph showing two distinct layers in the IMC layer.

The composition of the two IMC layers was identified by EDS spectrum analysis (Figure 3-3). The EDS results confirmed the IMC previously identified based on the morphology: the needle shape $FeAl_3$ with 62 wt% Al and thicker tongue shaped layer of Fe_2Al_5 with 56 wt% Al.

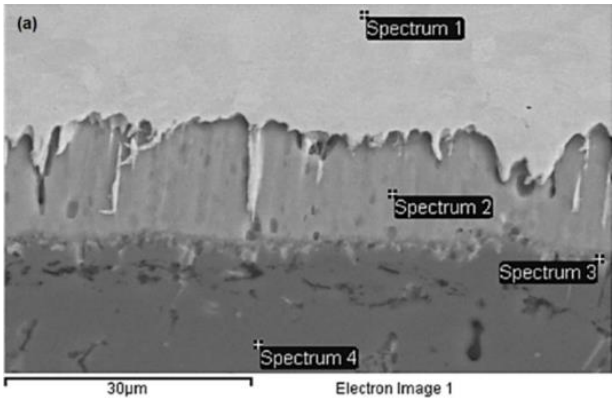

(b)

Weight %	Fe	Al	Mg	Phases
Spectrum 1	100	-	-	Fe
Spectrum 2	44.42	55.58	-	Fe_2Al_5
Spectrum 3	38.12	61.88	-	$FeAl_3$
Spectrum 4	-	95.28	4.72	Al

Figure 3-3: EDS spectrum analysis.

The same morphology is seen in the SEM micrographs (Figure 3-4a) but the two layers are not clearly distinguishable. The highlighted dots in the EDS mapping of Figure 3-4b and Figure 3-4c correspond to the Fe and Al elements, respectively. The lower concentration of dots in the centre of both pictures forming a horizontal band is explained by the presence of the Fe-Al IMC (Fe and Al elements were detected simultaneously in that region during the EDS analysis).

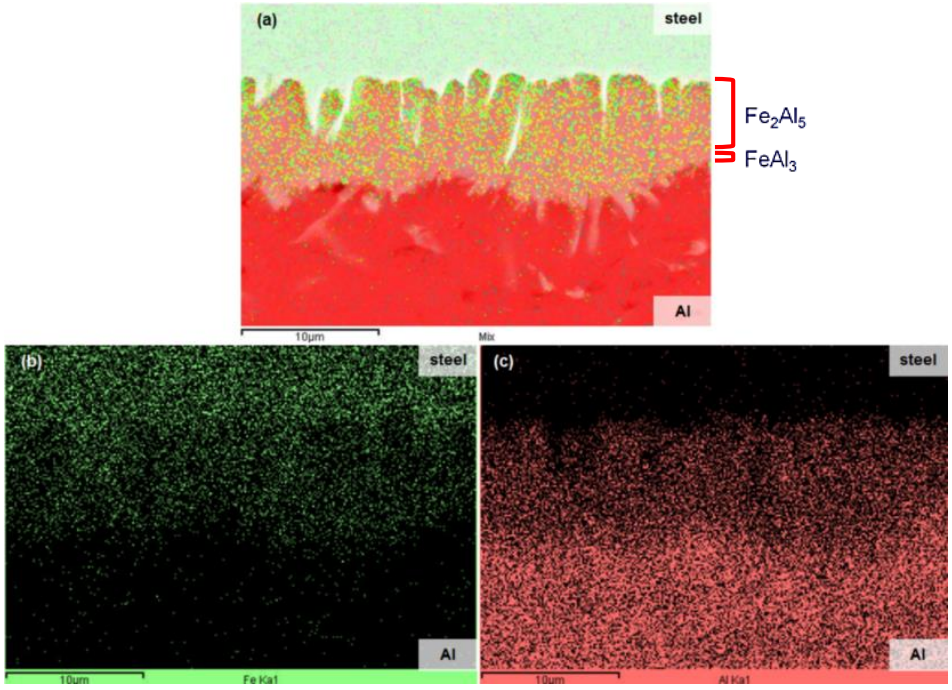

Figure 3-4: EDS mapping pictures: (a) Mix of Fe and Al elements, (b) Fe elements, (c) Al elements.

Microhardness testing was carried out along a vertical line in the cross sectional plane extending to both the parent metals as shown in Figure 3-5. The irregular behaviour on the hardness curve on the steel side is due to the partial melting of the material near the top that resulted into different metallurgical phase formations as compared to the part which remained solid throughout the process. On the Al side the hardness value showed very consistent and uniform results around 70 HV 0.025/10. As expected, the maximum value of hardness was observed on the IMC layer with 1145 HV 0.025/10. This value is similar to the one reported by Olsen (Olsen, 2009), 1100 HV.

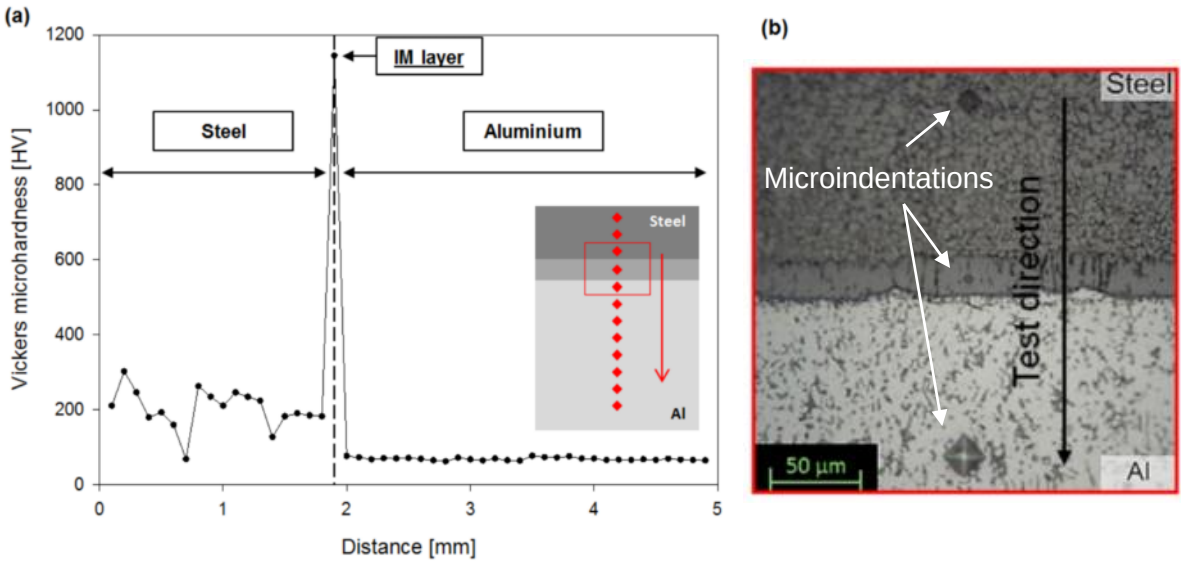

Figure 3-5: (a) Micro-hardness distribution along the thickness of the sample, from the top surface of the steel and (b) microscopic view of the indentations near the Fe-Al interface.

Figure 3-5b shows a micrograph where the microindentation on the IMC Fe_2Al_5 is visible. As the $FeAl_3$ IMC layer is very thin, about 2 µm, it was not possible to measure the hardness with the microindenter, it would be necessary to use a nanohardness tester.

3.3.2 Laser Welding Process

As mentioned in section 2.3.3, the experiments were carried out in conduction mode with the laser beam incident on the steel plate through which heat was conducted, melting the aluminum and bonding the two metals. Using this methodology, the temperature in the Fe-Al interface is lower than the melting point of the steel and as

steel was maintained in solid state, the diffusion of Fe and Al elements is minimized and thus, the Fe-Al reaction was reduced.

The visual inspection on the welds produced with laser process in conduction mode revealed no defects which was in agreement with (Assuncao et al., 2012; J.M. Sánchez-Amaya et al., 2009) – the weld seam was uniform with neither porosities nor cracks.

Laser welding applied in joining of thick plates of steel to aluminium, compared to other joining processes, such as hybrid laser-arc welding, has better process control in terms of energy transferred to the work piece and has lower complexity because it has less parameters to control. Another example is the explosion welding process in which the resultant welds have good mechanical properties due to the low levels of IMC layer thickness but the process is much less versatile in terms of material and geometries to weld than laser welding (Findik, 2011).

Figure 3-6 shows the micrographs of the cross section of the samples welded under different welding conditions: two different power density (*PD*) values and three different specific point energy (E_{sp}) values.

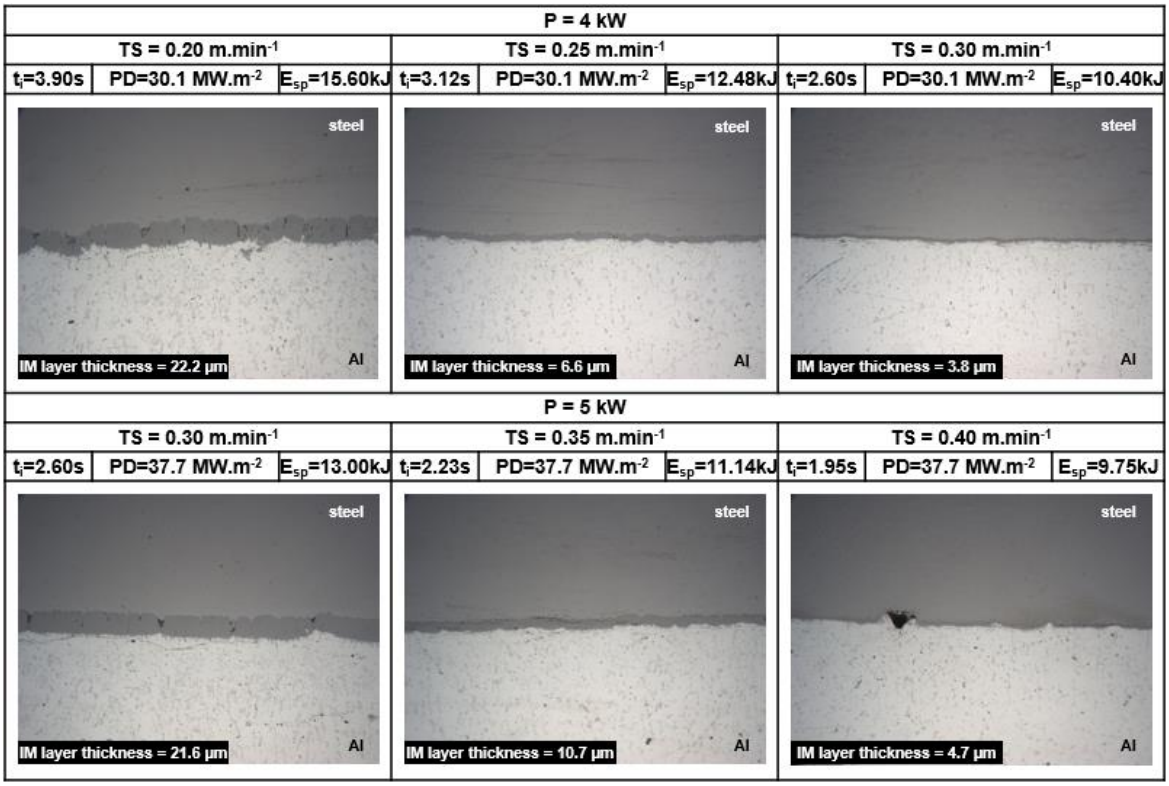

Figure 3-6: Microscopic cross sectional view showing the IMC layer formed under different welding conditions and constant laser beam diameter of 13 mm.

Figure 3-7 shows the evolution of the IMC layer thickness with specific point energy which was varied by changing either the power density or the interaction time to understand effect of these parameters independently. The error bars represented in the graph correspond to the variation of IMC layer thickness measured in two samples taken from two joints produced under identical welding conditions. The experimental results are considered to be acceptable since the variation of IMC layer thickness produced under different energy levels falls outside the error bars.

The point worth mentioning is the similar pattern of the two curves with the different *PD* values (Figure 3-7). The growth of IMC layer shows an exponential trend with the E_{sp}. It can be clearly seen that as the E_{sp} increases, IMC layer growth increases. This is expected as thermal cycle prolongs with increase in energy input.

Taking into account that E_{sp} is a function of *PD*, t_i and A_{beam} and considering in this case constant *PD* and A_{beam}, for each curve of uniform *PD*, the IMC layer thickness is actually a function of t_i (or *TS*, since A_{beam} is also constant). Therefore, higher E_{sp} values were obtained with higher t_i (heating time), result from welding with lower travel speed, which explains the thicker IMC layer for higher values of E_{sp}.

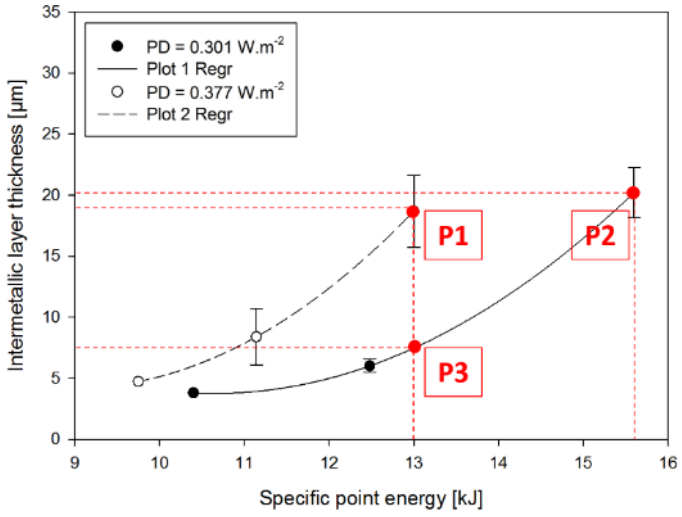

Figure 3-7: Graph with results from steel to aluminium joints performed with laser welding process – IMC layer thickness vs E_{sp}.

Figure 3-7 highlights two points, P1 and P2, with similar IMC layer thickness formed under different energy levels $E_{sp,P1}$ and $E_{sp,P2}$, with $E_{sp,P1} < E_{sp,P2}$ (Figure 3-7, equation 3-1).

$$E_{sp,P1} = PD_{P1} \times t_{i,P1} \times A_{beam,P1} < PD_{P2} \times t_{i,P2} \times A_{beam,P2} = E_{sp,P2} \quad (3\text{-}1)$$

Considering the *FLMIP*, the point P1 has higher PD and significantly lower t_i when compared to point P2, for the same A_{beam} (equation 3-2). In terms of system parameters the point P1 was obtained with higher *P* and *TS*. This means that even with a lower t_i (or higher *TS*), the temperature generated by the higher *PD* is enough to produce the same IMC layer thickness. Therefore, using lower *PD* values it is possible to work in a larger range of t_i and keep the IMC layer thickness low.

$$\begin{cases} E_{sp,P1} < E_{sp,P2} \\ A_{beam,P1} = A_{beam,P2} = A_{beam} \\ PD_{P1} > PD_{P2} \\ t_{i,P1} \ll t_{i,P2} \end{cases} \quad (3\text{-}2)$$

The other important point is the acceleration of the IMC layer formation with increased *PD* values. Considering P1 and P3 (highlighted points in Figure 3-7 as an example, such that $E_{sp,P1} = E_{sp,P3}$ which can be written as shown in equation 3-3.

$$E_{sp,P1} = PD_{P1} \times t_{i,P1} \times A_{beam,P1} = PD_{P3} \times t_{i,P3} \times A_{beam,P3} = E_{sp,P3} \quad (3\text{-}3)$$

From this equation and taking into account the individual FLMIP, the following relation can be derived (equation 3-4):

$$\begin{cases} E_{sp,P1} = E_{sp,P3} \\ A_{beam,P1} = A_{beam,P3} = A_{beam} \\ PD_{P1} > PD_{P3} \\ t_{i,P1} < t_{i,P3} \end{cases} \quad (3\text{-}4)$$

This equation shows again that for the same energy level and similar D_{beam}, the effect of using higher *PD* values is more important than the reduction on t_i on the growth of the IMC layer. This is even more evident when higher energy values are used. Thus, the temperature seems to play a more important role than the time on the Fe-Al reaction. According to the Fick's law for diffusion the temperature is the factor which most influences the diffusion coefficient and consequently, the diffusion rate (Callister, 2006). Therefore, it can be said with reasonable certainty that a thermal cycle with higher peak temperature would produce thicker IMC layer when compared to a longer thermal cycle but with lower peak temperature.

The IMC layer thickness, as observed from the experiments, ranges from 4 µm to 21 µm. According to (Schubert et al., 1997) IMC layer thickness of up to 10 µm has been considered not harmful to obtain a sound joint.

The results of the mechanical tests are represented in Figure 3-8 along with the evolution of the IMC layer thickness which has been previously analysed.

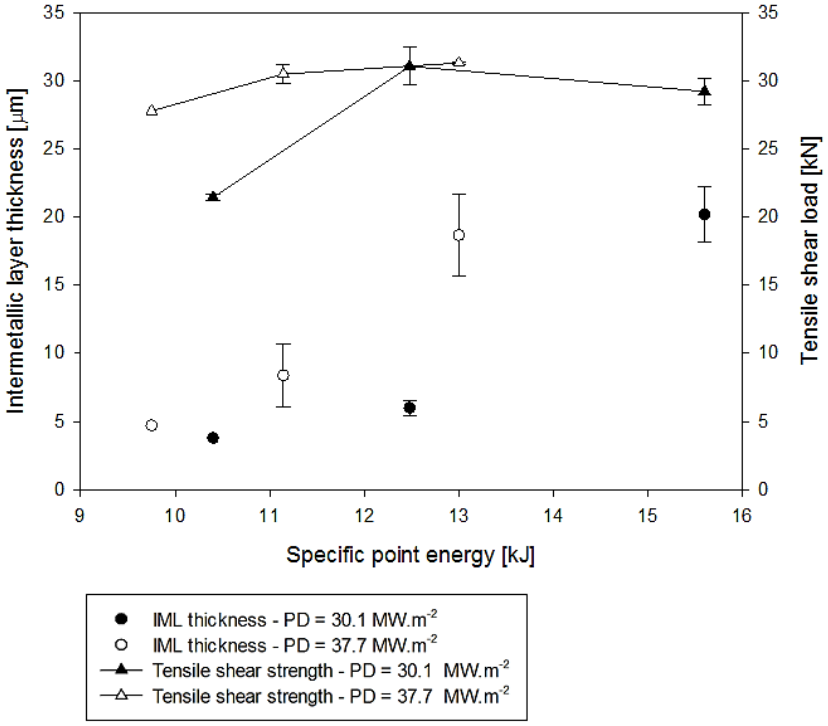

Figure 3-8: Correlation between specific point energy, mechanical strength and IMC layer thickness.

In both power densities (30.1 and 37.7 MW.m^{-2}) the mechanical shear tests showed similar strengths (although having a slight increase with E_{sp}) in all the experiments performed, even with the increase of IMC layer thickness. It can be explained by the fact that increasing the E_{sp} results in an increase in wetting area because of the longer thermal cycle (Figure 3-9 shows the increasing of wetting area on steel side when the t_i and E_{sp} are increased). In the experimental region, initially the strength response is positive with increase in E_{sp} as higher wetted area has better impact on the joint strength than the adverse impact due to thicker IMC layer. The mechanical strength quickly reached a plateau and a decrease in strength is likely as further IMC layer growth would outweigh the advantage of higher wetting area. This shows that the mechanical strength is not linearly dependent of bonding area but it is also dependent

of the IMC layer thickness. The failure was always observed at the Fe-Al interface and the maximum shear load bearing of approximately 30 kN (Figure 3-8).

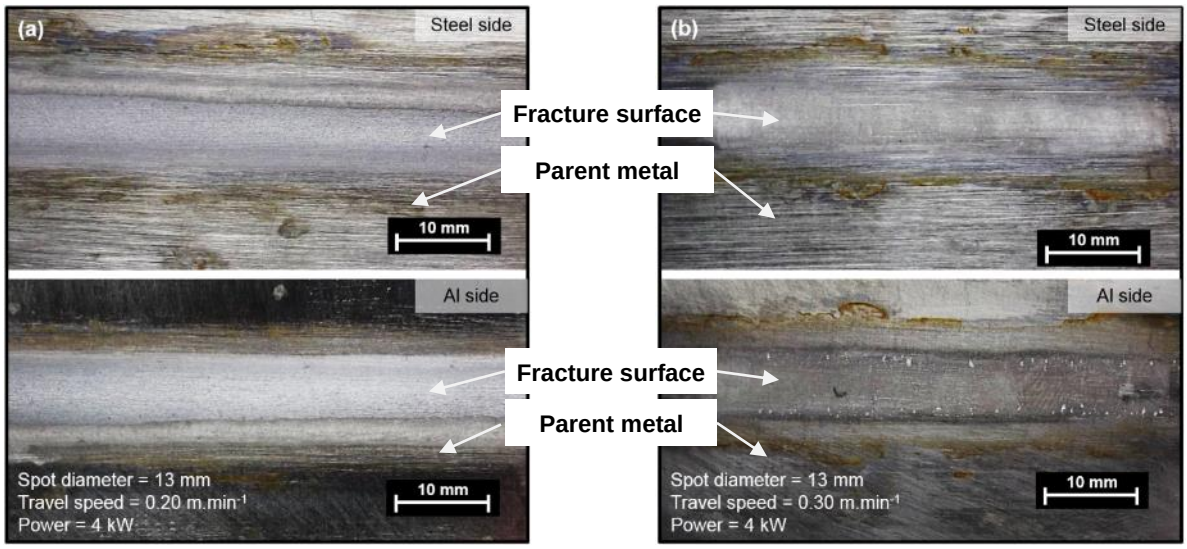

Figure 3-9: Pictures of the Al-Fe interface after interfacial failure on the mechanical shear test. (a) *PD* = 30.1 MW.m^{-2}; t_i = 3.9 s; E_{sp} = 15.6 kJ; (b) *PD* = 30.1 MW.m^{-2}; t_i = 2.6 s; E_{sp} = 10.4 kJ.

3.4 Summary

Laser welding has the capability of limiting the microstructural damage due to IMC formation as it allows aluminium to melt and wet the steel surface. Here it is worth noting that Al has some limited solid solubility in Fe, while Fe does not have any solubility in Al. Also diffusion is restricted when steel is in solid state and wetted by aluminium as compared to when both the alloys are in liquid state. The main conclusions are as follows;

- The study of the influence of the fundamental material interaction parameters on the IMC layer growth revealed exponential growth of IMC layer with E_{sp}. Powder density (PD) plays a vital role in determination of the IMC layer thickness and application of similar laser spot energy may result in thicker IMC formation for higher power density.
- In the current experimental situation, IMC layer thicknesses were observed to vary between 4 – 22 µm. The thickness data showed high quality welds in possible to manufacture using this route as IMC layer thickness below 10 µm is often referred to as an acceptable standard.

- The microstructure analysis showed the composite IMC layer was composed of a needle shaped $FeAl_3$ on the Al side and a tongue shaped Fe_2Al_5 on steel side. The Fe_2Al_5 was much thicker as compared to $FeAl_3$.
- The tensile shear load on breakage observed to vary between 21.4 to 31.3 kN. All the samples exhibited interfacial failure in tensile shear testing.
- An initial increase in mechanical strength with specific point energy has been observed which can be attributed to the increase in wetting area with the increase in specific point energy. Although an increase in IMC layer thickness has also been observed in this range it seems the advantage owing to increase in wetting area outweighs the adverse impact from the increase in IMC layer thickness.

In the next chapter a more in-depth analysis of the effect of the fundamental laser material interaction parameters on the IMC layer growth and on the strength will be carried out. The effect of each one of the fundamental laser material interaction parameters will be evaluated independently and the laser beam diameter will also be changed.

4.0 Investigation of the IMC layer growth with the fundamental laser material interaction parameters and different beam diameters

4.1 Introduction

In the previous sections the experiments were aimed towards the identification of the window of welding parameters for a unique laser beam diameter and the characterisation of the IMC constituent of the IMC layer and a correlation was found between the process energy with the IMC layer thickness and the joint strength. The main goal of the present chapter is to determine the importance and effect of each individual fundamental laser material interaction parameter (power density, interaction time and specific point energy) for different sizes of beam diameter on the growth of the IMC layer and the consequent influence on the mechanical properties of the dissimilar metal joint.

4.2 Experimental procedure

4.2.1 Materials

The materials used in the experiments were 2 mm thick plates of XF350 high strength low alloy steel and 6 mm thick plates of 5083 H22 aluminium. The chemical composition and mechanical properties of the materials are depicted in section 2.2, Table 2-1 and Table 2-2, respectively.

4.2.2 Laser welding

The welds were produced in a lap-joint configuration with steel positioned on top of aluminium. The joint dimensions and experimental setup are depicted in section 2.3.

The window of parameters used in the experimental work is given in Table 4-1, for both, system parameters and FLMIP. These parameters are present in greater detailed in Table B-1 in Appendix B. The FLMIP are calculated using the system parameters as shown in section 1.8.1.1 of this paper (equations 1-5 to 1-7).

Table 4-1: System and fundamental material interaction parameters range.

System parameters			Fundamental laser material interaction parameters		
Beam diameter, D_{beam}, mm	**Power, P, kW**	**Travel speed, TS, m.min^{-1}**	**Power density, PD, MW.m^{-2}**	**Interaction time, t_i, s**	**Specific point energy, E_{sp}, kJ**
9.28 – 14.85	2.55 – 6.52	0.19 – 0.43	28.9 – 73.9	1.29 – 3.35	5.67 – 14.52

4.2.3 Strategy applied to assess the effect of the FLMIP on the Fe-Al IMC layer growth

The study of the effect of the FLMIP on the IMC layer growth permits a better understanding of the interaction of the laser with the material, since the FLMIP directly correlates the energy input to the IMC layer formation.

This work was based on the mathematical expression of the E_{sp}, which is calculated as shown below (see equation 4-1).

$$E_{sp} = PD \times t_i \times A_{beam} \qquad (4\text{-}1)$$

Each term of the E_{sp} equation, i.e. PD, t_i and A_{beam}, was investigated according to Figure 4-1, where E_{sp} was varied with only one parameter at a time, while the two other were kept constant.

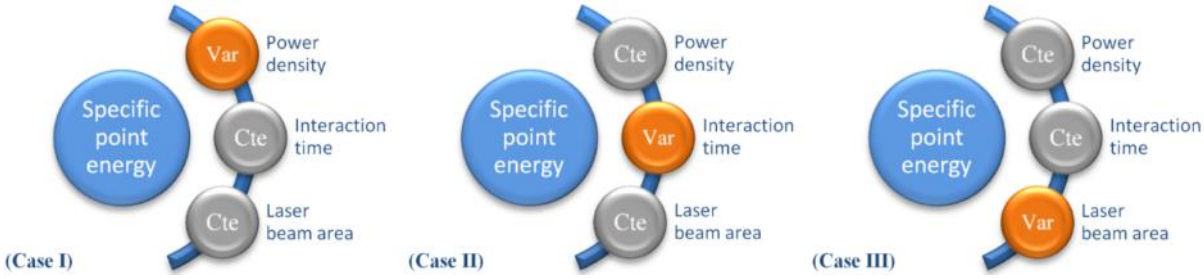

Figure 4-1: Schematic representation of the methodology applied on the present study: (Case I) Specific point energy variable with power density, (Case II) Specific point energy variable with interaction time and (Case III) Specific point energy variable with laser beam diameter.

All possible combinations are classified from Case I up to Case III. To keep two terms constant and vary the other two it is necessary to adjust the system parameters accordingly (see Table 4-2).

Table 4-2: Summary of the status of the FLMIP and system parameters during the welding experiments: V for variable parameters and C for constant parameters.

	FLMIP				System parameters		
	E_{sp}	PD	t_i	A_{beam}	P	TS	D_{beam}
Case I	V	V	C	C	V	C	C
Case II	V	C	V	C	C	V	C
Case III	V	C	C	V	V	V	V

For instance in case I, which represents both t_i and A_{beam} constant, to perform the experiments, laser power was varied while travel speed and beam diameter were kept constant. E_{sp} was then a function of P.

For case II where E_{sp} is variable with t_i, E_{sp} is only dependent on TS.

In case III, E_{sp} is variable with A_{beam} and for PD to be constant, P needs to change in the same proportion as A_{beam} so that the ratio remains constant. As t_i is also constant in this case, TS needs to vary in the same proportion of D_{beam} so that the ratio between these two system parameters remains constant. Thus, for the welding experiments with E_{sp} variable with A_{beam} (case III) all the system parameters (P, TS and D_{beam}) need to be varied simultaneously.

4.2.4 Metallurgical and mechanical characterization

The experimental error of the welding process was calculated based on two samples welded under similar conditions. Then, the welded specimens were machined to take three samples from each weld – one for mechanical test and the other two for microanalysis, as described in section 2.3.4.

The microstructural analysis was based on optical microscopy and scanning electron microscopy. The important features of the joints were the fusion zone geometry and dimension of the steel and aluminium and the IMC layer thickness. More details are present in section 2.3.4

The microhardness was also measured on the steel, aluminium and IMC layer, as described in section 2.3.5.

The mechanical strength of the joints was quantified by tensile-shear test according to the procedure described in section 2.3.6.

4.3 Results and Discussion

4.3.1 Weld seam geometry and Fe-Al IMC layer characterization

The macrosections of the samples were analysed to verify not only the presence of defects such as porosity or cracking, but also to ensure that the steel on the interface remained in solid state during the joining process. Figure 4-2a shows a macrograph of one of the samples where the fusion zones in the steel and aluminium plates are visible and no defects are detected. It was observed that the welding process was in conduction mode due to the small depth to width ratio of the fusion zone. The IMC layer formed between the steel and aluminium plates is usually continuous and thicker in the centre of the weld. The optical micrograph shown in Figure 4-2b indicates that the IMC layer formed between the steel and aluminium plates is composed of two IMCs. Further analysis using SEM/EDS was done in previous experiments to obtain the chemical composition of these two layers. The results showed that the most developed layer near the steel side is Fe_2Al_5 whereas the thinner layer, near the aluminium is $FeAl_3$.

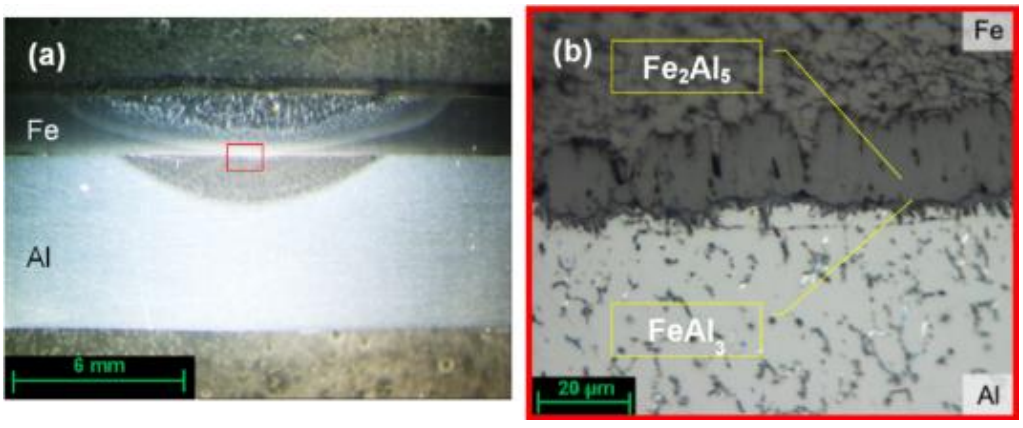

Figure 4-2: Results from the metallographic analysis: (a) Macrograph of the Fe-Al dissimilar metal joint and (b) micrograph.

Figure 4-3 shows the EDS mapping with the spatial distribution of the elements of Fe, Al and Mg. The IMC layer corresponds to the high density horizontal band at the centre of the image where both Fe and Al elements are present.

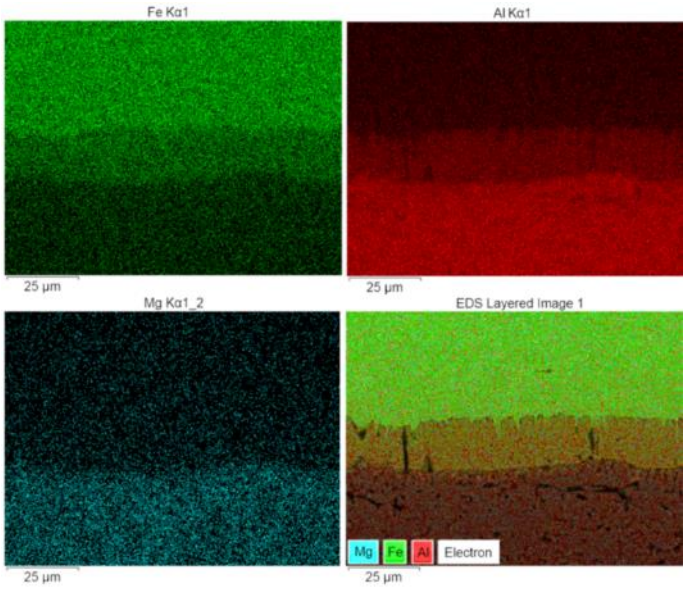

Figure 4-3: EDS mapping showing the spatial distribution of the main constituent elements of the samples: Fe, Al and Mg.

4.3.2 Effect of the FLMIP on the IMC layer growth

The correlation between the IMC layer thickness and E_{sp} is represented in the next three graphs. Each graph shows the evolution of the IMC layer growth when the E_{sp} increases either when PD (Figure 4-4), t_i (Figure 4-5) or even the A_{beam} (Figure 4-6) increases.

- **Case I – E_{sp} is variable with PD (t_i and A_{beam} remain constant), (Figure 4-4)**

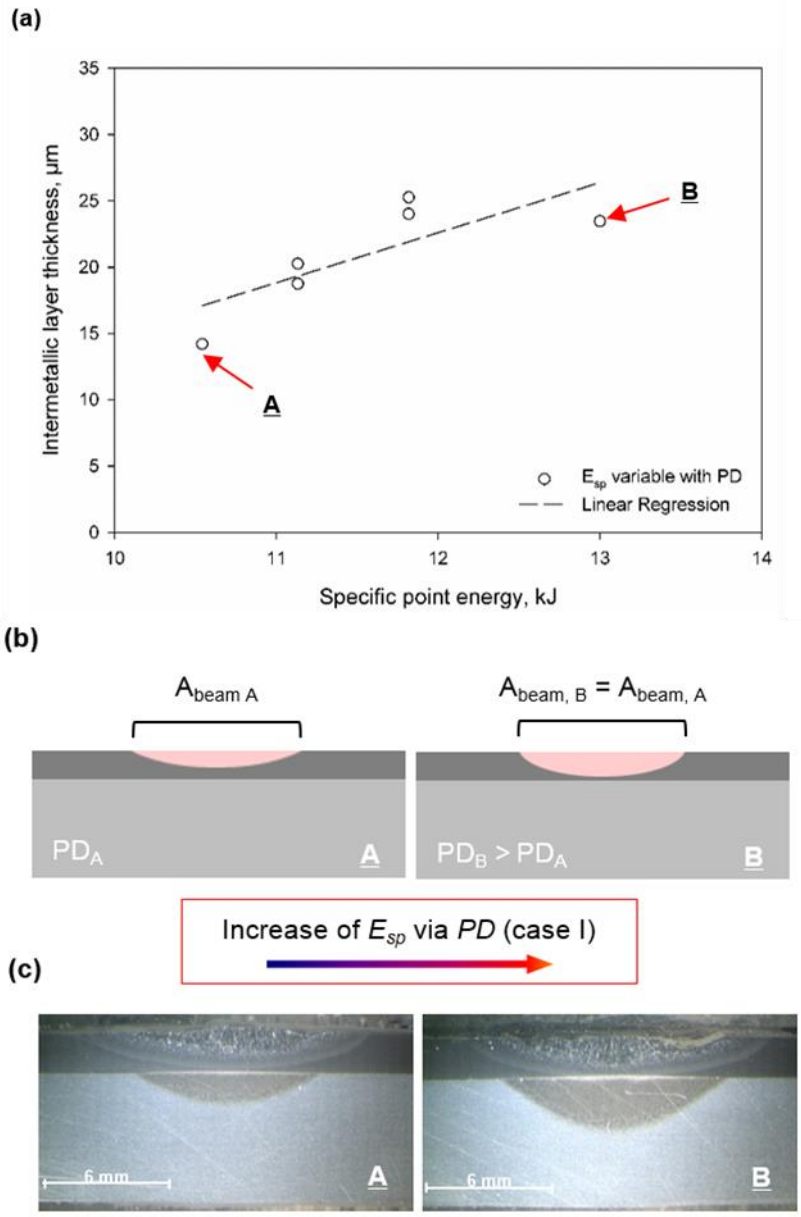

Figure 4-4: (a) Correlation between IMC layer thickness and Esp (via PD), (b) schematic representation of the effect of increasing PD on the geometry of the weld and (c) macroscopic cross-sectional view of the welded samples.

Figure 4-4a shows that the increase of E_{sp} by PD induces a near linear growth of the IMC layer. One possible reason for this behaviour may be explained by the geometry of the weld (Figure 4-4b-c). The penetration depth visible on steel or aluminium plates can give an indication about the temperature experienced at the joint interface. In other words, when a deeper fusion zone is formed during the welding process with higher

PD, the temperature at the Fe-Al interface is higher. Therefore, a deeper fusion zone is usually associated with a thicker IMC layer.

- **Case II – E_{sp} is variable with t_i (PD and A_{beam} are constant), (Figure 4-5)**

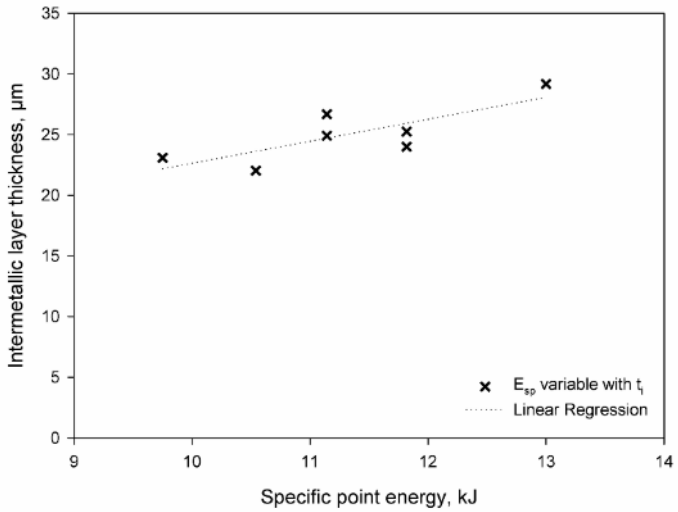

Figure 4-5: Correlation between E_{sp} (via t_i) and IMC layer thickness. E_{sp} was varied by changing the t_i.

Under this welding condition, with E_{sp} varying in function of the t_i, the growth of the IMC layer has also linear trend but with a less steeper slope. The reason for this seems to be as shown in the work produced by Shigeaki Kobayashi *et al* (Kobayashi and Yakou, 2002). The growth of the IMC layer is fast in the first stage of the formation but after certain thickness the growth becomes sluggish. This is apparently due to the lack of Fe atoms available for the reaction with Al to produce Fe_2Al_5. The author also reported that when the Fe_2Al_5 layer stops growing and if the temperature is high enough, the IMC layer already formed is consumed to form another IMC. It is relevant to say that the t_i (or heating time) in laser welding is much smaller than the one used in Kobayashi's work and therefore, in the present work there is only limited time for the Fe_2Al_5 and $FeAl_3$ to grow and not to transform to any other Fe-Al IMC.

- **Case III – E_{sp} is variable with A_{beam} (PD and t_i are constant), (Figure 4-6)**

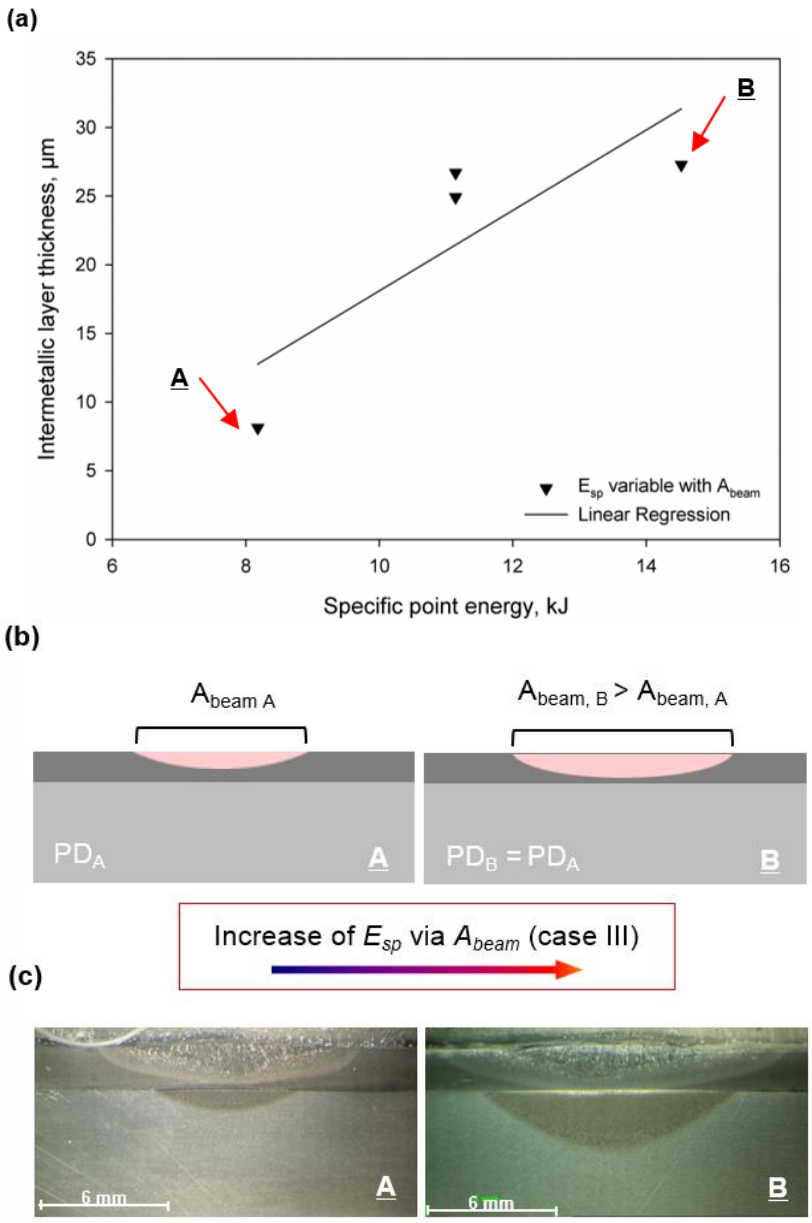

Figure 4-6: (a) Correlation between IMC layer thickness and E_{sp} (via A_{beam}), (b) schematic representation of the effect of increasing A_{beam} on the geometry of the weld and (c) macroscopic cross-section view of the welded samples.

The graph in Figure 4-6a indicates that when E_{sp} increases via A_{beam} the IMC layer also grows. The weld geometry can be used once again to explain this trend (see Figure 4-6b-c). The fusion zone on the steel and Al plates is deeper when a larger laser beam is used which means that the temperature on the Fe-Al interface (where the formation of the IMC layer takes place) is higher.

According to Assuncao (Assuncao, 2012), the D_{beam} plays an important role on the penetration depth. The author suggests that for particular welding conditions (which seem to be met in this experimental work since large D_{beam} and very slow TS are used) the penetration depth increases when D_{beam} increases (see Figure 4-6b-c). In this situation, the larger D_{beam} induces a smaller PD but the weld depth still increases. The reason for this is attributed to the temperature of the substrate that remains constant at the vaporization temperature with the increase of the D_{beam} creating a larger volume of molten metal. However, there is a point called optimum D_{beam} which gives the maximum penetration depth from which, the further increase of the D_{beam} has the opposite effect on the penetration depth. From this point the temperature on the material surface is lower than the vaporization temperature and the decrease of the PD with the increase of the D_{beam} doesn't permit the increase in penetration depth. Since in the present work (in case III) PD was maintained constant (P was adjusted in the same proportion as A_{beam} in order to keep PD constant), it is likely that the critical point was never reached and the penetration depth was always increased.

In general, the increase of the E_{sp} leads to the growth of the IMC layer, independent of the fact that whether it is through increase of PD, t_i or A_{beam} (see comparison in Figure 4-7a). However, if one considers the E_{sp} ranging between 10 to 13 kJ, the IMC layer thickness shows a relatively slower rate of increase with t_i which implies that the diffusion is sluggish in this region (the already formed IMC layer prevent further inter-diffusion of atoms and the growth becomes sluggish). This phenomenon is explained in detail in Figure 4-7, where four points in two different levels of E_{sp} were considered.

(a)

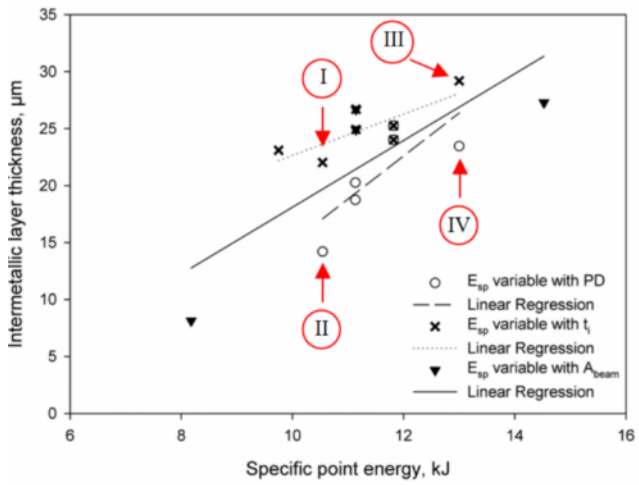

(b)

Point id	E_{sp}, kJ	PD, $MW.m^{-2}$	t_i, s	IMC layer thickness, µm	Tensile-shear strength, $N.mm^{-1}$	Bonding width, mm
I	10.54	37.7	2.11	22	498	9.68
II	10.54	33.6	2.36	14	107	8.86
III	13.00	37.7	2.60	29	83	10.78
IV	13.00	41.4	2.36	23	478	10.88

Figure 4-7: (a) Comparison of the correlation between E_{sp} (via PD, t_i and A_{beam}) and IMC layer thickness, (b) details of the highlighted points.

For a lower energy level, around 10.5 kJ (points I and II), the increase in PD results in more melting of the aluminium and thereby, create a larger bonding area (the variation in fusion zone width is near 1 mm), and the t_i is long enough to permit the wetting process. At a higher energy level, of about 13 kJ (points III and IV), PD doesn't contribute towards increase in bond area. This could be attributed to the fact that over a certain energy level and PD, the heat flux reduces and there is no further increase of temperature. The additional energy is then solely used towards maintaining the temperature at a higher level for longer time and thus helps in progressing diffusion which will increase the IMC layer thickness. Similarly, over a certain energy level and PD, if t_i is too long, the additional energy is used to feed the reaction between Fe and Al and the IMC layer growth becomes thicker. In summary, when the energy and PD is less than a critical value, the wetting of steel by molten aluminium is insufficient, as illustrated by point II and, t_i doesn't have a significant effect on the IMC layer growth and even though PD does, as illustrated by point I, the larger bonding area formed balances the presence of the IMC. On the other hand, over a critical energy and PD level, increasing the t_i can become extremely detrimental to the joint strength as shown by point III.

4.3.3 Mechanical tensile shear strength

The results of the mechanical tensile shear strength tests are plotted in the graphs illustrated in Figure 4-8. The tensile shear strength obtained by dividing the tensile load by the cross-welded specimen width (or, weld length) was found to be in the range between 83 and 575 N.mm^{-1} (equivalent to 4 and 30 kN).

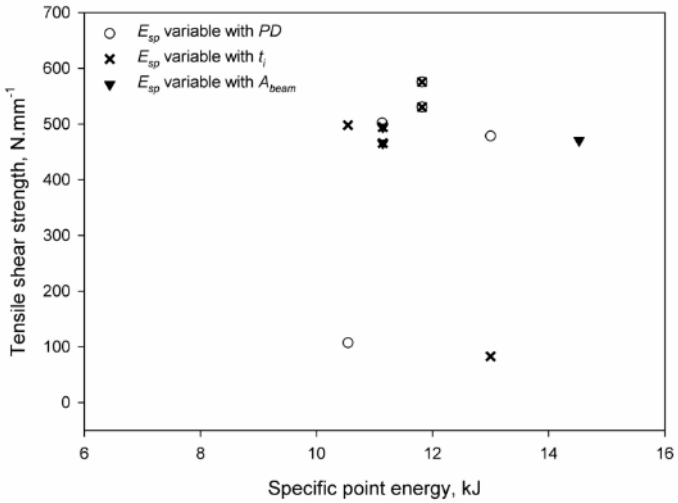

Figure 4-8: Correlation between E_{sp} (via PD, t_i and A_{beam}) and tensile shear strength.

Even though during the mechanical test the failure of all samples was always located at the Fe-Al interface, the specimen experienced some plastic deformation. Figure 4-9 shows the curve of strain versus tensile shear strength of the specimen with maximum tensile load registered (the FLMIP used to weld this sample are mentioned below). This joint had less than 0.7% of total elongation which is similar to that of the glass (near 0.5% of elongation).

The IMCs formed between the Fe and Al are known for their brittleness (1200 $HV_{0.025/10}$ was the micro-hardness measured on the Fe_2Al_5 IMC layer) and so this layer should be kept to a minimum thickness for better structural integrity. However, the results of the mechanical tensile shear strength tests indicate that mechanical strength and IMC layer thickness couldn't be directly correlated. In other words, the mechanical strength doesn't increase as the IMC layer becomes thinner. This may be explained by the fact that when the welding conditions induce the formation of a thicker IMC layer, the wetting area of the Al on the Fe surface also increases, which contributes to a stronger joint. Due to these opposing facts, the maximum strength of the specimens produced under different joining conditions seems to be of a constant level.

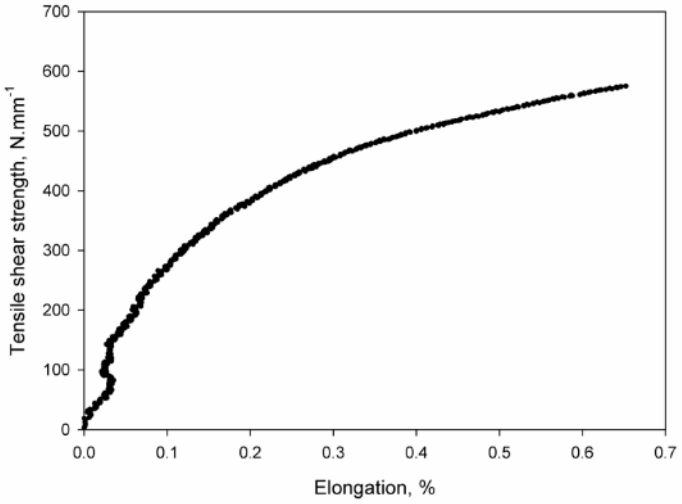

Figure 4-9: Tensile shear strength versus strain for the specimen with highest strength. The FLMIP used were E_{sp} = 11.82 kJ, PD = 37.7 MW.m^{-2}, t_i = 2.36 s and A_{beam} = 1.33 cm^2.

The strength of the dissimilar metal joints for automotive applications has been correlated with the IMC layer thickness by many authors who have determined the optimum thickness range to be up to 10 µm (Ozaki and Kutsuna, 2009; Schubert et al., 1997). Figure 4-10 shows that the highest mechanical strength of the specimens is when the IMC layer thickness is in the range between 18 – 27 µm. Even though in the present work only few samples had IMC layer thickness less than 15 µm, it seems that the optimum thickness for the IMC layer is not any unique value. Moreover, the mechanical strength is not only dependent on the IMC layer thickness but also dependent on the area of contact between the two plates resultant from the joining process. This may be the reason for the presence of the two points with the lowest strength in Figure 4-10. For the minimum value of IMC layer thickness (about 15 µm), the area of contact is small to produce a strong joint. On the other hand, when there is a large area of contact between the two metals, the IMC layer is very thick (about 30 µm) and the joint is brittle. In this situation the brittleness of the IMC layer is more damaging than the increased contact area resulting from the better wetting between the two surfaces. Mathieu *et al*. have also suggested that the weld geometry has a significant effect on the joint strength, after some samples with IMC layer thickness lower than 10 µm had failed on the Fe-Al interface (Mathieu et al., 2007).

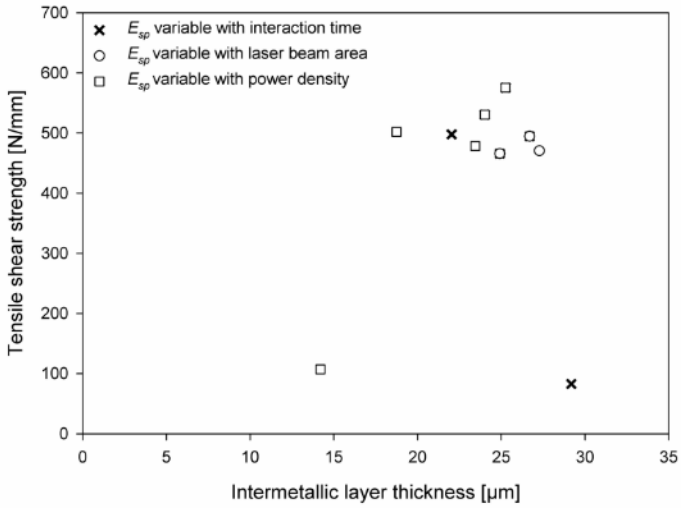

Figure 4-10: Dependency of tensile shear strength with the IMC layer thickness.

It is interesting to compare the mechanical strength of the samples prepared in this experimental work with the strength obtained by other researchers. The maximum mechanical strength measured in this work is similar to the other authors who had their samples failing on the parent material and thus, having successful joints. However, those results are for thin sheets (about 1 mm thick) whereas in the present work the aluminium and steel plates are 6 and 2 mm thick, respectively. The interfacial failure of the specimens is possibly related with the lap joint configuration and the material thickness. During the mechanical tensile shear test the lap joint experiences a complex state of stresses, with both shear and bending stresses acting on the joint, because the specimen is not symmetric to the loading. This is observed in the specimens with higher mechanical strength which were bent after the tensile shear test, showing the rotation experienced during the mechanical test (Figure 4-11).

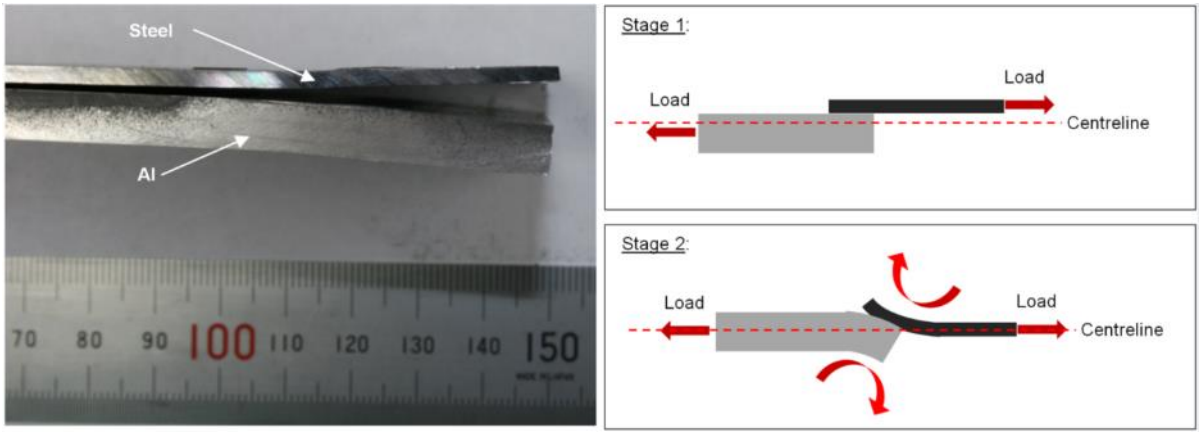

Figure 4-11: Detail of the rotation effect caused during the mechanical tensile shear test performed on the lap joint specimen and schematic representation of this effect.

Miyazaki et at. (Ref 15) have developed a model to qualitatively predict the position of failure of lap welded steel specimens in tensile shear test i.e. whether the failure would be from the base metal, near the base metal or at the weld metal. The equations of the model take into account the rotation experienced during the tensile test and consider the specimen width and thickness as variables. The weld width and length are the other variables. The model predicts that when the dimension of the weld metal width is constant, with increasing thickness the probability of failure from weld metal increases. Therefore, apart from the fact that more energy is required in the joining process of thick plates, which enhances the formation of the IMC compounds, it is apparent that a complex loading spectrum due to non-axisymmetric loading would also result in interfacial failure.

4.4 Summary

In this work the Fe-Al intermetallic layer growth is correlated with the laser welding process via the fundamental laser material interaction parameters – power density, interaction time and specific point energy. The best laser welding joining condition to minimize the intermetallic layer formation is also discussed. The results of this study indicate:

- Using low energy level, the interaction time doesn't have a significant effect on the IMC layer growth and even though power density does, the larger bonding area formed balances the presence of the IMC compounds. On the other hand, for higher energy, interaction time becomes more detrimental to the joint than power density;
- To maximize the joint strength, the power density should be over a threshold value, which in the experimental domain was found to be about 37.7 $MWcm^{-2}$, to enhance the melting of the aluminium and thus, create a large bonding area. Optimisation of interaction time is important as additional interaction would lead to further diffusion and IMC growth. In the experimental regime, the optimised interaction time was found to be about 2.11 s;
- The rotational force applied on the lap joint of 6 mm and 2 mm plates during the mechanical tensile shear test could be responsible for the interfacial failure of the joint, even when a very thin intermetallic layer is present. Therefore, this joining configuration could have better results in thinner plates.

In the next chapter a thermal model to predict the thermal cycle at the Fe-Al interface where the IMC layer grows is presented. With this it is possible to correlate the results previously presented with the thermal cycle and understand how the interaction of the laser with the material occurs for different welding conditions.

5.0 Laser welding of steel to aluminium: Thermal modelling and joint strength analysis

5.1 Introduction

The aim of this work is to understand how the IMCs and bond area affect the mechanical strength of the joints and how temperature and time affect these two parameters individually. A finite element (FE) thermal model of the laser conduction welding of steel to aluminium in a lap joint configuration was developed to predict the transient thermal cycle at the Fe-Al interface and the interfacial wetting for different levels of applied energy. The time-temperature profiles were then correlated to the weld geometry, IMC layer thickness and mechanical strength. In this process energy was varied by changing the power density and interaction time.

5.2 Materials and methodology

5.2.1 Materials

The materials used in the experiments were 2 mm thick XF350 high strength low alloy steel and 6 mm thick 5083 H22 aluminium. The chemical composition and mechanical properties of the materials are depicted in section 2.2, Table 2-1 and Table 2-2, respectively.

5.2.2 Laser welding

The joints were produced in a lap configuration, with steel positioned on the top of aluminium, as shown in section 2.3. The range of laser system parameters and fundamental laser material interaction parameters (FLMIP) is given in Table 5-1. The working envelop is very narrow due to the joint configuration in use and the restriction that the steel near the joint interface must remain solid during the joining process. For this reason the welding parameters needed to be controlled to have only partial melting on the 2 mm thick steel plate.

Table 5-1: System and fundamental material interaction parameters range.

System parameters			Fundamental laser material interaction parameters		
Beam diameter, D_{beam}, mm	**Power, P, kW**	**Travel speed, TS, m.min^{-1}**	**Power density, PD, MW.m^{-2}**	**Interaction time, t_i, s**	**Specific point energy, E_{sp}, kJ**
13.0	4.46 – 5.57	0.30 – 0.40	33.60 – 41.96	1.95 – 2.60	9.75 – 13.00

The specific point energy was varied either by changing the power density or the interaction time (see Figure 5-1). In turn, with laser beam diameter constant, the power density and interaction time varied with laser power and travel speed, respectively. The thermal cycle that results from the interaction of the laser with the material defines the bonding area created between the steel and the aluminium and the IMC layer thickness.

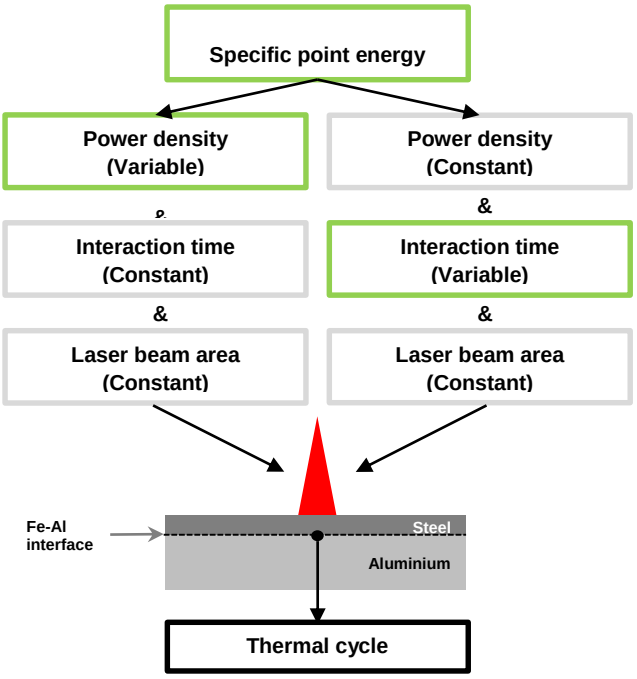

Figure 5-1: Schematic representation of the methodology used in the welding experiments to assess the importance of the FLMIP on the thermal profile and consequently on the weld geometry and IMC formation.

Similar methodology has been previously used by Meco *et al*. where the individual effect of power density, interaction time, laser beam diameter and specific point energy on the IMC layer growth and bond area was investigated (Meco et al., 2014).

5.2.3 Metallographic and mechanical strength characterization

The microstructural analysis was based on optical microscopy and scanning electron microscopy. The important features of the joints were the fusion zone geometry and dimension of the steel and aluminium and the IMC layer thickness. More details are present in section 2.3.4

The mechanical strength of the joints was quantified by tensile-shear test according to the procedure described in section 2.3.6.

5.2.4 Finite Element thermal model

FE models simulate the heat distribution produced by the laser welding process on the Fe-Al lap joints. The thermal cycles were calculated for the welding conditions indicated in Table 4-1. The aluminium 5083 and mild steel thermal properties were according to Kim *et al*. (Kim et al., 2010) and Cozzolino *et al*. (Cozzolino, 2013), respectively. These models are steady state heat transfer analyses, therefore the length of the modelled plates was assumed infinitely long to capture the entire heat cycle.

The type and number of elements and nodes is shown in Table 5-2.

Table 5-2: Elements, nodes, and elements types used in the model.

Part	Abaqus element type	Number of elements	Number of nodes
Al Plate	DCC3D8	438084	479960
Fe Plate	DCC3D8	146028	184600
Fe Shim	DCC3D8	41884	53960
Al Shim	DCC3D8	125652	140296

The aluminium and mild steel plates were overlapped by 46 mm with the mild steel above the aluminium, as shown in Figure 5-2. The additional tooling plates used to ensure a flat surface for clamping were simulated to include the thermal losses in those components. The aluminium and steel tooling plates were 6 mm and 2 mm thick, respectively. The laser heat source was simulated as a Gaussian surface distribution. It was applied on the steel plate and the spot size was 13 mm.

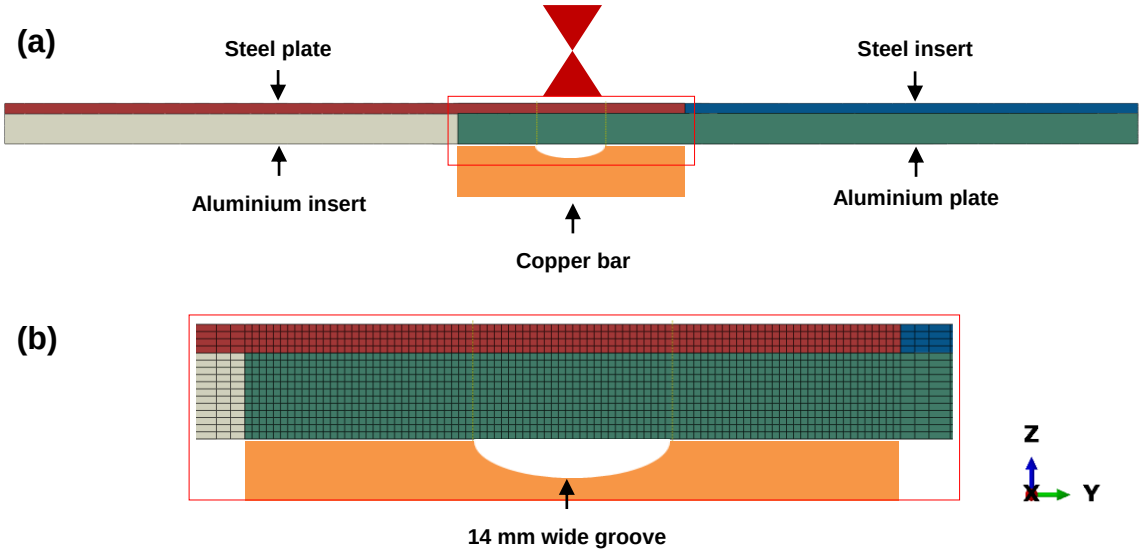

Figure 5-2: Schematic representation of the transverse section of the weldment arrangement, including steel and aluminium shims, and copper backing-bar. (a) General view and (b) magnified view of the red rectangle shown in Figure 5-2(a).

In this model, the thermal losses into the surroundings were taken into account by applying constant convection (10 W m^{-2} $^{o}C^{-1}$) and radiation (0.8 emissivity) from the outer surfaces. In the experiments, the plates were placed on a metallic backing support during welding. This backing support was composed of an aluminium plate and a copper backing-bar positioned under the weld. The copper backing-bar had a square section with 46 mm in each side and a groove of 14 mm wide in the middle of the contact surface with the aluminium plate, as shown in Figure 5-2. The thermal losses into the backing support were modelled by applying forced convection with different convection coefficients. The top bars of the clamping system were insulated with a fibreglass insulation strip to make the heat loss from the top surface of the material negligible.

The thermal contact conductance between the tooling plates and the substrates was taken into account (25×10^{4} W m^{-2} $^{o}C^{-1}$), as well as in the welding region (30×10^{4} W m^{-2} $^{o}C^{-1}$). To simplify the model the thermal conductance was considered constant even though in the weld region it should be time dependent. It should increase when the aluminium becomes liquid and decrease when the IMC layer grows as this has a very low conductivity. These parameters were determined by iterative recalculation of the model and comparison of the thermal profiles with the experimental results (cooling rates to determine the thermal losses and the temperature rise to determine the

absorbed energy). The pressure of the clamps in the experiments was kept consistent in all the samples by using a torque wrench to tighten the bolts. Therefore, the thermal conductance was considered pressure independent.

5.3 Results and discussion

5.3.1 Process modelling and experimental validation

At the point where the samples were taken the process was already in steady state condition because the weld seam was uniform and the weld profiles at the cross-sections A and B were similar, as shown in Figure 5-3.

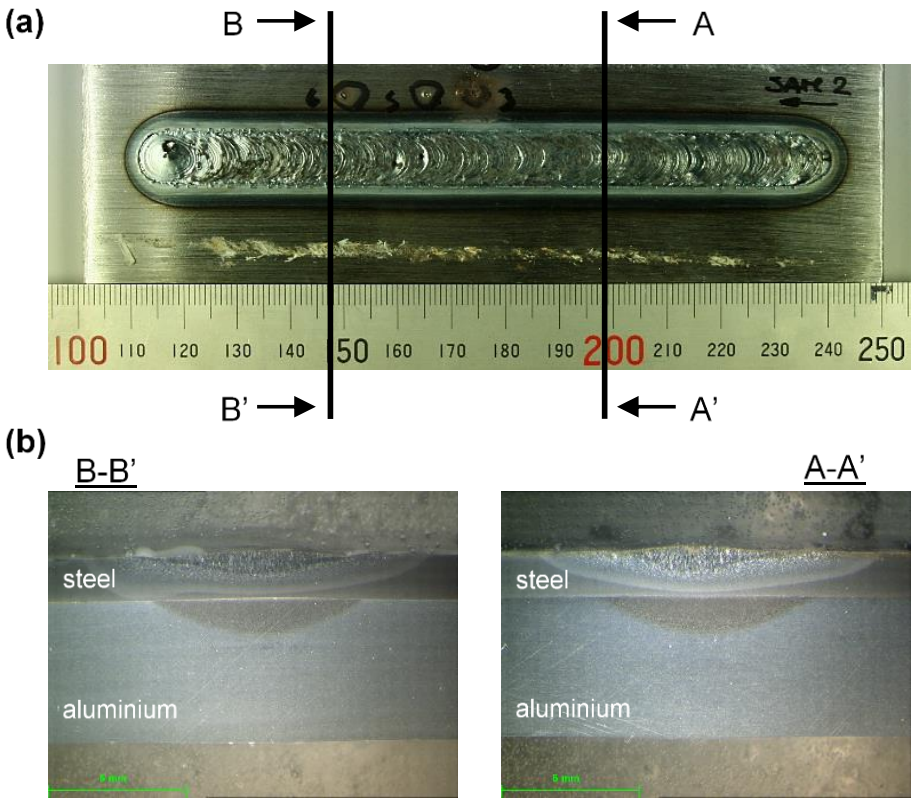

Figure 5-3: Laser welding of steel to aluminium in steady state condition. (a) Top view of the welded joint showing a uniform weld seam and (b) cross-sections A-A' and B-B' showing similar weld geometries.

For calibration of the model several experiments were carried out with different interaction time and power density values. K-type thermocouples were attached to the surface of the specimens at different positions to measure the thermal cycle during

welding. Figure 5-4 shows schematically the position of the thermocouples where the temperature was measured.

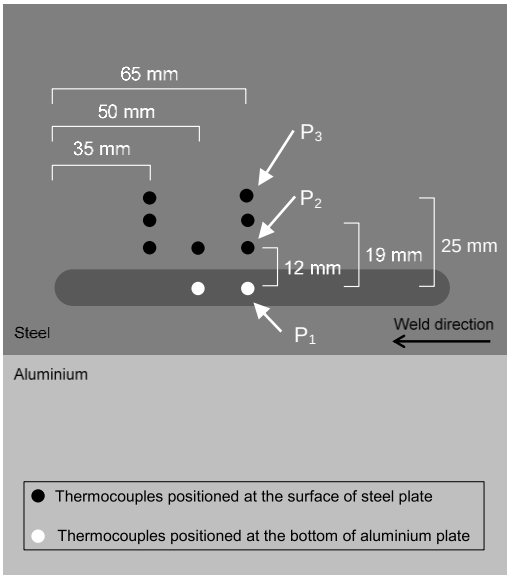

Figure 5-4: Schematic representation of the instrumented Fe-Al lap joint used to measure the thermal profiles showing the positions of the thermocouples.

The thermal profiles calculated by the FEM at different positions are in good agreement with the experimentally measured values (see Figure 5-5).

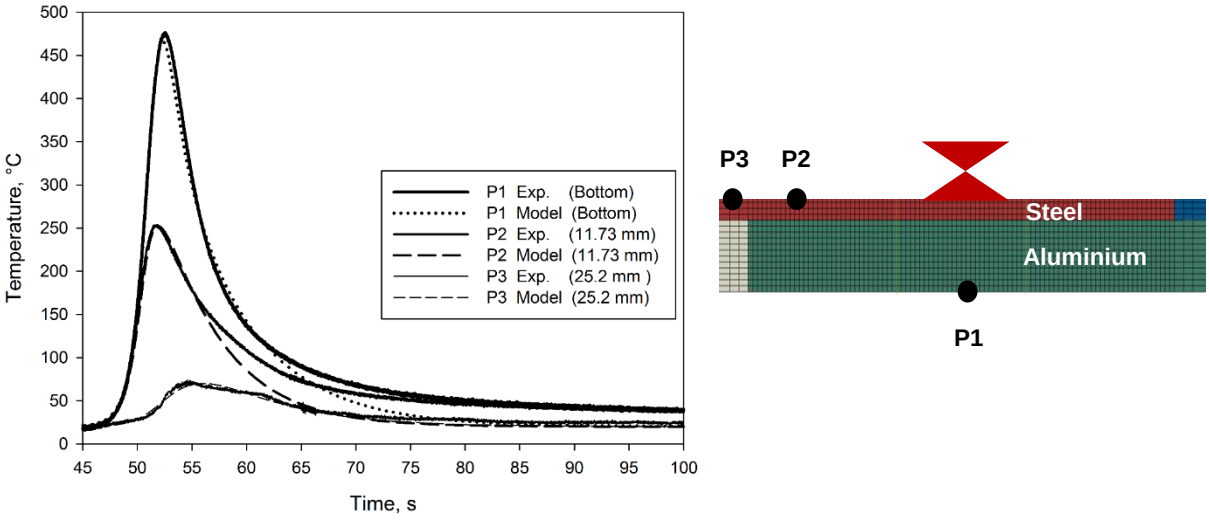

Figure 5-5: Comparison between experimental and calculated thermal cycles at different distances from the weld seam (P = 5.0 kW, TS = 0.35 m.min^{-1}, D_{beam} = 13 mm).

At three different positions on the sample, the peak temperature and the heating phase from the model match the experimental data. The cooling phase has a small deviation

mainly below 150 ºC which is acceptable because at this magnitude of temperature the weld width and the IMC growth are not affected. The heating phase and peak temperature in the model are related to the characteristics of the heat source, whereas the cooling phase is associated to the cooling conditions specified in the model. The deviation is due to the complexity of this setup. The cooling conditions need to take into account the material properties, contact between the steel and aluminium plates and the plates and the clamping system. The formation and growth of IMC layer may also play a role in the cooling of the material because during the joining process this layer grows and the heat conduction between both plates may change.

The aluminium weld width which defines the bonding area was also calculated by the model. For this, the area enclosed by the isotherm represented on the aluminium plate with temperature higher than the aluminium melting point was considered (see Figure 5-6a-c). These figures show how the model compare to the experimental data. The isotherm line indicated on the picture from the model represents the liquidus temperature of the aluminium. The fusion zones of the three welds produced using different interaction times and constant power density are very similar to the ones represented by the model. Figure 5-6b shows how the weld width estimated by the model compares to the experimental data. The data from the model shows an offset of -1.4 mm in relation to the experimental data. However, the growth of the weld width follows a similar trend (the slope is near 1) of that of the experimental data.

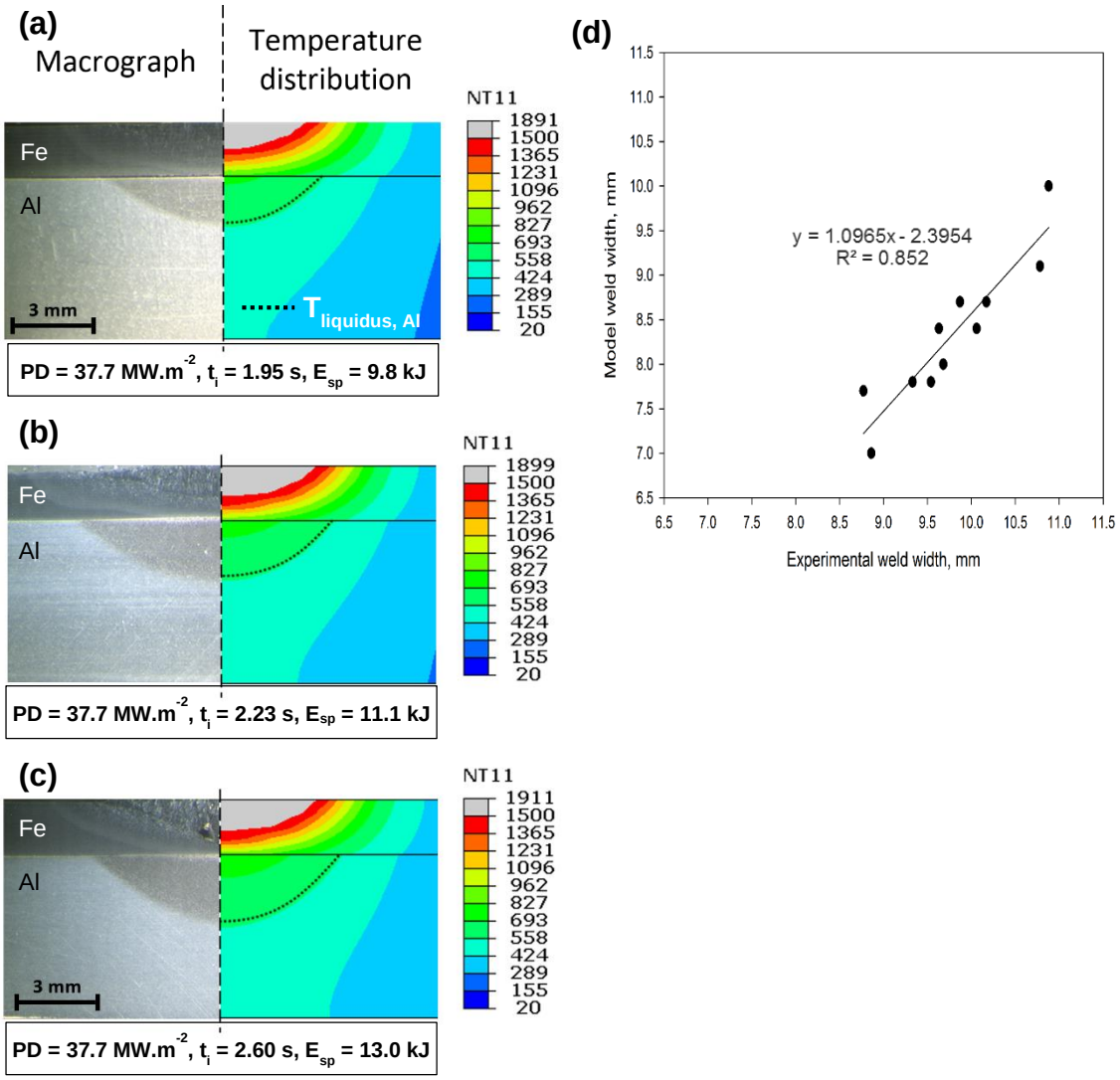

Figure 5-6: Comparison between the experimental and the FE results: (a) macrograph vs thermal profile and (b) experimental weld width vs weld width calculated by FEA.

5.3.2 Power density and interaction time vs time and temperature

The peak temperature and molten time calculated by FEA were analysed separately for different levels of power density and interaction time. According to graphs in Figure 5-7a and Figure 5-7b, both interaction time and power density have direct influence on the maximum temperature of the thermal cycle. Figure 5-7a shows the evolution of the peak temperature as a function of power density for different levels of interaction time. On the other hand, Figure 5-7b shows the evolution of the peak temperature as a function of interaction time for different levels of power density. Compared to the interaction time, the power density induces a larger variation of the peak temperature. The slope of the trend lines in the graphs also give an indication about the influence

of each parameter on the peak temperature. In Figure 5-7a the trend line is steeper than that in Figure 5-7b. Since specific point energy is a function of interaction time and power density, one could argue that the results could be influenced by the range investigated in each parameter. For this reason, the results were also presented as a function of process energy. In Figure 5-7c the specific point energy is variable with power density and in each series of the graph the interaction time is constant. One may observe that within a given range of energy, the peak temperature has a larger variation when the power density varies than when interaction time varies. Considering the equations of the trend lines, the maximum temperature increases nearly 50 °C/kJ with power density and only 13 °C/kJ with interaction time.

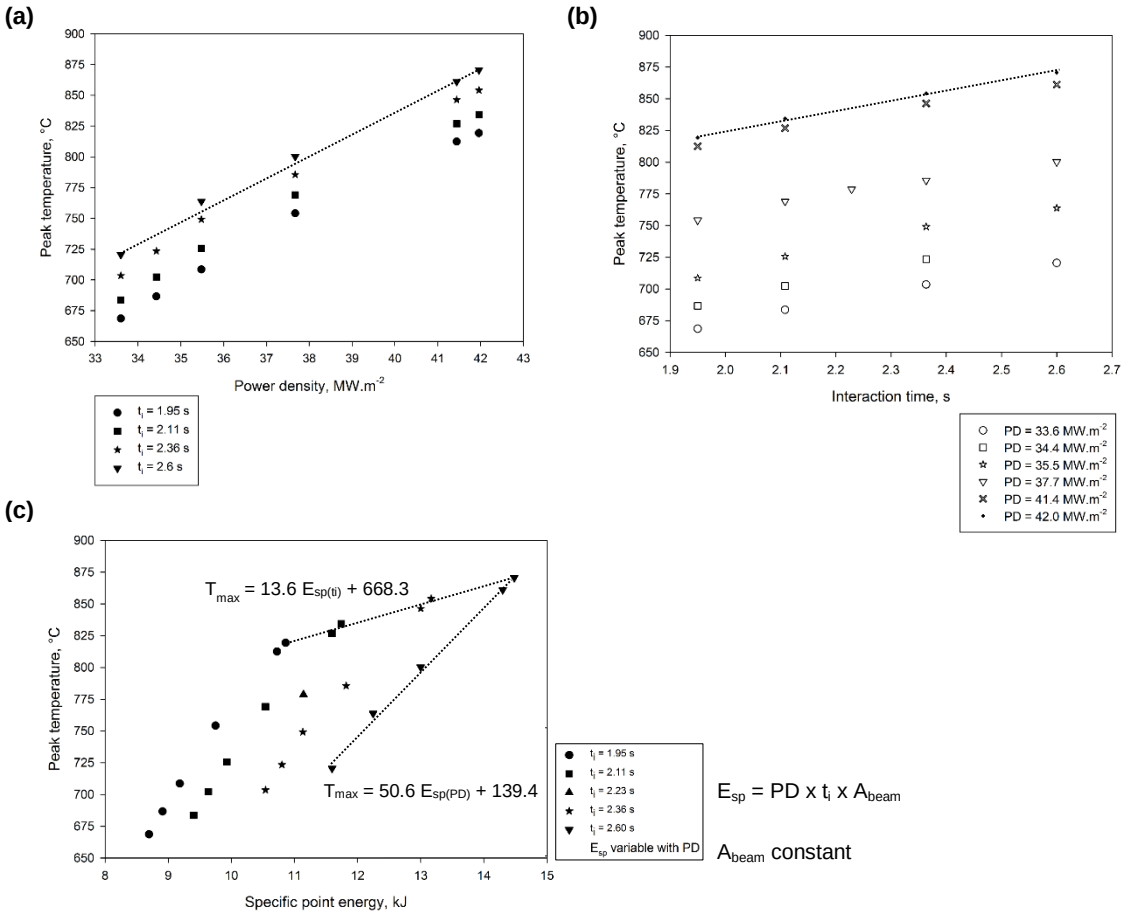

Figure 5-7: Maximum temperature calculated by the FEA at the Fe-Al interface and at the centre of the weld for different levels of (a) power density, (b) interaction time and (c) specific point energy variable with power density (from 33.6 MW.m^{-2} up to 42.0 MW.m^{-2}).

The Design Expert software was used to create the surface plot represented in Figure 5-8. The 3D graph has a linear regression of power density and interaction time as a function of peak temperature calculated at the centre of the weld at the joint interface. The red dots correspond to the FEA model run points. Equation 5-1 was obtained from the Design Expert software with coded factors to describe the trend of peak temperature in function of power density and interaction time over the range of the experiments. The coded factors give an indication about the relative weight of each individual parameter on the peak temperature and the factors are independent on the magnitude of each parameter. In this case, power density has about three times more influence on the peak temperature than interaction time.

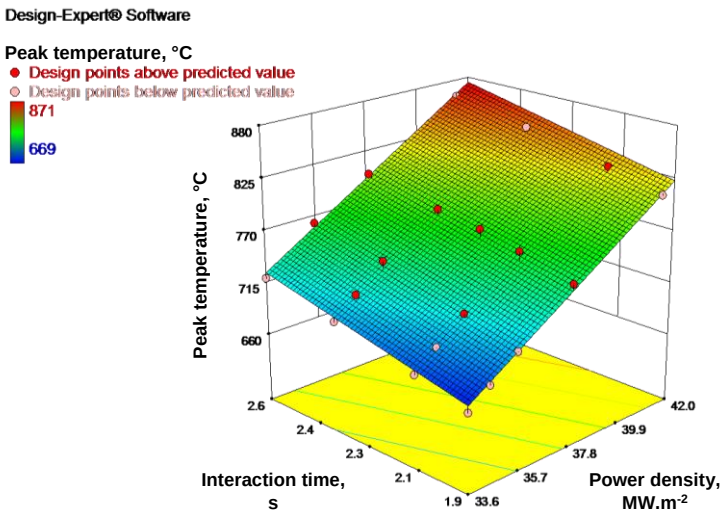

DOE equation with coded factors:

$$T_{max} = 775.24 + 73.87\ PD + 25.42\ t_i \quad (5\text{-}1)$$

Figure 5-8: Graphical representation of peak temperature calculated at the centre of the weld at the joint interface as a function of interaction time and power density.

A similar approach was used to correlate the fundamental material interaction parameters with the molten time (time corresponding to the temperature at Fe-Al interface higher than 570 °C, which is the aluminium melting temperature). The graphs in Figure 5-9a and b show that a longer melting time results from either higher power density or longer interaction time. Opposed to the peak temperature, power density and interaction time have a similar effect on the molten time. The slope of the trend lines is similar in Figure 5-9a and b. In terms of process energy, Figure 5-9c shows

that the time in molten state is directly proportional to specific point energy for any value of the power density or interaction time. Within a range of energy, the molten time increases 0.21 s/kJ with power density and 0.25 s/kJ with interaction time.

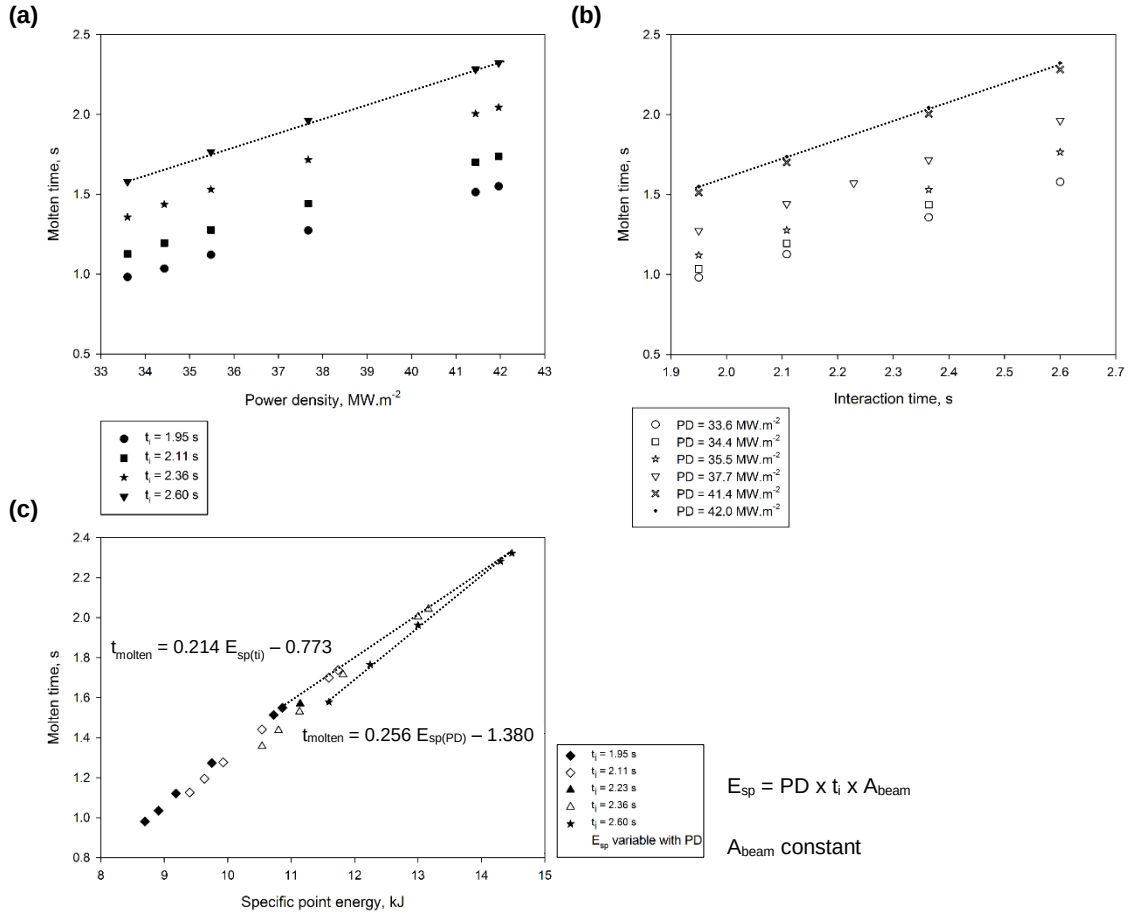

Figure 5-9: Molten time calculated by the FEA at the Fe-Al interface and at the centre of the weld for different levels of (a) power density, (b) interaction time and (c) specific point energy variable with power density (from 33.6 MW.m^{-2} up to 42.0 MW.m^{-2}).

The surface plot represented in Figure 5-10 is a linear regression of power density and interaction time as a function of molten time. The red dots correspond to the FEA model run points.

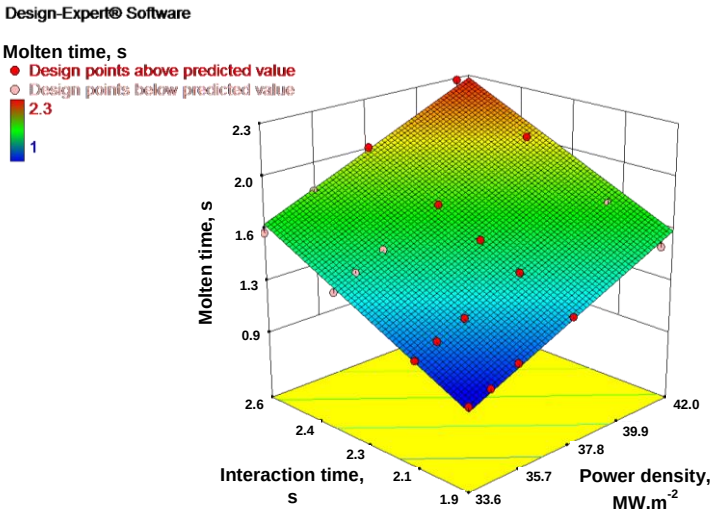

DOE equation with coded factors:

$$t_{molten} = 1.62 + 0.32\,PD + 0.34\,t_i \quad \textbf{(5-2)}$$

Figure 5-10: Graphical representation of molten time (considering temperature at Fe-Al interface higher than 570 °C corresponding to aluminium in liquid state) as a function of interaction time and power density.

The coded factors in equation 5-2 for power density and interaction time are similar, 0.32 and 0.34 respectively. Once again this confirms that these two parameters have identical effect on the molten time. The effect of the interaction time on the molten time is clear, a longer interaction time allows the material to be in liquid state for a longer period of time. On the other hand, the effect of the power density is associated to the inter-dependency of temperature and time. This means that for a higher peak temperature there is a longer time in which the metal is above its melting temperature. As shown in Figure 5-7, the peak temperature is highly dependent on power density, therefore a longer molten time is expected when power density increases.

5.3.3 IMC layer thickness and weld width vs Joint strength

The cross-section of a laser welded sample is shown in Figure 5-11a. The geometry of the fusion zone on the steel plate is a characteristic of the welds made in conduction mode. The macrograph also shows that the depth of penetration on the steel plate was less than half thickness (about 1 mm) and for this reason during joining there was no mixing of molten aluminium with molten steel. The IMC layer resulting from the reaction between atoms of Fe and Al is located between the steel and the aluminium plates, as shown in Figure 5-11b. The bonding area between steel and aluminium is given by the width of the aluminium fusion zone, as indicated in Figure 5-11a. Since

the weld length, or second dimension, is equal in all samples this dimension was disregarded.

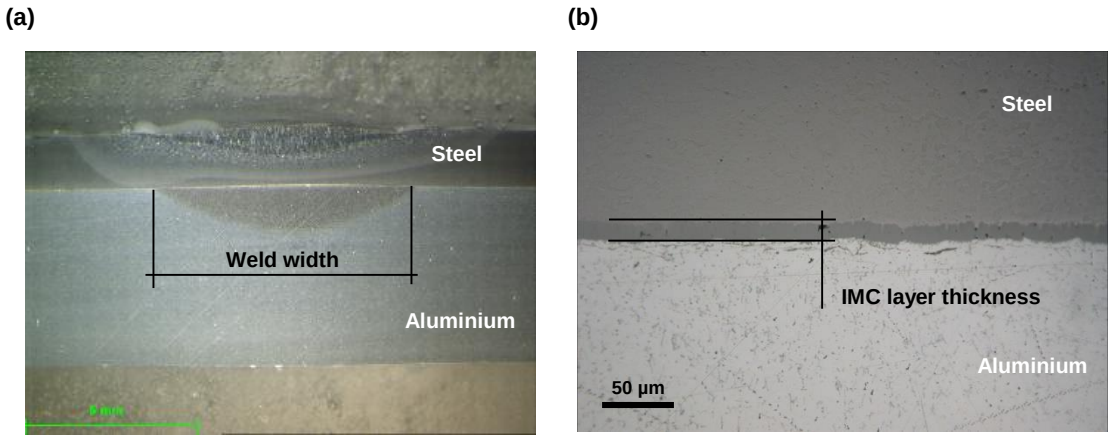

Figure 5-11: Cross-sectional view of the laser welded Fe-Al joint: (a) macrograph and (b) micrograph.

It is known that the thermal field resultant from the interaction of the laser with the material defines the dimension of the weld width and the IMC layer and the integrity of the joints is dependent of these two factors. However, when the thermal field is not known, the only way to correlate the welding process with the characteristics of the joints is by the process parameters. The graphs in Figure 5-12a-b show how the IMC layer thickness and the weld width evolved with specific point energy, within the range of the experiments with either power density (I) or interaction time (II) variable. As the energy of the process increases either by power density or interaction time, the IMC layer becomes thicker and the fusion zone of the aluminium becomes wider. This explains the non-linear behaviour of the mechanical strength of the joints with the specific point energy, which is represented in Figure 5-12c. This graph shows that the joints have minimum strength when the process energy is either minimum or maximum. Figure 5-13a-b show how the mechanical strength of the Fe-Al welded joints varies with the IMC layer thickness and the weld width formed during different welding conditions, respectively. Both graphs have similar trend, the mechanical strength is maximum only when the weld width and IMC layer have intermediate values. The thermal field during the welding process with high levels of energy induced the growth of the weld width and the IMC layer thickness simultaneously and these two parameters have opposite effects on the mechanical strength of the joints. When the weld width is large the IMC layer is very thick but when the IMC layer is thin the

bonding area is very small. Therefore, only for intermediate values it is possible to a relative high strength.

One would expect the mechanical strength of the joint to have a linear dependence with bonding area, however, in dissimilar metal joining an additional parameter must be taken into account, the IMC layer formed at the joint interface.

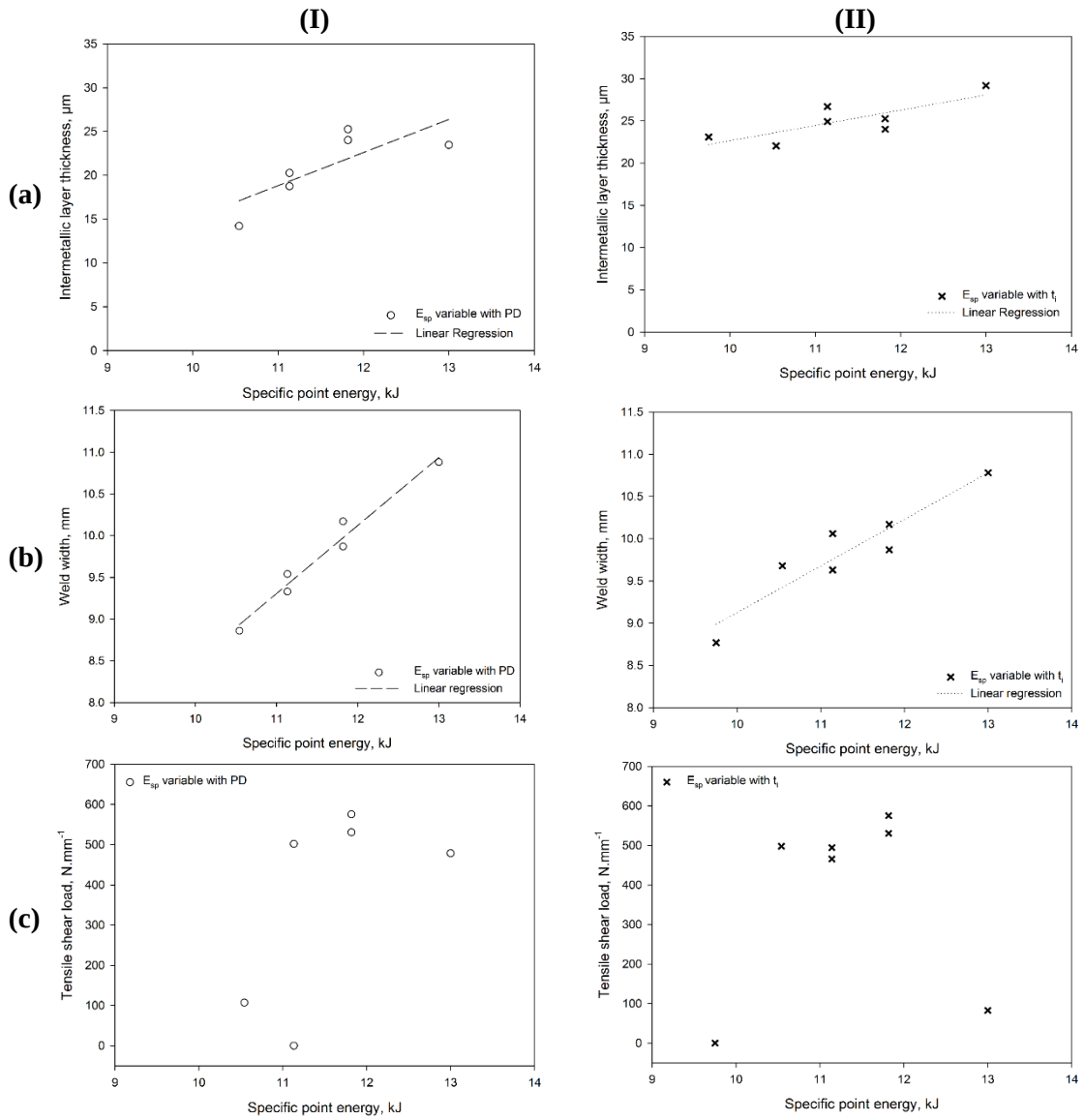

Figure 5-12: Graphical representation of (a) IMC layer thickness, (b) weld width and (c) tensile shear strength as a function of specific point energy variable with (I) power density and (II) interaction time.

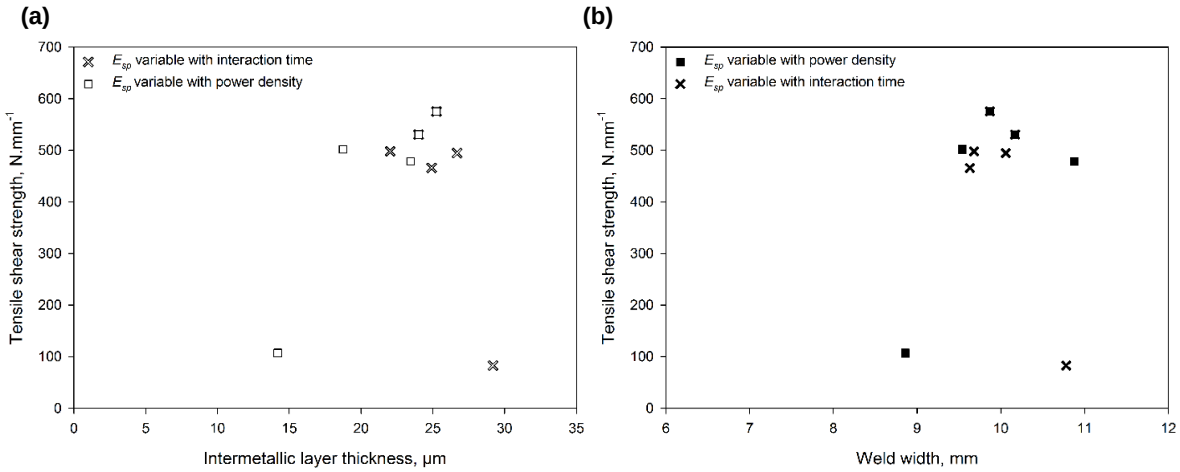

Figure 5-13: Correlation between maximum tensile-shear strength and (a) IMC layer thickness and (b) weld width.

5.3.4 IMC layer thickness and weld width vs temperature and time

The results from the thermal model explain why the weld width and IMC layer thickness vary with specific point energy (see Figure 5-14 where Figure 5-14a-b were reproduced from Figure 5-12a-b). It is clearly seen in Figure 5-14c-d that the thermal field within the experimental range is linearly proportional to the specific point energy. The maximum weld width and IMC layer thickness formed on samples welded with high level of energy (indicated in Figure 5-14a–b) are due to the maximum peak temperature and the molten time calculated at the centre of the weld at the joint interface. At the joint interface and within the experimental range with energy varying with power density, the temperature of the molten aluminium ranged between 700 and 850 °C. When the energy varied with interaction time, the range of temperature was from 750 up to 800 °C. In terms of time, the model estimated that independent of the way the energy was varied the aluminium remained in liquid state between 1.3 and 2.0 s.

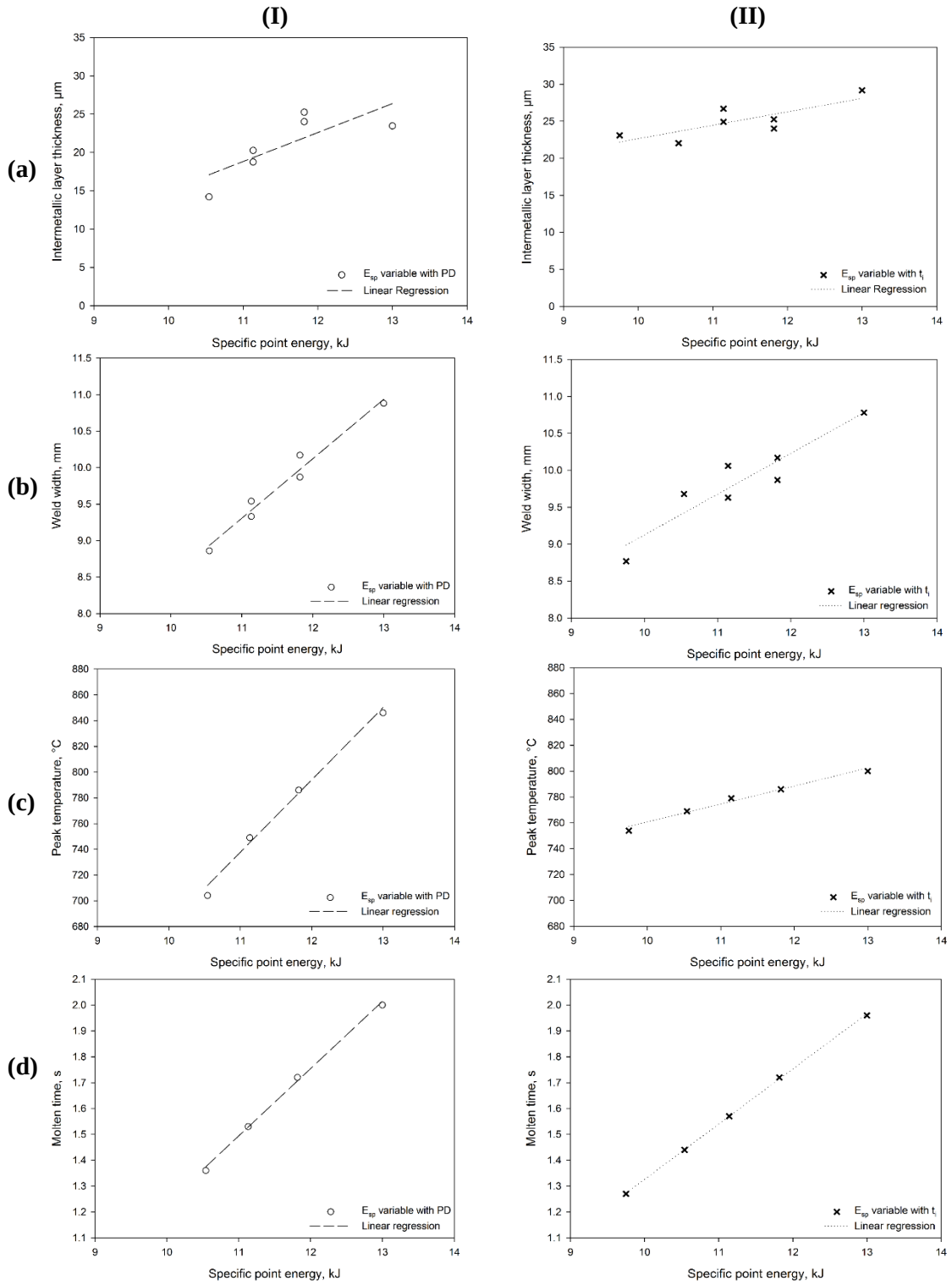

Figure 5-14: Graphical representation of (a) IMC layer thickness, (b) weld width, (c) peak temperature and (d) molten time as a function of specific point energy variable with (I) power density and (II) interaction time.

The effect of temperature and time on the IMC layer thickness and weld width is analysed separately in Figure 5-15 and Figure 5-16, respectively. The results suggest

that the IMC layer thickness is more dependent on peak temperature than that of time. As the temperature increases with the process energy, the IMC layer becomes thicker. This result is in agreement with the results published by other authors, in which the experiments were either in equilibrium conditions (Wang et al., 1998) or transient conditions (Fan et al., 2011). On the other hand, the molten time seems to not have a direct correlation with the IMC layer thickness. For instance, when the molten time is about 1.4 s, the IMC layer can be either 15 or 22 µm. Even though the molten time is similar, the peak temperature of these two points is different due to the inter-dependency of temperature and time. This results suggest that within the experimental range, the IMC growth is more influenced by temperature than by the time.

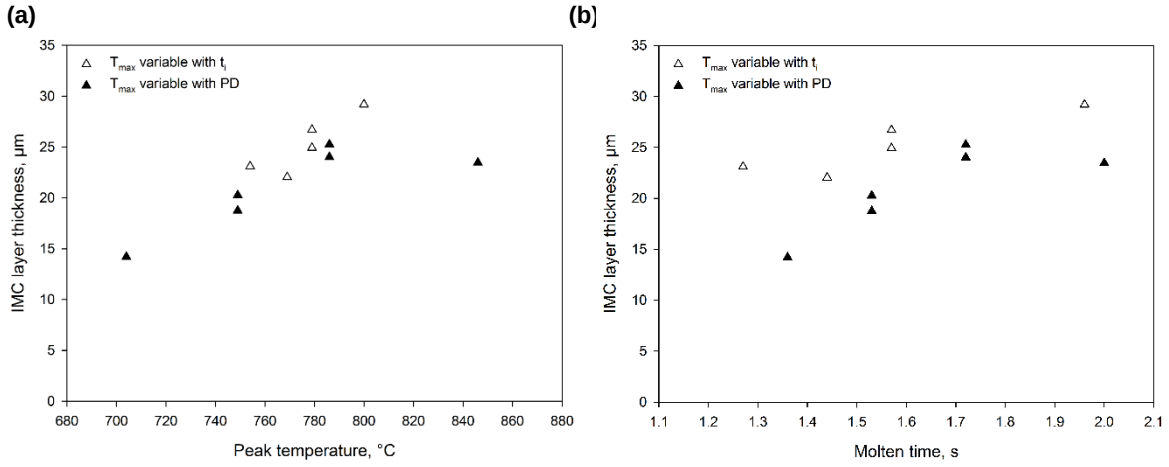

Figure 5-15: Correlation between IMC layer thickness and (a) peak temperature and (b) molten time.

Figure 5-16 shows how the weld width calculated by the FEA thermal model varies with the thermal profile during laser welding.

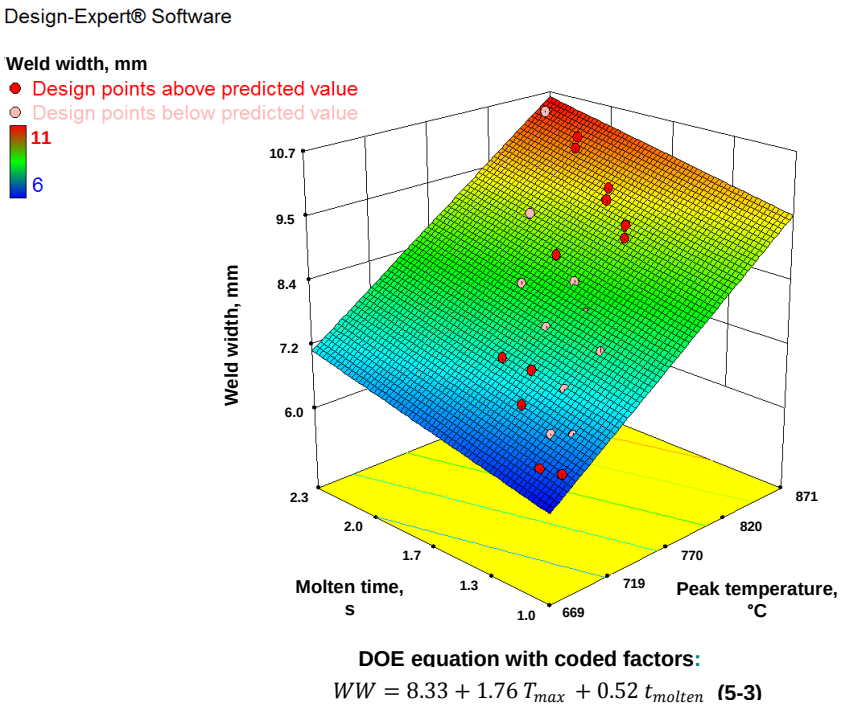

Figure 5-16: Surface plot of weld width as a function of peak temperature and molten time.

Considering the equation produced by the DOE model, it is possible to infer that the peak temperature is the parameter which most contributes to the formation of a larger bonding area. The peak temperature is about three times more important than molten time (see equation 5-3). The temperature field given by the model for different levels of power density and interaction time are shown in Figure 5-17. For a fixed energy input, 11 kJ for instance, the aluminium fusion zone is wider when higher power density and shorter interaction time is used to produce the joint.

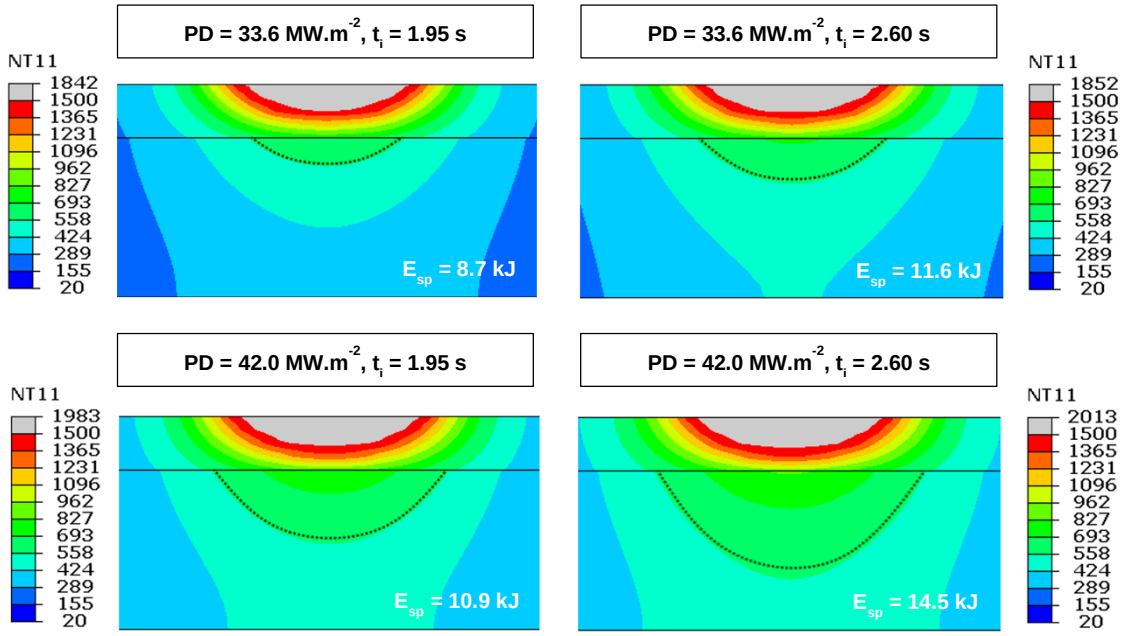

Figure 5-17: Temperature distribution on the plane perpendicular to the weld seam for different values of power density and interaction time.

This result corroborates what has been suggested in the previous work where it was referred that weld width increases with power density due to the peak temperature (Meco et al., 2014). The profile of the laser beam may be a reason for the growth of the weld width with power density. If the laser beam has a Gaussian profile, as the power density increases the effective size of the laser beam also increases. This effect has also been observed in laser cutting where it was found that the kerf width changed when increasing the laser power for a constant nominal beam diameter. The authors attributed the changes in kerf width to the non-perfect top hat power distribution. As the power density increases, the effective beam diameter increases due to the edges of the beam profile not being perpendicular. Therefore, by increasing the power, the diameter of the beam which exceeds the energy density threshold for melting of the material also increases. Then, this results in increasing the width of the weld. With a perfect top hat profile this effect would not be seen.

The results of this work suggests that it is not possible to further improve the mechanical strength of the Fe-Al joints by solely controlling the energy of the process. The IMC layer and the bonding area are the key factors for the integrity of the Fe-Al joints and both evolve in a similar manner with the thermal field, i.e. temperature and time. To improve the mechanical strength of the joints by increasing the bonding area,

it would be beneficial to increase the power density because this creates a larger weld. However, the power density is the parameter which most controls the temperature and since the IMC layer seems to be more sensitive to temperature than that to time under this welding condition the IMC growth would be also enhanced. An alternative solution to increase the bonding area and avoiding the negative effect of the IMCs could be by producing parallel weld seams and change the joint geometry.

5.4 Summary

It is known that IMC layer thickness and bonding area play an important role on the mechanical strength of dissimilar metal joints of steel to aluminium. In this work an FE model of the laser process was developed to predict the thermal cycle at the interface between the steel and aluminium plates using different laser parameters. The influence of the thermal cycle was correlated to the bonding area (via weld width) and to the IMC layer thickness and in turn, to the mechanical strength of the joints. Conclusions from this work are as follows:

- Power density is the factor with major significance in the variance of peak temperature, about three times more than interaction time;

- In terms of time in molten state (time correspondent to temperature higher than the aluminium melting point), power density and interaction time have similar contribution;

- Within the range of the experiments, the peak temperature and molten time are directly proportional to specific point energy (either via power density or interaction time);

- The strength of the joints increase with bonding area (defined by the width of the aluminium weld) and decreases with the IMC layer thickness. Therefore, an optimization is vital which would be geometry dependant;

- It was not possible to identify a thermal field able to produce simultaneously a large bonding area and a thin IMC layer for the optimization of the joint strength. Parallel weld seams could be an alternative solution to increase the bonding area without increasing the IMCs.

6.0 Interlayer of copper to improve the Fe-Al joint strength

6.1 Introduction

In direct joining of steel to aluminium by laser welding it was possible to create sound joints by controlling the fundamental laser material interaction parameters to have a balance between bonding area and IMC layer thickness. Even though the strongest Fe-Al joints failed with a maximum tensile-shear load of about 30 kN, all specimens had interfacial failure.

An alternative approach to prevent the formation of Fe-Al IMCs is to use an interlayer of a metal compatible with both Fe and Al. Copper may be used for this purpose because Fe does not form IMCs with Cu and even though Al does, it also has about 18% (at.%) solid solubility in Cu.

The main subject of this chapter is to investigate the feasibility of using copper as interlayer to restrict the formation of Al-Fe IMCs and therefore increase the joint strength. The objectives are as follows:

- Investigation of laser welding of steel to aluminium with copper interlayer in the form of a foil and wire;
- Investigation of Al-Cu IMC formation when depositing copper filler wire onto aluminium substrate by CMT arc welding;
- Investigation of IMC formation when depositing different grades of aluminium wire (AA2319, AA4043, AA4047 and AA5087) onto copper layer which was previously deposited onto steel by CMT arc welding.

6.2 Investigation of laser welding of steel to aluminium with copper interlayer in the form of a foil and wire

In the present section different forms of copper interlayers were investigated to prevent the reaction between Fe and Al in laser welding of steel to aluminium. The experimental setup used was similar to the one described in the previous

sections and the interlayers were positioned between the steel and the aluminium plates. To assess the effectiveness of the interlayer different welding parameters were tested, the microstructure of the welds was analysed and the IMCs were identified.

6.2.1 Experimental procedure

6.2.1.1 Material

Two different interlayers were tested in this work, 150 and 25 µm thick pure copper foil and 1.0 mm diameter copper-silicon welding wire ($CuSi_3$). The interlayers were used between the 2 mm thick XF350 high strength low alloy steel and the 6 mm thick 5083-H22 aluminium alloy in a lap-joint configuration. The chemical composition and the mechanical properties of the materials are in Table 2-1 and Table 2-2, respectively, in section 2.2.

6.2.1.2 Methodology and Experimental Setup

In this work the copper interlayer was used in different forms, as foil and wire. The copper interlayer is positioned between the steel and aluminium plates to form a physical barrier against the diffusion of Al elements into Fe and vice-versa, as this causes the formation of the brittle IMC layer. As the melting temperature of pure Cu is around 1080 °C, which is lower than that of the steel (1500 °C) and higher than aluminium (570 °C), the copper interlayer can be used between the steel plate (on top) and the aluminium plate (at the bottom). In this manner, the heat can be transferred through the steel plate to melt the copper interlayer and then the aluminium. For the success of this technique the thermal gradient needs to be such to melt the copper and the aluminium and keep the steel solid (at least at the Fe-Cu interface). In theory, the diffusion of Al and Fe elements between each other is blocked in the presence of the interlayer and the Fe-Al IMC formation is restricted.

Theoretically the gap induced by the presence of the interlayer is reduced during the joining process when the copper melts and the pressure is applied by the clamping device. The copper in the liquid state flows and wets the steel side and

on the aluminium side a molten pool is formed and wets the copper. Figure 6-1 shows different options for the application of the copper interlayer between the steel and the aluminium plates.

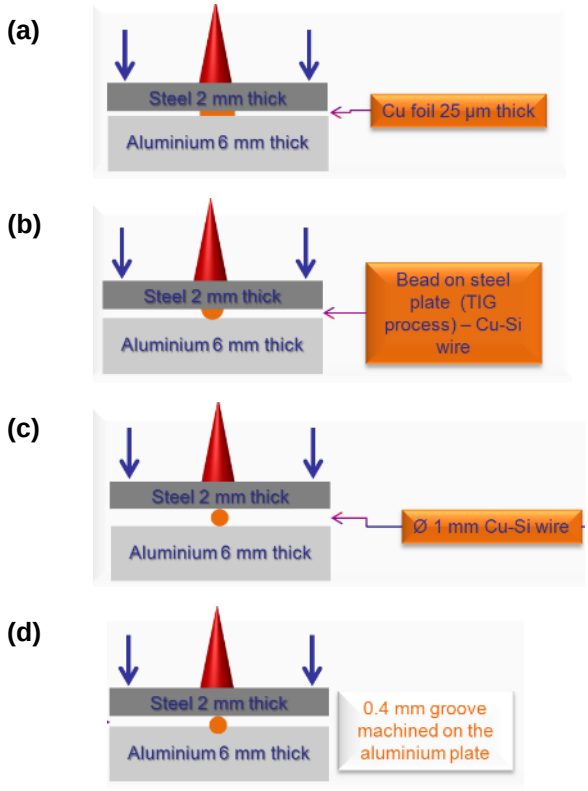

Figure 6-1: Schematic representation of the joint configuration with copper interlayer in the form of (a) foil, (b) $CuSi_3$ welding wire deposited on the steel plate by TIG welding (c) 1 mm diameter $CuSi_3$ wire positioned on the surface of the aluminium plate and (d) inserted in a 0.4 mm wide groove machined in the aluminium plate.

The advantage of using copper foil as showed in Figure 6-1a is the small gap created by the small foil thickness. Some researchers have reported the benefit of the presence of Si in the Fe-Al joint to reduce the IMC growth. For this reason, $CuSi_3$ welding wire as interlayer was tested in three different configurations (see Figure 6-1b,c and d). In Figure 6-1a the copper foil is positioned between the upper plate (steel) and the lower plate (aluminium) and covers the entire length of the plate as well as the width of the weld seam. The joint configuration showed in Figure 6-1b requires the (Tungsten Inert Gas) TIG process to deposit the

copper on the steel plate (bead on plate configuration). The process parameters used to deposit the copper layer onto the steel are indicated in Table 6-1.

Table 6-1: Welding parameters used on the TIG process to deposit the copper layer onto the steel. CTWD stands for contact tip to workpiece distance.

Backing bar	CTWD, mm	I, A	TS, $m.min^{-1}$	WFS, $m.min^{-1}$
Copper	4.0	100	0.5	2

TIG is a suitable process for this purpose since the heat input is lower than that of other arc welding processes and thus, the distortion on the work piece due to residual stresses is minimized. Before welding the plate with the copper bead it was cleaned and positioned on the aluminium plate (with the copper bead facing the aluminium plate). The joint configurations represented in Figure 6-1c and Figure 6-1d use copper wire positioned either directly on the aluminium plate or inserted in a 0.4 mm wide machined groove on the aluminium. The groove reduces the gap between the steel and the aluminium plates.

The setup in use was similar to the one shown in section 2.3 for direct joining of steel to aluminium. The laser parameters, viz. system and fundamental material interaction parameters, used in the experiments are shown in Table 6-2. The latter parameters are calculated using the system parameters as shown in section 1.8.1.1 of this Thesis (equations 1-5 to 1-7).

The experimental parameters needed to be adjusted for each interlayer to ensure that there was only partial melting of the steel, the welds were in conduction mode and most important, that there was bonding between the steel and the aluminium plates. During the experimental work no shielding gas was used.

Table 6-2: System and fundamental material interaction parameters used in the laser welding experiments.

Interlayer type	System parameters		Fundamental laser material interaction parameters			
	Beam diameter, D_{beam}, mm	Power, P, kW	Travel speed, TS, m.min^{-1}	Power density, PD, MW.m^{-2}	Interaction time, t_i, s	Specific point energy, E_{sp}, kJ
Foil	16	6	0.30	29.8	3.20	19.2
			0.25		3.84	23.0
			0.20		4.80	28.8
			0.15		6.40	38.4
	13	6	0.15	45.2	5.20	31.2
			0.20		3.90	23.4
	13	4	0.15	30.1	5.20	20.8
Wire	13	6	0.15	45.2	5.20	31.2
			0.25		3.12	18.7
			0.30		2.60	15.6
			0.35		2.23	13.4
Wire & 0.4 mm groove	13	6	0.30	45.2	2.60	15.6
Bead on plate	13	6	0.30	45.2	2.60	15.6
			0.35		2.23	13.4
			0.45		1.73	10.4

6.2.1.3 Metallographic analysis

The metallographic analysis of the dissimilar joints with copper interlayer followed a procedure similar to the one depicted in section 2.3.4. It included sample cutting, mounting in resin, grinding and polishing, optical microscopy and macroscopy and finally, SEM and EDS analysis.

Even though the phase diagrams show phases formed under equilibrium conditions, the binary phase diagrams were used to identify the IMCs present in the cross sections, as an approximation.

6.2.2 Results and Discussion

Table 6-3 shows a summary of the laser welding parameters used to join steel to aluminium with a copper foil interlayer. Symbols were added to this table to indicate the success of the joints. The red crosses represent the experiments in

which there was no bonding or where a weak bond was achieved. The green symbols indicate that the joint was successfully bonded.

Table 6-3: Laser welding parameters and results.

Interlayer	Spot size [mm]	Power [kW]	Travel speed [cm/min]	Interaction time [s]	Power density [kW/cm^2]	Specific point energy [kJ]	Welded?
Foil	16	6	0.30	3.2	2.98	19.2	✗
Foil	16	6	0.25	3.84	2.98	23.04	✗
Foil	16	6	0.20	4.8	2.98	28.8	✗
Foil	16	6	0.15	6.4	2.98	38.4	✗
Foil	13	6	0.15	5.2	4.52	31.2	✓✗
Foil	13	6	0.20	3.9	4.52	23.4	✗
Foil	13	4	0.15	5.2	3.01	20.8	✗
Wire	13	6	0.15	5.2	4.52	31.2	✓✗
Wire	13	6	0.25	3.12	4.52	18.72	✓
Wire	13	6	0.30	2.6	4.52	15.6	✓
Wire	13	6	0.35	2.23	4.52	13.37	✗
Wire & 0.4 mm groove	13	6	0.30	2.6	4.52	15.6	✓
Bead on plate	13	6	0.30	2.6	4.52	15.6	✗
Bead on plate	13	6	0.35	2.23	4.52	13.37	✗
Bead on plate	13	6	0.45	1.73	4.52	10.4	✗

✓ Successful bonding ✗ Weak bonding or no bonding ✓✗ Joint failure during cutting

As a general observation, the results showed that it is difficult to produce sound joints with the majority of the forms of interlayers.

When using copper foil it was only possible to create joints when welding with higher interaction time and power density. However, this sample broke during cutting for sample preparation. A possible reason for these poor results may be the small thickness of the foil that was not enough to prevent the diffusion between Al and Fe and thus, the formation of Fe-Al IMCs could not be avoided.

The results of the experiments in which the interlayer was a copper bead deposited prior to the laser experiment on the steel plate were not different from the previous results. All the samples broke whilst removing them from the clamping system, irrespective of the welding parameters used. The premature failure of these samples may be related to the distortion of the steel plate induced by the TIG process during the deposition of copper bead on the steel plate. The distorted plate with the copper bead was positioned on the aluminium plate and clamped but after the joining process more residual stresses were induced. These residual stresses were enough to break the fragile bond between the steel and the aluminium.

The only satisfactory results were the joints produced with copper welding wire positioned either on the surface or inside the groove of the aluminium plate. In both configurations the thickness of the interlayer was enough to minimize the Al-Fe reaction and the joint showed less distortion.

The macrographs of the welded samples are shown in Table 6-4. Besides the poor mechanical strength, the samples have also major defects such as cracking and porosity in the fusion zone. The macrosections also indicate that part of the copper wire melted and wet the steel surface whereas the other part of the wire was mixed with the molten aluminium. Ideally, the copper on the aluminium side should remain solid during the welding process to minimize the diffusion between Al, Cu and Fe and thus, the formation of binary or even ternary IMCs. However, for this joint configuration the thermal gradient to produce the joint is such that the temperature on the copper wire is higher than its melting temperature and therefore, the wire melts during the joining process (see Table 6-4).

The macrosections of the samples with a copper foil interlayer only show small traces of the foil near the edges of the fusion zone. Many IMCs structures, either on the Fe-Al interface or dispersed in the aluminium fusion zone are visible at higher magnification (see Table 6-4).

Table 6-4: Macro and micrographs of the samples joined with different forms of copper interlayer and different laser welding parameters.

	D_{beam} mm	P kW	TS $m.min^{-1}$	Macrograph
$CuSi_3$ wire – 1 mm diameter	13	6	0.15	
			0.25	
			0.30	
Wire inserted in 0.4 mm deep groove	13	6	0.30	
Pure Cu foil - 25 µm thickness	13	6	0.15	
	16	6	0.15	
			0. 25	
Foil – 150 µm thickness	13	5	0.35	

The presence of Fe in the aluminium fusion zone in the form of IMCs was confirmed by SEM / EDS analysis on the sample with the wire inserted in the groove (see spectrum analysis in Figure 6-3 and Figure 6-4). The results from the spectrum analysis were used together with the ternary Al-Cu-Fe phase diagram shown in Figure 6-3 for the identification of the IMCs. Two zones of interest were analysed, viz. Test 1 region which is located near the edge of the aluminium fusion zone and Test 2 region which is at the centre of the aluminium fusion zone and just under the copper welding wire. In Test 1 area the EDS analysis detected the presence of $FeAl_3$ and Fe_2Al_5 either mixed in Fe or in Al. According to the phase diagram there are also ternary Al-Cu-Fe IMCs formed in this area, which can be Al_7Cu_2Fe or $Al_{13}Cu_5Fe_2$. The EDS mapping in Figure 6-4c confirms the presence of the three elements in this region. In Test 2 region also $FeAl_3$ was identified (Test 2, Figure 6-3b). This may be explained by the diffusion of Fe into Cu which in turn reacted with Al to form this IMC. In the same figure, at spectrum 1, there is a phase of solid solution of Cu and Al into Fe. In this area the Cu seems to improve the solubility of Al into Fe (from 23% to 52%). This can be beneficial because less Fe-Al IMCs are formed at the joint interface.

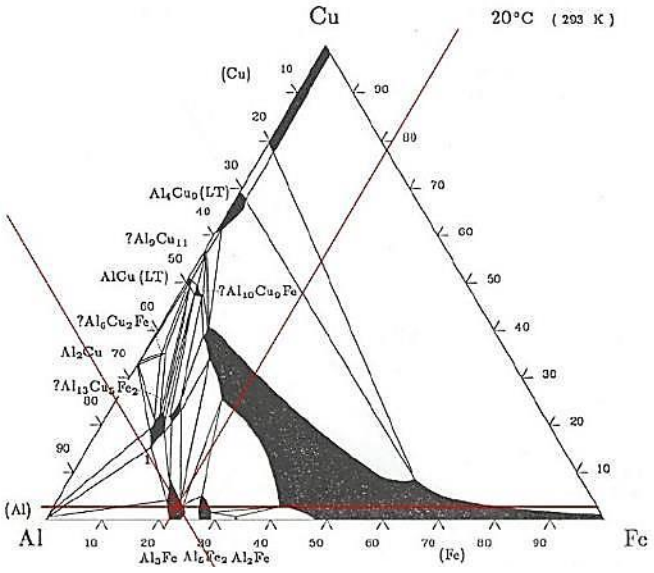

Figure 6-2: Al-Cu-Fe ternary phase diagram (in at.%) used to identify the IMC phases.

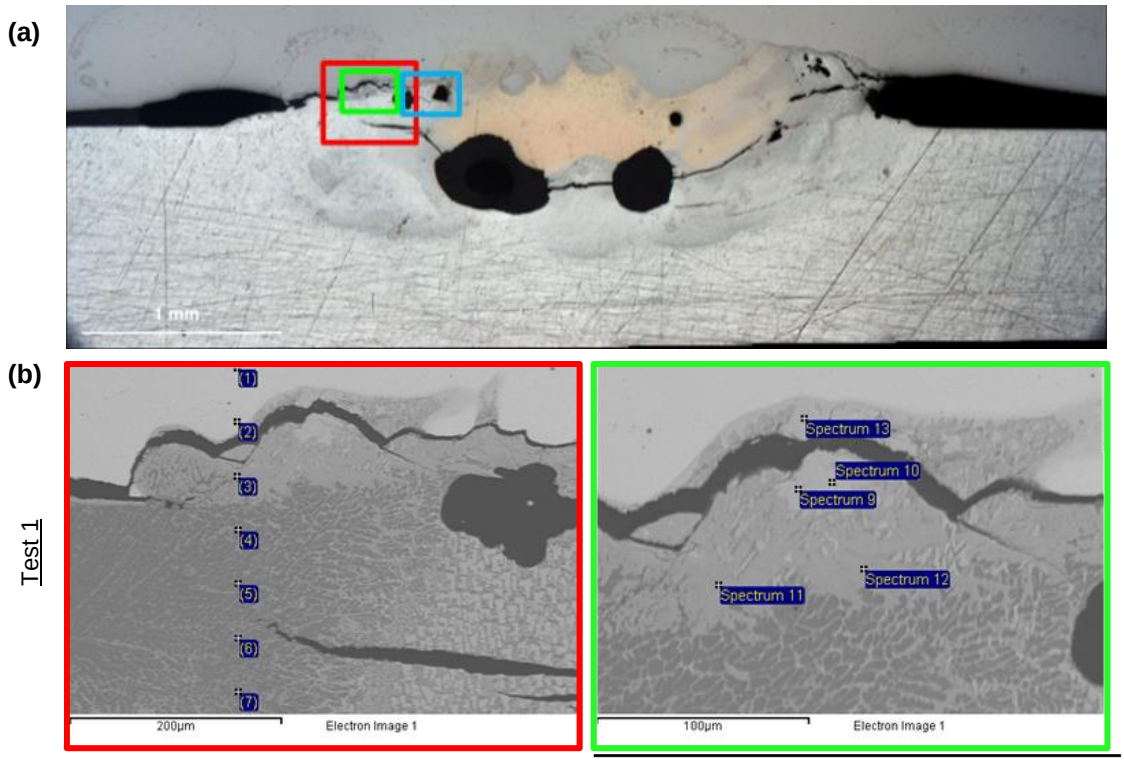

Spectrum	Al [At.%]	Cu [Al.%]	Fe [At.%]	Phase composition
Test 1				
1	2.07	-	97.93	(α Fe)
2	10.27	-	89.73	(α Fe)
3	70.62	12.32	17.06	$FeAl_3$ + $Al_{13}Cu_5Fe_2$
4	97.82	2.18	-	(Al)* + Al_2Cu
5	97.41	2.59	-	(Al)* + Al_2Cu
6	95.53	4.47	-	(Al)* + Al_2Cu
7	92.72	5.24	2.04	(Al) + Al_7Cu_2Fe
9	55.91	24.02	20.07	(α Fe)* + Fe_2Al_5
10	51.99	20.23	27.77	(α Fe)
11	75.80	5.57	18.63	$FeAl_3$* + Al_7Cu_2Fe
12	82.34	8.48	9.17	(Al) + $FeAl_3$ + Al_7Cu_2Fe
13	59.74	16.16	24.1	(α Fe) + Fe_2Al_5
Test 2				
1	49.07	33.61	17.32	(α Fe)
2	75.02	5.8	19.18	$FeAl_3$
3	72.25	23.28	4.47	(Al) + Al_2Cu + Al_7Cu_2Fe

Figure 6-3: Metallographic analysis of the joint welded with $CuSi_3$ wire of 1 mm diameter inserted in a 0.4 mm deep groove: (a) macrograph, (b) SEM/EDS spectrum results. The IMC with marked with * is the one in higher concentration. Laser welding parameters: D_{beam}=13 mm, P=6 kW, TS=0.30 m.min^{-1}.

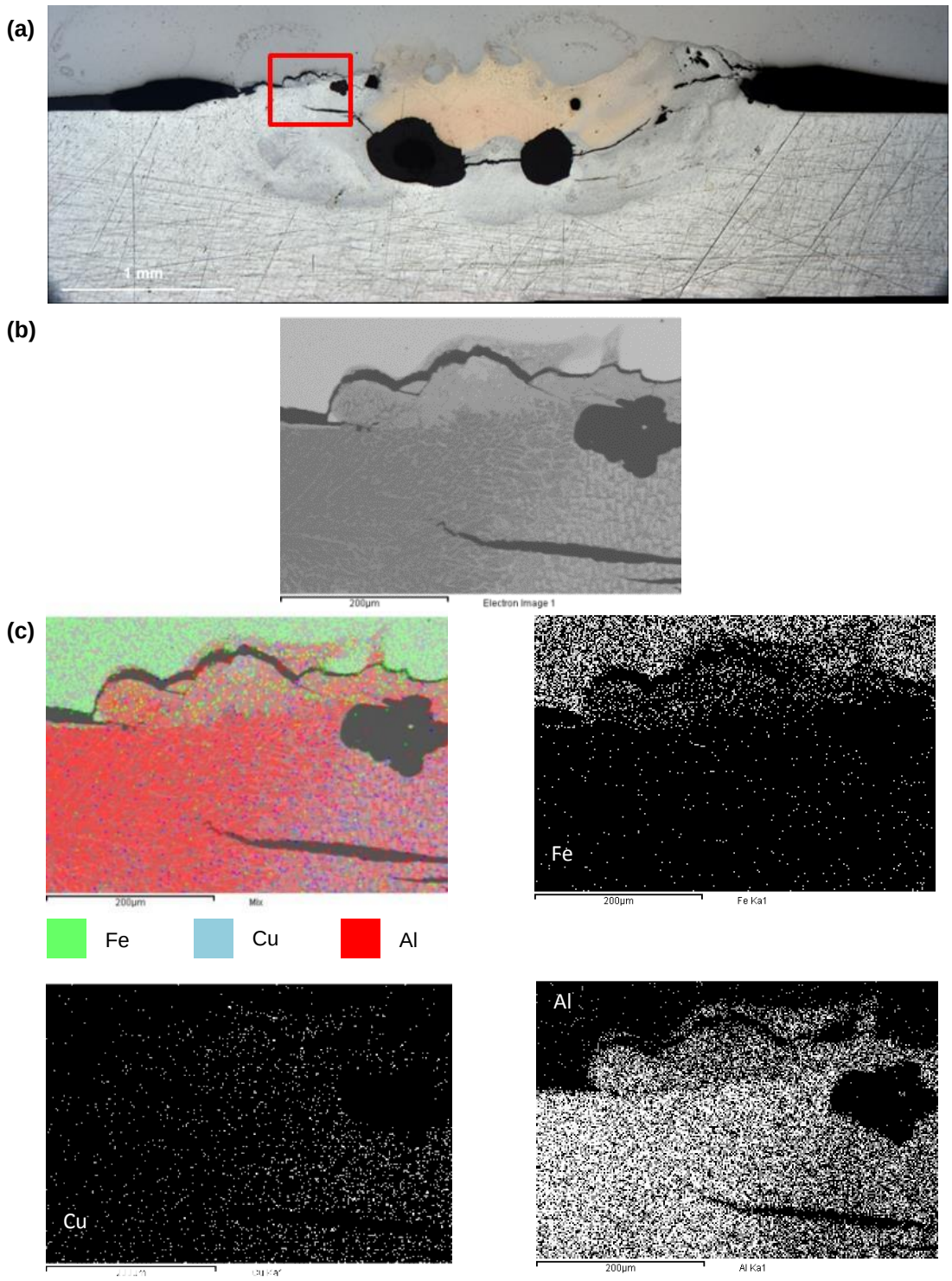

Figure 6-4: Metallographic analysis of the joint welded with $CuSi_3$ wire of 1 mm diameter inserted in a 0.4 mm deep groove: (a) macrograph, (b) SEM micrograph and (c) elemental mapping by EDS. Laser welding parameters: D_{beam}=13 mm, P=6 kW , TS=0.30 m.min^{-1}.

Similar analysis was carried out with the sample joined with copper foil as interlayer. This joint was not strong enough and broke during cutting and for this reason in Figure 6-5 only the aluminium plate and the copper foil on the sides of the weld are visible. At the centre of the weld the copper foil is not visible because it melted and it was dissolved in the aluminium during welding (Figure 6-5a). Several IMCs were formed in the aluminium fusion zone as shown in Figure 6-5b and c. However, the IMCs are spread in the Al fusion zone instead of being in a single layer opposed to what was observed before in the Fe-Al joints. The EDS elemental mapping in Figure 6-5d shows the presence of Fe and Cu in the Al fusion zone.

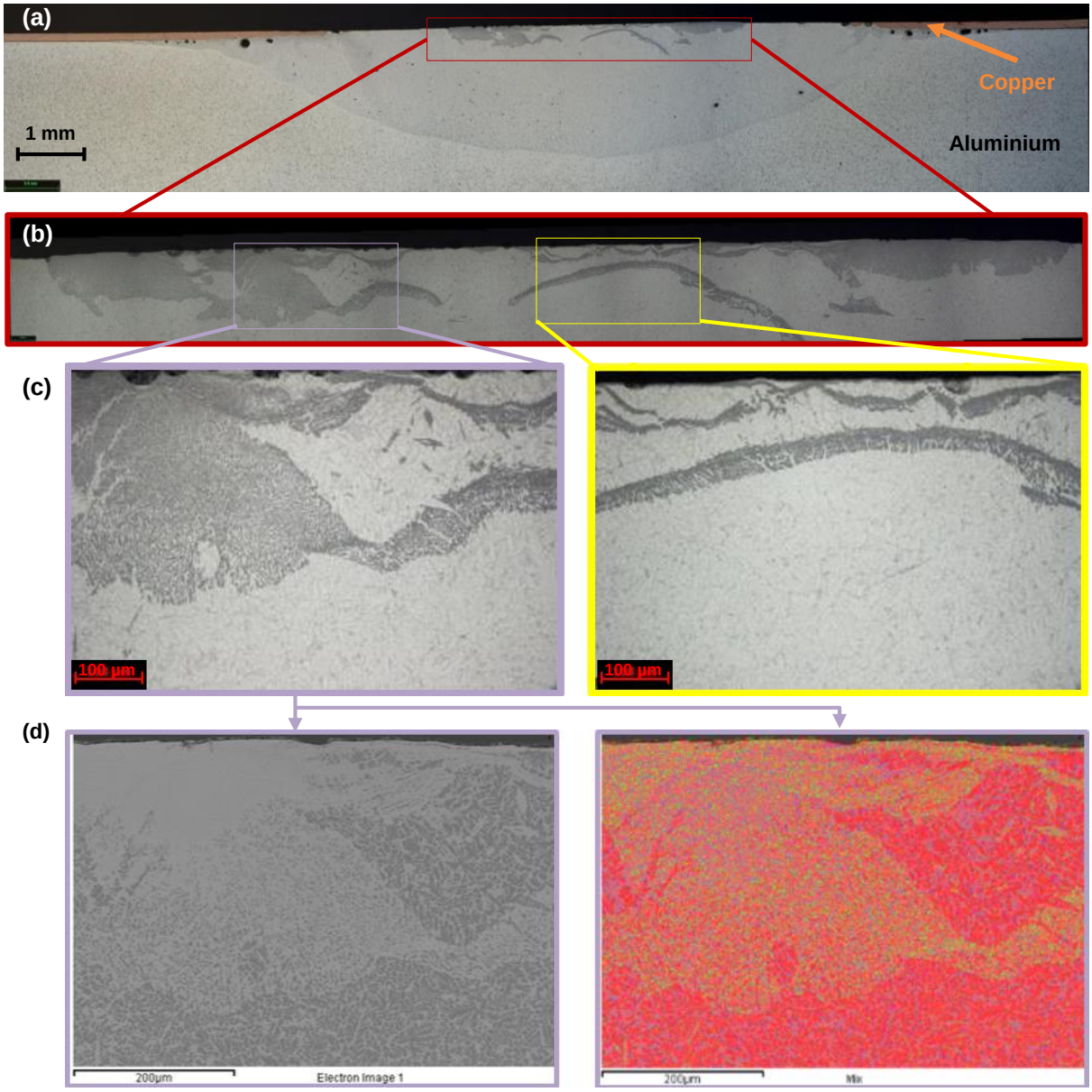

Figure 6-5: Metallographic analysis of the sample welded with a 150 µm thick pure Cu foil: (a) macrograph, (b) SEM micrograph and EDS elemental mapping. Laser welding parameters: D_{beam}=13 mm, P=5 kW, TS=0.35 m.min^{-1}.

Figure 6-6 shows two areas of interest, viz. Test 1 region represented in red which is located on the left hand side of the fusion zone and Test 2 region which is represented in blue and it is located at the centre of the weld. The EDS elemental mapping suggests that under certain welding conditions the copper foil is effective in preventing the diffusion of Fe into Al because no traces of Fe were found in

this region. However, at the centre of the weld the interlayer was completely melted and dissolved in the aluminium. The reaction between Fe, Al and Cu could not be avoided and IMCs were formed. According to the EDS spectrum analysis and the ternary phase diagram the only IMC found was $FeAl_3$ (see Figure 6-2).

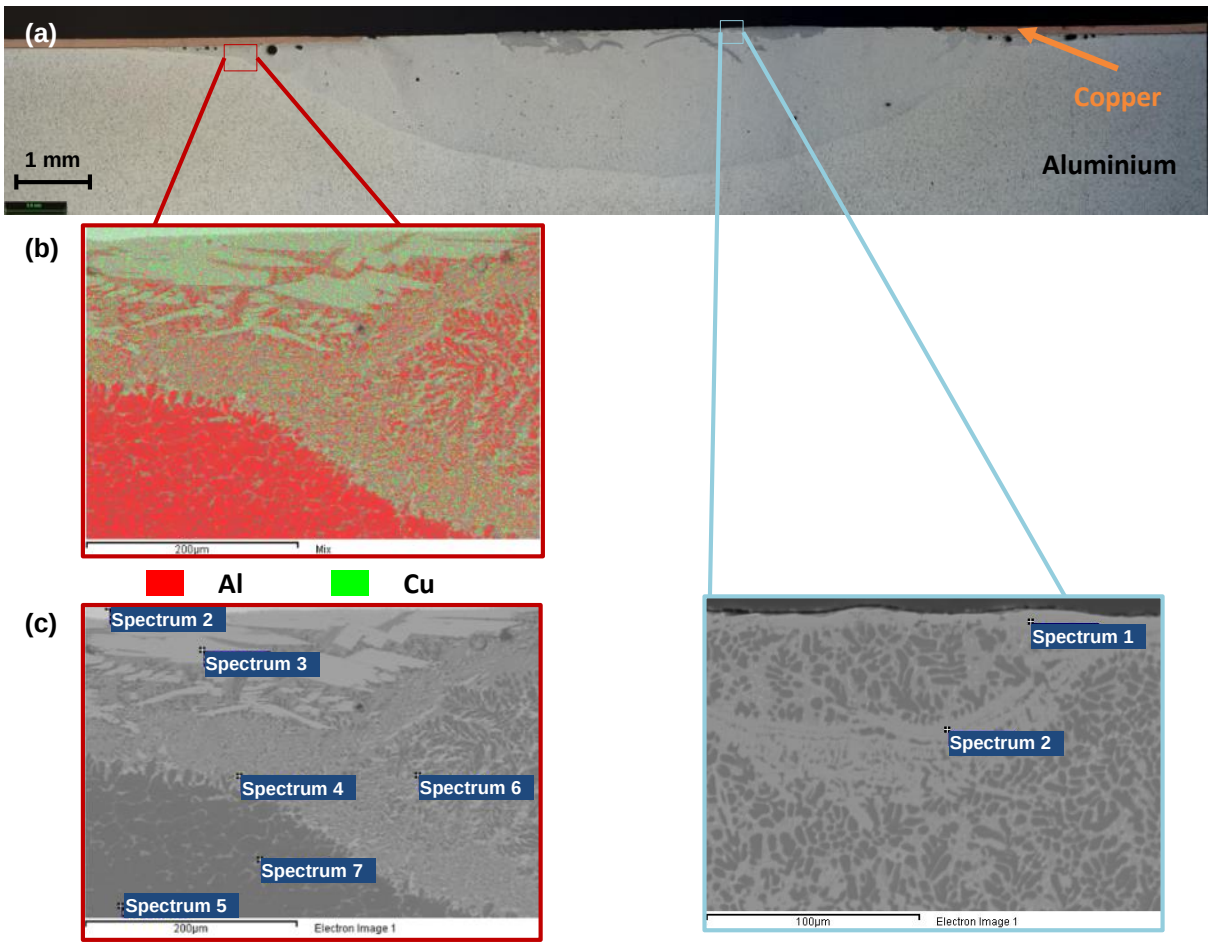

Spectrum	Al [At.%]	Cu [Al.%]	Fe [At.%]	Phase composition
2	1.97	98.03	-	Cu
3	66.87	33.13	-	Al_2Cu
4	67.97	32.03	-	Al_2Cu
5	100	-	-	Al
6	73.98	26.02	-	Al + Al_2Cu
7	88.29	11.71	-	Al + Al_2Cu

Spectrum	Al [At.%]	Cu [At.%]	Fe [At.%]	Phase composition
1	75.55	2.38	22.06	$FeAl_3$
2	76.03	3.26	20.70	$FeAl_3$

Figure 6-6: Metallographic analysis of the sample welded with a 150 µm thick pure Cu foil. Test 1 and 2 regions are represented in red and blue, respectively. (a) Macrograph, (b) EDS elemental mapping and (c) SEM/EDS spectrum analysis. Laser welding parameters: D_{beam}=13 mm, P=5 kW , TS=35 cm.min^{-1}.

The low percentage of Cu on those spectrums can be due to the small amount of copper added to the aluminium fusion zone and also the high diffusivity of this element.

The mechanical strength of the samples produced with copper interlayers was not measured because even though some of the samples were bonded, the macrosections showed many defects such as cracking, porosity and gaps which affect the joint strength. However, microhardness measurements were taken at different positions along the joint interface (see Figure 6-7). The results suggest that Al-Cu IMCs are more ductile than Fe-Al IMCs. On the left hand side of the fusion zone, at the Cu-Al interface (Figure 6-7b) the hardness of the Al_2Cu sub-layer measures 454 HV whereas at the centre of the weld where the $FeAl_3$ IMCs are spread in the Al fusion zone the hardness is about 759 HV (Figure 6-7c). There is also a large area in the fusion zone where fine IMCs are spread and the hardness is even lower, about 400 HV (Figure 6-7d).

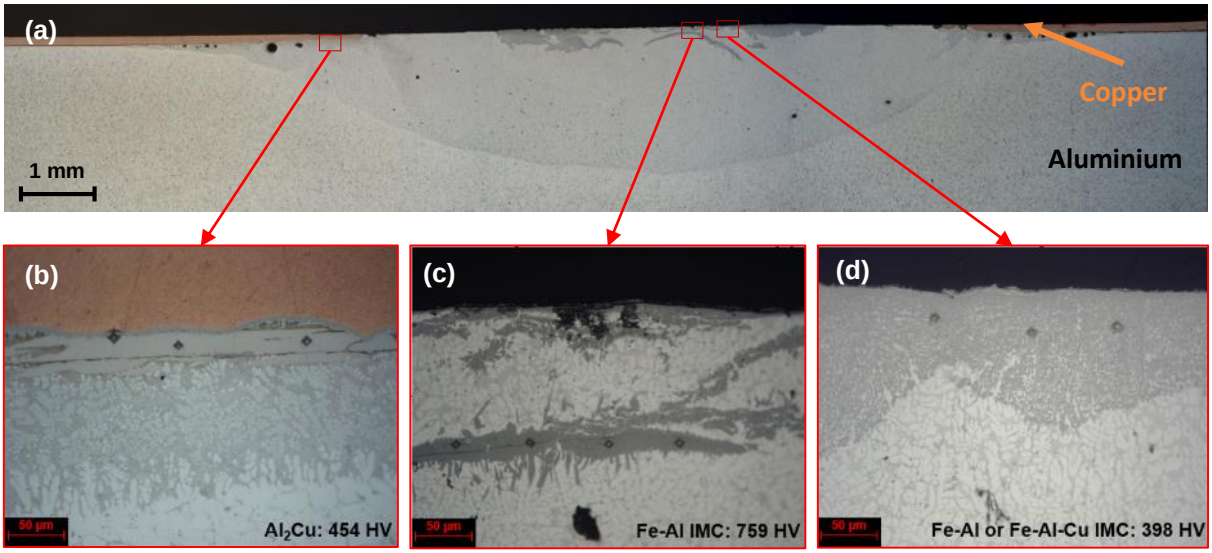

Figure 6-7: Results from the microhardness test: (a) Macrograph, micrograph of the indentations on (b) Al_2Cu under the copper foil and (c) $FeAl_3$ and (d) mixed IMCs at the centre of the weld.

6.2.3 Summary

In general, if an interlayer is to be used between the steel and the aluminium plates with the current joining principle, more energy is required to produce the joint when compared to joints with no interlayer. The temperature at Cu-Fe interface has to be higher than the melting temperature of the copper (around 1000 °C) and the heat needs to be transferred through the Cu wire/foil to melt the aluminium. However, with this experimental conditions it was not possible to prevent the melting of the steel at the joint interface due to the combination of thermal resistivity and high temperature required at the Cu-Fe interface. Moreover, Cu having much higher thermal conductivity than Fe resulted in lower temperature rise as compared to the steel and therefore, some part of it was not even molten. For these reasons, the reaction between the three main elements of the joint, Fe, Al and Cu, could not be avoided and the formation of binary and ternary IMC phases was confirmed by SEM/EDS analysis.

6.3 Investigation of Al-Cu IMC formation when depositing copper filler wire onto aluminium substrate by CMT arc welding

In the previous section copper was used as interlayer to create a bridge between steel and aluminium using laser welding process. However, this technique showed some limitations for the joint configuration in use and the reaction between Fe and Al could not be avoided and IMCs were formed.

An alternative approach to use a copper interlayer in dissimilar metal joining is proposed in this section. The aim is to verify the viability of using copper as interlayer between the steel and the aluminium using CMT welding process and produce strong joints. For this reason, the effect of the arc energy on the Al-Cu IMC formation will be assessed using several welding modes, wire feed speeds and gas mixtures. The IMCs resultant from the reaction between aluminium and copper will be identified and the microhardness mapping of the weld bead cross-section will be determined.

6.3.1 Experimental procedure

6.3.1.1 Material

In this section the substrate used was 5083-H22 aluminium alloy which dimensions were 200 mm in width, 400 mm in length and 6 mm in thickness. The welding wire used in the welding experiments was a copper-silicon alloy ($CuSi_3$) with 1.0 mm diameter. The details of the chemical composition and physical properties of the substrate and the welding wire were provided in section 2.2.

6.3.1.2 Methodology and experimental setup

The joining process applied in this section is Cold Metal Transfer or CMT. An arc welding process is more suitable to weld copper than the general laser welding processes because of the poor absorption of the metal at the near and far infrared spectrum of the laser radiation and because of the thermal conductivity which makes it difficult to produce deep welds. At 1 µm of wavelength (infrared laser radiation) which correspond to the laser used in this project, more than 95% of

the light is reflected by the material (see Figure 6-8). The remaining energy that is absorbed by the material is easily conducted away from the point where the laser is incident due to the high conductivity of the metal. The use of lasers operating in the green region of the spectrum is recommended to weld copper because at this wavelength the absorptivity of copper is substantially improved (Rüttimann et al., 2011)(Engler et al., 2011).

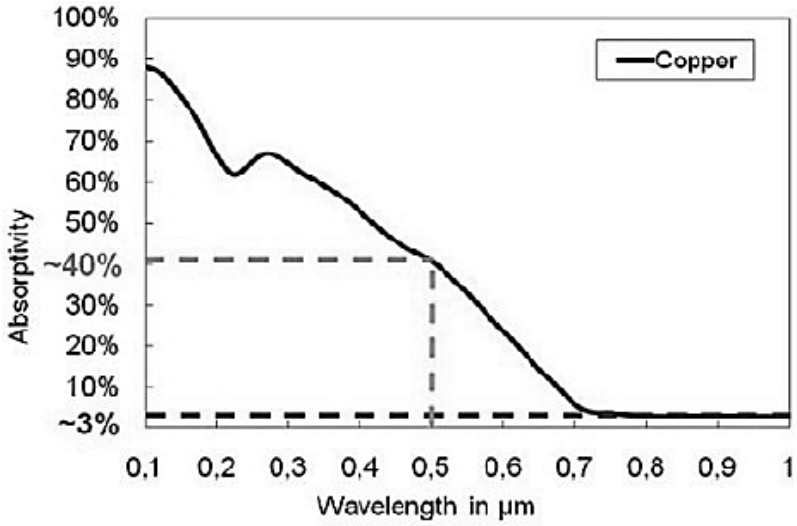

Figure 6-8: Absorptivity of copper at room temperature as a function of wavelength (Hess et al., 2011).

Continuous and parallel weld seams of copper were welded onto aluminium substrate using CMT welding process, according to the schematic representation in Figure 6-9.

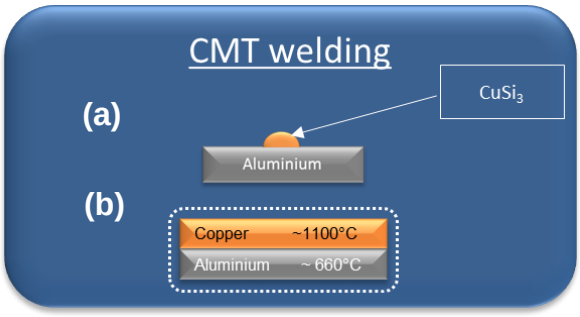

Figure 6-9: (a) Bead on plate welds using copper welding wire and aluminium substrate. (b) Material configuration.

Before welding, the aluminium plates were linished to remove the oxides from the substrate surface and degreased with acetone.

A global picture of the experimental setup is shown in Figure 6-10. The CMT Advanced welding process was used which is the most recent power source developed by Fronius (Figure 6-10d). The Robacta drive CMT welding torch (Figure 6-10c) was attached to the 3 axis VPPA2 manipulator. The movement of the welding torch was controlled through the VPPA2 controller (Figure 6-10a) whereas the welding parameters were set in the RCU 5000i remote control unit. To prevent the distortion of the aluminium during the welding process, the plates were clamped to the table of the manipulator (Figure 6-10b). The voltage and current signals were recorded during the welding process with the Triton Electronics Limited's AMV 4000 arc watch system (Figure 6-10e). The recorded data was then analysed and used to calculate the heat input of the process. The fumes produced during the welding experiments were extracted using local exhaust ventilation (so-called LEV, Figure 6-10f).

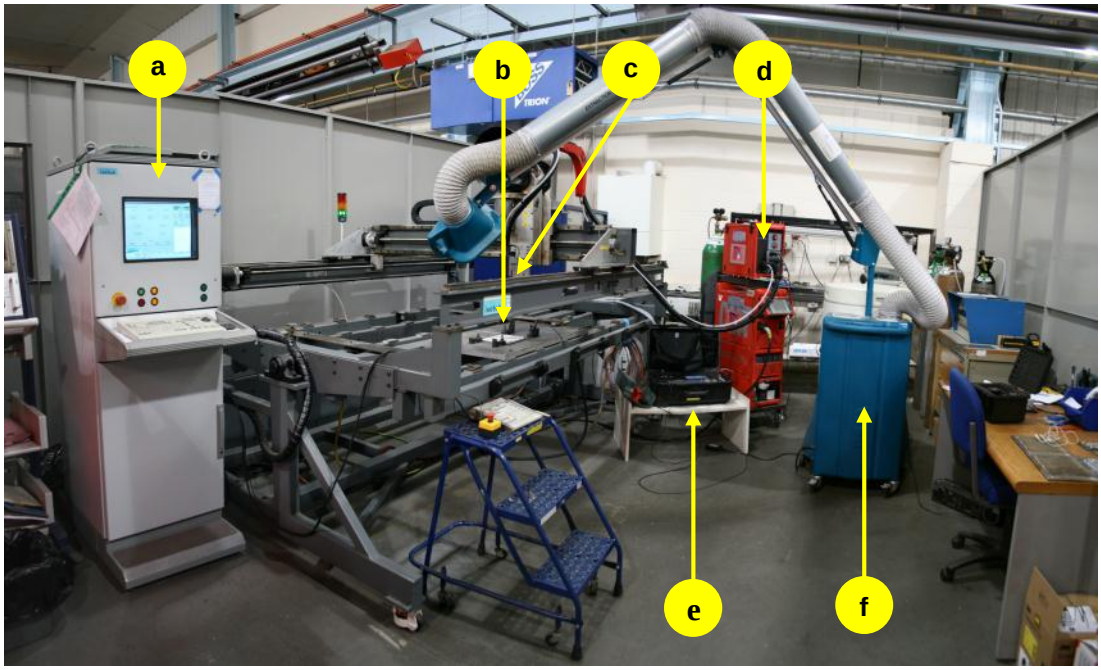

a – VPPA2 manipulator controller

b – Substrate clamped to the table of the manipulator

c – Robacta CMT torch

d – TPS CMT Advanced plus power source

e – Triton Electronics Limited's AMV 4000 arc watch system

f – LEV (Local Exhaust Ventilation)

Detailed pictures:

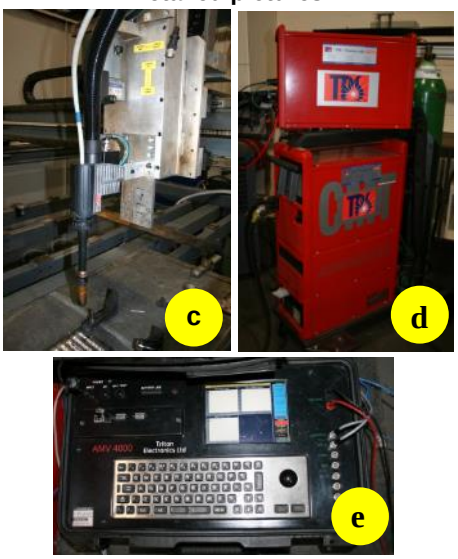

Figure 6-10: Picture of the experimental setup for CMT welding.

The welding torch position and the distance between the contact tip to the work piece (CTWD) were kept constant (see Table 6-5). The shielding gas flow rate used was 22 l/min and the composition of the shielding gas was changed (100% of Argon and a mixture of 50% Argon plus 50% He) in order to assess its influence on the IMC formation. The synergic curve program used was recommended for $CuSi_3$ welding wire. The welding conditions are summarized in Table 6-5.

Table 6-5: Summary of the experimental parameters used in the deposition of copper onto aluminium.

Torch position	**Lead angle**	90 °
	Approach angle	90 °
	CTWD	13 mm
Shielding gas	**Flow rate**	22 l.min^{-1}
	Composition	100% Argon
		50% Argon + 50% Helium
Welding parameters	**CMT modes**	C878, C1182 and C1183
	Travel speed	0.5 m.min^{-1}
	Wire feed speed	7.5, 8.0 and 8.5 m.min^{-1}

6.3.1.3 Metallographic analysis and microhardness testing

The metallographic analysis of the dissimilar Al-Cu bead on plate welds followed a procedure similar to the one depicted in section 2.3.4. It includes sample cutting, mounting in resin, grinding and polishing, optical microscopy and macroscopy. The identification of the IMCs in the cross-sections was based on SEM and EDS results and on the binary Al-Cu phase diagram. However, the phases identified are only an approximation because the phases in the phase diagram were determined for equilibrium conditions. The data from the EDS spectrum analysis was simplified and the elements for which the composition was under 8% were excluded. The microhardness of the Al-Cu IMCs formed in the weld metal was measured following standard procedure, as described in section 2.3.5.

6.3.2 Results and Discussion

The heat input was calculated based on the voltage and current intensity recorded by the AMV 4000 arc watch system. In order to analyse the transient data of the welding process, hundreds or thousands of measurements per second were taken from the voltage and current signals during the welding process. Instantaneous heat input was calculated based on these two parameters before calculating the average of the heat input for the entire data recording time.

As shown in Table 6-6 the heat input is varied by changing both, welding mode and wire feed speed. The maximum heat input measured was with C878 welding mode and 8.5 $m.min^{-1}$ of wire feed speed.

Table 6-6: Heat input calculated from the transient data recorded with the AMV 4000 arc watch system in each welding condition.

Sample number	CMT mode	Travel speed, $m.min^{-1}$	Wire feed speed, $m.min^{-1}$	Shielding gas @ 22 $l.min^{-1}$	Average power, kW	Arc energy, $J.mm^{-1}$	HI (η=0.85), $J.mm^{-1}$
5	878	0.5	7.5	100 % Ar	2.32	278	236
6	878	0.5	8.5	100 % Ar	2.81	337	286
7	878	0.5	8.0	100 % Ar	2.57	309	263
8	1182	0.5	7.5	100 % Ar	1.85	222	189
9	1182	0.5	8.0	100 % Ar	1.98	237	201
10	1182	0.5	8.5	100 % Ar	2.25	270	230
11	1183	0.5	7.5	100 % Ar	1.68	202	172
12	1183	0.5	8.0	100 % Ar	1.93	231	196
13	1183	0.5	8.5	100 % Ar	2.06	247	210
14	1182	0.5	7.5	50% Ar + 50% He	-	-	-
15	1183	0.5	7.5	50% Ar + 50% He	1.90	228	194
16	1183	0.5	7.5	50% Ar + 50% He	1.92	230	196

The macrographs of the cross-section of the welds are presented in Table 6-7. The weld seams are uniform and do not show signs of porosity and only one has a large crack. All macrographs show a distinctive band located between the copper bead and the aluminium substrate which seems to contain Al-Cu IMCs.

The effect of the arc energy on the weld shape and Al-Cu reaction was assessed by welding with different wire feed speeds and the results are given in Table 6-8. The dilution presented in this table intends to demonstrate the amount of aluminium dissolved in the fusion zone. The dilution is calculated by the area of the fusion zone on the aluminium by the total area of the weld bead (copper and aluminium).

Table 6-7: Macrographs of the cross-sectional view of copper weld beads on aluminium plate.

Sample number	CMT mode	TS, $m.min^{-1}$	WFS, $m.min^{-1}$	Shielding gas @ 22 $l.min^{-1}$	HI (η=0.85), $J.mm^{-1}$	Macro
5	C878	0.5	7.5	100 % Ar	236	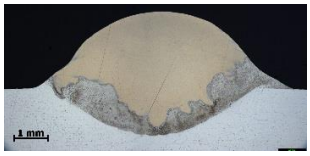
6	C878	0.5	8.5	100 % Ar	286	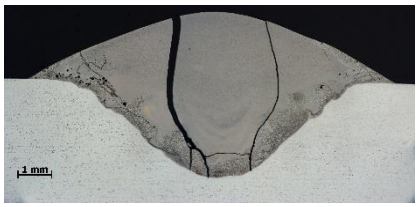
7	C878	0.5	8.0	100 % Ar	263	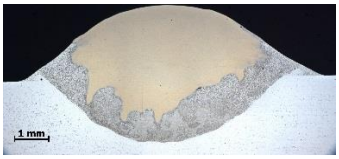
8	C1182	0.5	7.5	100 % Ar	189	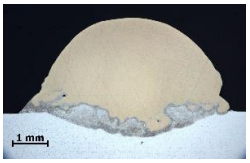
9	C1182	0.5	8.0	100 % Ar	201	
10	C1182	0.5	8.5	100 % Ar	230	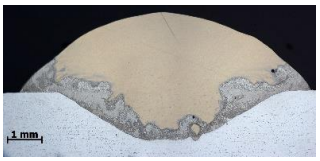
11	C1183	0.5	7.5	100 % Ar	172	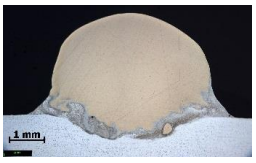
12	C1183	0.5	8.0	100 % Ar	196	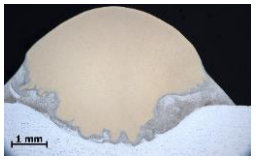

Sample number	CMT mode	TS, m.min^{-1}	WFS, m.min^{-1}	Shielding gas @ 22 l.min^{-1}	HI (η=0.85), J.mm^{-1}	Macro
13	C1183	0.5	8.5	100 % Ar	210	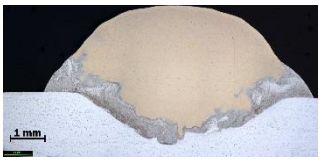
14	C1182	0.5	7.5	50% Ar + 50% He	-	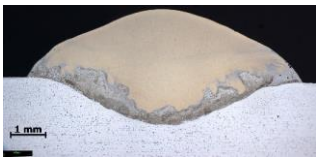
15	C1183	0.5	7.5	50% Ar + 50% He	194	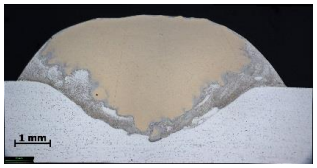
16	C1183	0.5	7.5	50% Ar + 50% He	196	

Table 6-8: Dimensions of the copper weld bead on aluminium plate.

Sample no.	CMT mode	TS, m.min^{-1}	WFS, m.min^{-1}	HI (η=0.85), J.mm^{-1}	Weld height, mm	Weld width, mm	Weld depth, mm	Weld area, mm^2	Dilution, %
5	C878	0.5	7.5	236	2.3	7.7	1.4	16.0	34
6	C878	0.5	8.5	286	2.1	11.0	2.9	26.9	51
7	C878	0.5	8.0	263	2.1	9.0	1.9	20.2	42
8	C1182	0.5	7.5	189	2.7	6.0	0.7	13.5	15
9	C1182	0.5	8.0	201	2.5	7.5	1.0	16.0	19
10	C1182	0.5	8.5	230	2.3	8.4	1.4	18.7	30
11	C1183	0.5	7.5	172	3.0	6.1	0.7	14.3	14
12	C1183	0.5	8.0	196	2.8	7.1	1.2	17.1	23
13	C1183	0.5	8.5	210	2.6	7.9	1.4	19.6	26
14	C1182	0.5	7.5	-	2.0	7.9	1.3	15.6	32
15	C1183	0.5	7.5	194	1.9	7.7	1.6	16.8	33
16	C1183	0.5	7.5	196	2.4	7.6	1.3	16.2	27

The results corresponding to the welds produced with C878 CMT welding mode are shown in Figure 6-11. The macrographs of the cross sections of the weld seams are represented by I and the top view of the weld seam is indicated by II.

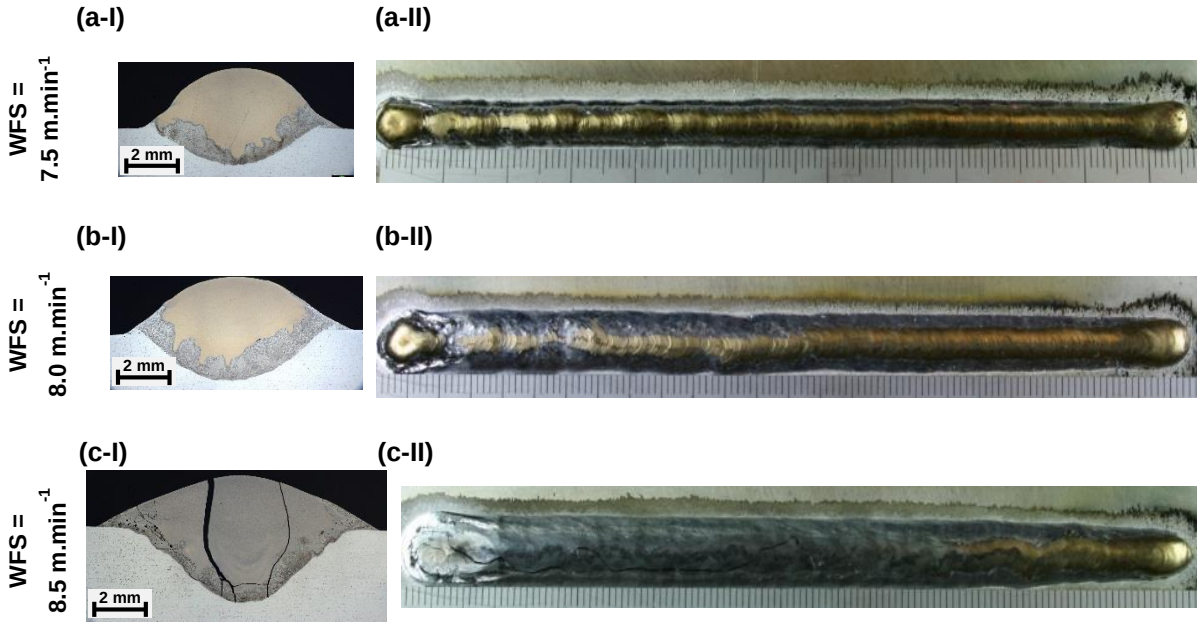

Figure 6-11: Effect of welding mode on the weld shape and Al-Cu IMC formation. (I) Cross-sectional view and (II) top view of the weld seam. Welding parameters: C878 CMT mode, TS = 0.5 m.min^{-1}, shielding gas = 100% Argon, WFS = (a) 7.5 m.min^{-1}, (b) 8.0 m.min^{-1} and (c) 8.5 m.min^{-1}.

There are two main consequences to the weld profile and band of IMCs when higher wire feed speed is used. In terms of weld profile it becomes wider when higher wire feed speeds are used because more filler wire is deposited in the weld (see Figure 6-11a-II and c-II). The second point is related with the synergic curve used by the CMT welding process to control the current and voltage of the process according to the wire feed speed in use. Higher levels of energy are used when welding with higher wire feed speed. Table 6-8 shows that the dilution of aluminium in the weld bead is nearly 34% and 51% when the wire feed speed used is 7.5 and 8.5 m.min^{-1}, respectively. Therefore, if one compares Figure 6-11a-I and b-I one will see that the band of IMCs is thicker when 8.0 m.min^{-1} of WFS is used. Moreover, if the WFS is further increased the reaction between Al and Cu is even stronger and the whole copper bead becomes brittle and large

cracks in the weld seam are formed. In order to minimize the reaction between Al and Cu it is advised to weld with low energy and thus, with low wire feed speed.

The macrographs of the welds produced with different welding modes are shown in Figure 6-12.

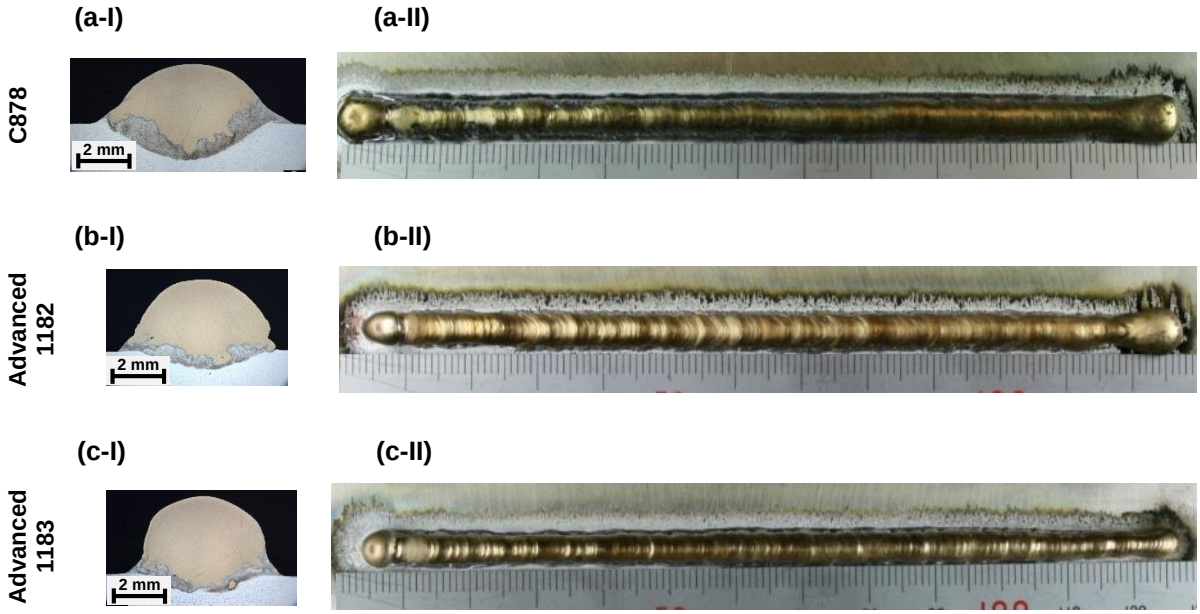

Figure 6-12: Effect of welding mode on the weld shape and Al-Cu IMC formation. (I) Cross-sectional view and (II) top view of the weld seam. Welding parameters: TS = 0.5 m.min^{-1}, WFS = 7.5 m.min^{-1}, shielding gas = 100% Argon, CMT welding mode (a) C878, (b) Advanced C1182 and (c) Advanced C1183.

The standard CMT welding mode (C878) is more energy intensive than the Advanced modes C1182 and C1183, 236 J.mm^{-1} compared to 189 and 172 J.mm^{-1}, respectively. The weld profiles shown in Figure 6-12 are in agreement with this, the weld seam produced by the standard CMT mode is wider and deeper than the welds produced by the advanced modes. The welds produced with the standard CMT process show a thicker band of IMCs demonstrating that during the welding process there was a stronger reaction between Al and Cu.

The effect of shielding gas composition on the weld shape and Al-Cu IMC band is clear on the macrographs in Figure 6-13.

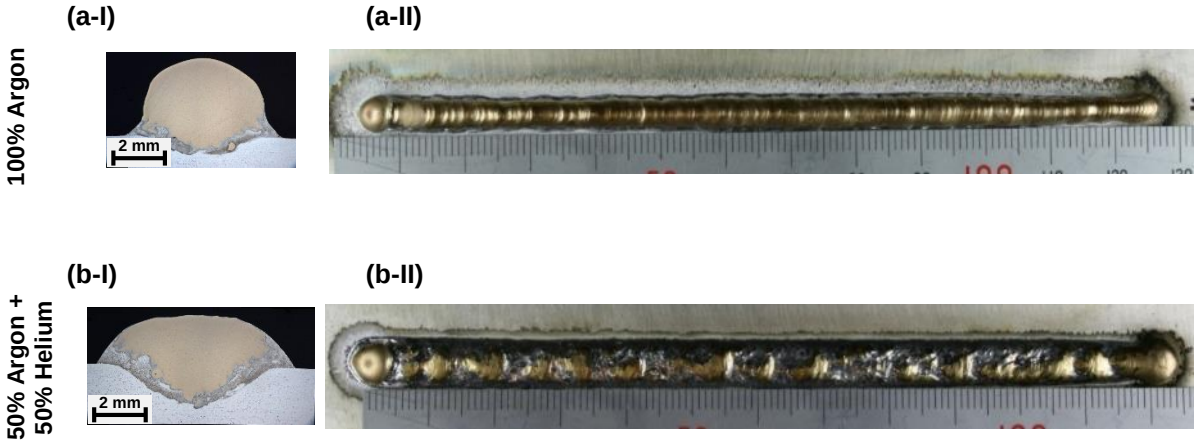

Figure 6-13: Effect of shielding gas on weld shape and Al-Cu IMC formation. (I) Cross-sectional view and (II) top view of the weld seam. Welding parameters: 1183 CMT Advanced mode, TS = 0.5 m.min^{-1}, WFS = 7.5 m.min^{-1}, shielding gas = (a) 100% Argon and (b) 50% Argon + 50% Helium.

The addition of Helium in the shielding gas increases the energy of the welding process (from 172 J.mm^{-1} to 194 J.mm^{-1}) and for this reason the weld seams are wider and with a lower reinforcement curve (see Figure 6-13c and d) and the dilution of aluminium in the weld bead increases from 14% to 33%. This is due to the ionization energy of Helium being higher than that of Argon and thereby inducing a hotter weld. For this reason the Al-Cu IMC band is also thicker when He is added to the shielding gas mixture.

SEM and EDS analysis were carried out in three samples to characterize the Al-Cu IMCs formed during the welding process. The results are indicated in Table D-2 to Table D-3 in Appendix D. The samples chosen were produced by standard CMT with 8.0 and 8.5 m.min^{-1} of WFS and CMT Advanced with 8.5 m.min^{-1} of WFS. One can see that all these samples do not show the continuous reaction layer that is characteristic from Fe-Al joints. Instead, the Al-Cu IMCs are spread in a matrix of Al substrate (see Figure 6-14). As copper has a higher melting temperature than aluminium, it is not possible to deposit copper onto aluminium without melting both metals. Nevertheless, having the IMCs spread in the aluminium fusion zone may be less detrimental to the joint than having a

continuous IMC layer along the interface between both metals, as in the case of the laser welded Fe-Al joints.

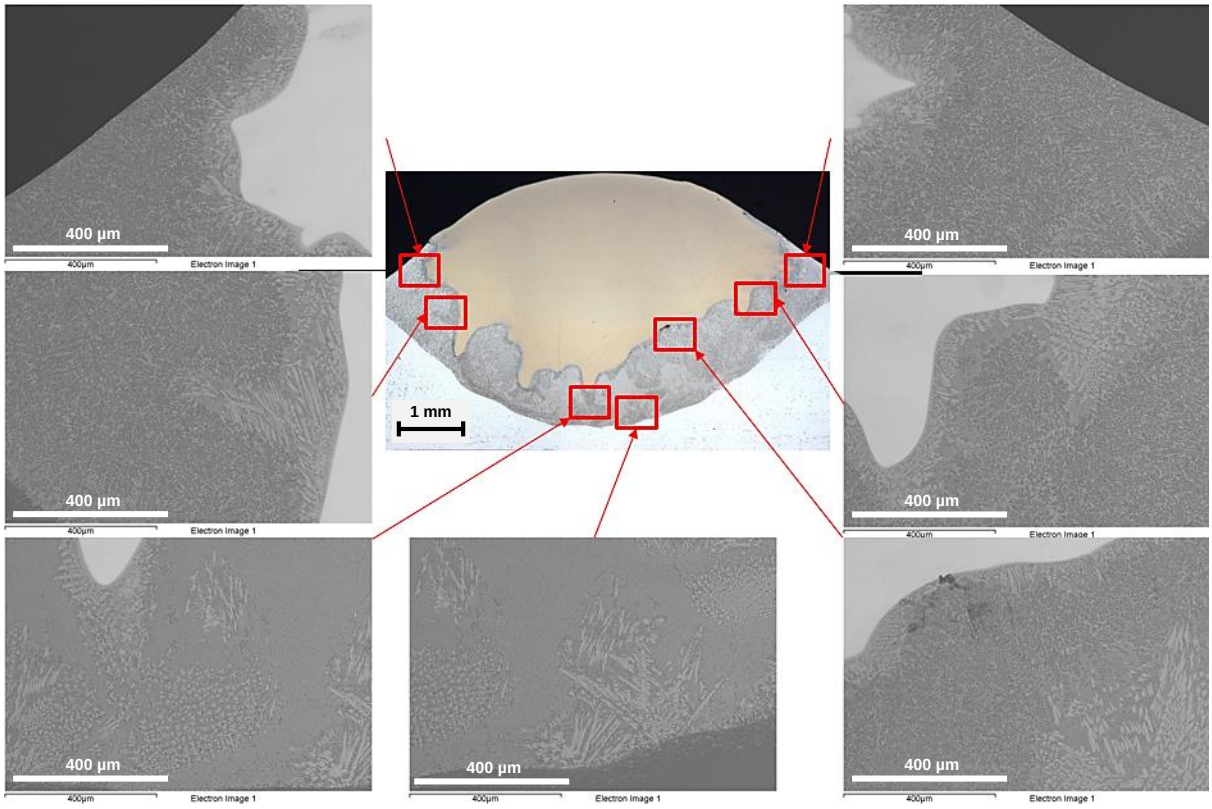

Figure 6-14: SEM images taken along the band of Al-Cu IMCs located between the copper weld bead and the aluminium substrate. Welding parameters: C878 CMT mode, TS = 0.5 m.min^{-1}, 100% Argon shielding gas and WFS = 8.0 m.min^{-1}.

In Figure 6-15a there are three areas in the copper bead where the chemical composition was determined by EDS. The results showed that the weld bead composition has a small variation from the top to the bottom: Cu content is lower at the top (87 at.%) and higher at the bottom (93 at.%). One possible reason is the different densities of Cu and Al. According to the binary Al-Cu phase diagram all these areas have a solid solution of Al in Cu and no Al-Cu intermediate phases are observed. Two different IMCs were found in the Al-Cu transition band, viz. AlCu and Al_2Cu (see Figure 6-15b). The region near the Cu bead is mainly composed of Al_2Cu mixed with AlCu and the IMCs have a solid structure. However, closer to the aluminium substrate there is only fine Al_2Cu spread in a matrix of Al. Elements such as Mg, Si and Mn were not taken into account in

order to simplify the identification of the IMCs and due to the low concentration in the mixture.

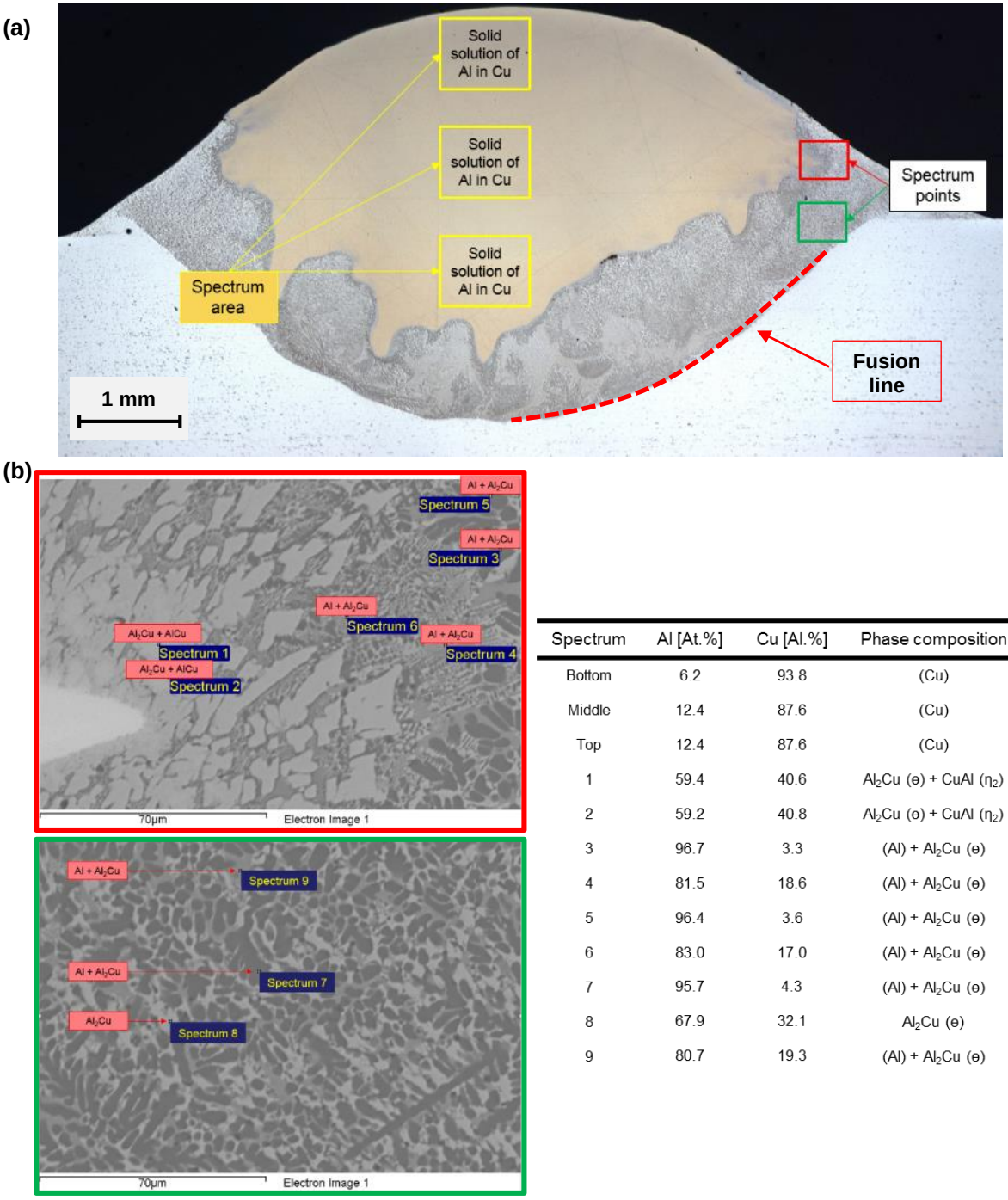

Spectrum	Al [At.%]	Cu [Al.%]	Phase composition
Bottom	6.2	93.8	(Cu)
Middle	12.4	87.6	(Cu)
Top	12.4	87.6	(Cu)
1	59.4	40.6	Al_2Cu (ɵ) + CuAl (η_2)
2	59.2	40.8	Al_2Cu (ɵ) + CuAl (η_2)
3	96.7	3.3	(Al) + Al_2Cu (ɵ)
4	81.5	18.6	(Al) + Al_2Cu (ɵ)
5	96.4	3.6	(Al) + Al_2Cu (ɵ)
6	83.0	17.0	(Al) + Al_2Cu (ɵ)
7	95.7	4.3	(Al) + Al_2Cu (ɵ)
8	67.9	32.1	Al_2Cu (ɵ)
9	80.7	19.3	(Al) + Al_2Cu (ɵ)

Figure 6-15: Elemental composition analysis by EDS of copper weld bead and transition band. (a) Macrograph showing the areas of interest and (b) identification of IMC phases based on the EDS analysis and Al-Cu binary phase

diagram. Welding parameters: C878 CMT mode, TS = 0.5 m.min^{-1}, 100% Argon shielding gas and WFS = 8.0 m.min^{-1}.

Similar analysis was done to two other samples produced by standard and advanced CMT modes with 8.5 m.min^{-1} of WFS (see Figure 6-16 and Figure 6-17). The main difference in these welds is the composition of the weld beads. The EDS analysis carried out in three different height levels inside the Cu weld bead indicates that there is a solid solution of Al in Cu in the weld produced by advanced mode whereas using the CMT standard mode the weld bead was mainly $AlCu_2$. This IMC phase was not identified in the transition band where the following phases are usually present: Al_2Cu+AlCu, Al_2Cu and Al+Al_2Cu (see Figure 6-16b and Figure 6-17b). When higher energy is used to weld copper to aluminium there is more melting of the aluminium substrate and therefore the amount of Al mixed in Cu is higher. In this condition the dilution of aluminium in the weld bead increases from 34% to 51% when the energy goes from 236 J.mm^{-1} to 286 J.mm^{-1}. If the amount of Al into Cu is above the maximum threshold to obtain solid solution of Al in Cu then more IMCs are formed. This may explain the weld bead composition and the formation of $AlCu_2$. The higher Al concentration at the top of the weld may indicate that $AlCu_2$ was initially formed at the top of the weld and therefore, it is not observed at the band. Even though the weld bead of the sample showed in Figure 6-17a is mainly composed of $AlCu_2$ it also has a band similar to the samples previously depicted. However, due to higher content of Cu in this band there are more Al_2Cu + AlCu phases. Figure 6-16c and Figure 6-17c show the distribution of Al and Cu elements in both samples.

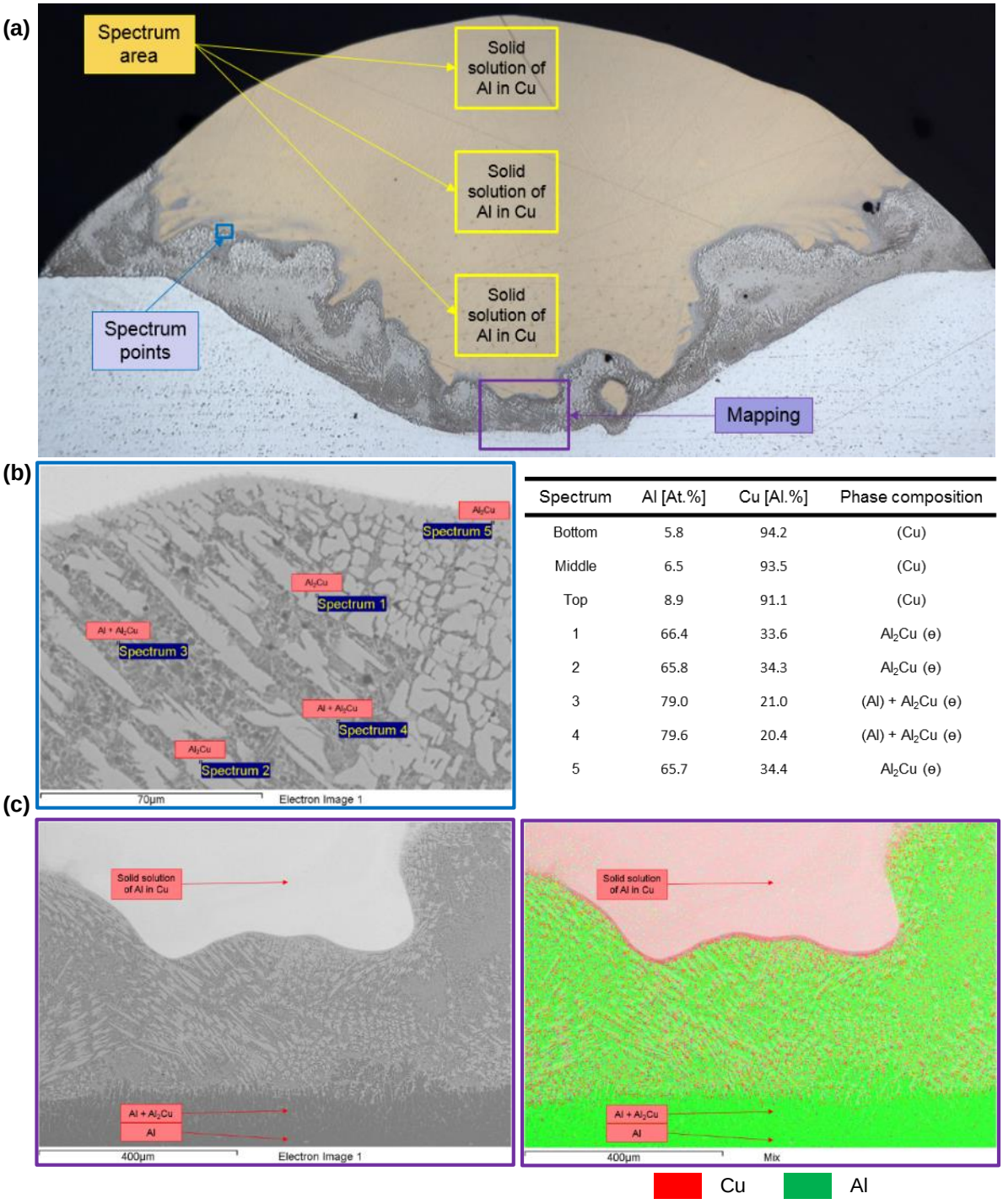

Spectrum	Al [At.%]	Cu [Al.%]	Phase composition
Bottom	5.8	94.2	(Cu)
Middle	6.5	93.5	(Cu)
Top	8.9	91.1	(Cu)
1	66.4	33.6	Al_2Cu (ɵ)
2	65.8	34.3	Al_2Cu (ɵ)
3	79.0	21.0	(Al) + Al_2Cu (ɵ)
4	79.6	20.4	(Al) + Al_2Cu (ɵ)
5	65.7	34.4	Al_2Cu (ɵ)

Figure 6-16: Elemental composition analysis by EDS of copper weld bead and transition band. (a) Macrograph showing the areas of interest, (b) EDS elemental mapping and (c) identification of IMC phases based on the EDS analysis and Al-Cu binary phase diagram. Welding parameters: C1182 CMT Advanced mode, TS = 0.5 m.min^{-1}, 100% Argon shielding gas and WFS = 8.5 m.min^{-1}.

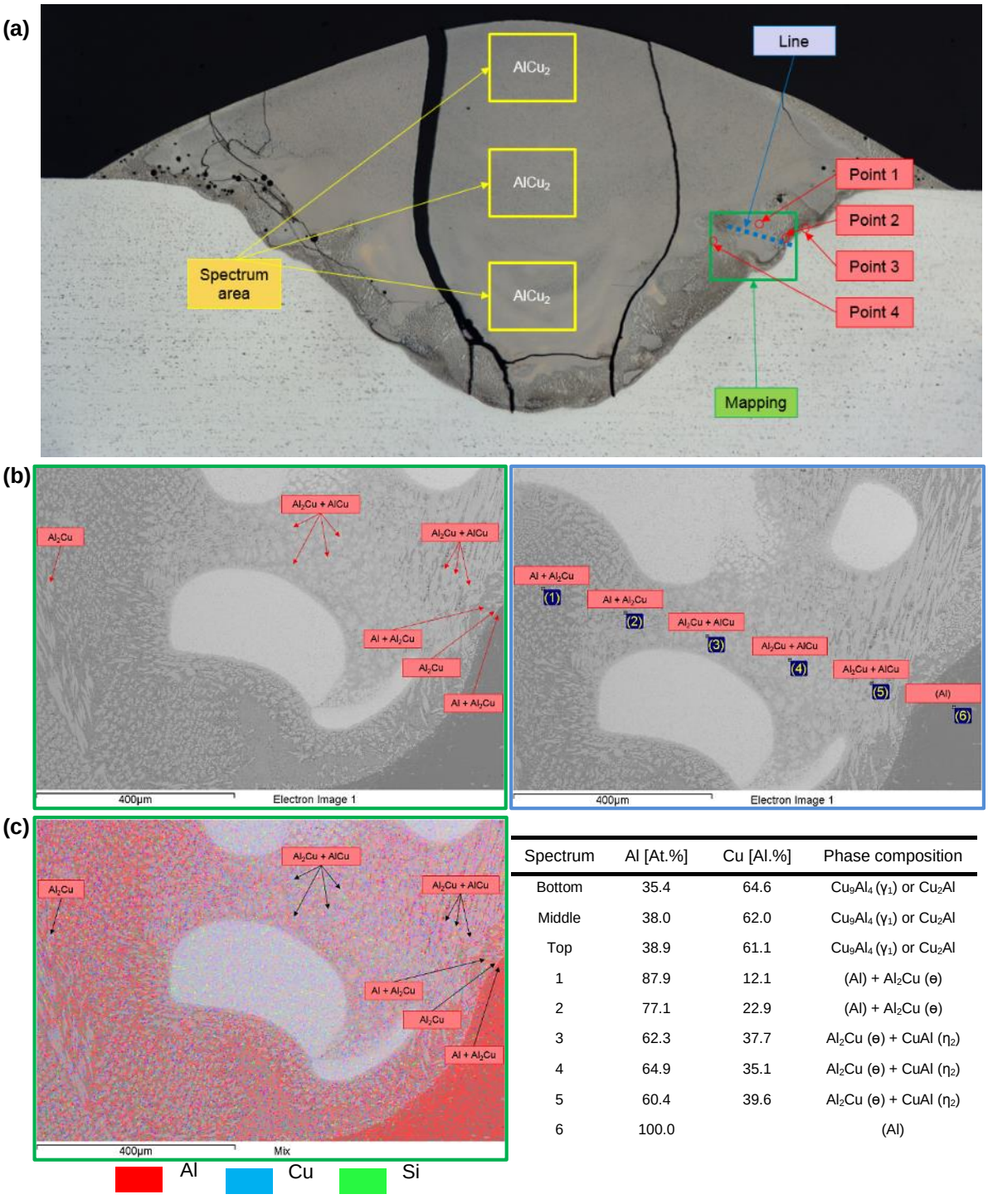

Spectrum	Al [At.%]	Cu [Al.%]	Phase composition
Bottom	35.4	64.6	Cu_9Al_4 (γ_1) or Cu_2Al
Middle	38.0	62.0	Cu_9Al_4 (γ_1) or Cu_2Al
Top	38.9	61.1	Cu_9Al_4 (γ_1) or Cu_2Al
1	87.9	12.1	(Al) + Al_2Cu (θ)
2	77.1	22.9	(Al) + Al_2Cu (θ)
3	62.3	37.7	Al_2Cu (θ) + CuAl (η_2)
4	64.9	35.1	Al_2Cu (θ) + CuAl (η_2)
5	60.4	39.6	Al_2Cu (θ) + CuAl (η_2)
6	100.0		(Al)

Figure 6-17: Elemental composition analysis by EDS of the transition band. (a) Macrograph showing the areas of interest, (b) identification of IMC phases based on EDS analysis and Al-Cu binary phase diagram and (c) elemental mapping. Welding parameters: C878 CMT mode, TS = 0.5 m.min^{-1}, 100% Argon shielding gas and WFS = 8.5 m.min^{-1}.

The microhardness of the welds produced by standard CMT and 8.0 and 8.5 m.min^{-1} of WFS was measured and the results are shown in Figure 6-18.

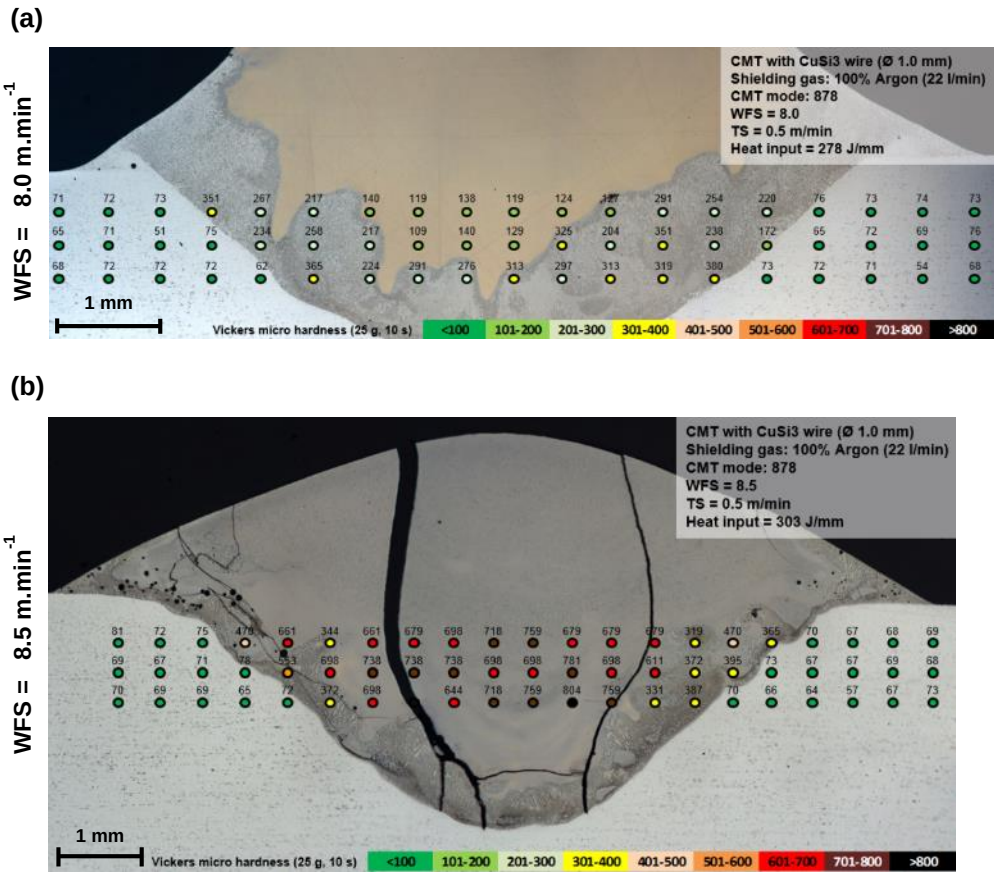

Figure 6-18: Microhardness mapping of the CMT welds. Welding parameters: C878 CMT mode, TS = 0.5 m.min^{-1}, shielding gas = 100% Argon, WFS = (a) 8.0 m.min^{-1} and (b) 8.5 m.min^{-1}.

The microhardness mapping shows that the centre of the sample welded with 8.5 m.min^{-1} (Figure 6-18a) of WFS is nearly four times harder than the centre of the weld produced with 8.0 m.min^{-1} of WFS (Figure 6-18b). This justifies the presence of the crack in this sample. In both samples the average microhardness measured on the aluminium parent metal is 69 HV. At the centre of the weld showed in Figure 6-18a the average microhardness is 125 HV and thus, there are no visible cracks. The reason for the relatively low hardness compared to the sample showed in Figure 6-18b is the chemical composition of the weld which corresponds to solid solution of Al in Cu with no intermediate phase of Al-Cu

according to the spectrum analysis. On the contrary, the majority of the weld showed in Figure 6-18b is composed by $AlCu_2$ which is a copper rich Al-Cu IMC with average microhardness about 700 HV. The microhardness of the band of Al-Cu IMCs located between the Cu bead and the aluminium substrate in Figure 6-18a was in a range between 217 and 380 HV whereas in Figure 6-18b this thin band was about 350 HV. This region is harder than the weld bead in Figure 6-18a but more ductile than that of Figure 6-18b because it contains Al_2Cu mixed with AlCu and in some areas only a mix of Al with Al_2Cu.

6.3.3 Summary

The results of the experiments using CMT arc welding process with copper filler wire deposited onto aluminium showed that:

- It is possible to create sound welds between copper and aluminium, free of defects such as porosity or cracking and uniform weld seams under specific welding conditions, i.e. low arc energy;
- All welds are not homogeneous and have three different areas: Aluminium substrate, Cu-Al weld bead and in between a transition band composed of Al-Cu IMCs dispersed in aluminium
- Controlling the arc energy either by wire feed speed, CMT welding mode or even shielding gas, it is possible to create good wetting of $CuSi_3$ onto the Al substrate and keep the reaction between Cu and Al as small as possible;
- High heat input values used in the welding process enhances the mixture of Cu and Al and thus the formation of IMCs is highly observed;
- The sample welded with the maximum energy (286 $J.mm^{-1}$) showed a large crack formed whilst cooling down caused by the high content of Al in Cu, 37 at%Al and 63 at%Cu, forming $AlCu_2$, and lack of ductility;

❖ Low energy reduces the diffusion of Al and Cu atoms and thus the formation of Al-Cu IMC is minimized. On the other hand, a very good wetting is enhanced with high energy; The analysis of the macrographs suggests that there is a threshold value for the energy from which the

entire copper bead is used in the reaction with aluminium and is transformed in a new IMC phase;

- Microhardness in the weld bead can be as high as 800 HV when $AlCu_2$ is formed but if the arc energy is controlled it can be 125 HV in the weld bead;
- The band is no more than 380 HV hard but because the IMCs are spread in the aluminium the behaviour of the sample should be more ductile.

6.4 Investigation of IMC formation when depositing four different grades of aluminium wire onto copper by CMT arc welding

The deposition of copper onto aluminium by CMT welding as an alternative approach to add an interlayer between steel and aluminium was investigated in the previous section (section 6.3). The Al-Cu IMC formation under different welding conditions was also investigated and the results were promising. However, it was observed that when the arc energy is above a certain threshold the entire weld bead is transformed in $AlCu_2$ and the weld seam shows large cracks. If the joining process involves the melting of both metals, there is a stronger reaction between them and then, more IMCs are formed. Since the melting temperature of aluminium is lower than that of copper, in this section it is proposed to study the feasibility of using copper as interlayer between the steel and the aluminium but in this case using CMT brazing process (by deposition of aluminium onto copper).

The reaction between Al-Cu-Fe is evaluated under different energy levels by using several wire feed speeds and welding modes. Moreover, to assess the influence of the alloying elements on the IMC formation, different grades of aluminium welding wire were brazed onto copper ($CuSi_3$) weld seams previously deposited onto a steel substrate. Metallographic analysis to verify the geometry of the weld and the composition of the IMCs was done. To determine the benefit of having the copper interlayer between the steel and the aluminium plates by brazing process, microhardness measurements were carried out.

6.4.1 Experimental procedure

6.4.1.1 Material

In this section $CuSi_3$ welding wire with 1.0 mm diameter was deposited onto DH36 steel which dimensions were 200 mm wide, 250 mm long and 6 mm thick. A second layer was deposited onto the copper bead with four different grades of aluminium welding wire and all with 1.2 mm diameter. The chemical composition

and physical properties of the welding wires and steel substrate are in Table 6-9 and, Table 6-10 respectively.

Table 6-9: Chemical composition of the substrate and the welding wires used in CMT brazing experiments.

	Substrate		**Welding wire**				
	DH36	**AA5083 (H22)**	**$CuSi_3$**	**AA 2319**	**AA 4043**	**AA 4047**	**AA 5087**
Standard	ASTM A131:Part 4	-	AWS A5.7 ER CuSi-A *	AMS 4191H *	AWS A5.10 ER 4043 *	AWS A5.10 ER 4047	ISO 18273 – S Al 5087
Cu	0.010	-	**Bal.**	**6.41**	0.02	< 0.3	< 0.05
Zn	-	-	0.019	< 0.01	0.01	< 0.2	< 0.25
Pb	-	-	0.007	-	-	-	-
Al	0.035	-	< 0.01	**Bal.**	**Bal.**	**Bal.**	**Bal.**
Fe	**Bal**.	-	0.016	0.08	0.2	< 0.6	< 0.4
Ni	0.017	-	-	-	-	-	-
Mn	**1.370**	**-**	**1.08**	0.32	0.00	< 0.15	**0.7 – 1.1**
Si	**0.390**	**-**	**2.95**	0.03	**4.9**	**11 – 13**	< 0.25
Sn	0.002	-	-	-	-	-	-
S	0.009	-	-	-	-	-	-
P	0.014	-	0.008	-	-	-	-
Ag	-	-	-	-	-	-	-
TOE	-	-	-	< 0.15	-	-	-
Zr	-	-	-	0.13	-	-	0.10 – 0.20
Ti	0.002	-	-	0.11	0.02	< 0.15	< 0.15
Mg	-	-	-	< 0.01	0.01	0.1	**4.5 – 5.2**
V	0.003	-	-	0.08	-	-	-
Be	-	-	-	< 0.0001	0.0001	< 0.0003	< 0.0003
Other	-	-	-	< 0.05	-	-	-
Cr	0.018	-	-	-	-	0.00	0.05 – 0.25

	Substrate		Welding wire				
	DH36	**AA5083 (H22)**	**$CuSi_3$**	**AA 2319**	**AA 4043**	**AA 4047**	**AA 5087**
C	0.140	-	-	-	-	-	-
Nb	0.020	-	-	-	-	-	-
N	0.005	-	-	-	-	-	-
Mo	0.001	-	-	-	-	-	-

Table 6-10: Physical properties of the substrate and welding wires used in CMT brazing experiments.

	Substrate		Welding wire				
	DH36	**AA5083 (H22)**	**$CuSi_3$**	**AA 2319**	**AA 4043**	**AA 4047**	**AA 5087**
Standard	ASTM A131:Part 4		AWS A5.7 ER CuSi-A *	AMS 4191H *	AWS A5.10 ER 4043 *	AWS A5.10 ER 4047	ISO 18273 – S Al 5087
Yield Strength, $N.mm^{-2}$	355	250 (Metalweb, 2013)	250 (Schwartz, 2003)	179	20 – 40 (70)	60 – 80	125 – 140
Tensile Strength, $N.mm^{-2}$	490 – 630	377	380	241	120 – 165 (145)	130 – 190	275 – 300
Elongation, %	22	8	46		3 – 18 (22)	5 – 20	17 – 30
Melting temperature, °C		570	910 - 1025	543 - 643	573 - 625	573 - 585	568 - 638
Vaporization temperature (alloying elements), °C			Cu – 2595 Si – 3265	Al – 2327 Cu – 2595	Al – 2327 Si – 3265	Al – 2327 Si – 3265 Fe – 2862 Zn – 906	Al – 2327 Mg – 1110 Mn – 2150 Fe – 2862 Zn – 906 Cr – 2672

Figure 6-19 shows the main alloying elements existent in each grade of aluminium and the respective applications and mechanical strength.

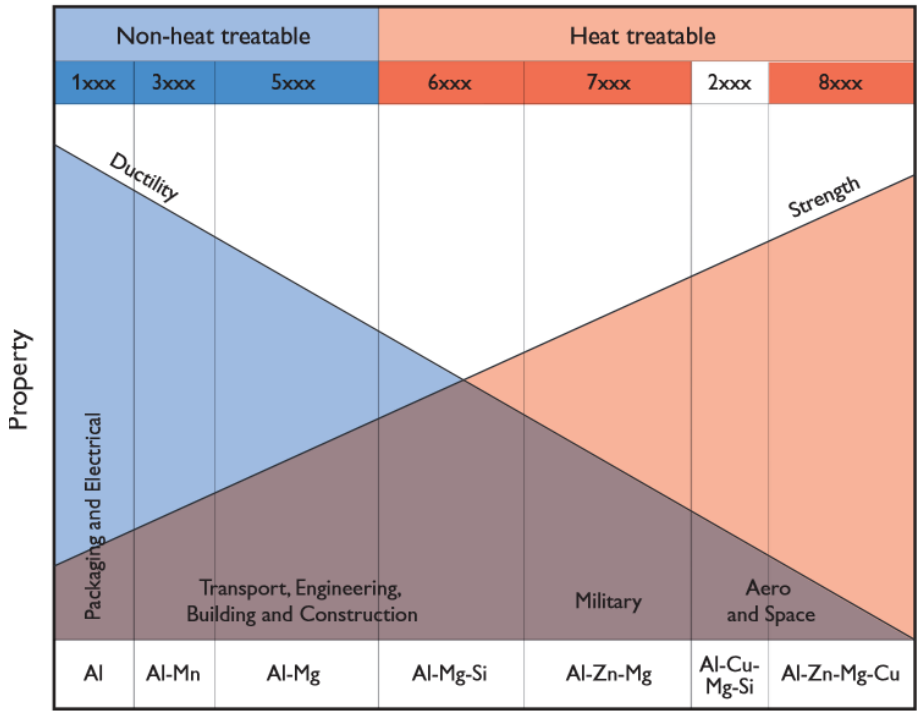

Figure 6-19: Applications and mechanical properties of different grades of aluminium (BOC, 2007).

The reasons for the choice of the aluminium grades are below:

AA4043 – The melting temperature of this wire is lower than the other series of aluminium alloys. Welding with this wire produces bright welds due to the high wettability. Silicon is known to be a good alloying element to use in the joining of Al to Cu. On the other hand, the metal supplier doesn't recommend the use of this wire to weld AA5083 because of the high content of Mg which together with the Si from the welding wire form Mg_2Si IMCs, reducing the ductility of the joint and increasing the crack sensitivity.

AA4047 – The higher content in silicon (compared to 4043 welding wire) decreases the melting temperature of the alloy and increases the fluidity. The reason for using this wire is that a good wettability is achievable with lower welding temperatures. Therefore, the reaction between Al and Cu can be minimal. On the other hand, a good stirring in the melt pool is enhanced with this wire due to the higher fluidity. This may be either a disadvantage or an advantage. The former because higher reaction between Al and Cu is permitted and the latter

because even though the reaction is higher, the IMCs to be formed would be spread in a matrix of aluminium.

AA5087 – This wire contains magnesium and manganese. The grade of this welding wire is similar of the base material (for the joining of the final application). This welding wire contains more than 3% of Mg so it is less prone to cracking. Welding with less than 1% of Si and Mg the weld tend to crack in the HAZ due to a mechanism called liquation cracking if high heat inputs are used.

AA2319 – This wire contains copper as main alloying element. This series of aluminium is considered to be unweldable and tend to crack when using fusion welding processes due to the formation of Al-Cu IMCs (BOC, 2007). Despite the limitations, this welding wire was chosen so that the Al-Cu IMCs could be analysed.

$CuSi_3$ is widely used in the automotive industry because of its lower melting temperature compared to other steel wires (ER 70-S6). The lower melting temperature results in the welding process with higher travel speeds, better wetting, better gap bridging and excellent corrosion resistance.

6.4.1.2 Methodology and experimental setup

In order to assess the viability of using copper as interlayer with CMT brazing process and study the interaction of Al-Cu-Fe, the metal configuration was chosen according to their melting temperatures, the lowest melting temperature on the top (see Figure 6-20). It is important to have Al-rich IMCs because they are less hard than the Cu-rich IMCs. Different techniques have been tried to increase the mechanical strength of the Al-Cu joints. Enrichment of the Al percentage in the fusion zone is one example (Klages, 2006) and then the control of the energy which has been done in this work.

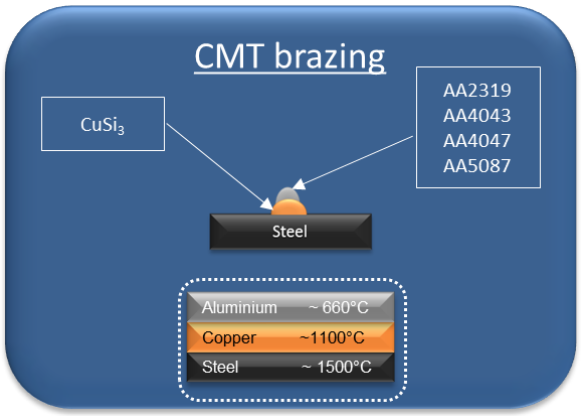

Figure 6-20: Material configuration used in the CMT brazing experiments with steel, copper and aluminium.

The experimental setup in use is similar to the one already described in section 6.3.1.2. The surfaces of the steel plates were ground using a manual angle grinder with abrasive disks to remove the protective coating and oxides, followed by a manual belt grinding machine to smoothen the surface of the substrate. Just before welding, the plates were degreased with acetone.

The deposition of several parallel beads of $CuSi_3$ onto the DH36 steel plate was also part of the sample preparation. These beads were produced using virtually identical welding conditions, viz. welding wire, torch angles and position, travel speed, wire feed speed, shielding gas composition and flow rate. The welding parameters were chosen to allow copper to braze steel and thus, have minimal interaction between these two metals (see Table 6-11). If the diffusion of Fe into Cu is minimized during the deposition of the first layer, then the reaction between Fe and Al and the Fe-Al IMC formation during the deposition of the second layer is unlikely to happen.

Table 6-11: CMT welding parameters for the deposition of the first layer ($CuSi_3$ onto DH36).

CMT mode	Travel speed, $m.min^{-1}$	Wire feed speed, $m.min^{-1}$	Shielding gas @ 22 $l.min^{-1}$	Average power, W	Arc energy, $J.mm^{-1}$	Average heat input (η=0.85), $J.mm^{-1}$
C0878	0.5	9.0	Argon	3385	406.2	345.3

The shielding gas used in the welding process was 100% Argon with 22 $l.min^{-1}$ of flow rate (this shielding gas is recommended by the supplier of the welding wire). The selected welding mode was one of the various available developed by Fronius to weld $CuSi_3$.

Figure 6-21 indicates that the energy of the process in consecutive welds under similar welding conditions using the CMT welding process was uniform. This characteristic and the stability of the welding process are beneficial to the repeatability of the experiments.

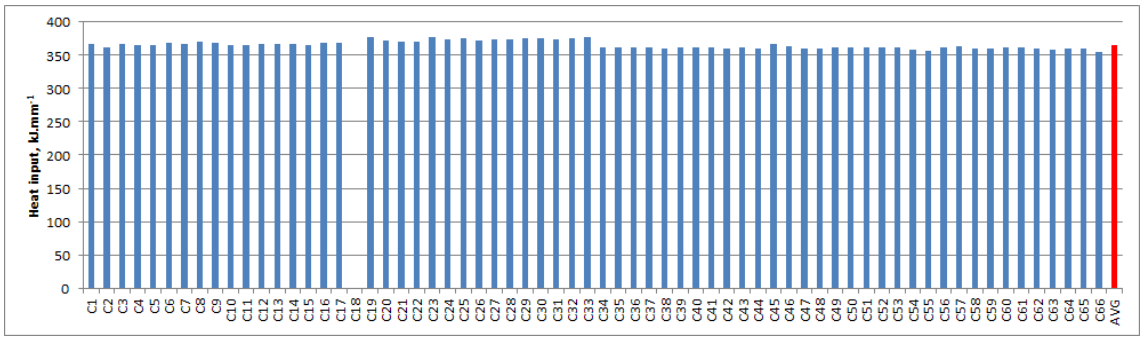

Figure 6-21: Graphical representation of the heat input of the CMT process in the deposition of each copper layer onto steel.

Eleven parallel copper weld beads were deposited onto each steel plate to allow eleven experiments per plate. The temperature between welds was controlled to ensure that the next layer was deposited at the same bulk temperature, about 30 °C. For this purpose, a thermocouple was attached to the steel surface and the temperature was monitored in the thermocouple reader.

The second layer counting from the steel substrate was built by deposition of aluminium onto copper. Before brazing, the copper weld seams were cleaned with a fine grit Scotch-Brite™ hand pad to remove the oxides and then cleaned with acetone.

Four different aluminium grades were used to braze the copper weld beads (AA2319, AA4043, AA4047 and AA5087) and different energy levels were created by changing the welding modes (standard CMT, CMT + Pulsed, CMT Advanced and CMT Advanced + Pulsed) and wire feed speeds (5.0, 5.5 and 6.0).

Figure 6-22 shows a schematic representation of the welding conditions used for the deposition of different aluminium alloys on $CuSi_3$.

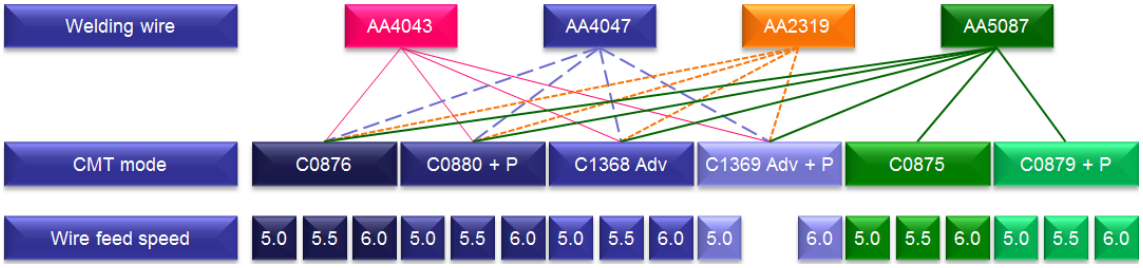

Figure 6-22: Schematic representation of the CMT welding conditions used in the deposition of the second layer (aluminium onto $CuSi_3$).

The CMT remote control unit (RCU) contains several welding programs for different welding modes and materials. For each welding mode and material, Fronius has adjusted the synergic curve (wire feed speed versus voltage and current) to improve the quality of the welds. Therefore, in each welding mode or material chosen, the energy transferred to the work piece is different. To avoid this situation and keep the energy constant for each welding mode, only one program was chosen. Therefore, the CMT welding modes represented in blue in Figure 6-22 are all programmed for $AlSi_5$ aluminium welding wire, except the welding modes C0875 and C879+P (represented with green) which are suitable for AlMg5 or AA5356 welding wire.

Each layer of aluminium was brazed onto copper with a travel speed of 0.5 $m.min^{-1}$ and shielded with 100% Argon with a flow rate of 20 $l.min^{-1}$. The travel speed was the maximum which could be used with the VPPA2 manipulator. More details about the average power, arc energy and heat input calculated based on the AMV 4000 arc watch system measurements can be found in Table 6-12.

Table 6-12: CMT welding parameters used in the deposition of the second layer (aluminium onto $CuSi_3$).

CMT mode	Travel speed, $m.min^{-1}$	Wire feed speed, $m.min^{-1}$	Welding wire	Average power, kW	Arc energy, $J.mm^{-1}$	Average heat input (η=0.85), $J.mm^{-1}$
C0876	0.5	5.0	AA2319	1.694	203.3	172.8
			AA4043	1.708	205.0	174.3
			AA4047	1.671	200.5	170.4
			AA5087	1.414	169.7	144.2
		5.5	AA2319	2.268	272.2	231.4
			AA4043	2.261	271.3	230.6
			AA4047	2.016	241.9	205.6
			AA5087	2.043	245.1	208.3
		6.0	AA2319	2.815	337.8	287.1
			AA4043	2.840	340.8	289.7
			AA4047	2.770	332.4	282.5
			AA5087	2.542	305.0	259.3
C0880+P	0.5	5.0	AA2319	2.173	260.7	221.6
			AA4043	2.189	262.7	223.3
			AA4047	2.472	296.6	252.1
			AA5087	2.010	241.2	205.0
		5.5	AA2319	2.523	302.8	257.4
			AA4043	2.493	299.2	254.3
			AA4047	2.857	342.8	291.4
			AA5087	2.259	271.0	230.4
		6.0	AA2319	2.868	344.1	292.5
			AA4043	2.828	339.4	288.5
			AA4047	-	-	-
			AA5087	2.558	306.9	260.9
C1368 Adv	0.5	5.0	AA2319	1.178	141.3	120.1
			AA4043	1.151	138.2	117.5
			AA4047	1.158	139.0	118.2
			AA5087	1.058	127.0	108.0
		5.5	AA2319	1.480	177.6	151.0
			AA4043	1.472	176.7	150.2
			AA4047	1.490	178.8	152.0

CMT mode	Travel speed, $m.min^{-1}$	Wire feed speed, $m.min^{-1}$	Welding wire	Average power, kW	Arc energy, $J.mm^{-1}$	Average heat input (η=0.85), $J.mm^{-1}$
C1369 Adv+P	0.5	6.0	AA5087	1.357	162.9	138.5
			AA2319	2.582	309.9	263.4
			AA4043	2.541	304.9	259.2
			AA4047	2.523	302.8	257.4
			AA5087	2.330	279.6	237.7
		5.0	AA2319	1.263	151.5	128.8
			AA4043	1.262	151.5	128.8
			AA4047	1.261	151.4	128.7
			AA5087	1.162	139.4	118.5
		6.0	AA2319	1.367	164.0	139.4
			AA4043	1.401	168.1	142.9
			AA4047	1.454	174.5	148.3
			AA5087	1.405	168.5	143.2

The comparison of heat input calculated for the different welding modes, wire feed speed and welding wires is in appendix B.

6.4.1.3 Metallographic analysis and microhardness testing

The metallographic analysis of the samples produced in this section followed the procedure described in section 2.3.4. It included sample cutting, mounting in resin, grinding and polishing, optical microscopy and macroscopy. The identification of the IMCs in the cross-sections was based on SEM and EDS results and on binary Al-Cu and ternary Al-Cu-Fe phase diagrams. However, the phases identified are only an approximation because the phases in the phase diagram were determined assuming equilibrium conditions. The microhardness was measured following standard procedure, as described in section 2.3.5. However, the load applied to produce the indentations was 50 g instead of 25 g, as described before.

6.4.2 Results and discussion

The results from the macro and microscopic analysis carried out on the brazed samples are shown in this section. As this study contains many factors (welding

wire composition, welding mode, wire feed speed), only a few samples will be used for comparison to assess the influence of those factors in the reaction between the three main elements (Fe, Cu and Al).

The first point to be observed is the effect of the welding mode on the morphology of the weld seam, keeping the remaining welding parameters constant. The pictures in Table 6-13 show that the weld seams produced either with standard CMT or pulsed CMT are continuous, whereas the CMT advanced and CMT advanced plus pulsed produced discontinuous weld seams. The reason for this can be found with the analysis of the voltage and current waveforms of each CMT welding mode (Figure 6-23).

Table 6-13: Pictures of the weld seams produced with $AlSi_5$ welding wire, WFS = 5.0 $m.min^{-1}$, TS = 0.5 $m.min^{-1}$ and different CMT welding modes.

CMT mode	Longitudinal cut	Cross-section	Top view of the weld seam	HI, $J.mm^{-1}$
C0876				174.3
C0880 + P		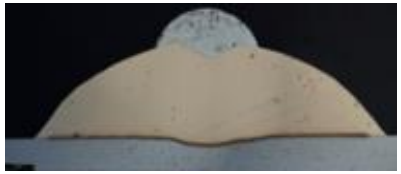		223.3
C1368 Adv				117.5
C1369 Adv + P	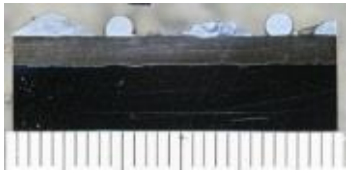			128.7

The waveforms of the CMT advanced and advanced plus pulsed modes have both positive and negative values because of the inversion of the polarity during the welding process, characteristic of these two new welding modes. When the signal is negative, there is less heating of the substrate and more metal deposition. To increase the continuity of the weld seam the travel speed needs to be reduced but this would increase the heat input. The reaction between the Fe, Cu and Al would be enhanced. It is possible to say that CMT is generally a stable welding process, independently of the welding mode in use.

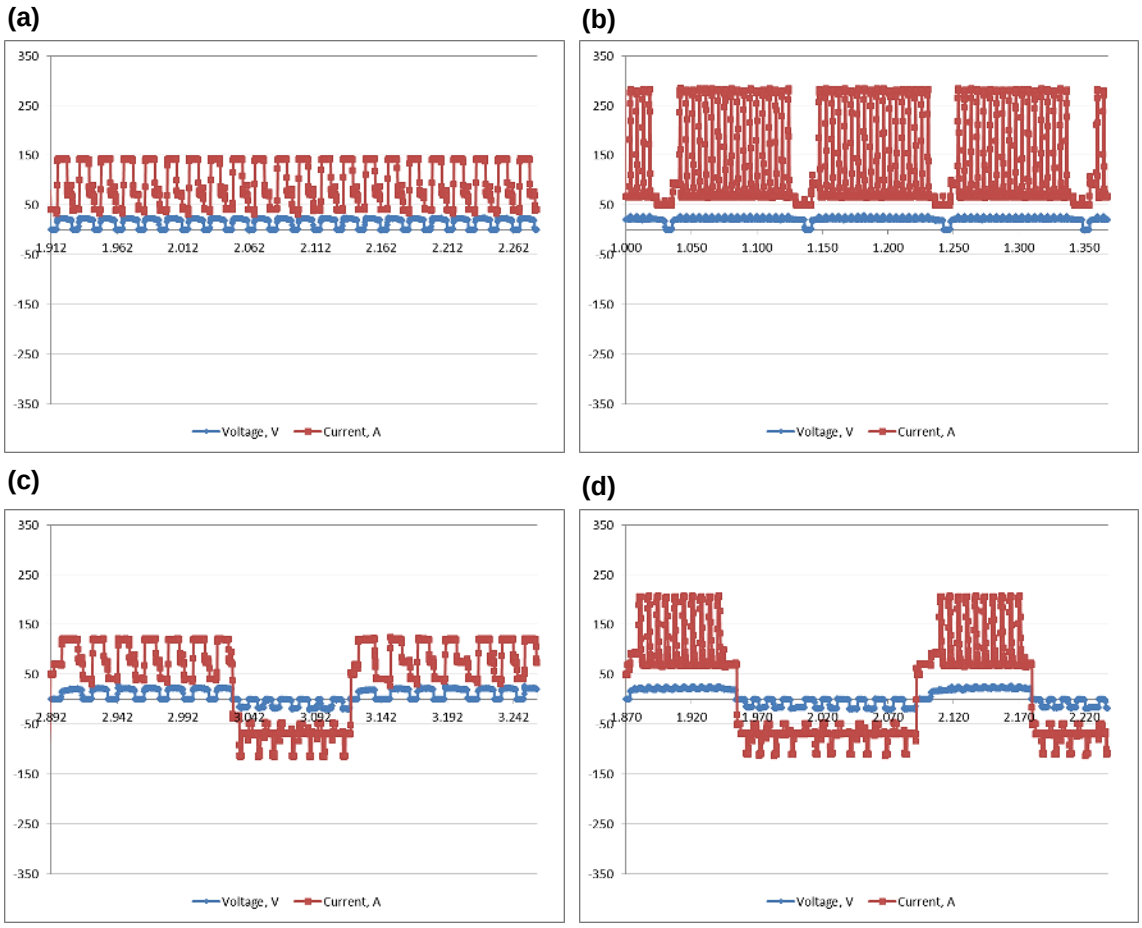

Figure 6-23: Voltage and current waveforms characteristic of (a) CMT standard, (b) CMT pulsed, (c) CMT advanced and (d) CMT advanced + pulsed.

The macrograph of the cross-sectional view of the sample produced with CMT pulsed mode shown in Table 6-14 indicates significant interaction of the aluminium with the copper. In this condition the heat input generated during the

process was sufficiently high to melt the copper and therefore, the brazing of the copper with the aluminium was not achieved. However, with the other three CMT modes it was possible to have brazing.

Table 6-14: Macrographs of the cross-section of the weld seams produced with $AlSi_5$ welding wire, WFS = 5.0 m.min^{-1}, TS = 0.5 m.min^{-1} and different CMT welding modes.

CMT welding mode	HI (η=0.85), J.mm^{-1}	Macrograph
C0876	174.3	
C0880 + P	223.3	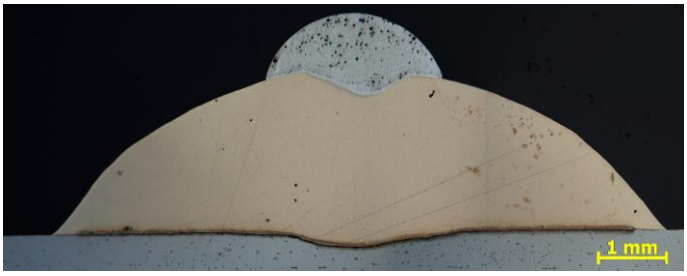
C1368 Adv	117.5	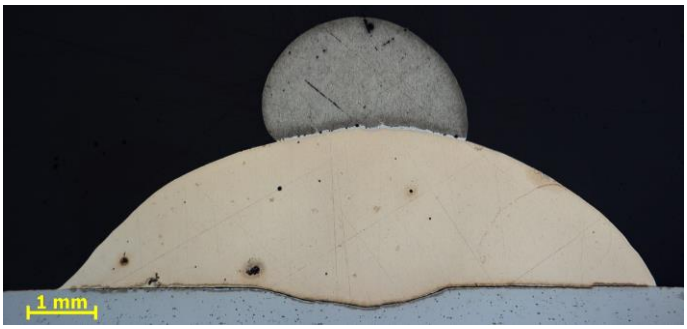
C1369 Adv + P	128.7	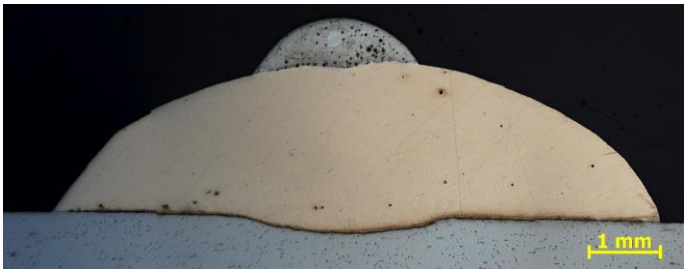

The effect of the composition of the welding wire on the morphology of the weld seam is shown in Table 6-15. One can see that the geometry of the aluminium weld bead does not have a significant effect. However, with regards to the continuity of the weld seam, it seems that the AA4047 and AA5087 welding wires tend to produce a more uniform weld seam when compared to the other two aluminium alloys (see longitudinal cut of the weld seams). This can be due to the slightly lower melting temperature of these two welding wires.

Table 6-16 and Table 6-17 show the macrographs and the micrographs of the aluminium weld beads in a cross-sectional view. The majority of the micrographs clearly shows porosity which in most of the cases are caused by the presence of hydrogen gas mixed in the molten pool. This problem is very common in arc welding of aluminium. Spatter deposited inside the gas nozzle may reduce the shielding efficiency which can contribute for the instability of the welding process. Hydrocarbons present on the surface of the substrate, such as oil, lubricants or paint, can also be a source of the problem. The cleaning of the substrate surface or the cutting of the plates with abrasive/cutting discs can leave residues on the material which can then be the cause of porosities.

Table 6-15: Pictures of the weld seams produced using CMT advanced welding mode (C1368), WFS = 5.0 m.min^{-1}, TS = 0.5 m.min^{-1} and different welding wires.

CMT mode	Longi tudinal cut	Cross-section	Top view of the weld seam	HI, J.mm^{-1}
AA2319 (AlCu)	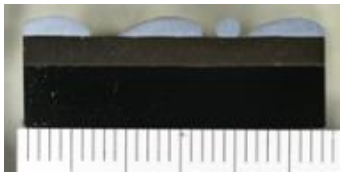			120.1
AA4043 (AlSi5)	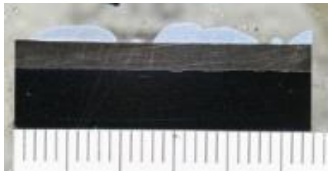	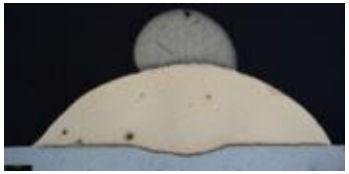		117.5
AA4047 (AlSi12)	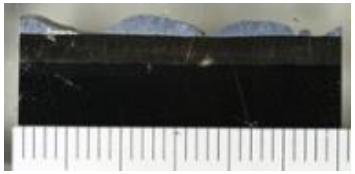			118.2
AA5087 (AlMg)	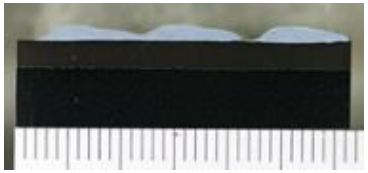	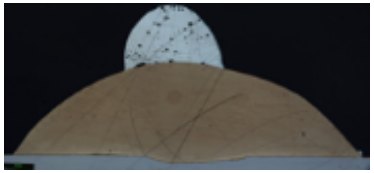		108.0

Table 6-16: Macrographs of the cross-section of the weld seams produced using CMT advanced welding mode (C1368), WFS = 5.0 m.min^{-1}, TS = 0.5 m.min^{-1} and different welding wires.

Welding wire	HI (η=0.85), J.mm^{-1}	Macrograph
AA2319 (AlCu)	120.1	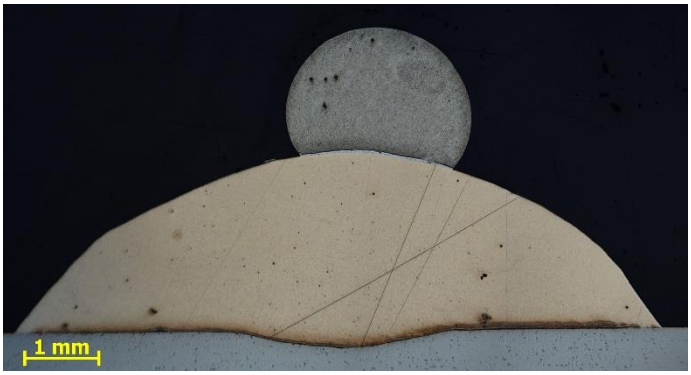
AA4043 ($AlSi_5$)	117.5	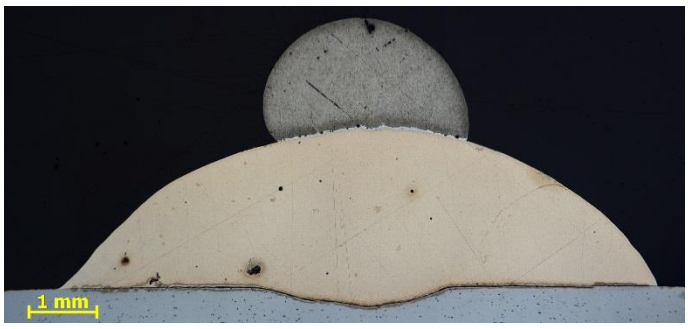
AA4047 ($AlSi_{12}$)	118.2	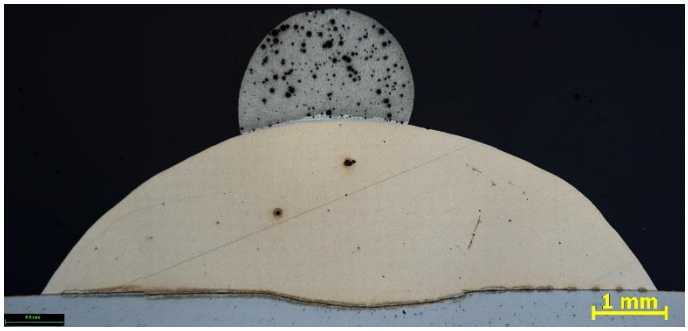
AA5087 (AlMg)	108.0	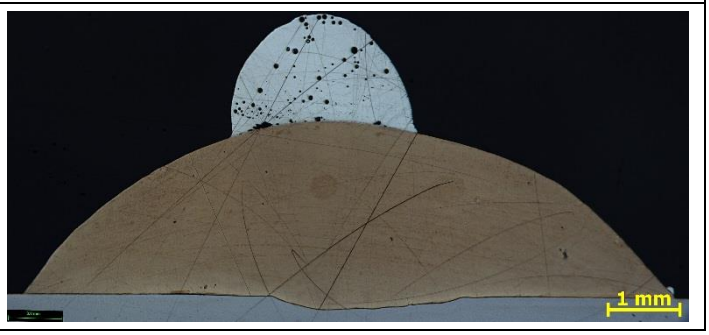

Macrographs and micrographs of the cross-sections of the welds produced with different grades of aluminium by standard and advanced CMT modes are shown in Table 6-17. Even though the welds produced by the CMT advanced mode are not acceptable due to the discontinuity of the weld seams, these samples were also analysed. The aim was to investigate whether due to the lower heat input there were less IMCs formed across the weld.

Table 6-17: Macrographs of the cross-sections of the brazed samples and micrographs of the centre of the aluminium weld bead.

Welding mode	Welding wire			
	AA2319 (AlCu)	AA4043 ($AlSi_5$)	AA4047 ($AlSi_{12}$)	AA5087 (AlMg)
C0876 WFS=5.0 m.min^{-1} TS=0.5 m.min^{-1}	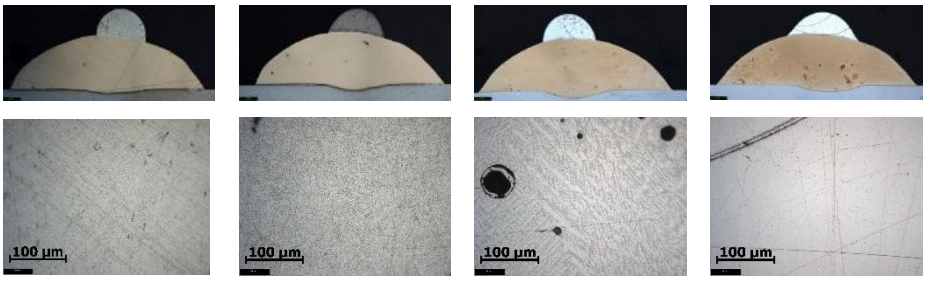			
HI (η=0.85), J.mm^{-1}	172.8	174.3	170.4	144.2
C0876 WFS=6.0 m.min^{-1} TS=0.5 m.min^{-1}	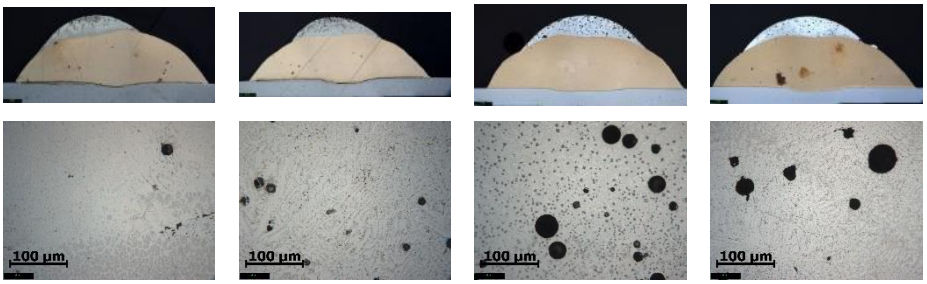			
HI (η=0.85), J.mm^{-1}	287.1	289.7	282.5	259.3
C1368 Adv WFS=5.0 m.min^{-1} TS=0.5 m.min^{-1}	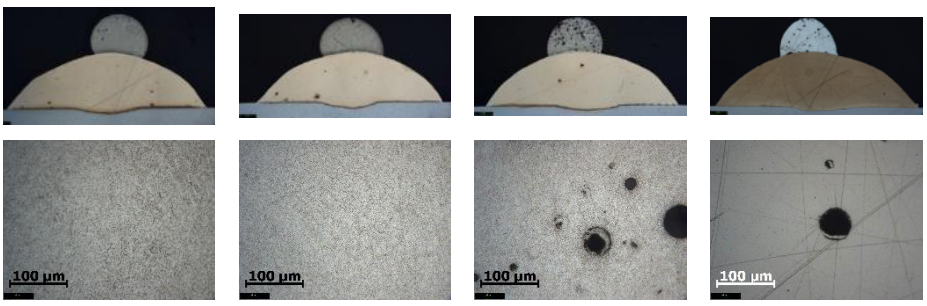			
HI (η=0.85), J.mm-1	120.1	117.5	118.2	108.0

Generally, the aluminium welding wires with copper and low silicon content showed less porosity than the aluminium wires with 12% silicon and magnesium. These two welding wires are the two with better wetting properties. However, it is also visible that when the processing energy increases, either via the increase of the wire feed speed or the use a more energetic CMT welding mode, the formation of porosity is accentuated. Using AA5087 welding wire it was possible to obtain porosity free weld seams but only for low levels of energy (CMT standard mode with the minimum wire feed speed). On the other hand, brazing with AA4047 welding wire, even with the minimum energy level tends to form porosity.

Since all samples were prepared using similar methodology, the contamination does not seem to be the reason for high level of porosity in the weld beads of AA4047 and AA5087. Possibly the explanation can be in the alloying elements of the welding wires. Generally, the vaporization temperature of the main constituents of the wires is higher than 2000 °C except zinc, for which the vaporization temperature is about 900 °C. This element is present in both wires and therefore, its vaporization can be related with the formation of porosity.

The presence of porosities can also be attributed to the aluminium oxides. In the presence of high temperature and moisture, complex oxide layers are formed on the aluminium, especially when alloying elements are magnesium and copper. In wet environments a duplex film is formed and one continuous layer is changed to hydroxylated film (*Aluminum: Properties and Physical Metallurgy*, 1984). The reaction between solid aluminium and moisture in the atmosphere forms oxides and hydrogen. The amount of hydrogen can be greater than the solubility limit and therefore this may cause porosity (Yang et al., 2013).

The effect of arc energy and welding wire composition on IMC formation is illustrated in Table 6-18. A higher concentration of IMCs is visible in the optical micrographs between the copper layer (orange area) and the aluminium weld bead (at the top) when the wire feed speed increased. The optical micrographs also indicate that when the CMT process is used with higher wire feed speed (higher heat input) the copper layer melts and the reaction between aluminium

and copper is more intense and consequently, more IMCs are formed. In this case brazing is not achieved.

Either with 5.0 or 6.0 of wire feed speed, the growth of the IMCs seems to be less when AA5087 welding wire is used in the second layer. However, in the micrograph correspondent to the sample produced with more energy, there is a visible crack near the Al-Cu transition. The reason for the growth of this crack may be associated either with the wire composition or the IMCs. The latter doesn't seem to be reasonable justification because the samples welded with AA2319, AA4043 and AA4047 aluminium welding alloys have even thicker IMCs and no cracks are visible.

The effect of changing welding modes and wire composition on the IMCs formation is illustrated in Table 6-19. In this case, there are no significant differences in terms of IMC formation between the two welding modes.

Table 6-18: Optical micrographs of the Al-Cu layer transition, CMT welding mode – C0876, TS=0.5 m.min^{-1} and different wire feed speeds and welding wires.

Welding wire	Wire feed speed, m.min^{-1}	
	5.0	6.0
AA2319 (AlCu)	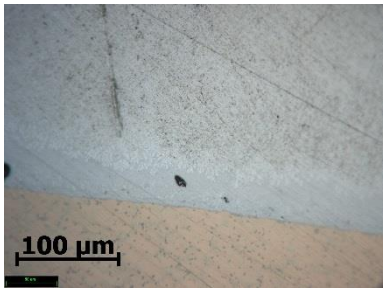	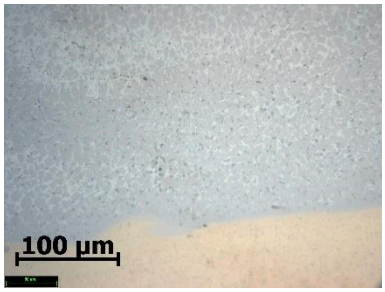
HI (η=0.85), J.mm^{-1}	172.8	287.1
AA4043 ($AlSi_5$)	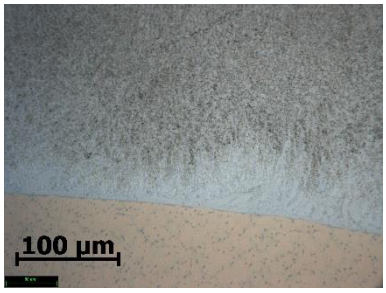	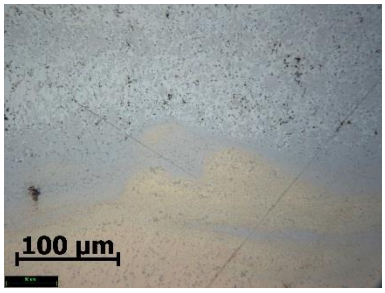
HI (η=0.85), J.mm^{-1}	174.3	289.7
AA4047 ($AlSi_{12}$)	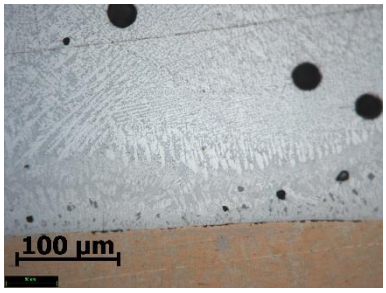	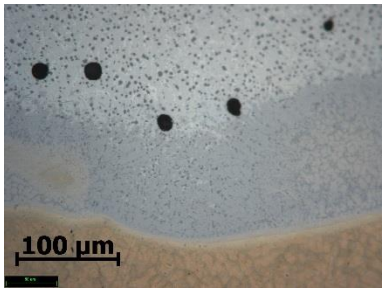
HI (η=0.85), J.mm^{-1}	170.4	282.5
AA5087 (AlMg)	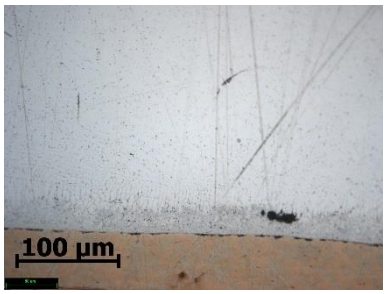	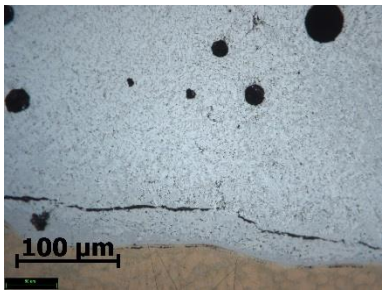
HI (η=0.85), J.mm^{-1}	144.2	259.3

Table 6-19: Optical micrographs of the Al-Cu layer transition, WFS = 5.0 m.min^{-1}, TS = 0.5 m.min^{-1} and different welding modes and welding wires.

Welding wire	CMT welding mode	
	C0876	C1368 Adv
AA2319 (AlCu)	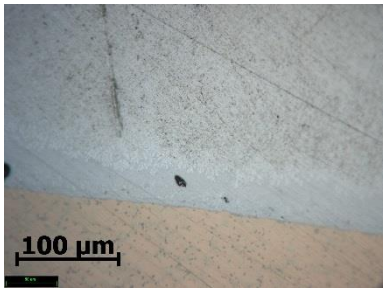	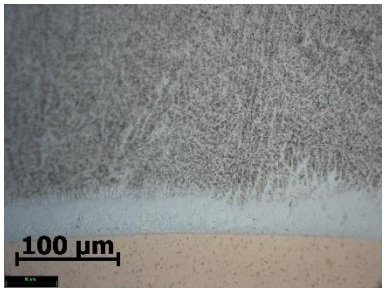
HI (η=0.85), J.mm^{-1}	172.8	120.1
AA4043 (AlSi$_5$)	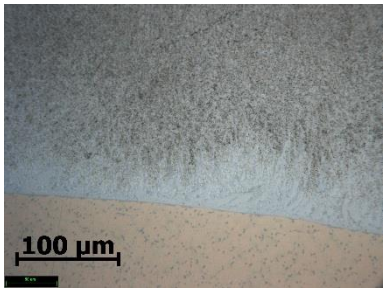	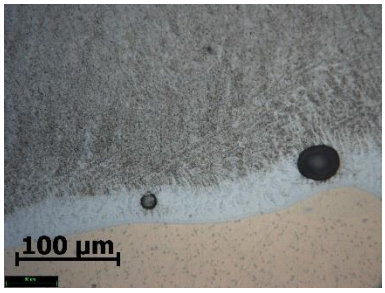
HI (η=0.85), J.mm^{-1}	174.3	117.5
AA4047 (AlSi$_{12}$)	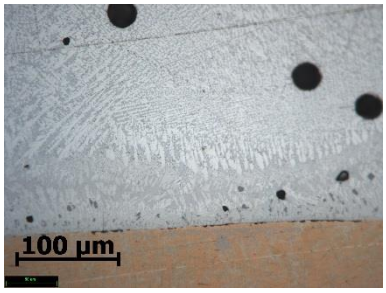	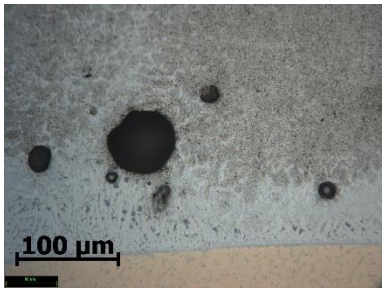
HI (η=0.85), J.mm^{-1}	170.4	118.2
AA5087 (AlMg)	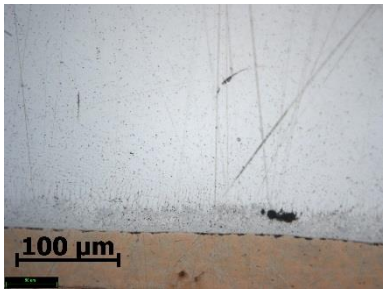	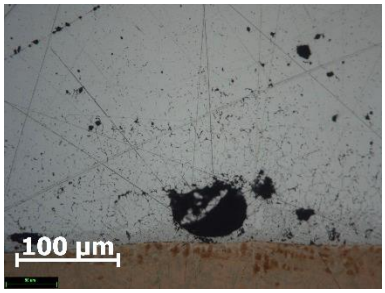
HI (η=0.85), J.mm^{-1}	144.2	108.0

Table 6-20 shows the micrographs by SEM of the samples previously shown in Table 6-19. Two levels of IMCs are visible in all samples. Closer to the Al-Cu interface there is a type of IMC more compact whereas between this IMC and the aluminium the IMCs are spread in a matrix of aluminium.

It was observed that either brazing with CMT standard or advanced mode, AA2319 tends to form a large area of IMCs spread in the matrix of aluminium when compared to the other welding wires. The reason for this can be the extra 6% of copper coming from the welding wire which increases the copper concentration in the molten aluminium. However, with regards to mechanical strength these IMCs seem to be less harmful than the other closer to the Al-Cu interface because they are spread in the matrix of aluminium but can be detrimental from a corrosion point of view as Al_2Cu may form a galvanic cell within the aluminium matrix.

Table 6-20: SEM micrographs at the Al-Cu layer transition, WFS = 5.0 m.min^{-1}, TS = 0.5 m.min^{-1} and different welding modes and welding wires.

Welding wire	CMT welding mode	
	C0876	C1368 Adv
AA2319 (AlCu)	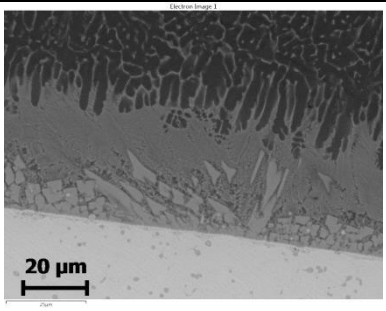	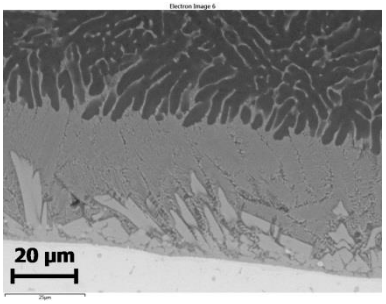
HI (η=0.85), J.mm^{-1}	172.8	120.1
AA4043 ($AlSi_5$)	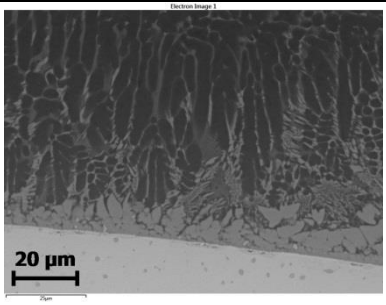	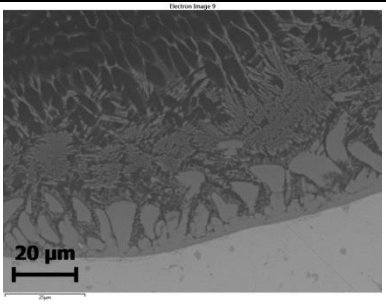
HI (η=0.85), J.mm^{-1}	174.3	117.5
AA4047 ($AlSi_{12}$)	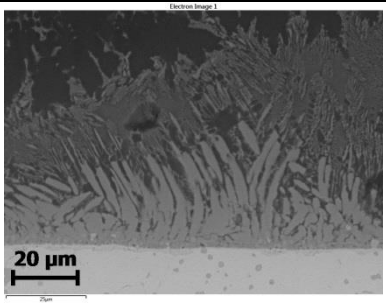	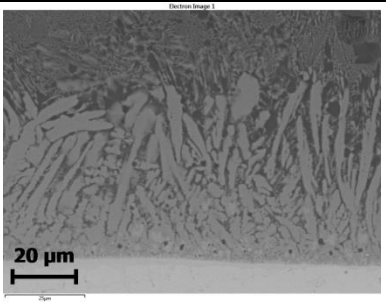
HI (η=0.85), J.mm^{-1}	170.4	118.2
AA5087 (AlMg)	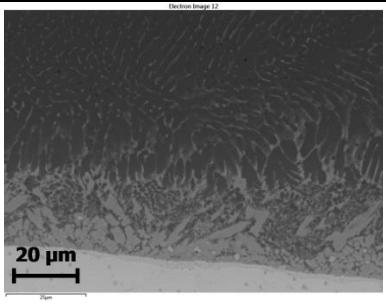	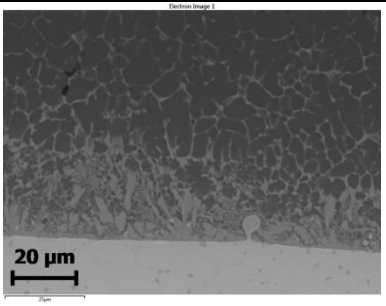
HI (η=0.85), J.mm^{-1}	144.2	108.0

The silicon content in the welding wire seems to play an important role on the IMC formation. The growth of the IMCs was more intense when the welding wire had 12% of silicon than that with only 5% of silicon. The composition of AA4047 is in the eutectic point which means that the transition between liquid to solidus state is immediate and the melting temperature is minimal in this point. Therefore, during the brazing process the aluminium wire can remain in liquid state more time than the other welding wires with different chemical compositions. Consequently, the IMC growth is enhanced. Moreover, the micrograph of the sample brazed with AA4043 shows a much smaller band of IMCs spread in the aluminium matrix than AA4047. With 5% of Si the molten aluminium starts the solidification process at higher temperatures. Since the tendency to form IMCs is lower in the solid state than in the liquid state, it is possible that this can be a reason for the presence of fewer IMCs under these circumstances.

A thinner layer of IMCs was observed in the SEM picture of the sample brazed with AA5087, which is about 20 µm thick. The IMCs band spread in the aluminium matrix is smaller than that of the samples brazed using the AA2319 and AA4047 welding wires. The thickness of the IMC layers of the welds produced with the AA5087 and AA4043 alloys are comparable to each other and are more than 30 µm thick. In terms of the compact IMCs formed near the Al-Cu interface, they seem to be smaller than those compounds observed in the samples produced with the other welding wires.

When comparing welding modes, C0876 and C1368 advanced, one can see that the morphology of the IMCs is very similar. However, CMT advanced mode seems to produce more IMCs.

Different microstructures were formed at the centre of the aluminium layer produced with different welding wires and similar brazing conditions (see Table 6-21). The optical micrographs show IMCs in the form of precipitates when using wires with Cu, 5%Si and Mg content and IMCs in a form of dendritic structures when the welding wire with 12%Si was used.

Table 6-21: Optical micrographs of the centre of the aluminium layers, CMT welding mode - C0876, TS=0.5 m.min^{-1} and different wire feed speeds and welding wires.

Welding wire	Wire feed speed, m.min^{-1}	
	5.0	6.0
AA2319 (AlCu)	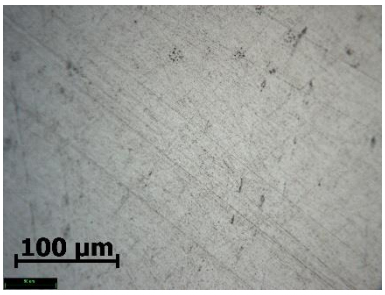	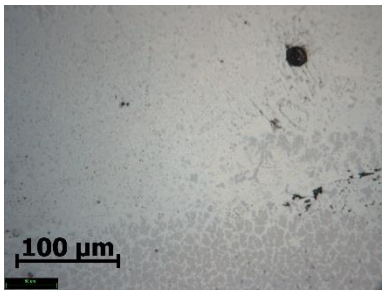
HI (η=0.85), J.mm^{-1}	172.8	287.1
AA4043 (AlSi$_5$)	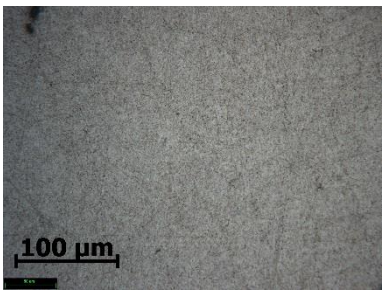	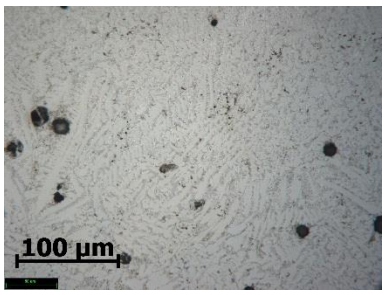
HI (η=0.85), J.mm^{-1}	174.3	289.7
AA4047 (AlSi$_{12}$)	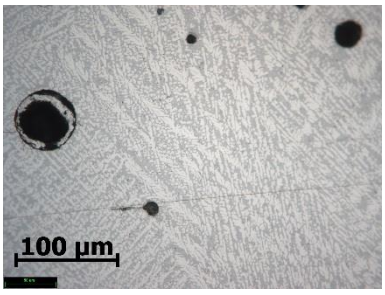	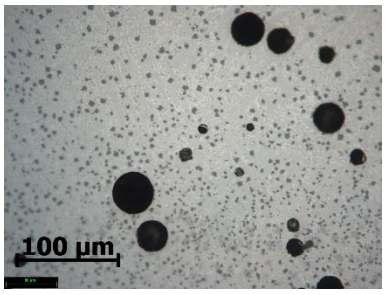
HI (η=0.85), J.mm^{-1}	170.4	282.5
AA5087 (AlMg)	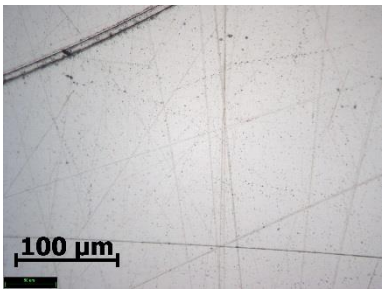	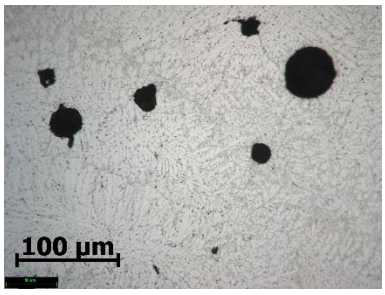
HI (η=0.85), J.mm^{-1}	144.2	259.3

The increase of energy produces a higher interaction between the aluminium welding wire and the copper layer. As a result of the partial melting of the copper layer more IMCs are formed within the Al matrix. This situation is more visible when $AlSi_{12}$ is used and there are small clusters of IMCs instead of dendritic structures formed under lower energy. The presence of IMCs within the aluminium matrix makes the weld bead behave as a composite material and thus, the mechanical properties of the weld bead might be better than those of the welding wire.

Elemental mapping by SEM-EDS analysis of the macrosections was done and the results are shown in Table E-1 in Appendix E. The pictures show the distribution of the main constituent elements of the samples. Beside Al, Cu and Fe elements which are the main constituents of the samples, there are also other elements present in some of the samples such as Si, Mn and Mg. Mn is part of the steel substrate, whereas Si is part of the copper welding wire, reason for it to be identified in all samples. However, there is one sample where Si is in higher concentration and corresponds to the sample brazed with $AlSi_{12}$ welding wire. Mg was only identified in one sample due to the composition of the welding wire (AA5087).

Similar analysis was carried out with the samples produced with CMT Advanced welding mode and the results are shown in Table E-2 in Appendix E.
Two samples were chosen for analysis of the IMC composition and possible phase identification. These samples correspond to the ones processed with the lowest energy, i.e. CMT standard (C0876) and advanced (C1368 Adv) modes with the minimum wire feed speed of 5.0 $m.min^{-1}$ (see Table 6-22).

Table 6-22: SEM-EDS analysis at the Al-Cu layer transition with accelerating voltage of 20 kV. WFS = 5.0 m.min^{-1}, TS = 0.5 m.min^{-1} and different welding modes and welding wires.

Welding wire	CMT welding mode	
	C0876	C1368 Adv
AA2319 (AlCu)	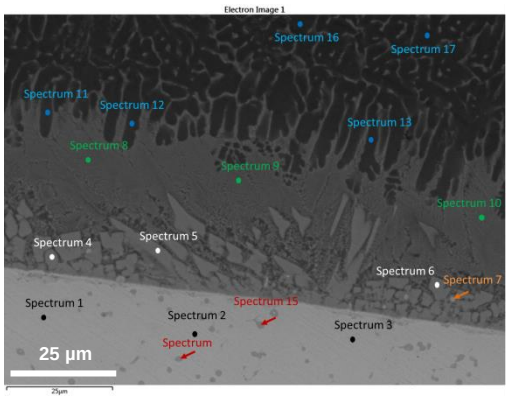	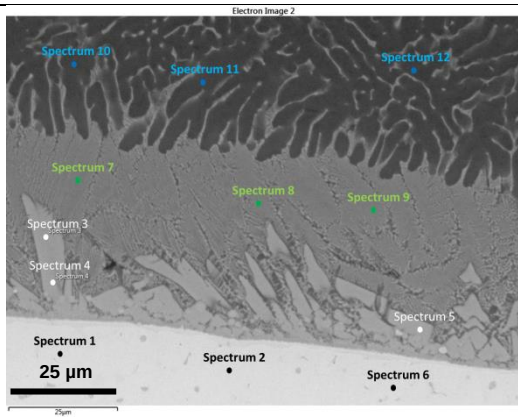
HI, kJ.mm^{-1}	172.8	120.1
AA4043 (AlSi$_5$)	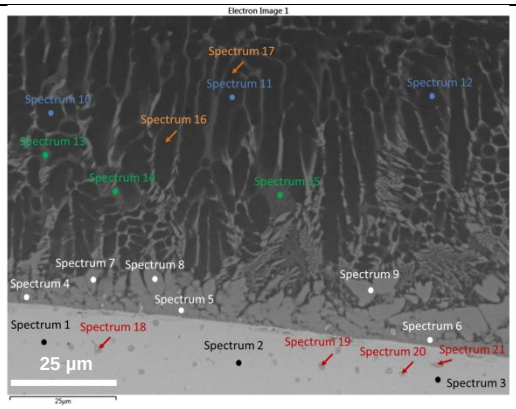	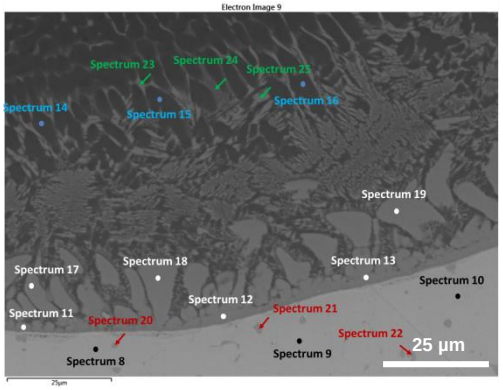
HI, kJ.mm^{-1}	174.3	117.5
AA4047 (AlSi$_{12}$)	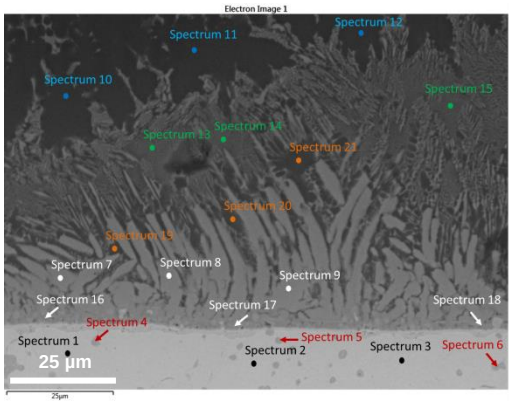	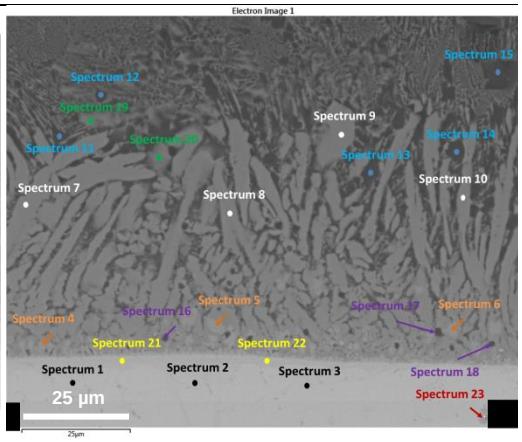
HI, kJ.mm^{-1}	170.4	118.2

Welding wire	CMT welding mode	
	C0876	C1368 Adv
AA5087 (AlMg)	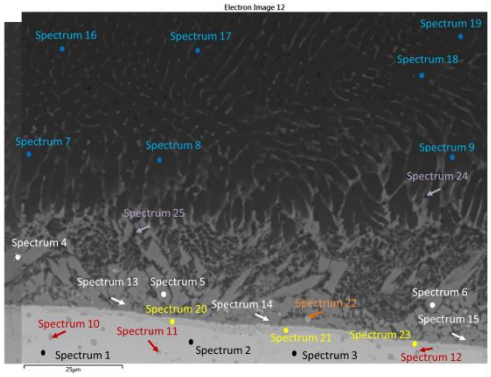	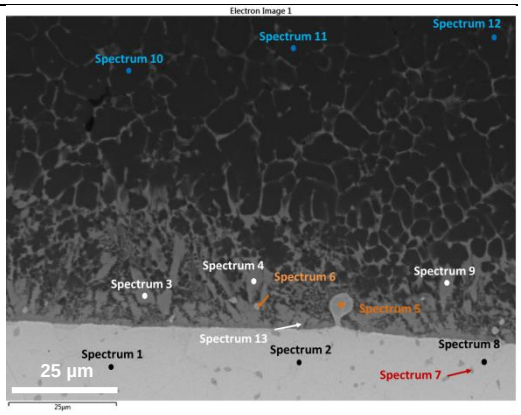
HI, kJ.mm^{-1}	144.2	108.0

The elemental composition of the samples was determined and it is reported in Table D-4, Table D-5, Table D-6 and Table D-7 in Appendix D. To simplify the identification of the phases, only elements with composition higher than 8% (at.%) were considered. Consequently, the results can be represented as indicated in Table D-8, Table D-9, Table D-10 and Table D-11.

With the phase diagrams it is possible to roughly estimate the phases present in the welded samples. Several simplifications were done in this process, for instance, elimination of elements under 8 at.% and use of phase diagrams which are only valid in equilibrium conditions. Therefore, the phases identified in this section need to be considered as only approximations. In order to better understand the distribution of the phases formed during the brazing process, SEM images and EDS analysis were combined, and a graphical representation of the phases was produced (see Figure 6-24, Figure 6-26, Figure 6-28 and Figure 6-30). It is important to mention that this graphical representation is simplified and therefore, small IMC phases identified in the spectrum analysis may have been omitted.

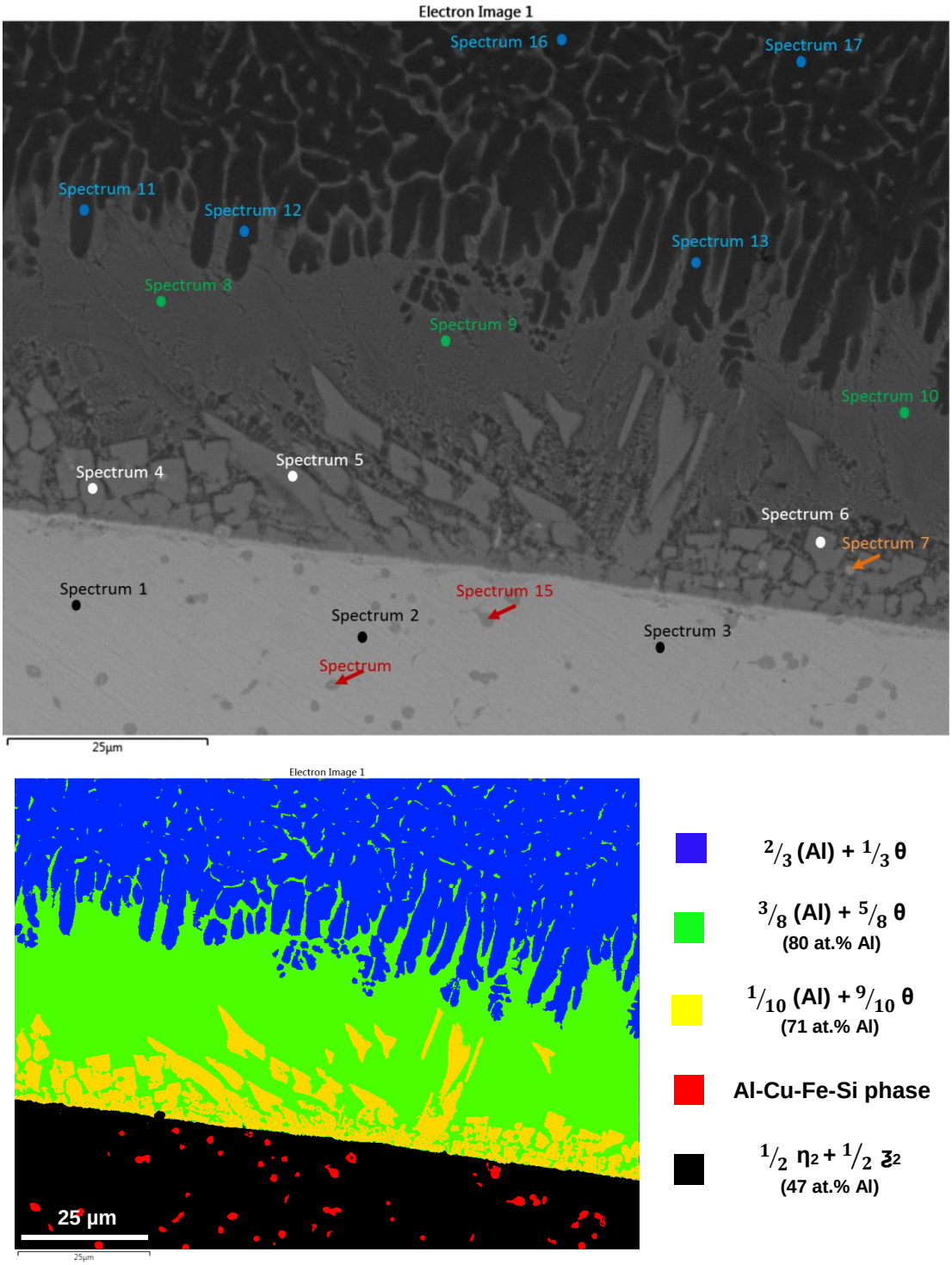

Figure 6-24: SEM-EDS image and schematic representation of the phases formed on the samples brazed using AA2319 (AlCu) welding wire alloy and CMT standard (D23).

(a)

At% Spectrum Label	Al	Si	Mn	Fe	Cu	Total
Spectrum 1	44.4	2.5	0.5	1.6	51.1	100
Spectrum 2	44.1	2.7	0.6	1.8	50.7	100
Spectrum 3	44.8	3.0	0.7	1.5	49.9	100
Spectrum 4	68.3	1.1	0.3	0.9	29.3	100
Spectrum 5	69.9	1.0	0.4	0.8	28.1	100
Spectrum 6	69.8	1.1	0.2	0.9	28.0	100
Spectrum 7	54.3	8.3	0.9	16.7	19.8	100
Spectrum 8	78.8	1.2	0.4	0.7	19.0	100
Spectrum 9	79.1	0.9	0.3	0.7	19.0	100
Spectrum 10	78.3	1.1	0.3	0.7	19.6	100
Spectrum 11	86.2		0.2	0.5	13.1	100
Spectrum 12	88.1		0.2	0.4	11.3	100
Spectrum 13	89.0		0.2	0.5	10.3	100
Spectrum 14	36.7	11.1	1.3	22.5	28.4	100
Spectrum 15	39.1	11.9	1.7	24.1	23.2	100
Spectrum 16	91.9		0.2	0.4	7.5	100
Spectrum 17	89.1			0.4	10.5	100

(b)

At% Spectrum Label	Al	Si	Mn	Fe	Cu	Total	Phase
Spectrum 1	46.5				53.5	100.0	η2+ζ2
Spectrum 2	46.5				53.5	100.0	η2+ζ2
Spectrum 3	47.3				52.7	100.0	η2+ζ2
Spectrum 4	70.0				30.0	100.0	(Al)+ɵ
Spectrum 5	71.3				28.7	100.0	(Al)+ɵ
Spectrum 6	71.4				28.6	100.0	(Al)+ɵ
Spectrum 7	54.8	8.4		16.8	20.0	100.0	Al-Cu-Fe-Si
Spectrum 8	80.6				19.4	100.0	(Al)+ɵ
Spectrum 9	80.7				19.3	100.0	(Al)+ɵ
Spectrum 10	80.0				20.0	100.0	(Al)+ɵ
Spectrum 11	86.8				13.2	100.0	(Al)+ɵ
Spectrum 12	88.7				11.3	100.0	(Al)+ɵ
Spectrum 13	89.6				10.4	100.0	(Al)+ɵ
Spectrum 14	37.2	11.2		22.8	28.7	100.0	Al-Cu-Fe-Si
Spectrum 15	39.8	12.1		24.5	23.6	100.0	Al-Cu-Fe-Si
Spectrum 16	92.5				7.5	100.0	(Al)+ɵ
Spectrum 17	89.5				10.5	100.0	(Al)+ɵ

Figure 6-25: (a) Raw data and (b) simplified data from the SEM/EDS spectrum analysis of the samples brazed using AA2319 (AlCu) welding wire alloy and CMT standard (D23).

The composition of the blue phase represented in Figure 6-24 is a mix between a solid solution of Cu into Al and θ phase ((Al) + ɵ). The proportion of this mixture is ⅔ of (Al) and ⅓ of θ. Within the blue phase the variation of composition is not significant, about 3 at.%, and it is mainly composed of aluminium. The chemical composition of the yellow phase indicates the presence of the mixture composed by $^{1}/_{10}$ of (Al) and $^{9}/_{10}$ θ. Between the yellow and blue phases there is a green region which composition lays between the two previously reported phases. By looking at the SEM image, it is believed that the θ phase in this region form a fine net shape immersed in the aluminium substrate. This may explain the intermediate composition of the green region (about 80 at.% of Al and 20 at.% of Cu) in relation with the yellow (about 90 at.% of Al and 10 at.% of Cu) and blue (about 70 at.% of Al and 30 at.% of Cu) regions. In terms of mechanical properties, it is less detrimental to the joint to have dispersed IMCs in a soft matrix of aluminium than only a compact structure of IMCs at the Cu-Al interface. The black region represents the copper layer. It is interesting to observe that even with a virtually zero interaction of the aluminium wire with copper, characteristic of the brazing process, it was not possible to prevent the diffusion of aluminium

atoms into copper. This is evident in the spectrum analysis which indicates a uniform distribution of a dual phase structure composed by ½ of η_2 and ½ of ζ_2, with about 50 at.% of Al and 50 at.% Cu. In the copper layer it is also visible the presence of quaternary phases (represented in red) of Al, Si, Fe and Cu in a 40 at.%, 10 at.%, 25 at.% and 25 at.% distribution, respectively. The high Fe content in these structures is due to interaction between the Cu and the Fe produced during the deposition of the copper layer onto the steel substrate. In the macrographs it is visible that the steel surface was partially melted and there is a slight penetration of copper into steel. The phase determination is complex and therefore, will not be done. In terms of mechanical strength these structures are not likely to be detrimental to the joint due to their distribution and morphology.

A similar approach for the identification of the phases was applied to the other three samples produced with different welding wires. The IMCs found in the sample brazed with AA4043 ($AlSi_5$) are similar to the ones previously represented in Figure 6-24. Compared to the previous sample, the blue region in Figure 6-26 covers a larger area and based on spectrum analysis, the composition is $^7/_9$ of (Al) and $^2/_9$ of θ phase. However, the yellow phase seems to be more compact than that of the previous sample and the composition indicates a mixture of $^1/_8$ of (Al) and $^7/_8$ of θ phase. The composition of the green area is very similar but with higher content of Si. Previously it was 80 at.% of Al and 20 at.% of Cu ((Al) + θ) but now with higher percentage of Si mixed with Al and Cu. If Si is excluded from the elemental composition, the phase of the green area becomes similar to the previous (Al) + θ. If Si is taken into account then a new ternary phase may exist but it has not been determined. The green region is much smaller possibly because of lack of copper in the welding wire as opposed to the previous example. The composition of this green area falls between the blue and yellow regions.

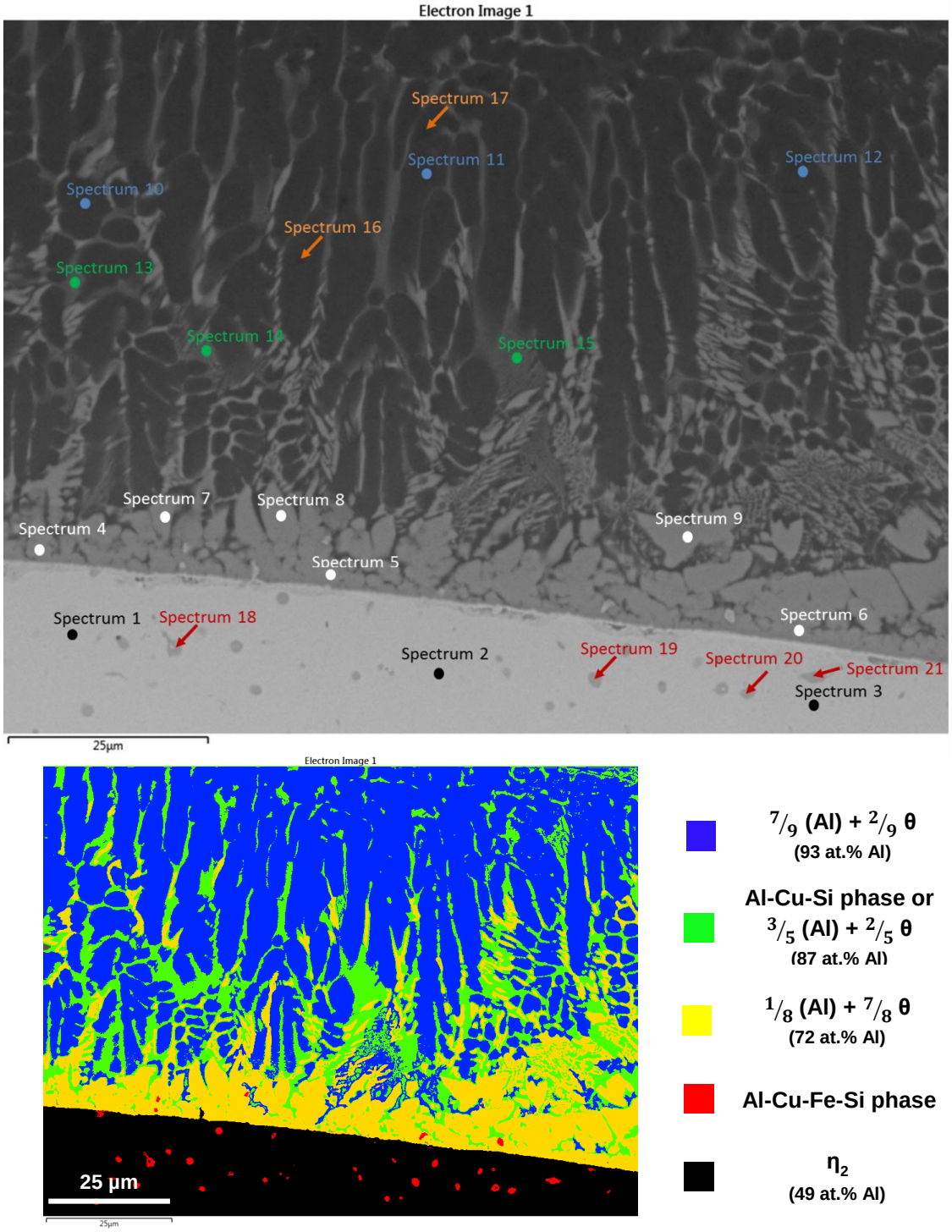

Figure 6-26: SEM-EDS image and schematic representation of the phases formed on the samples brazed using AA4043 ($AlSi_5$) welding wire alloy and CMT standard (D12).

(a)

At% Spectrum Label	Al	Si	Mn	Fe	Cu	Total
Spectrum 1	47.0	3.4	0.6	1.4	47.6	100
Spectrum 2	46.6	3.5	0.6	1.4	48.0	100
Spectrum 3	46.1	4.4	0.7	1.2	47.5	100
Spectrum 4	68.3	3.0	0.5	1.2	27.0	100
Spectrum 5	67.9	2.7	0.5	1.1	27.8	100
Spectrum 6	66.5	3.0	0.6	1.4	28.4	100
Spectrum 7	71.2	2.5	0.3	0.8	25.3	100
Spectrum 8	70.7	2.6	0.3	0.8	25.7	100
Spectrum 9	70.8	2.4	0.3	0.6	25.9	100
Spectrum 10	90.1	2.2		0.2	7.4	100
Spectrum 11	90.8	2.3		0.4	6.5	100
Spectrum 12	90.9	2.3		0.3	6.5	100
Spectrum 13	80.4	7.7		0.5	11.5	100
Spectrum 14	79.1	7.8	0.3	0.5	12.3	100
Spectrum 15	76.3	10.1	0.2	0.5	12.9	100
Spectrum 16	89.5	2.5		0.3	7.7	100
Spectrum 17	90.9	2.3		0.3	6.5	100
Spectrum 18	42.0	11.3	1.6	16.2	28.8	100
Spectrum 19	40.5	12.1	1.4	22.1	24.1	100
Spectrum 20	40.9	11.9	1.3	19.7	26.1	100
Spectrum 21	41.3	12.2	1.7	23.4	21.4	100

(b)

At% Spectrum Label	Al	Si	Mn	Fe	Cu	Total	Phase
Spectrum 1	49.7				50.3	100	η_2
Spectrum 2	49.2				50.8	100	η_2
Spectrum 3	49.3				50.7	100	η_2
Spectrum 4	71.7				28.3	100	(Al)+θ
Spectrum 5	70.9				29.1	100	(Al)+θ
Spectrum 6	70.1				29.9	100	(Al)+θ
Spectrum 7	73.8				26.2	100	(Al)+θ
Spectrum 8	73.4				26.6	100	(Al)+θ
Spectrum 9	73.3				26.7	100	(Al)+θ
Spectrum 10	92.4				7.6	100	(Al)+θ
Spectrum 11	93.3				6.7	100	(Al)+θ
Spectrum 12	93.4				6.6	100	(Al)+θ
Spectrum 13	80.8	7.7			11.5	100	Al-Cu-Si
Spectrum 14	79.7	7.8			12.5	100	Al-Cu-Si
Spectrum 15	76.9	10.2			12.9	100	Al-Cu-Si
Spectrum 16	92.1				7.9	100	(Al)+θ
Spectrum 17	93.3				6.7	100	(Al)+θ
Spectrum 18	42.7	11.5		16.5	29.3	100	Al-Cu-Fe-Si
Spectrum 19	41.0	12.2		22.4	24.4	100	Al-Cu-Fe-Si
Spectrum 20	41.5	12.1		20.0	26.4	100	Al-Cu-Fe-Si
Spectrum 21	42.0	12.4		23.8	21.8	100	Al-Cu-Fe-Si

Figure 6-27: (a) Raw data and (b) simplified data from the SEM/EDS spectrum analysis of the samples brazed using AA4043 ($AlSi_5$) welding wire alloy and CMT standard (D12).

The black region is mainly η_2 phase instead of the dual phase of η_2 and γ_2 in equally proportion as observed in the previous sample. According to the binary Al-Cu phase diagram η_2 corresponds to a phase with copper ranging from 49 to 51.5 at.% and in this case the elemental composition is higher than this and thus, this point falls in a mix of η_2 and γ_2.

Some structures were found within the yellow region and they are believed to be quaternary phases of Al-Cu-Fe-Si but as before, they have not been identified.

Figure 6-28 shows the sample brazed with $AlSi_{12}$ welding wire. By increasing the silicon content in the welding wire, long dendritic IMCs ($^1/_{10}$ (Al) + $^9/_{10}$ θ) are formed at the Al-Cu interface (represented in yellow in Figure 6-28). A distinct layer composed by a θ phase was found in this sample and it is represented in purple. The concentration of Si in this sample is significant and for this reason it was considered in the graphical representation of the IMCs. The blue and green zones have now about 11 at.% of Si mixed and for this reason ternary Al-Cu-Si

phases might be present. However, these phases could not be identified since the existent ternary phase diagrams are either for liquidus projection or for high concentration of Cu. If Si is excluded from the analysis then the IMCs are very similar to the ones previously discussed. A new region represented in orange was included in this diagram containing in average 49 at.% of Si. This layer is located between the long dendritic IMCs and the green region.

This sample is by far the one with more IMC formed in the aluminium layer. The only difference between this sample and the previous is the Si content which is 12 at.% instead of 5 at.%. These results suggest that IMC formation is favoured by the presence of Si and the reason can be the thermal cycle or related to the diffusion of the elements. These results are different from the ones reported by Mai et. al. The authors have produced successful joints by pulsed laser welding between pure copper and AA4047 without filler material (Mai and Spowage, 2004). The Al-Cu IMCs were not found in the fusion zone and the composition across the fusion zone was uniform with the following elemental composition: 48%Al + 24%Si + 27%Cu which is apparently a solid solution and the microhardness at the Al-Cu interface was about 250 HV. One possible reason for the different results can be associated with the welding process. When comparing to arc welding, laser pulsed welding permits a faster cooling and solidification of the molten pool and the heat transferred to the work piece is lower.

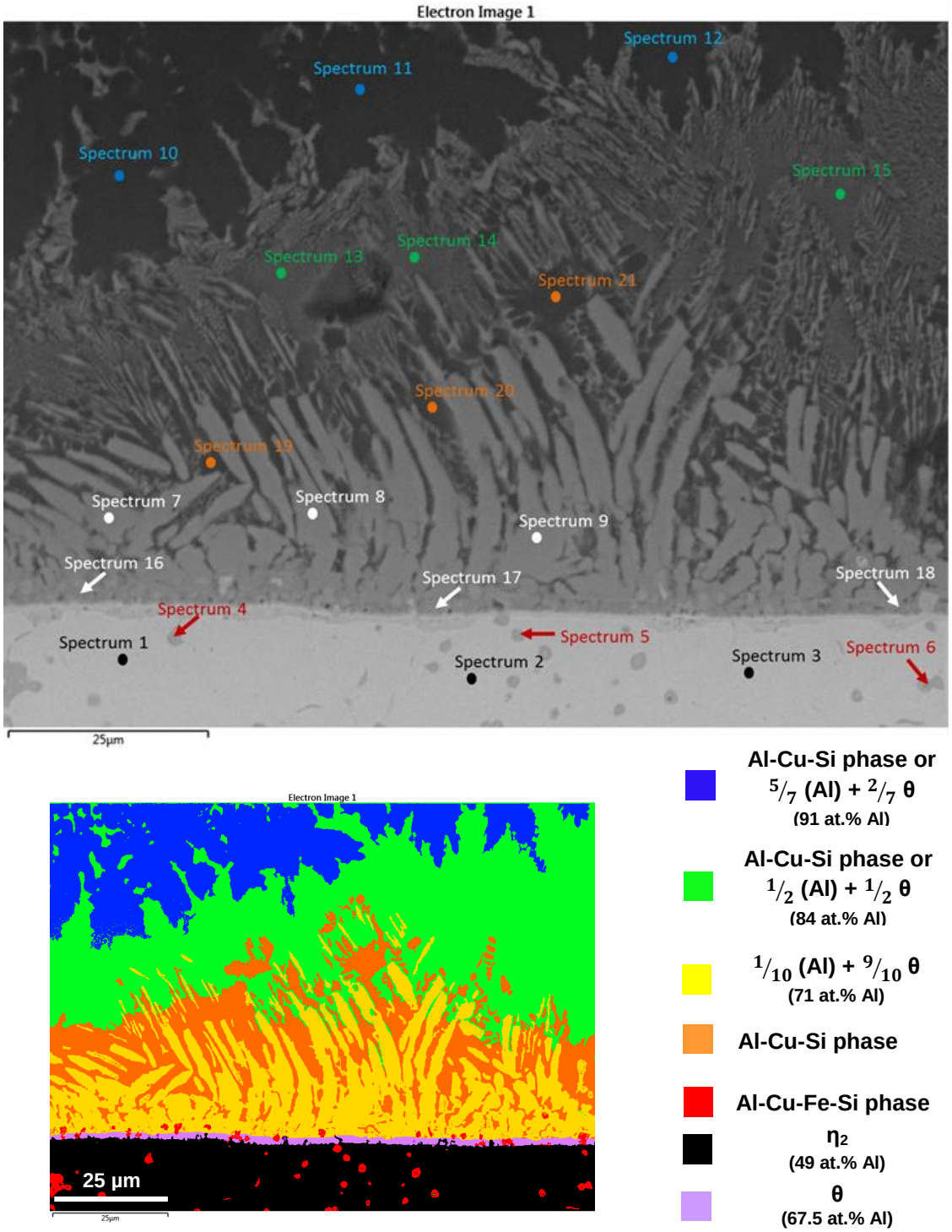

Figure 6-28: SEM-EDS image and schematic representation of the phases formed on the samples brazed using AA4047 ($AlSi_{12}$) welding wire alloy and CMT standard (D5).

(a)

At% Spectrum Label	Al	Si	Mn	Fe	Cu	Total
Spectrum 1	45.8	5.5	0.6	1.8	46.2	100
Spectrum 2	44.9	5.2	0.4	1.8	47.7	100
Spectrum 3	45.0	5.5	0.7	1.6	47.2	100
Spectrum 4	40.7	12.8	1.5	22.0	23.0	100
Spectrum 5	42.6	11.0	0.6	19.2	26.6	100
Spectrum 6	40.3	12.4	1.2	19.4	26.8	100
Spectrum 7	66.2	6.0	0.3	1.4	26.2	100
Spectrum 8	66.0	5.9	0.3	1.4	26.4	100
Spectrum 9	65.7	5.4	0.3	1.2	27.5	100
Spectrum 10	79.8	11.3	0.2	0.4	8.3	100
Spectrum 11	80.2	11.6	0.2	0.4	7.6	100
Spectrum 12	82.3	9.1		0.4	8.2	100
Spectrum 13	74.7	9.4	0.3	0.8	14.9	100
Spectrum 14	74.8	10.0	0.3	0.8	14.0	100
Spectrum 15	75.5	9.8	0.2	0.7	13.8	100
Spectrum 16	62.1	6.0	0.7	2.3	28.9	100
Spectrum 17	62.6	5.2	0.4	1.4	30.4	100
Spectrum 18	60.9	6.4	0.4	1.7	30.6	100
Spectrum 19	41.6	43.3		0.8	14.2	100
Spectrum 20	40.3	46.3		0.7	12.8	100
Spectrum 21	32.1	58.1	0.2	0.6	9.0	100

(b)

At% Spectrum Label	Al	Si	Mn	Fe	Cu	Total	Phase
Spectrum 1	49.8				50.2	100	η_2
Spectrum 2	48.4				51.6	100	η_2
Spectrum 3	48.8				51.2	100	η_2
Spectrum 4	41.3	13.0		22.3	23.3	100	Al-Cu-Fe-Si
Spectrum 5	42.9	11.0		19.3	26.8	100	Al-Cu-Fe-Si
Spectrum 6	40.8	12.5		19.6	27.1	100	Al-Cu-Fe-Si
Spectrum 7	71.6				28.4	100	(Al)+θ
Spectrum 8	71.4				28.6	100	(Al)+θ
Spectrum 9	70.5				29.5	100	(Al)+θ
Spectrum 10	80.3	11.4			8.4	100	Al-Cu-Si
Spectrum 11	80.7	11.7			7.6	100	Al-Cu-Si
Spectrum 12	82.6	9.2			8.2	100	Al-Cu-Si
Spectrum 13	75.5	9.5			15.0	100	Al-Cu-Si
Spectrum 14	75.6	10.1			14.2	100	Al-Cu-Si
Spectrum 15	76.2	9.9			13.9	100	Al-Cu-Si
Spectrum 16	68.2				31.8	100	θ
Spectrum 17	67.4				32.6	100	θ
Spectrum 18	66.5				33.5	100	θ
Spectrum 19	42.0	43.7			14.3	100	Al-Cu-Si
Spectrum 20	40.5	46.6			12.9	100	Al-Cu-Si
Spectrum 21	32.4	58.6			9.1	100	Al-Cu-Si

Figure 6-29: (a) Raw data and (b) simplified data from the SEM/EDS spectrum analysis of the samples brazed using AA4047 ($AlSi_{12}$) welding wire alloy and CMT standard (D5).

Figure 6-30 and Figure 6-31 shows the microstructure of the sample welded with AA5087 aluminium welding wire which contains magnesium as the main alloying element and the SEM/EDS spectrum analysis. The IMC phases and their distribution across the sample are very similar to the samples welded with Cu and 5% Si based wires (Figure 6-24 and Figure 6-26). However, there is a thin layer at the Cu-Al interface represented in pink which is composed of 7 at.% of Si, 53 at.% of Al and 40 at.% of Cu. Ternary phases may be existent but if Si is excluded then the phase is $^2/_5\ \theta + {}^3/_5\ \eta_2$.

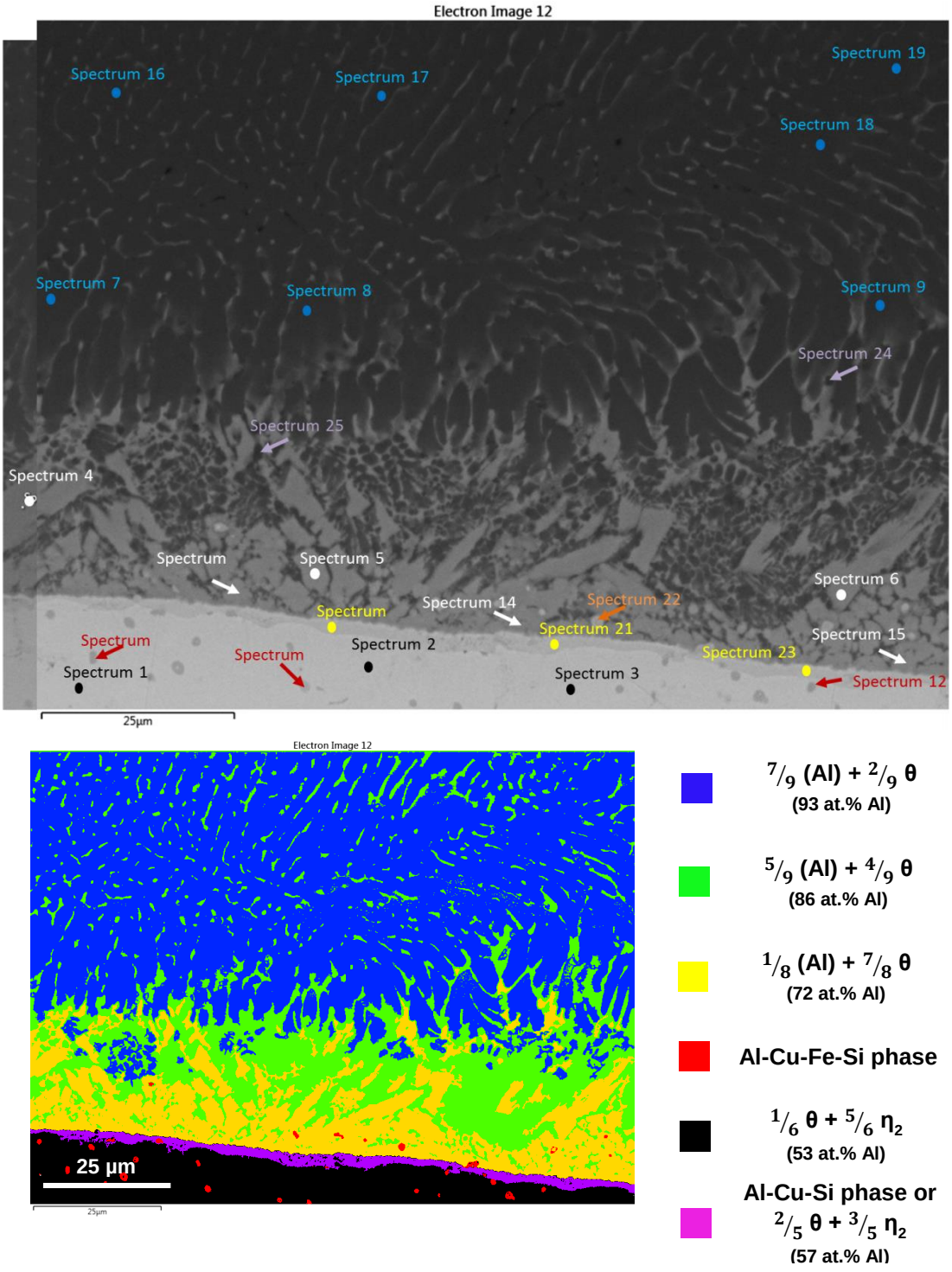

Figure 6-30: SEM-EDS image and schematic representation of the phases formed on the samples brazed using AA5087 (AlMg) welding wire alloy and CMT standard (D34).

(a)

At% Spectrum Label	Al	Si	Mg	Mn	Fe	Cu	Total
Spectrum 1	46.0	3.8	3.2	0.9	1.3	44.8	100
Spectrum 2	49.5	2.5	3.4	0.6	1.3	42.7	100
Spectrum 3	49.0	2.5	3.4	0.7	1.4	43	100
Spectrum 4	70.0	1.0	2.8	0.3	0.7	25.2	100
Spectrum 5	68.5	1.3	3.2	0.4	0.7	25.9	100
Spectrum 6	69.6	1.0	3.1	0.3	0.8	25.2	100
Spectrum 7	87.3		3.8	0.5	0.4	8.0	100
Spectrum 8	88.0		3.5	0.4	0.4	7.7	100
Spectrum 9	87.5		3.6	0.4	0.4	8.1	100
Spectrum 10	43.6	9.6	2.7	1.3	16.9	25.9	100
Spectrum 11	44.3	8.0	2.9	1.2	8.5	35.1	100
Spectrum 12	45.1	8.8	3.1	1.0	18.3	23.7	100
Spectrum 13	66.6	1.5	3.0	0.6	1.3	27	100
Spectrum 14	66.3	1.5	2.9	0.6	1.1	27.6	100
Spectrum 15	66.7	1.6	3.1	0.6	1.2	26.8	100
Spectrum 16	88.8		4.4	0.4	0.3	6.1	100
Spectrum 17	89.1		4.0	0.4	0.4	6.1	100
Spectrum 18	88.6		4.2	0.4	0.4	6.4	100
Spectrum 19	88.9		4.5	0.4	0.4	5.8	100
Spectrum 20	50.9	6.3	2.9	0.8	1.4	37.7	100
Spectrum 21	50.1	6.7	3.5	0.8	1.1	37.8	100
Spectrum 22	50.0	9.0	3.1	1.1	17.2	19.7	100
Spectrum 23	51.0	6.6	3.2	0.7	1.4	37	100
Spectrum 24	81.4	2.2	4.9	0.5	0.4	10.7	100
Spectrum 25	74.8	3	7.2	0.4	0.5	14.2	100

(b)

At% Spectrum Label	Al	Si	Mg	Mn	Fe	Cu	Total	Phase
Spectrum 1	50.6					49.4	100	η_2
Spectrum 2	53.7					46.3	100	$\eta_2+\xi_2$
Spectrum 3	53.3					46.7	100	$\eta_2+\xi_2$
Spectrum 4	73.6					26.4	100	(Al)+θ
Spectrum 5	72.6					27.4	100	(Al)+θ
Spectrum 6	73.4					26.6	100	(Al)+θ
Spectrum 7	91.6					8.4	100	(Al)+θ
Spectrum 8	92.0					8.0	100	(Al)+θ
Spectrum 9	91.6					8.4	100	(Al)+θ
Spectrum 10	45.5	10.0			17.6	26.9	100	Al-Cu-Fe-Si
Spectrum 11	46.2	8.3			8.8	36.6	100	Al-Cu-Fe-Si
Spectrum 12	47.0	9.2			19.0	24.8	100	Al-Cu-Fe-Si
Spectrum 13	71.1					28.9	100	(Al)+θ
Spectrum 14	70.6					29.4	100	(Al)+θ
Spectrum 15	71.3					28.7	100	(Al)+θ
Spectrum 16	93.5					6.5	100	(Al)+θ
Spectrum 17	93.6					6.4	100	(Al)+θ
Spectrum 18	93.2					6.8	100	(Al)+θ
Spectrum 19	93.8					6.2	100	(Al)+θ
Spectrum 20	53.7	6.6				39.7	100	Al-Cu-Si
Spectrum 21	53.0	7.1				40.0	100	Al-Cu-Si
Spectrum 22	52.2	9.4			17.9	20.5	100	Al-Cu-Fe-Si
Spectrum 23	53.9	7.0				39.1	100	Al-Cu-Si
Spectrum 24	88.4					11.6	100	(Al)+θ
Spectrum 25	84.1					15.9	100	(Al)+θ

Figure 6-31: (a) Raw data and (b) simplified data from the SEM/EDS spectrum analysis of the samples brazed using AA5087 (AlMg) welding wire alloy and CMT standard (D34).

In the literature it was found that direct laser pulsed welds of pure Al and pure Cu induced cracking in the fusion zone (Weigl et al., 2011). When using Al-Si_{12} welding wire the cracking was almost negligible and with $CuSi_3$ wire the cracking was still existent but less than between pure alloys. The authors attributed the improvement to the Si existent in the wire and said that the viscosity of the molten metal is decreased and thus, the turbulence is higher in the fusion zone and there are more fine IMCs dispersed into the weld instead of forming a layer at the Al-Cu interface. The results presented in this work do not show cracking across the weld bead but when the Si content increases not only are there more fine Al-Cu IMCs dispersed in the fusion zone but also a thicker layer at the Al-Cu interface is formed. One possible reason for the contradictory results could be related to the fact that the reported work was done in keyhole mode and thus, both metals were melted and formed the fusion zone whereas in the present work the copper remained solid and it was brazed by the molten aluminium. Therefore, there is a

distinct chemical gradient from copper-rich IMCs to the solid solution of Cu into Al.

The microhardness of the four samples in analysis was measured and the results are shown in Figure 6-32. One can see that all samples have similar microhardness distribution. There are two main areas near the Fe-Cu and Cu-Al interfaces where the microhardness is as high as 450 HV. This result was expected near the Al-Cu interface because in this region the reaction between elements was more intense and new phases were created. In turn, Fe and Cu do not form IMCs. One possible reason for the high hardness at the Cu-Fe interface can be related to the fact that these two elements are not 100% soluble in each other and therefore, maybe this is the reason why the hardness was equally high.

The microhardness in the steel substrate and the layer of copper ranges between 150 and 200 HV whereas the top layer of aluminium remains below 100 HV

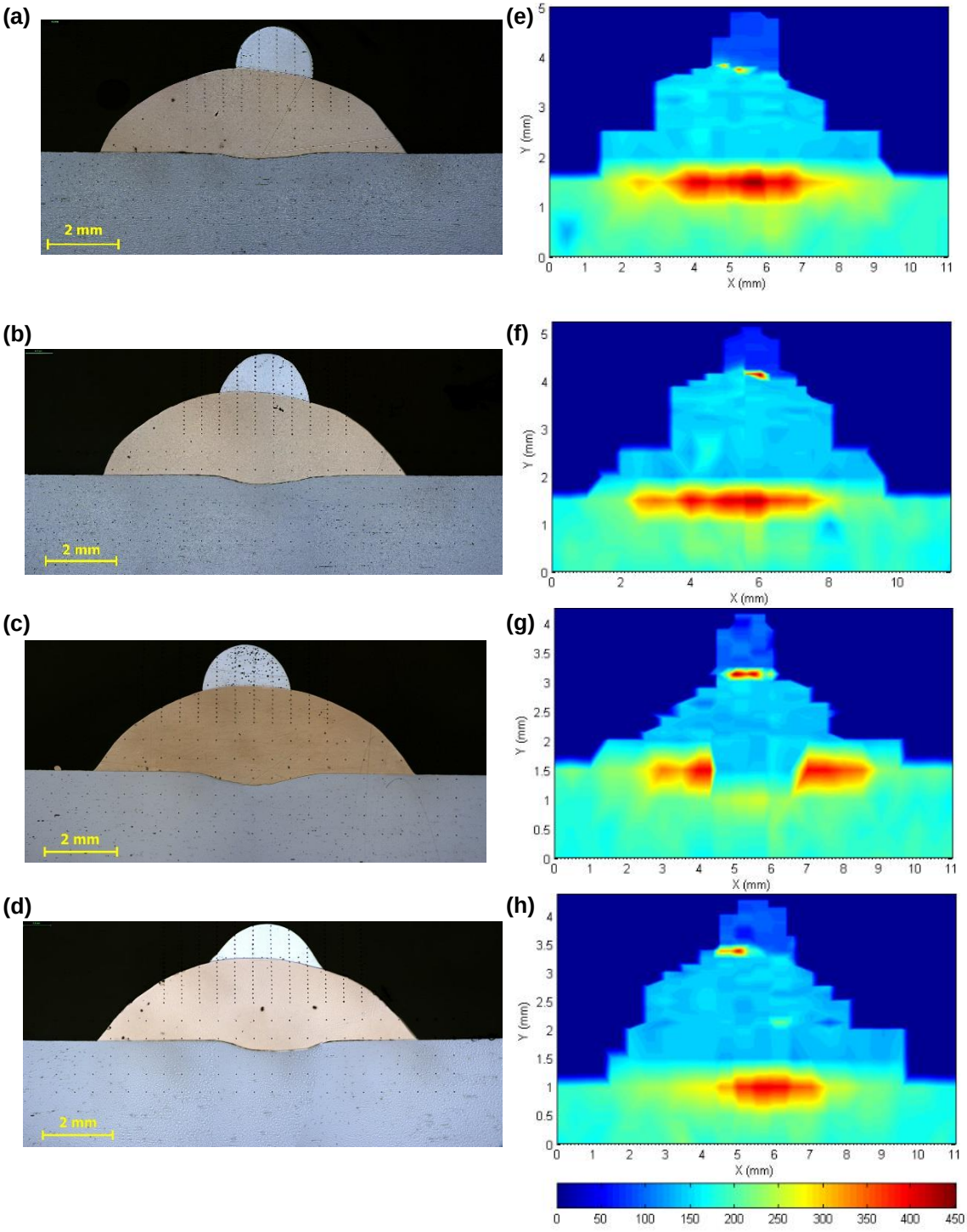

Figure 6-32: Macrographs (a)-(d) and mapping of the microhardness distribution (e)-(h) of the samples welded using AA2319, AA4043, AA4047 and AA5087 welding wires, respectively. Welding parameters: C0876 CMT welding mode, WFS = 5.0 m.min^{-1}, TS = 0.5 m.min^{-1}.

It is important to highlight that even though the microhardness distribution is not uniform across the samples, the maximum value measured was well below 1200 HV of the hardness measured in the Fe-Al joints.

6.4.3 Summary

The investigation of IMC formation when depositing four different grades of aluminium wire onto copper by CMT arc welding showed that:

- It was possible to produce sound welds with copper interlayer between steel and aluminium using CMT welding process;
- There is no benefit in using CMT advanced and advanced plus pulsed welding modes because the welds are discontinuous for the speed used and the Al-Cu IMCs are not avoided. The standard and pulsed CMT welding modes produce continuous weld seams but the first has lower arc energy which is beneficial to minimize the formation of IMCs
- Higher levels of WFS improves the wetting of aluminium on copper layer but the higher arc energy enhances the formation of IMCs;
- Al-Cu IMCs were identified in all samples and the majority were a mix of (Al) with ɵ phase on the aluminium layer and ɳ phase on the copper layer;
- Scattered Al-Cu-Fe IMCs were identified within the copper layer but they are not detrimental to the weld strength because of their morphology and distribution within the metal;
- The growth of the IMCs seems to be influenced by the composition of the welding wire. The minimum IMCs were observed for AA4043, followed by, AA5087, AA2319 and the largest area of IMCs was observed for AA4047 correspondent to the maximum Si content;
- There was no difference in the microhardness mapping in the samples brazed with different aluminium alloys. In the aluminium and copper layers the hardness ranged between 50 – 100 HV and 100 – 200 HV, respectively. The maximum value was measured at Fe-Cu and Cu-Al

interface and it was about 450 HV. The hardness was much lower than 1100 HV measured on direct welds of steel to aluminium.

6.5 Conclusions

Different methodologies were investigated in this chapter for the application of copper interlayer between steel and aluminium using laser welding and CMT welding. The aim was to use copper as physical barrier to prevent the reaction of Fe and Al. The feasibility of each methodology was assessed based on mechanical properties of the welds and supported by SEM and EDS analysis to determine the extension and identity of the IMCs. The following conclusions were taken from this work:

Application of copper interlayer in different forms using laser welding in conduction mode

- Mechanical strength of samples produced with copper interlayers is low (most of the samples broke during cutting)
- Foils of 25 µm and 150 µm can prevent the diffusion of Fe into Al near the edges of the fusion zone. However, in all welding conditions tested the foils were totally melted at the centre of the joint and Fe-Al IMC were formed.
- The best form of copper interlayer was with a welding wire inserted in a groove 0.4 mm deep. The joints were stronger and the copper was not completely melted. However, Fe-Al IMCs were found near the edges of the Cu wire
- To improve the mechanical strength of these joints the thickness of the interlayer must be optimized and the gap between the steel and the aluminium plates must be eliminated.

Deposition of $CuSi_3$ welding wire with CMT onto aluminium substrate

- CMT can be easily used to deposit copper onto aluminium and join steel to aluminium;

- If arc energy is controlled to a minimum level (less than 260 $J.mm^{-1}$) then it is possible to have only Al-Cu IMCs scattered in the fusion zone of aluminium whereas the copper weld bead is a solid solution of Al in copper;
- If the arc energy is too high (more than 260 $J.mm^{-1}$) then the copper weld bead is completely transformed in $AlCu_2$. In this case the weld is very brittle and cracking occurs.

Deposition of different grades of aluminium welding wire with CMT onto a layer of copper

- It is possible to weld aluminium onto copper and produce sound welds, with low formation of Al-Cu IMCs
- This technique minimizes the formation of Fe-Al IMCs. There are only scattered IMCs spread in the Cu layer;
- The hardness on the samples with copper interlayer was lower than that on direct joints of steel to aluminium, less than 400 HV compared to 1100 HV;
- The welding mode and wire feed speed are directly related to the arc energy and therefore, are important factors in the Al-Cu IMCs formation;
- The composition of the welding wire affects the formation of the Al-Cu IMCs. High Si content in the welding wire enhances the growth of the IMCs whereas the Mg and low Si content minimizes their formation. Higher Cu content in the aluminium layer when AA2319 welding wire is used enhances the growth of fine IMCs distributed.

7.0 Innovative design and laser welding process control for dissimilar metal processing of T-joints of steel to aluminium

In the previous chapters, successful lap welded joints with steel positioned on the top of aluminium were investigated, for which the maximum tensile load was more than 30 kN. The Fe-Al IMC layer thickness and the bonding area were correlated to the mechanical strength of the joints for different laser welding conditions. In the present section the aim is to join steel to aluminium in a T-joint configuration and to use a similar welding technique in addition to an innovative design, aiming to maximize the mechanical strength of this joint. This process could be an alternative solution for the Triclad® bar (Tricarico et al., 2009), i.e. the transition joint used to join dissimilar metals with thick sections, and could benefit in processing time and cost. It is shown that a T-joint having a groove on the flat plate where the vertical plate is inserted has a better resistance at tension than the traditional T-joint configuration. The power density and interaction time were adjusted to this new joint configuration to ensure that the laser was in conduction mode and the bonding occurred between solid (Fe) – liquid (Al) phases. The combination of the laser welding strategy with the innovative design for the T-joint enables an improvement on the mechanical strength.

The objectives of this work are as follows:

- Use an alternative joint design to produce Fe-Al T-joints without the Triclad bar and to apply the methodology previously used to produce laser welded Fe-Al joints in a lap joint configuration. For this to be possible, the steel (horizontal plate) will have a groove in which the aluminium plate will be inserted.
- Assess the joint integrity and quality in terms of cracking, porosity and IMC layer formation under different welding conditions (power density and interaction time).

7.1 Experimental procedure

7.1.1 Material

Low-carbon steel (grade DH36) and AA5083-H22 aluminium alloy plates with 6 mm thickness were used. Both materials are used in shipbuilding. The chemical composition and mechanical properties of the materials are indicated in Table 7-1 and Table 7-2, respectively. The plate's dimensions were 250 mm long and 200 mm wide.

Table 7-1: Chemical composition of base metals.

Material	Elements (wt. %)												
	Al	Fe	C	Si	Mn	P+S	Ni	Ti	Cu	Mg	Zn	Cr	Other
DH36	0.035	Bal.	0.14	0.39	1.37	0.025	0.017	0.002	0.010	-	-	0.018	0.031
5083-H22	Bal.	0.400	-	0.400	0.500	-	-	0.150	0.100	2.600 - 3.600	0.200	0.300	-

Table 7-2: Mechanical properties of the base materials.

Material	Yield strength [MPa]	Ultimate tensile strength [MPa]	Total elongation [%]
DH36	355	490 - 620	22 (at 50 mm of gauge length)
5083-H22	250	337	8

Before welding the steel plates were ground to remove the coating protection and degreased with acetone, whereas the aluminium plates were linished to remove the oxide layer (alumina) and cleaned with ethanol.

A 6.2 mm wide and 4.0 mm deep groove was machined at the centre of each steel plate into which the aluminium plate was tightly inserted.

7.1.2 Methodology and Experimental Setup

Laser conduction welding of steel to aluminium was previously studied in a lap-joint configuration. The welding parameters were adjusted so that the steel remained solid at the joint interface and only the aluminium was melted during the process, as represented in Figure 7-1. In this work an identical joining principle was applied to the T-joint configuration (see Figure 7-1).

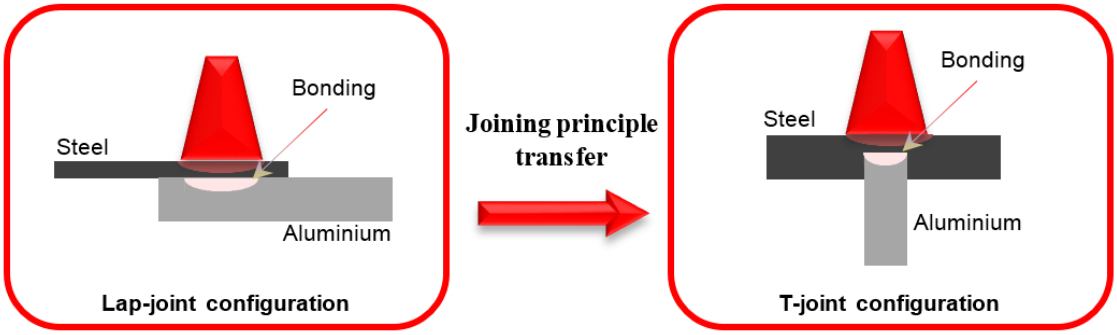

Figure 7-1: Schematic representation of laser conduction welding of steel to aluminium transfer from lap-joint to T-joint configuration.

In order to transfer the study done in lap joint configuration to the new T-joint configuration it was necessary to take into consideration the joint design. The T-joint design should allow the weld to be done with the laser in conduction mode, with steel positioned onto the aluminium and a 2 mm thick steel to produce solid-liquid interface between steel and aluminium during the joining process. Moreover, the brittle IMC layer formed at the joint interface requires a T-joint with a minimum stress at this point. Researchers have investigated the distribution of the intensity of stresses developed during tensile testing in different joint designs of brazed T-joints (Tsumarev et al., 2014). They have showed that the maximum stresses on the brazed joint are 48% lower when the vertical plate is inserted in a rectangular groove machined in the horizontal plate than when a standard T-joint is used. Further improvement is still possible if fillet welds are used instead of the groove. In this situation the stresses in the brazed joint are reduced approximately 30% in comparison with the joints with the groove.

The clamping system was designed to permit the laser to irradiate the top of the steel plate and produce a seam weld along the plate between the steel and the aluminium (see Figure 7-2). The bolts tighten with a torque wrench along the top plate to ensure constant pressure along the joint and virtually zero gap between the steel and the aluminium plates which is important for an effective heat transfer from the steel to the aluminium plate.

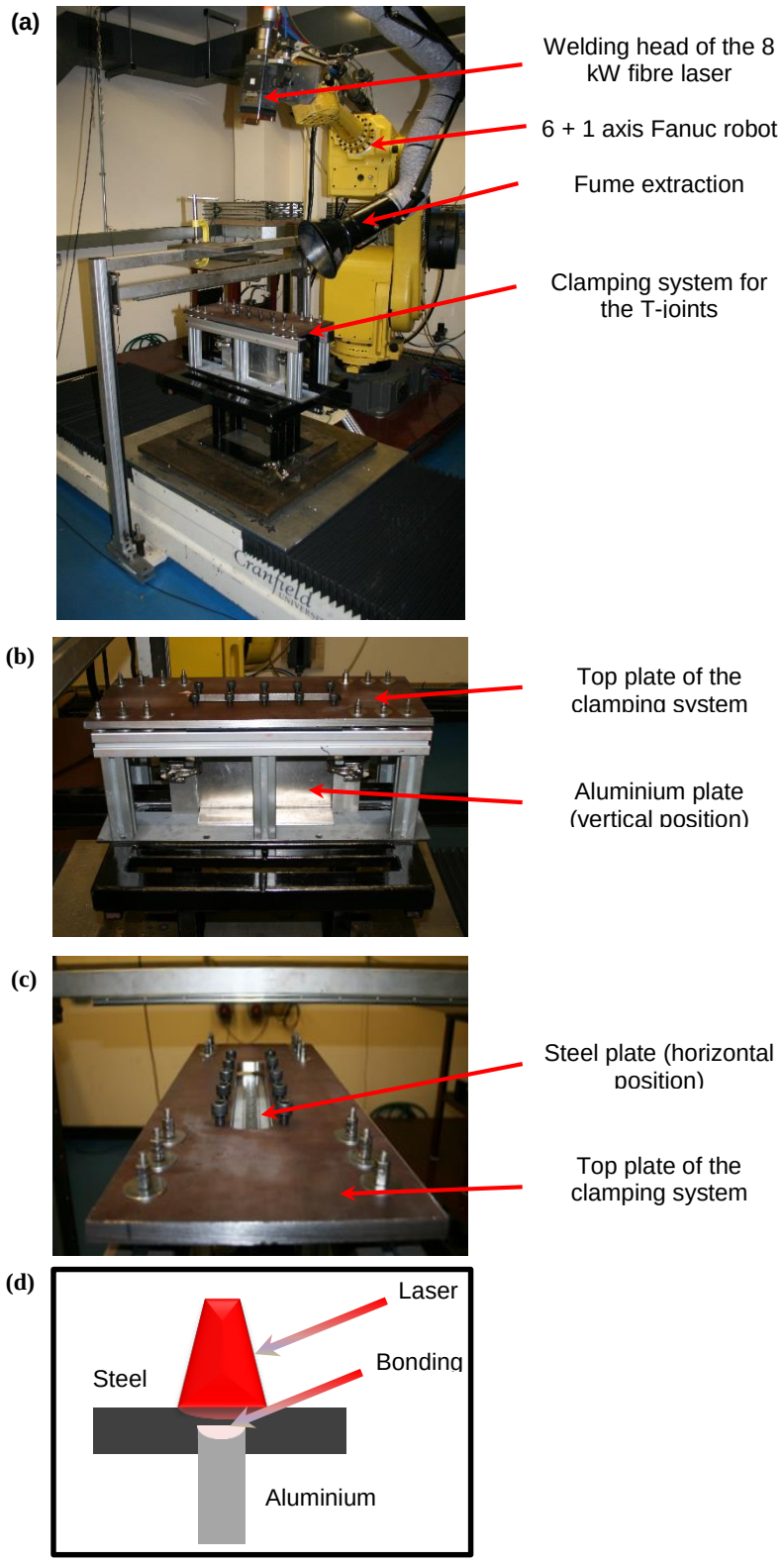

Figure 7-2: Experimental setup for laser welding of steel to aluminium in a T-joint configuration. (a) General view of the setup, (b) lateral and (c) top view of the clamping system and (d) schematic representation of the welding process.

No welding flux or shielding gas was used during the experimental work. The welding flux would create a thermal barrier between the steel and the aluminium plates which could be detrimental to the joining process. The use of the shielding gas is not required in this joint configuration because the weld is mechanically protected.

The same laser was used in these experiments (see details in section 2.3.3). All the tests were carried out with constant and defocused laser beam diameter of 13 mm. In the previous chapters it was found that a balance between IMC layer thickness and bonding area is required to achieve a strong joint. The thermal model showed that the power density is responsible for a much higher change in temperature than the interaction time. Even though a thicker IMC layer is formed when processing with higher temperatures there is also the advantage of creating a larger bonding area. Based on these findings, the laser parameters were chosen so that the specific point energy was similar but the power density was higher. The welding parameters can be found in Table 7-3.

Table 7-3: Welding parameters for Fe-Al T-joints.

Test no.	System parameters		Fundamental material interaction parameters		
	Laser power, kW	Travel speed, $m.min^{-1}$	Power density, $MW.m^{-2}$	Interaction time, s	Specific point energy, kJ
T5	5.5	0.50	41.44	1.56	8.58
T6	5.0	0.40	37.67	1.95	9.75
T7	5.0	0.33	37.67	2.36	11.82
T8	5.0	0.50	37.67	1.56	7.80
T9	5.5	0.40	41.44	1.95	10.73
T10	6.5	0.50	48.97	1.56	10.14
T11	5.0	0.50	37.67	1.56	7.80
T12	6.5	0.50	48.97	1.56	10.14
T13	5.0	0.33	37.67	2.36	11.82
T14	6.0	0.40	45.20	1.95	11.70
T15	6.0	0.50	45.20	1.56	9.36

7.1.3 Metallurgical characterization

For macrostructure and microstructure observations of the joint, two samples were taken across the 230 mm long weld seam (Figure 7-3).

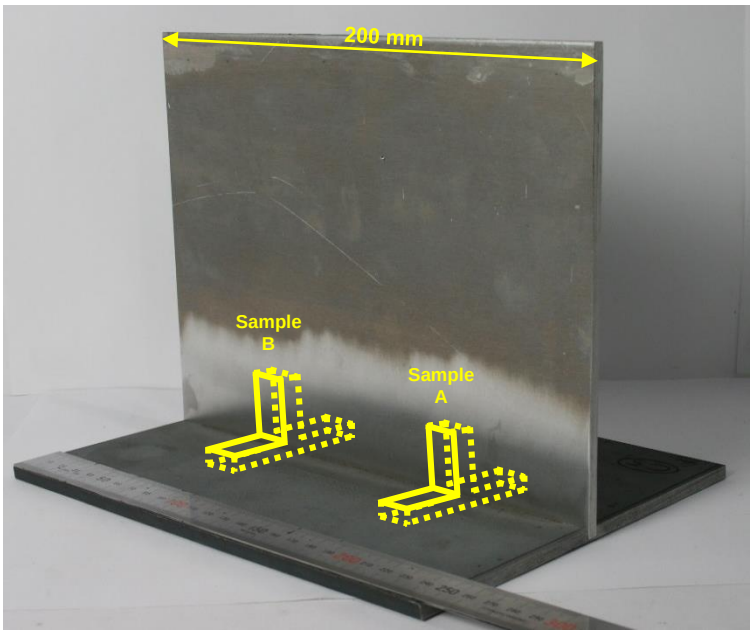

Figure 7-3: Schematic representation of the position where the samples for metallographic analysis were machined out from the T-joint.

The samples were ground and polished according to standard procedure (see section 2.3.4). Micrographs of the cross-section were taken with the lowest magnification of the optical microscope (2.5x objective) to investigate major defects on the weld, such as porosity or cracking. Microsoft ICE (Image Composite Editor) software was afterwards used to compose the whole macrograph of the T-joint (see Figure 7-4).

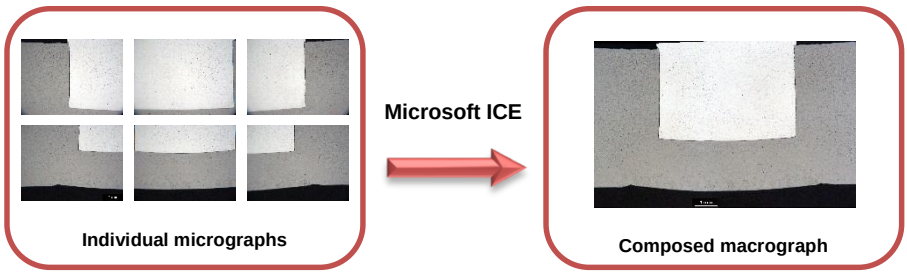

Figure 7-4: Composition of individual micrographs into a macrograph using Microsoft ICE software.

For the microstructure analysis nine micrographs with a magnification of 40x were taken along the joint using an optical microscope.

7.2 Results and discussion

The results presented in this section refer to the cross-sections of the T-joints.

7.2.1 Macrostructural analysis – Weld aspects

Laser conduction welding of steel to aluminium has successfully been transferred from the lap-joint configuration to the T-joint (see Figure 7-5). The weld seams along the joints were uniform, no defects were observed and no gaps between the steel and the aluminium were visible. The groove machined on the steel plate seems to favour the Fe-Al joint strength. A small distortion on the steel plate was observed in all samples after welding causing a mechanical lock of the aluminium plate. This effect was found to be beneficial to the integrity of the joint since it contributes to a better clamping of the aluminium plate (vertical plate).

(a)

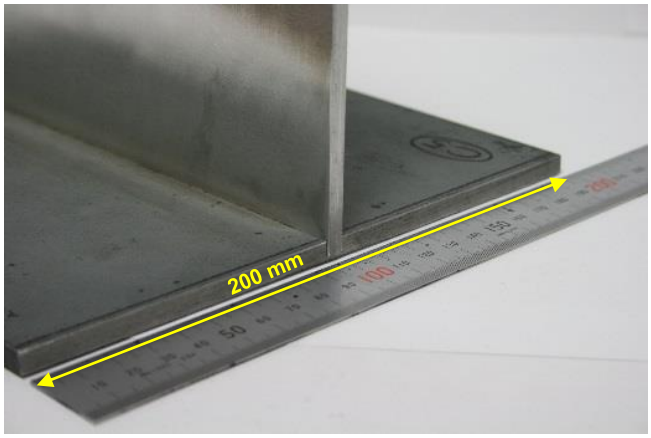

(b)

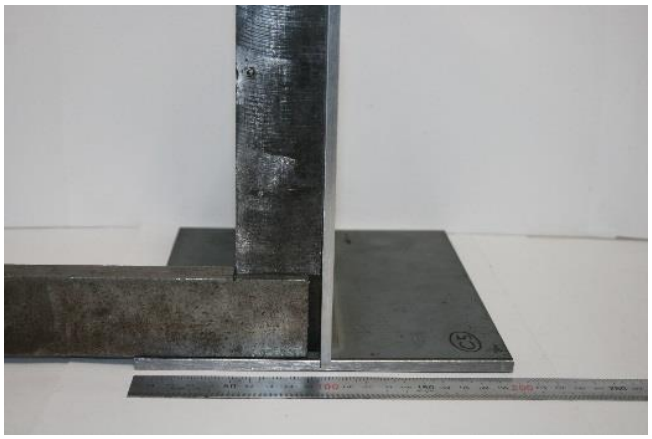

Figure 7-5: Pictures of dissimilar metal Fe-Al T-joints after laser welding in (a) perspective view and (b) side view.

The macrographs of the samples are shown in Table 7-4. One can see that there was more melting of the edge of the aluminium plate when the specific point energy was higher, either by increasing the power density or the interaction time. For instance, when the joint was produced with E_{sp} = 7.8 kJ the edge of the aluminium was completely flat. On the contrary, when higher levels of energy were used the edge of the aluminium plate became more round. This could indicate a more effective wetting of the groove by the molten aluminium and therefore stronger bonding. However, the joints produced with more energy were more susceptible to cracking at the Fe-Al interface. The tensile-compressive state at the Fe-Al interface resultant from the welding process could be the reason for the cracking along the joint interface. For this reason, the higher the energy level, the higher the cracking. On the other hand, no porosity was observed in any of the welded specimens.

Table 7-4: Cross-sectional view of Fe-Al T-joints welded with different welding parameters.

		PD, MW.m^{-2} (P, kW)			
		37.7 (5.0)	**41.4** (5.5)	**45.2** (6.0)	**49.0** (6.5)
t_i, s (TS, m.min^{-1})	**1.56** (0.50)	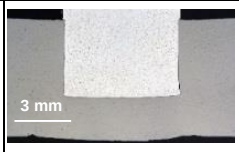 (E_{sp}=7.8 kJ)	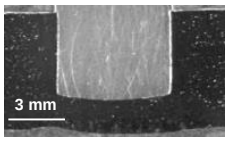 (E_{sp}=8.6 kJ)	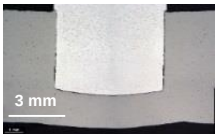 (E_{sp}=9.4 kJ)	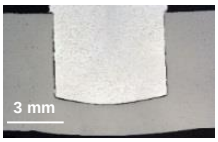 (E_{sp}=10.1 kJ)
	1.95 (0.40)	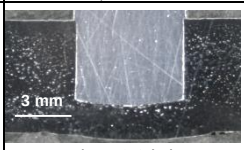 (E_{sp}=9.8 kJ)	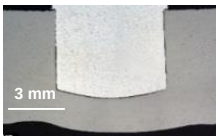 (E_{sp}=10.7 kJ)	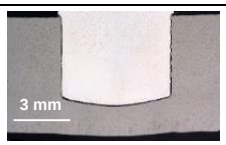 (E_{sp}=11.7 kJ)	-
	2.36 (0.33)	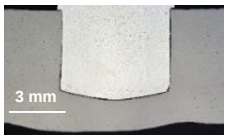 (E_{sp}=11.8 kJ)	-	-	-

However, there is one particular case corresponding to the joint welded with the minimum energy (E_{sp}=7.8 kJ) which showed good bonding between the steel and the aluminium (see Figure 7-6). At the edge of the aluminium plate where the bonding occurs, there is no cracking (this is observed in Figure 7-6 micrograph 3-C). This indicates a sound bonding between the two alloys. The mechanical lock resultant from the residual stresses is clear in micrographs 1-L and 1-R of the same figure. The corners of the groove (micrographs 3-L and 3-R) were filled with molten aluminium but there are still small gaps on the sides which require further improvement. A new design of the groove would be recommended to improve the flow of the molten aluminium and thus, improve the bonding between both metals. Lack of fusion/wetting is also observed on the sides of the groove (micrographs 2-L and 2-R). The small gap between the side of the groove and the aluminium plate forced the molten aluminium to flow upwards by capillarity. Rapid cooling of the molten aluminium happens when it touches the colder

surfaces. The micrograph 2-L in Figure 7-6 shows solidified aluminium between the steel and the aluminium gap, inside the groove.

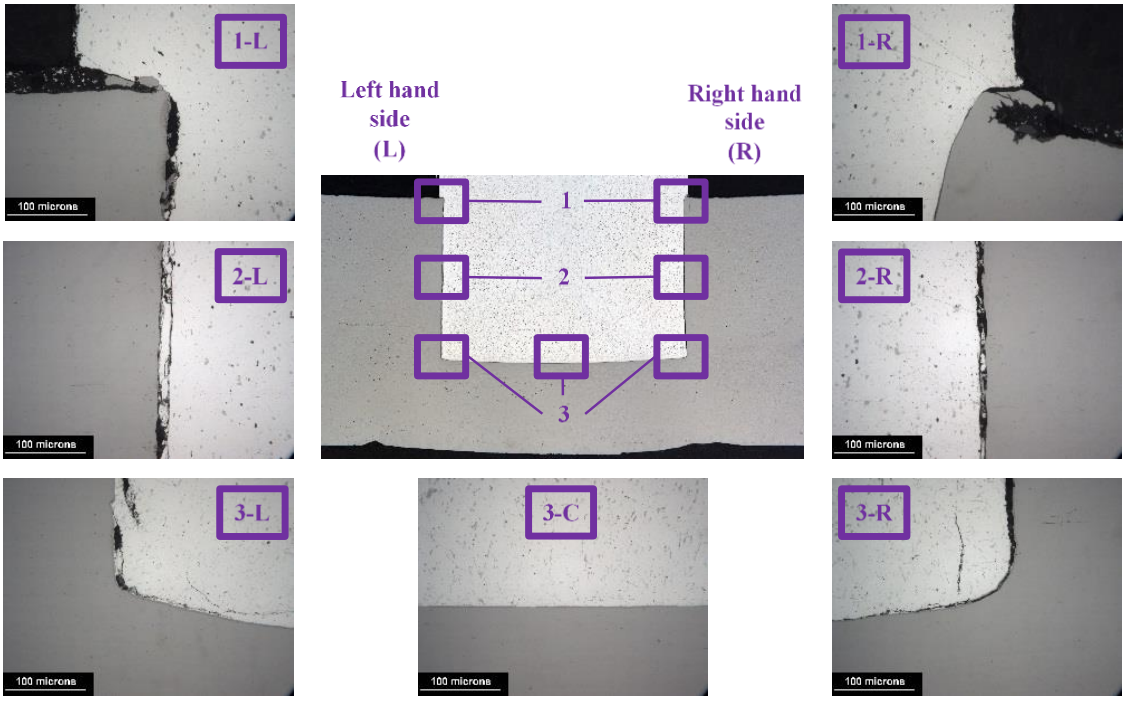

Figure 7-6: Micrographs of the Fe-Al interface at different positions - top, middle and bottom lines, at the centre, left and right hand side.

7.2.2 Microstructural analysis – IMC layer

Similar to what was previously observed in laser welding with the plates in overlap configuration and steel positioned on the top, in the T-joint configuration a continuous layer of IMCs was also formed (Meco et al., 2015)(Meco et al., 2014). In both joint configurations the energy of the process was controlled to produce partial melting of the steel and simultaneously melting of the aluminium. Under this condition the reaction between Fe and Al was restricted and the formation of the IMC was minimized. Table 7-5 shows the micrographs of the IMC layer at the bottom Fe-Al interface at the centre of the weld where the IMC layer is thicker (position 3-C).

Table 7-5: Micrographs of the Fe-Al T-joints welded with different welding parameters. Micrographs taken at position 3-C which corresponds to the centre of the Fe-Al interface.

		PD, MW.m^{-2} (P, kW)			
		37.7 (5.0)	**41.4** (5.5)	**45.2** (6.0)	**49.0** (6.5)
t_i, s (TS, m.min^{-1})	**1.56** (0.50)	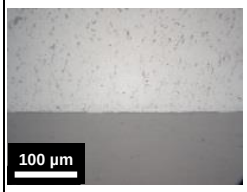 (E_{sp}=7.8 kJ)	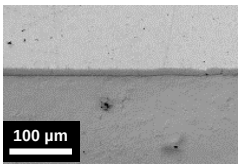 (E_{sp}=8.6 kJ)	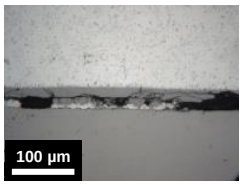 (E_{sp}=9.4 kJ)	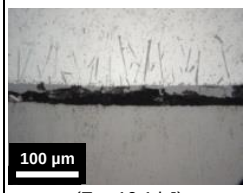 (E_{sp}=10.1 kJ)
	1.95 (0.40)	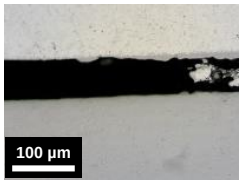 (E_{sp}=9.8 kJ)	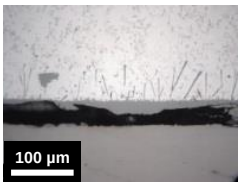 (E_{sp}=10.7 kJ)	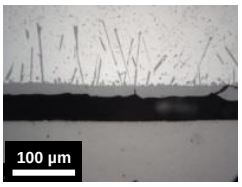 (E_{sp}=11.7 kJ)	-
	2.36 (0.33)	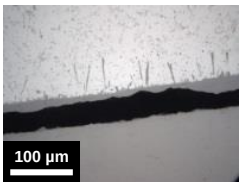 (E_{sp}=11.8 kJ)	-	-	-

The micrographs show that the IMC layer thickness grows as the specific point energy increases either via power density or interaction time. Similar behaviour was observed in laser conduction welding of steel to aluminium in lap-joint configuration, where the growth of this layer was studied with the variation of power density, interaction time and specific point energy.

The micrographs showed in Table 7-6 permit the comparison of the IMC layers formed in the T-joint and lap-joint configurations for similar welding conditions. Even though the IMC layer thickness was not measured in all the T-joint samples (due to the crack developed along the IMC layer) it seems that the IMC layer growth follows a similar trend to that found in the lap-joints. For both joint

configurations, the thickness of the IMC layer of the samples welded with the minimum energy was less than 5 µm. For higher value of energy, the IMC layer is thicker and shows the Fe_2Al_5 layer near the steel (with uniform thickness) and the irregular and needle shape $FeAl_3$ on the aluminium side. However, the $FeAl_3$ formed in the T-joint configuration was more irregular than that observed in the lap-joint. This may be due to different cooling rates existent in both joint configurations. In lap-joint configuration the contact area between the steel and the aluminium plates is larger than that in the T-joint configuration, 46 mm against 6 mm, respectively. Therefore, one would expect the cooling time to be longer in the T-joint configuration which allows the $FeAl_3$ phase to grow more.

Table 7-6: Comparison between the IMC layer formed in the lap-joint and T-joint configuration with similar welding conditions.

T-joint configuration								
P = 5 kW								
TS = 0.50 m.min^{-1}			**TS = 0.40 m.min^{-1}**			**TS = 0.33 m.min^{-1}**		
t_i=1.56 s	**PD=37.7 MW.m^{-2}**	**E_{sp}= 7.8kJ**	**t_i=1.95 s**	**PD=37.7 MW.m^{-2}**	**E_{sp}=9.8 kJ**	**t_i=2.36 s**	**PD=37.7 MW.m^{-2}**	**E_{sp}=11.8kJ**
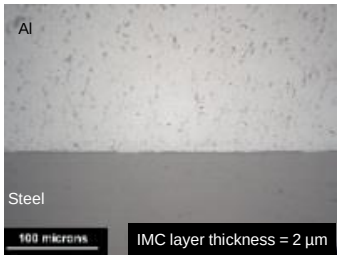			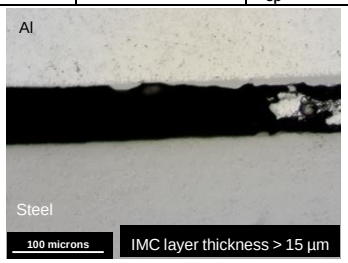			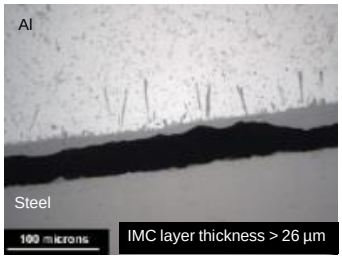		
Lap-joint configuration								
P = 5 kW								
TS = 0.40 m.min^{-1}			**TS = 0.35 m.min^{-1}**			**TS = 0.30 m.min^{-1}**		
t_i=1.95 s	**PD=37.7 MW.m^{-2}**	**E_{sp}=9.8 kJ**	**t_i=2.23 s**	**PD=37.7 MW.m^{-2}**	**E_{sp}=11.1kJ**	**t_i=2.60 s**	**PD=37.7 MW.m^{-2}**	**E_{sp}=13.0kJ**
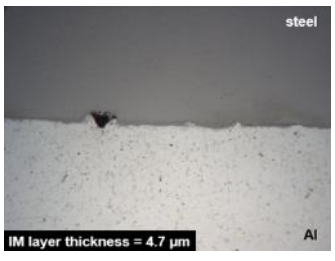						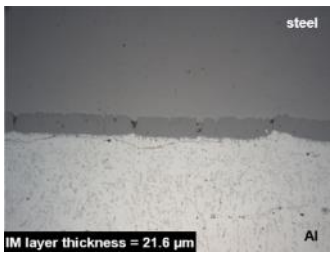		

The micrographs also show cracks along IMC layer only on the T-joints. The reason why the cracks are present in the T-joints is because in this joint

configuration there is a tensile-compressive state at the joint interface, between the steel and aluminium inside the groove, resultant from the welding process to which the brittle Fe-Al IMCs are not able to resist.

7.3 Summary

In this work the feasibility of producing sound dissimilar metal Fe-Al T-joints with laser conduction welding and joint design were studied. The methodology previously used to produce laser welded Fe-Al joints in lap joint configuration was applied to the new T-joint configuration. In order to transfer the methodology from the lap joint configuration to the T-joint in this new joint design it was required a groove on the steel plate (horizontal plate) in which the aluminium plate was inserted. Several welding parameters were tested and the cross-section of the joints were analysed. The results showed that:

- It is possible to transfer the technique of laser welding from lap-joint to T-joint configuration and still have the solid-liquid joint interface required to form a thin intermetallic compound layer;
- The intermetallic compound layer thickness found on the T-joints was similar to the lap-joints but with more cracking due to small distortion of the steel plate;
- The strength of the T-joints was improved due to the mechanical lock created by the residual stresses/distortion resultant from the welding process – Even though some samples were cracked at the Fe-Al interface the T-joints were still bonded;
- Defect free T-joints were produced with minimum power density (37.7 $MW.m^{-2}$) and interaction time (1.56 s). In this case the intermetallic compound layer thickness was less than 5 µm;
- In order to improve the wetting of molten aluminium on steel inside the groove and reduce cracking it is suggested further investigation of the groove geometry;

- This technique seems to be a feasible alternative to the Triclad transition joint. However, mechanical tests should be done to quantify the strength of the laser welded T-joints.

8.0 Conclusions and Future Work

The findings of the thesis are summarized and the most important points of the project are highlighted and discussed in this chapter. This section also contains a list of recommendations for future work which result from the experimental work presented in this thesis.

8.1 Thesis Summary

Joining of steel to aluminium is difficult not only because of the dissimilarities in thermo-physical properties of both metals but also due to the formation of brittle IMCs in the joint zone. The combination of these factors usually lead to joints with poor mechanical strength. Nowadays in shipbuilding a transition bar, half aluminium and half steel, is used in joining of thick plates of steel and aluminium. The transition bar is made by explosion bonding. The advantage associated with the use of the transition bar is the negligible formation of IMCs during the joining process. However, this bar brings additional cost, logistic issues and extra time to produce the 4 welds instead of the 2 needed to assemble the whole structure which could alternatively be done by direct joining of steel to aluminium.

The research in dissimilar metal joining is extensive and it has been focused either in the formation and growth of the IMC layer or in controlling the IMCs using different joining processes. Moreover, the majority of the research is focused in the automotive industry where thin materials are used. It was found that temperature at the joining interface and heating time are the main factors in the Fe-Al IMC layer growth.

Several methodologies were investigated in this work in an effort to understand and thus control the mechanism of formation of the IMCs and their effect on the mechanical properties of the dissimilar metal joints:

- **Effect of laser welding parameters on IMC formation and bond strength**

In the first stage of the project direct joining of steel to aluminium was investigated. Laser welding was used in this work because it permits good control of the energy transferred to the material and therefore, the thermal cycle applied to the substrate. In laser welding the heat source is concentrated in a small spot with high energy density therefore, the welds have a small heat affected zone. This process also gives high flexibility to produce different joint configurations and better control of the dilution of the metals.

The objective was to minimize the diffusion of Fe and Al atoms and thus, minimize the IMC formation. The joints were produced in a lap joint configuration with steel positioned on top. The heat resulting from the interaction of the laser with the steel was conducted through the thickness of the steel plate and induced melting of the aluminium near the interface whereby aluminium wets the steel surface creating bonding between the plates. The joint was produced by wetting the steel near the interface with molten aluminium.

Most of the researchers focused their research on the laser system parameters viz. the laser power (P), travel speed (TS), and spot size (D_{beam}) where the effect of spot size is often disregarded. These system parameters are interdependent and the variation in resulting thermal cycle is not a simple function of either of these parameters. This also may cause non-reproducibility of results due to difference in individual laser characteristics. In order to overcome this, power density (PD), interaction time (t_i), and specific point energy (E_{sp}) were introduced in this study as fundamental laser material interaction parameters (FLMIP), and the dependency of joint strength and IMC layer on the FLMIP was analysed. The FLMIPs are calculated based on the system parameters and correspond to the physical interaction of the laser energy with the material.

The study showed that a continuous layer was formed during laser welding between the steel and aluminium plates. The layer was composed of two distinct IMCs, Fe_2Al_5 near the steel side and $FeAl_3$ on the aluminium side. The study also showed that the IMC layer grows exponentially with the specific point energy

when the thickness is less than 20 µm. However, the growth became sluggish when the IMC layer was thicker than 20 µm.

The results suggested that a balance between area of wetting, or bonding area, and IMC layer thickness is required to produce a strong joint. The linearity between load and bonding area is not observed in the dissimilar metal joints due to the presence of the IMC layer. These factors are dependent of the thermal field generated during the welding process. Power density seems to be the parameter which most affects the growth of the IMC layer and the wetting area, whilst interaction time seems to have less contribution. A finite element (FE) thermal model developed to predict the thermal cycle in the centre of the weld and at the interface between the steel and aluminium plates showed that when power density rises, the peak temperature at the Fe-Al interface increases and the bonding area becomes larger. Simultaneously, the thermal cycle also enhances the growth of the IMC layer. The results also indicated that there is a trade-off between bonding area and IMC layer thickness on bond strength. In the mechanical tensile shear test all specimens had interfacial failure. However, the maximum strength measured was as high as 31 kN (600 $N.mm^{-1}$) and the specimen showed some amount of plasticity.

- **Study on the feasibility of using an interlayer of copper to prevent the Al-Fe reaction in laser welding of steel to aluminium**

An alternative methodology to produce sound dissimilar metal joints, instead of controlling the energy and the thermal cycle applied to the joint during the joining process, was to use a third material to create a bridge between the steel and the aluminium, the so called interlayer. Ideally, the interlayer should be compatible with both steel and aluminium in order to avoid the formation of IMCs. However, for this metallic combination there were only a few elements in this condition, for instance mercury, potassium, sodium or indium which were not suitable for welding or joining. The option was then to find one metal that was compatible either with Fe or Al. Copper was chosen because it does not form any IMC with Fe and even though it does with Al, Al also has partial solid solubility into Cu. Different forms of Cu interlayer (foils of 25 µm and 150 µm, copper bead

deposited onto the steel plate, copper welding wire positioned between the steel and aluminium plates or inserted in a groove 0.4 mm deep in the aluminium) were studied using similar laser welding setup. It was found that foils can prevent the diffusion of Fe into Al near the edges of the fusion zone. However, in all welding conditions the foils were totally melted at the centre of the joint which allowed diffusion of Fe and Al through the molten pool and therefore, Fe-Al IMCs were formed. The IMCs in these joints were more ductile than the Fe-Al IMCs previously studied (Fe-Al (Cu) IMCs with 759 HV and Al_2Cu with 454 HV against 1100 HV for Fe-Al IMCs). Binary and ternary Fe-Al-Cu IMCs were identified near the joint interface and for this reason the joints were weak. Possibly the heat of welding transmitted through the copper interlayer could not maintain the thermal gradient required to melt the aluminium without melting the copper interlayer. For this reason, the use of a copper interlayer in this joint configuration was found to be not effective in preventing the reaction between Fe and Al.

- **Study the feasibility of using an interlayer of copper to prevent the Al-Fe reaction in arc welding of steel to aluminium – copper deposited onto aluminium**

Aiming to understand the IMC formation between Cu and Al a variant of Gas Metal Arc Welding was used, Cold Metal Transfer, also known as CMT. Bead on plate welds were produced with Cu deposited onto Al. Since copper has a higher melting temperature than aluminium, when copper is deposited onto aluminium there is higher dilution of the two metals into each other. The objective was to investigate the effect of the energy (varied by wire feed speed and welding mode) on the Al-Cu IMC formation. Two different types of IMCs were identified in samples welded with different levels of energy. When welding with higher level of energy, the entire area of the weld bead was composed by $AlCu_2$. The weld bead showed large cracks due to the high brittleness of this IMC (up to 800 HV). However, when the energy was low, the weld bead was mainly composed of solid solution of Al into Cu and there was only a layer of Al_2Cu precipitates spread in aluminium. In terms of mechanical strength, as mentioned before, the Al-Cu IMCs

are less harmful than Fe-Al IMCs because the hardness is lower and they are dispersed in the weld.

- **Study the feasibility of using an interlayer of copper to prevent the Al-Fe reaction in arc welding of steel to aluminium – aluminium deposited onto copper**

The hypothesis in this study was that less IMCs would be formed when Al was deposited onto Cu than if the deposition was done with Cu onto Al. The objective was to investigate the effect of the energy (varied by wire feed speed and welding mode) and composition of the Al wire on the Al-Cu IMC formation. Aluminium wires containing 5% Si, 12% Si, Mg and Cu were used. It was found that the Al-Cu IMC growth is enhanced by using aluminium wire with higher Si content and by welding with higher energy (higher wire feed speed). Even though the thickness of the Al-Cu IMC layer is much bigger than that of the Fe-Al IMC layer, the microhardness measurements showed that the maximum hardness on the Al-Cu samples was about 400 HV and it was located not only at the Al-Cu interface but also at the Cu-Fe interface. This value was well below 1100 HV characteristic from the Fe-Al joints. In terms of joint configuration, it is beneficial to use Cu onto Al instead of Al onto Cu. In both configurations the formation of Al-Cu IMCs was not avoided and by using copper filler wire it is possible to weld directly steel to aluminium in a T joint configuration, instead of creating two layers, first Cu and then Al. However, for this configuration the heat input of the process must be kept low to prevent cracking of the weld seam due to the formation of $AlCu_2$.

- **Joint design and joining of T joints of steel and aluminium by laser welding**

At the final stage of the project the methodology investigated in a lap joint configuration was applied to T-joint configuration. In this stage an alternative joint design was proposed and tested according to the welding process in use. Successful T joints were produced with autogenous laser welding. Even though cracking was observed along the IMC layer when higher levels of energy were

used, the joints were still strong due to the mechanical lock effect caused by the small distortion resultant from the welding process. For lower levels of energy the IMC layer was less than 5 µm and showed similar characteristics to those observed in the lap-joint.

The main conclusions of this work were:

- Good control of the IMC layer thickness by autogenous laser welding (4 µm up to 29 µm);
- Autogenous laser welding is not enough to prevent interfacial failure of joints with thick sections however the joints had a maximum load capacity of 31 kN and showed some plasticity;
- The thermal cycle during welding is extremely important for the mechanical strength of the dissimilar metal joints, i.e. to maximise the bonding contact and minimise the formation of IMCs on the joint interface;
- Care must be taken when using interlayers to prevent the reaction between Fe and Al. The success of the interlayer relies on the welding process in use and on the form of the interlayer. Copper interlayer between Fe and Al cannot be use in laser welding but may be used in CMT welding to joint Fe to Al as fillet welds;
- Joint design is extremely important in dissimilar metal joining. The joint strength increases significantly if the stress is minimized on the IMC layer.

The most relevant points of the thesis were:

- Extension of the investigation of dissimilar metal joining of steel to aluminium using laser welding for thick materials and characterization of the IMC growth based on the fundamental laser material interaction parameters;
- Development and optimization of the clamping system for laser welding of steel to aluminium in a lap-joint and T-joint configurations;
- Development of the FE thermal model to predict the thermal field at the joint interface, where the reaction between Fe and Al takes place;
- Investigation of the viability of using copper as transition metal between steel and aluminium in laser and CMT welding;

- Application of the knowledge acquired in laser welding of steel to aluminium in lap-joint configuration to the required T-joint configuration.

8.2 Recommendations for Future Work

The following points were identified as relevant for future investigation within the scope of dissimilar metal joining of steel to aluminium.

- **Development of the thermal model for laser welding of steel to aluminium for different laser beam diameter**

In the present work it has been presented a FE thermal model that has been developed to predict the thermal cycle at the Fe-Al interface where the IMC layer is formed and grows. This model has been tested and used for a single laser beam diameter (13 mm). For a better understanding of the influence of the laser beam diameter on the thermal cycle and thus on the joint characteristics it would be interesting to have a thermal model built for a range of beam diameters. For the development of the new thermal models, it would be necessary to measure the thermal profile of a few lap joints during laser welding process with different beam diameters (according to the procedure presented in section 4.0). The acquired data would be used for the validation of the new thermal models.

- **Joint design**

Lack of wetting was one of the problems found in autogenous laser welding of steel to aluminium in a T-joint configuration, in which the aluminium plate was inserted inside a groove machined in the steel. Therefore, a further investigation on the joint design, focused on the geometry of the groove, should be carried out to address this issue.

CMT welding process with either $CuSi_3$ or aluminium welding wire to produce fillet welds could also be tested.

In the future, autogenous laser welding, CMT welding or even both welding processes simultaneously could be investigated to improve the mechanical

strength of the Fe-Al T-joints. Figure 8-1 shows three examples of alternative joint designs for the T-joint made of steel and aluminium. Figure 8-1a combines both laser and CMT welding in which the first stage is to weld the edge of the flange to the web of the stiffener with the laser and the second stage is to do two fillet welds with copper welding wire using the CMT welding process to reinforce the joint. The second design proposed in Figure 8-1b requires autogenous laser to weld the sides of the stiffener using the same principle described in this manuscript (section 2.3.1). The alternative represented in Figure 8-1c suggests the use other welding wires which even though are not metallurgically compatible with both Fe and Al, they still have a minimum solubility in one of the elements. In this study either laser and cold wire or CMT welding processes may be used.

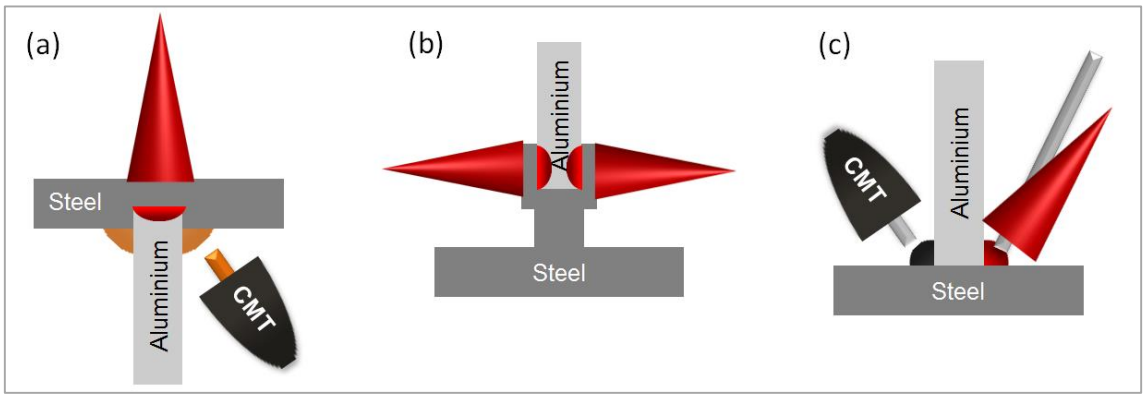

Figure 8-1: Different joining configurations for the dissimilar metal tee joint.

The design of the clamping system to be used in the first design proposed in Figure 8-1a is proposed in Figure 8-2. In this figure there is a 3D model of the clamping system in various stages of rotation. This system has been designed in such a way that it is possible to access both sides of the substrate to produce both laser and CMT welds.

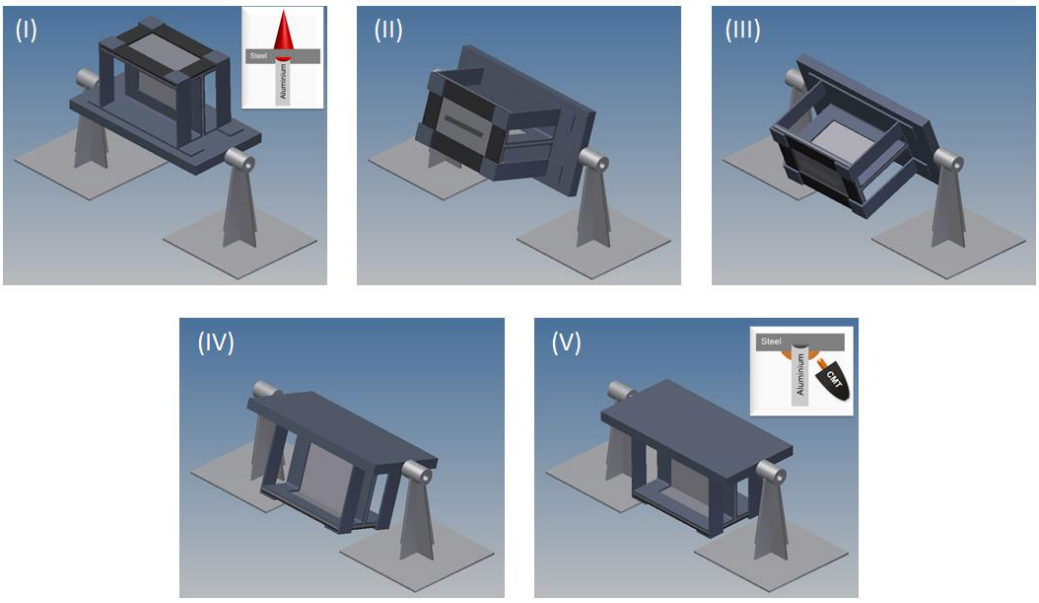

Figure 8-2: 3D model of the future clamping system for the T joint configuration, on different stages of rotation (I to V). In stage (I) autogenous laser welding is used and in stage (V) CMT welding with copper welding wire is used.

This device is versatile since it can be used either with the laser or other arc processes. Using this clamping system all the sides of the plates are accessible for the joining process. The top side has the steel plate (flange of the stiffener) which has underneath the aluminium (web of the stiffener).

The mechanical strength of the T-joints should also be quantified to compare to that of the joints produced with the Triclad transition joint.

There is still much work to do in this subject to improve the mechanical strength of the dissimilar metal joints of steel to aluminium. The joint configuration and the limitation of the reaction between the iron and the aluminium are the key points for the success of the hybrid joint.

- **Cryogenic cooling**

The results from the FEA for autogenous laser welding showed that to create maximise the bonding area on the Fe-Al joints, higher levels of power density have to be used. However, under such condition the thermal cycle enhances the growth of the IMC layer and therefore, the further improvement of the mechanical

strength of the joints by solely controlling the laser parameters is not possible. Cryogenic cooling could be the solution for this problem. By controlling the relative position of the cryogenic cooling in relation to the laser spot, the thermal field around the laser spot could be modify to remove the residual heat from the material just after the bonding of the Al to Fe is completed. The cryogenic cooling would restrict the growth of the IMC layer and would enable the use of higher levels of power density to form a larger bonding area and thus, improve the mechanical strength of the joints.

- **Application of autogenous laser welding with the same joining configuration to thinner sections of Fe and Al**

In this work it was found that the thickness of the material in use could be the cause of the interfacial failure of the joints. For this reason, the same experimental setup should be used to weld thin sheets (less than 2 mm) of Fe to Al and investigate whether the failure mode changes from interfacial failure to failure on the base metal.

Appendix A

In this section there is information about the Fe-Al intermetallic compounds. It also has a description of the phases that can be formed when using copper as interlayer to prevent the diffusion of Fe and Al.

Fe-Al intermetallic compounds

Table A-1: Crystal structure of the Fe-Al IMCs formed at room temperature (*Metals Handbook, vol. 63*, 1992)**(Shahverdi et al., 2002).**

Phases	Crystal structure	Stability range (at.%)	Density (Mg mm^{-3})
Fe solid solution	BCC	0–45	7.8
γ-Fe	FCC	0–1.3	7.8
FeAl (β2)	BCC (order)	23–55	5.58
Fe_3Al (β1)	Do3	23–34	6.72
Fe_2Al_3 (ε)	Cubic (complex)	58–65	–
$FeAl_2$ (ζ)	Triclinic	66–66.9	–
Fe_2Al_5 (η)	Orthorhombic	70–73	4.11
$FeAl_3$ (θ)	Monoclinic	74.5–76.5	3.9
Al solid solution	FCC	99.998–100	2.69

Table A-2: Thermodynamic constants for the Fe-Al IMCs formed (Richards et al., 1994).

Intermetallic compound	ΔH_{298} (J mol^{-1})	ΔS_{298} (K^{-1} mol^{-1})	ΔG_{973} (J mol^{-1})
$FeAl_3$ (θ)	−112560	95.6	−22869
Fe_2Al_5 (η)	−194040	166.7	−19636
$FeAl_2$ (ζ)	−81900	73.3	−16999
FeAl (β2)	−51240	51	−11090
Fe_3Al (β1)	−57372	28	−4827

Appendix B

This section shows both the laser system parameters and the fundamental laser material interaction parameters used in section 4.0.

Table B-1: Laser system and fundamental laser material interaction parameters used in section 4.0.

Beam diameter, mm	Power, kW	Travel speed, $m.min^{-1}$	Power density, $MW.m^{-2}$	Interaction time, s	Specific point energy, kJ
13.0	5.0	0.35	37.7	2.2	11.1
13.0	5.0	0.30	37.7	2.6	13.0
13.0	5.0	0.37	37.7	2.1	10.5
13.0	5.0	0.40	37.7	2.0	9.8
13.0	5.0	0.33	37.7	2.4	11.8
13.0	5.5	0.33	41.4	2.4	13.0
13.0	4.7	0.33	35.5	2.4	11.1
13.0	4.5	0.33	33.6	2.4	10.5
13.0	5.0	0.33	37.7	2.4	11.8
13.0	4.6	0.32	34.4	2.4	11.1
13.0	5.6	0.39	42.0	2.0	11.1
13.0	4.7	0.33	35.5	2.4	11.1
13.0	5.0	0.35	37.7	2.2	11.1
11.1	5.0	0.30	51.3	2.2	11.1
11.1	3.7	0.30	37.7	2.2	8.2
11.1	4.8	0.39	48.9	1.7	8.2
11.1	4.8	0.39	48.9	1.7	8.2
9.3	5.0	0.25	73.9	2.2	11.1
9.3	2.6	0.25	37.7	2.2	5.7
9.3	4.4	0.43	64.8	1.3	5.7
14.9	5.0	0.40	28.9	2.2	11.1
14.9	6.5	0.40	37.6	2.2	14.5
14.9	5.1	0.31	29.2	2.9	14.5
10.6	3.3	0.19	37.7	3.3	11.1
11.9	4.2	0.27	37.7	2.6	11.2
13.9	5.7	0.43	37.7	1.9	11.1

Appendix C

In this section there is a comparison of heat input calculated for the different welding modes, wire feed speed and welding wires.

Effect of the wire feed speed on the heat input of the welding process

- It is clearly seen that the composition of the welding wires affect the energy of the process;
- The welding process energy increases when the wire feed speed increases. This is true for all welding modes even though the difference of energy between the maximum and minimum wire feed speed changes with the welding mode.

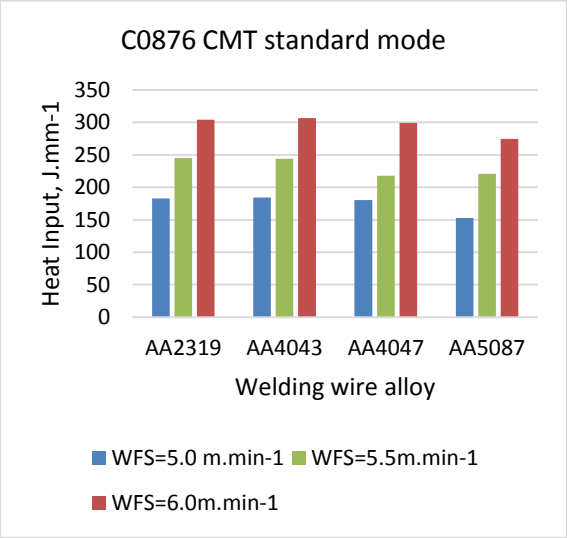

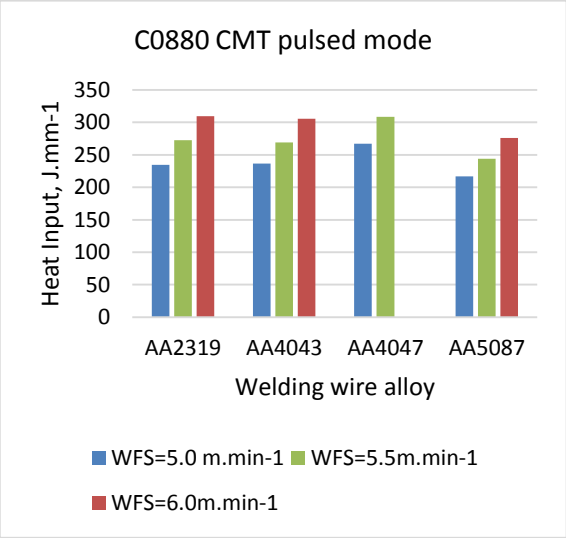

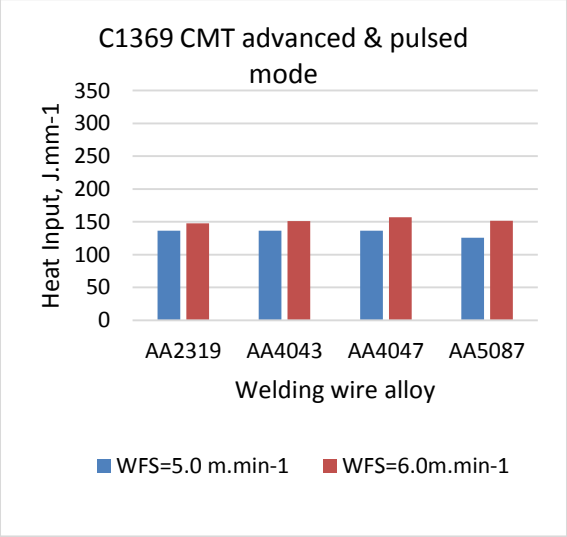

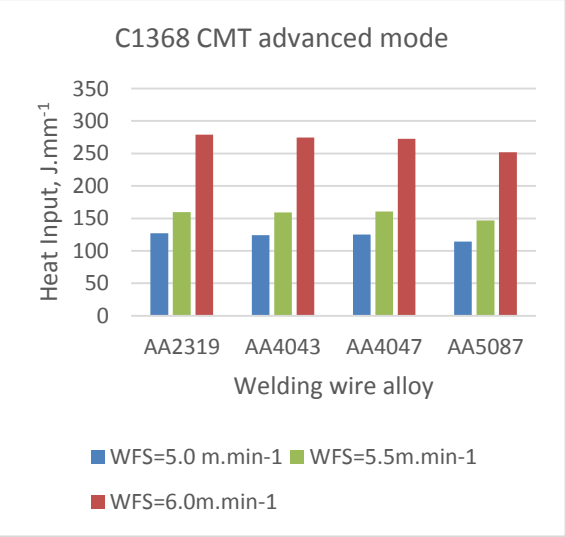

Effect of the welding mode on the heat input of the welding process

The heat input of the process changes with the welding mode. The most energetic welding mode is the CMT pulsed, followed by the CMT standard and both CMT advanced modes.

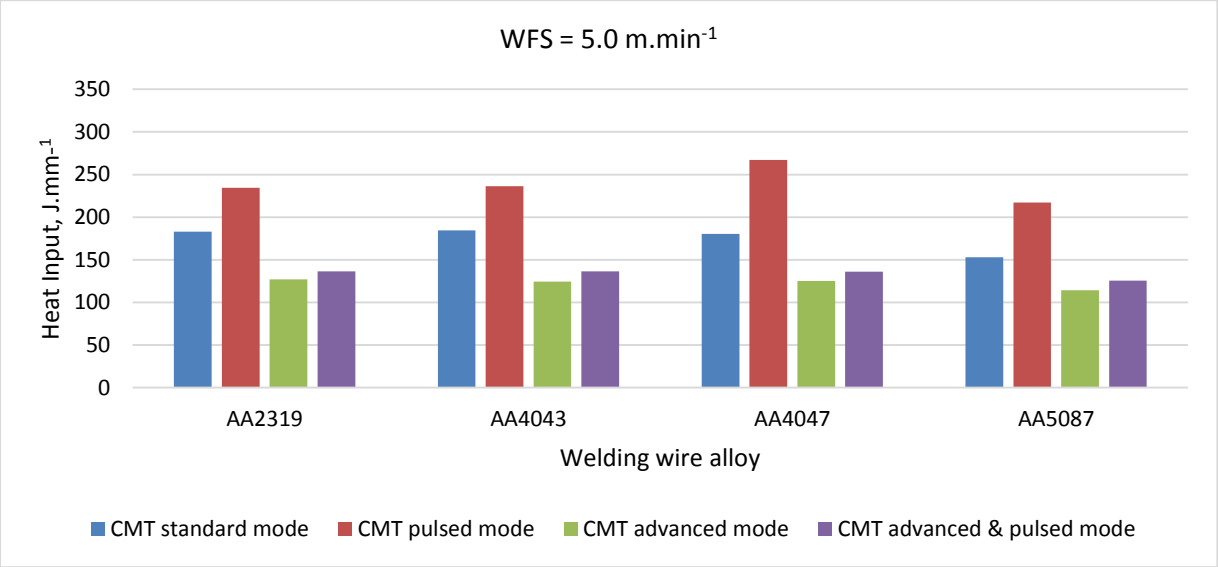

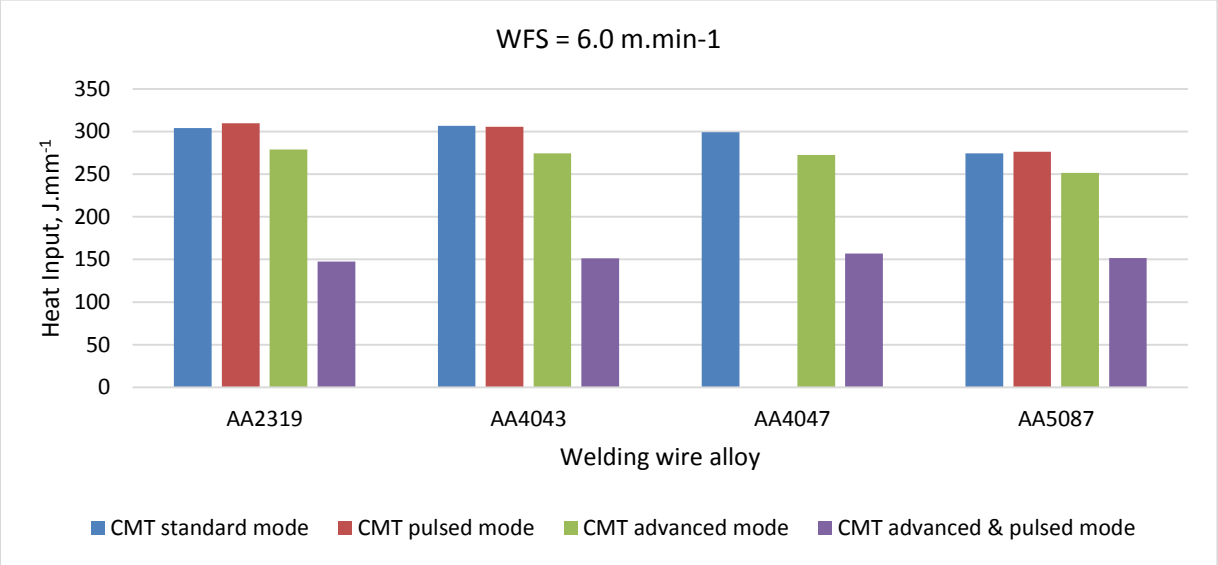

Appendix D

This section contains the raw and simplified data from the SEM/EDS spectrums that were analysed in sections 6.3 and 6.4.

Raw data from SEM/EDS spectrum analysis

Table D-1: SEM-EDS spectrum results in weight % of the samples with copper wire deposited onto aluminium. Welding parameters: C878 CMT mode, TS = 0.5 m.min^{-1}, 100% Argon shielding gas and WFS = 8.0 m.min^{-1} (section 6.3).

Spectrum label	Mg	Al	Si	Mn	Cu	Total
Spectrum 1	-	37.58	-	1.97	60.45	100
Spectrum 2	-	37.57	-	1.47	60.96	100
Spectrum 3	-	92.15	-	0.48	7.37	100
Spectrum 4	0.60	64.75	-	-	34.65	100
Spectrum 5	0.99	90.70	-	0.56	7.75	100
Spectrum 6	5.50	61.14	2.73	1.41	29.22	100
Spectrum 7	1.41	88.76	-	0.68	9.14	100
Spectrum 8	0.87	46.62	-	0.67	51.84	100
Spectrum 9	9.49	58.63	-	-	31.88	100

Table D-2: SEM-EDS spectrum results in weight % of the samples with copper wire deposited onto aluminium. Welding parameters: C1182 CMT Advanced mode, TS = 0.5 m.min^{-1}, 100% Argon shielding gas and WFS = 8.5 m.min^{-1}. (section 6.3).

Spectrum label	Mg	Al	Si	Mn	Cu	Total
Spectrum 1	-	45.63	-	-	54.37	100
Spectrum 2	-	44.90	-	-	55.10	100
Spectrum 3	2.85	58.10	1.77	0.97	36.31	100
Spectrum 4	3.99	57.68	2.37	1.12	34.84	100
Spectrum 5	-	44.80	-	-	55.20	100

Table D-3: SEM-EDS spectrum results in weight % of the samples with copper wire deposited onto aluminium. Welding parameters: C878 CMT mode, TS = 0.5 m.min^{-1}, 100% Argon shielding gas and WFS = 8.5 m.min^{-1}. (section 6.3).

Spectrum label	Mg	Al	Si	Mn	Cu	Total
Spectrum 1	1.75	73.07	0.78	0.93	23.48	100
Spectrum 2	1.91	57.28	0.80	-	40.01	100
Spectrum 3	-	39.96	1.12	1.42	57.51	100
Spectrum 4	0.74	41.90	2.06	1.02	54.28	100
Spectrum 5	-	38.65	-	1.66	59.69	100
Spectrum 6	3.72	95.73	-	0.56	-	100

Table D-4: Results from the SEM-EDS spectrum analysis in at. %. CMT welding mode - C0876, WFS = 5.0 m.min^{-1}, TS=0.5 m.min^{-1}, AA4047 welding wire (D5) (section 6.4).

Spectrum label	Al	Si	Mn	Fe	Cu	Mg	Total
Spectrum 1	45.83	5.5	0.63	1.8	46.24	-	100
Spectrum 2	44.85	5.19	0.39	1.81	47.76	-	100
Spectrum 3	44.96	5.5	0.73	1.62	47.19	-	100
Spectrum 4	40.71	12.83	1.46	22.02	22.98	-	100
Spectrum 5	42.63	10.98	0.6	19.17	26.62	-	100
Spectrum 6	40.29	12.36	1.17	19.4	26.78	-	100
Spectrum 7	66.19	5.97	0.26	1.36	26.22	-	100
Spectrum 8	65.99	5.92	0.34	1.38	26.38	-	100
Spectrum 9	65.67	5.41	0.3	1.17	27.46	-	100
Spectrum 10	79.79	11.29	0.17	0.44	8.31	-	100
Spectrum 11	80.18	11.63	0.18	0.41	7.59	-	100
Spectrum 12	82.31	9.13	-	0.41	8.15	-	100
Spectrum 13	74.68	9.37	0.25	0.81	14.88	-	100
Spectrum 14	74.79	10.03	0.28	0.83	14.06	-	100
Spectrum 15	75.48	9.81	0.2	0.7	13.8	-	100
Spectrum 16	62.1	5.98	0.7	2.3	28.93	-	100
Spectrum 17	62.62	5.22	0.41	1.39	30.35	-	100
Spectrum 18	60.88	6.43	0.39	1.65	30.65	-	100
Spectrum 19	41.64	43.34	-	0.83	14.19	-	100
Spectrum 20	40.25	46.29	-	0.68	12.78	-	100
Spectrum 21	32.13	58.11	0.16	0.61	8.99	-	100

Table D-5: Results from the SEM-EDS spectrum analysis in at. %. CMT welding mode - C0876, WFS = 5.0 m.min^{-1}, TS=0.5 m.min^{-1}, AA4043 welding wire (D12) (section 6.4).

Spectrum label	Al	Si	Mn	Fe	Cu	Mg	Total
Spectrum 1	47.02	3.37	0.61	1.39	47.61	-	100
Spectrum 2	46.56	3.46	0.56	1.38	48.04	-	100
Spectrum 3	46.14	4.37	0.72	1.23	47.54	-	100
Spectrum 4	68.33	2.95	0.52	1.23	26.96	-	100
Spectrum 5	67.89	2.7	0.45	1.13	27.83	-	100
Spectrum 6	66.52	3.01	0.61	1.43	28.43	-	100
Spectrum 7	71.19	2.48	0.28	0.79	25.26	-	100
Spectrum 8	70.68	2.63	0.25	0.78	25.66	-	100
Spectrum 9	70.84	2.4	0.27	0.64	25.85	-	100
Spectrum 10	90.09	2.23	-	0.24	7.44	-	100
Spectrum 11	90.79	2.33	-	0.37	6.52	-	100
Spectrum 12	90.93	2.34	-	0.28	6.46	-	100
Spectrum 13	80.35	7.68	-	0.52	11.45	-	100
Spectrum 14	79.08	7.75	0.28	0.54	12.34	-	100
Spectrum 15	76.28	10.11	0.23	0.53	12.85	-	100
Spectrum 16	89.54	2.47	-	0.33	7.66	-	100
Spectrum 17	90.89	2.25	-	0.34	6.52	-	100
Spectrum 18	42.04	11.32	1.61	16.19	28.84	-	100
Spectrum 19	40.46	12.08	1.35	22.07	24.05	-	100
Spectrum 20	40.93	11.92	1.32	19.73	26.1	-	100
Spectrum 21	41.27	12.22	1.68	23.42	21.41	-	100

Table D-6: Results from the SEM-EDS spectrum analysis in at. %. CMT welding mode - C0876, WFS = 5.0 m.min^{-1}, TS=0.5 m.min^{-1}, AA2319 welding wire (D23) (section 6.4).

Spectrum label	Al	Si	Mn	Fe	Cu	Mg	Total
Spectrum 1	44.4	2.5	0.5	1.6	51.1	-	100
Spectrum 2	44.1	2.7	0.6	1.8	50.7	-	100
Spectrum 3	44.8	3	0.7	1.5	49.9	-	100
Spectrum 4	68.3	1.1	0.3	0.9	29.3	-	100
Spectrum 5	69.9	1	0.4	0.8	28.1	-	100
Spectrum 6	69.8	1.1	0.2	0.9	28	-	100
Spectrum 7	54.3	8.3	0.9	16.7	19.8	-	100
Spectrum 8	78.8	1.2	0.4	0.7	19	-	100
Spectrum 9	79.1	0.9	0.3	0.7	19	-	100
Spectrum 10	78.3	1.1	0.3	0.7	19.6	-	100
Spectrum 11	86.2	-	0.2	0.5	13.1	-	100
Spectrum 12	88.1	-	0.2	0.4	11.3	-	100
Spectrum 13	89	-	0.2	0.5	10.3	-	100
Spectrum 14	36.7	11.1	1.3	22.5	28.4	-	100
Spectrum 15	39.1	11.9	1.7	24.1	23.2	-	100
Spectrum 16	91.9	-	0.2	0.4	7.5	-	100
Spectrum 17	89.1	-	-	0.4	10.5	-	100

Table D-7: Results from the SEM-EDS spectrum analysis in at. %. CMT welding mode - C0876, WFS = 5.0 m.min^{-1}, TS=0.5 m.min^{-1}, AA5087 welding wire (D34) (section 6.4).

Spectrum label	Al	Si	Mn	Fe	Cu	Mg	Total
Spectrum 1	45.95	3.84	0.91	1.25	44.84	3.22	100
Spectrum 2	49.47	2.46	0.6	1.34	42.7	3.44	100
Spectrum 3	49.05	2.54	0.67	1.37	43	3.37	100
Spectrum 4	70.04	0.98	0.25	0.72	25.17	2.84	100
Spectrum 5	68.52	1.28	0.38	0.74	25.88	3.2	100
Spectrum 6	69.61	0.97	0.34	0.79	25.19	3.1	100
Spectrum 7	87.32	-	0.45	0.4	8.01	3.83	100
Spectrum 8	88.02	-	0.35	0.39	7.7	3.53	100
Spectrum 9	87.55	-	0.41	0.4	8.06	3.57	100
Spectrum 10	43.66	9.61	1.26	16.91	25.88	2.68	100
Spectrum 11	44.29	7.99	1.23	8.48	35.08	2.92	100
Spectrum 12	45.07	8.79	1.04	18.26	23.76	3.08	100
Spectrum 13	66.57	1.51	0.6	1.34	27	2.99	100
Spectrum 14	66.29	1.53	0.62	1.09	27.56	2.9	100
Spectrum 15	66.65	1.61	0.64	1.26	26.78	3.06	100
Spectrum 16	88.78	-	0.38	0.28	6.13	4.42	100
Spectrum 17	89.09	-	0.41	0.36	6.1	4.04	100
Spectrum 18	88.6	-	0.37	0.37	6.48	4.18	100
Spectrum 19	88.89	-	0.42	0.35	5.84	4.5	100
Spectrum 20	50.92	6.29	0.77	1.44	37.65	2.94	100
Spectrum 21	50.1	6.69	0.77	1.11	37.81	3.52	100
Spectrum 22	50.02	8.97	1.14	17.16	19.66	3.06	100
Spectrum 23	51.04	6.6	0.7	1.43	37	3.24	100
Spectrum 24	81.39	2.17	0.49	0.42	10.65	4.88	100

Simplified data from SEM/EDS spectrum analysis

The simplified data excludes the elements which composition is less than 8 at.%.

Table D-8: Simplified list of results from the SEM-EDS spectrum analysis in at. %. CMT welding mode - C0876, WFS = 5.0 m.min^{-1}, TS=0.5 m.min^{-1}, AA4047 welding wire (D5) (section 6.4).

Spectrum label	Al	Si	Mn	Fe	Cu	Mg	Total
Spectrum 1	50		-		50	-	100
Spectrum 2	48		-		52	-	100
Spectrum 3	49		-		51	-	100
Spectrum 4	41	13	-	22	23	-	100
Spectrum 5	43	11	-	19	27	-	100
Spectrum 6	41	13	-	20	27	-	100
Spectrum 7	72		-		28	-	100
Spectrum 8	71		-		29	-	100
Spectrum 9	71		-		30	-	100
Spectrum 10	80	11	-		8	-	100
Spectrum 11	81	12	-		8	-	100
Spectrum 12	83	9	-		8	-	100
Spectrum 13	76	10	-		15	-	100
Spectrum 14	76	10	-		14	-	100
Spectrum 15	76	10	-		14	-	100
Spectrum 16	68		-		32	-	100
Spectrum 17	67		-		33	-	100
Spectrum 18	67		-		34	-	100
Spectrum 19	42	44	-		14	-	100
Spectrum 20	41	47	-		13	-	100
Spectrum 21	32	59	-		9	-	100

Table D-9: Simplified list of results from the SEM-EDS spectrum analysis in at. %. CMT welding mode - C0876, WFS = 5.0 m.min^{-1}, TS=0.5 m.min^{-1}, AA4043 welding wire (D12) (section 6.4).

Spectrum label	Al	Si	Mn	Fe	Cu	Mg	Total
Spectrum 1	50		-		50	-	100
Spectrum 2	49		-		51	-	100
Spectrum 3	49		-		51	-	100
Spectrum 4	72		-		28	-	100
Spectrum 5	71		-		29	-	100
Spectrum 6	70		-		30	-	100
Spectrum 7	74		-		26	-	100
Spectrum 8	73		-		27	-	100
Spectrum 9	73		-		27	-	100
Spectrum 10	92		-		8	-	100
Spectrum 11	93		-		7	-	100
Spectrum 12	93		-		7	-	100
Spectrum 13	88		-		12	-	100
Spectrum 14	87		-		13	-	100
Spectrum 15	86		-		14	-	100
Spectrum 16	92		-		8	-	100
Spectrum 17	93		-		7	-	100
Spectrum 18	43	12	-	16	29	-	100
Spectrum 19	41	12	-	22	24	-	100
Spectrum 20	41	12	-	20	26	-	100
Spectrum 21	42	12	-	24	22	-	100

Table D-10: Simplified list of results from the SEM-EDS spectrum analysis in at. %. CMT welding mode - C0876, WFS = 5.0 m.min^{-1}, TS=0.5 m.min^{-1}, AA2319 welding wire (D23) (section 6.4).

Spectrum label	Al	Si	Mn	Fe	Cu	Mg	Total
Spectrum 1	47		-		54	-	100
Spectrum 2	47		-		54	-	100
Spectrum 3	47		-		53	-	100
Spectrum 4	70		-		30	-	100
Spectrum 5	71		-		29	-	100
Spectrum 6	71		-		29	-	100
Spectrum 7	55	8	-	17	20	-	100
Spectrum 8	81		-		19	-	100
Spectrum 9	81		-		19	-	100
Spectrum 10	80		-		20	-	100
Spectrum 11	87		-		13	-	100
Spectrum 12	89		-		11	-	100
Spectrum 13	90		-		10	-	100
Spectrum 14	37	11	-	23	29	-	100
Spectrum 15	40	12	-	25	24	-	100
Spectrum 16	93		-		8	-	100
Spectrum 17	90		-		11	-	100

Table D-11: Simplified list of results from the SEM-EDS spectrum analysis in at. %. CMT welding mode - C0876, WFS = 5.0 m.min^{-1}, TS=0.5 m.min^{-1}, AA5087 welding wire (D34) (section 6.4).

Spectrum label	Al	Si	Mn	Fe	Cu	Mg	Total
Spectrum 1	51				49		100
Spectrum 2	54				46		100
Spectrum 3	53				47		100
Spectrum 4	74				26		100
Spectrum 5	73				27		100
Spectrum 6	73				27		100
Spectrum 7	92				8		100
Spectrum 8	92				8		100
Spectrum 9	92				8		100
Spectrum 10	46	10		18	27		100
Spectrum 11	46	8		9	37		100
Spectrum 12	47	9		19	25		100
Spectrum 13	71				29		100
Spectrum 14	71				29		100
Spectrum 15	71				29		100
Spectrum 16	94				7		100
Spectrum 17	94				6		100
Spectrum 18	93				7		100
Spectrum 19	94				6		100
Spectrum 20	54	7			40		100
Spectrum 21	53	7			40		100
Spectrum 22	52	9		18	21		100
Spectrum 23	54	7			39		100
Spectrum 24	88				12		100

Appendix E

This section shows the EDS mapping of the specimens welded with AlCu, AlSi5, AlSi12 and AlMg welding wires and two different CMT welding modes, i.e. standard CMT and advanced CMT.

EDS mapping of the specimens welded with standard CMT (C0876)

Table E-1: SEM/EDS macro mapping of the samples produced with different welding wires and similar brazing conditions (C0876, WFS = 5.0 m.min^{-1}, TS = 0.5 m.min^{-1}).

Welding wire			
AA2319 (AlCu)	AA4043 ($AlSi_5$)	AA4047 ($AlSi_{12}$)	AA5087 (AlMg)
HI (η=0.85), J.mm^{-1}			
172.8	174.3	170.4	144.2
Macro			
			
Mix			
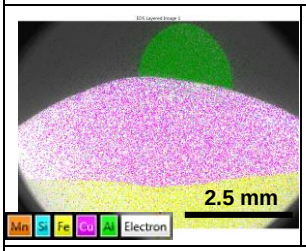	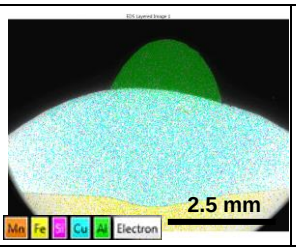	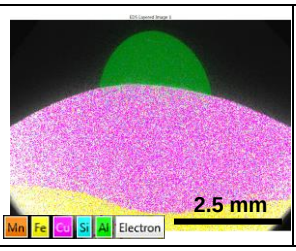	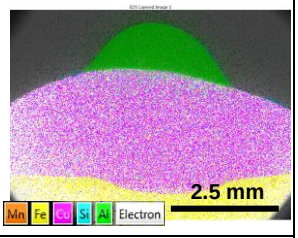
Al			
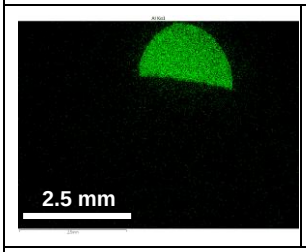	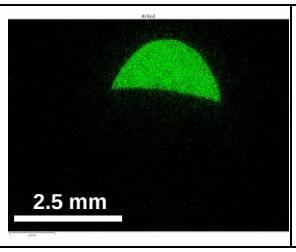	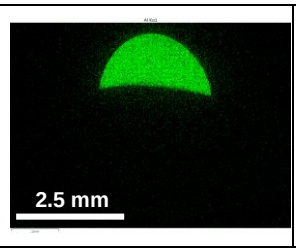	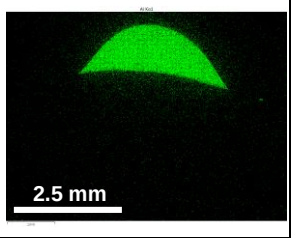
Cu			
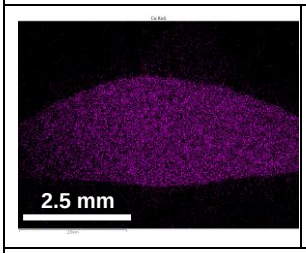	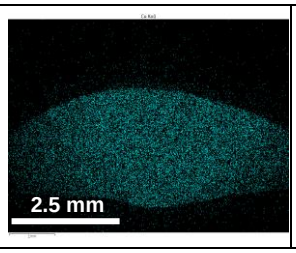	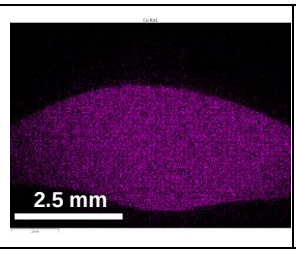	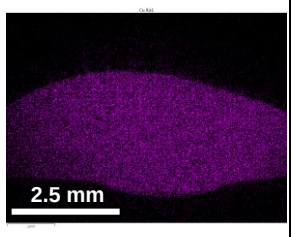
Fe			

Welding wire			
AA2319 (AlCu)	AA4043 ($AlSi_5$)	AA4047 ($AlSi_{12}$)	AA5087 (AlMg)
HI (η=0.85), $J.mm^{-1}$			
172.8	174.3	170.4	144.2
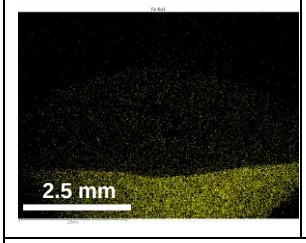	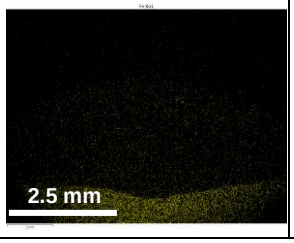	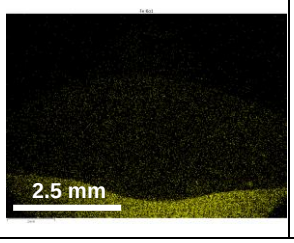	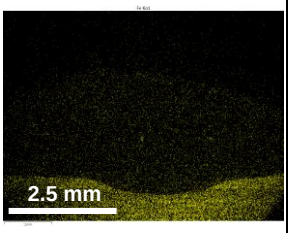
Si			
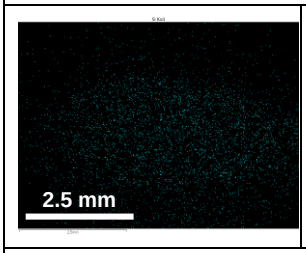	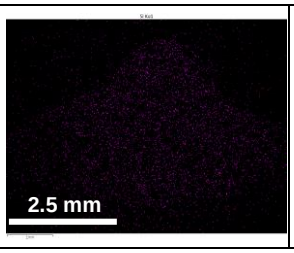	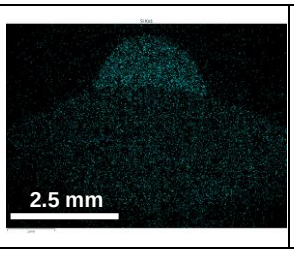	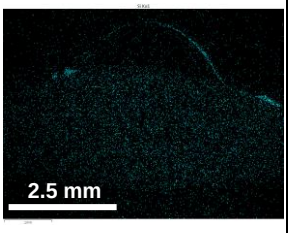
Mn			
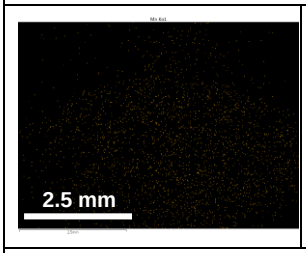	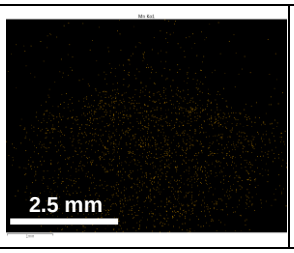	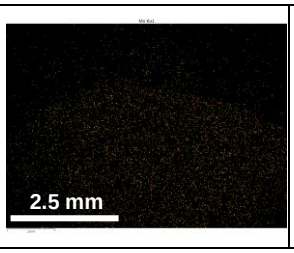	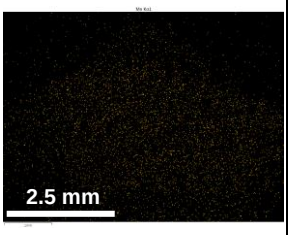
Mg			
-	-	-	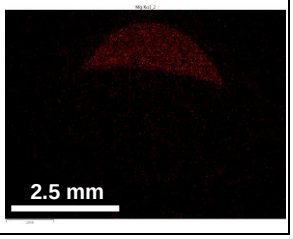

EDS mapping of the specimens welded with standard CMT (C0876)

Table E-2: SEM/EDS macro mapping of the samples produced with different welding wires and similar brazing conditions (C1368 Adv, WFS = 5.0 m.min^{-1}, TS = 0.5 m.min^{-1}).

Welding wire			
AA2319 (AlCu)	AA4043 ($AlSi_5$)	AA4047 ($AlSi_{12}$)	AA5087 (AlMg)
HI (η=0.85), J.mm^{-1}			
120.1	117.5	118.2	108.0
Macro			
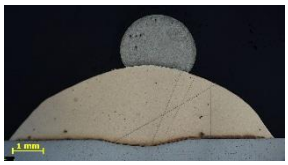	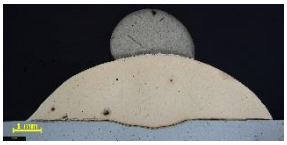	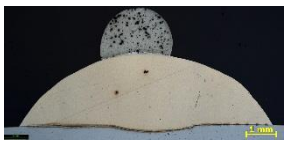	
Mix			
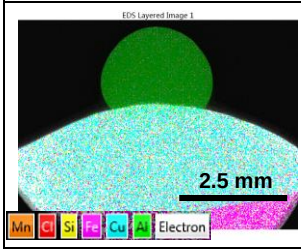	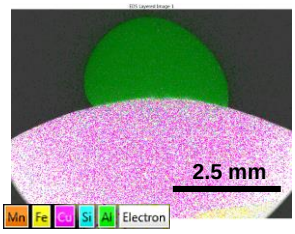	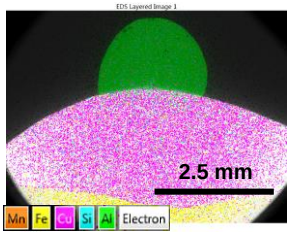	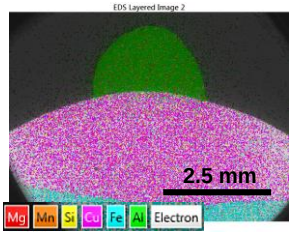
Al			
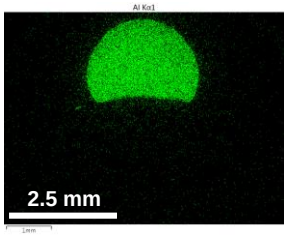	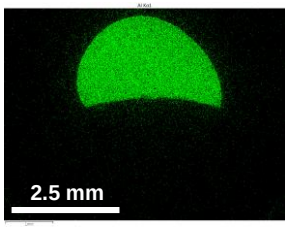	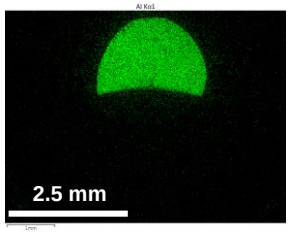	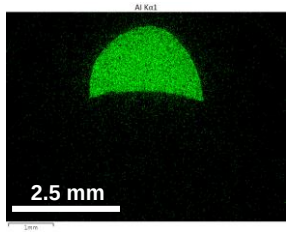
Cu			
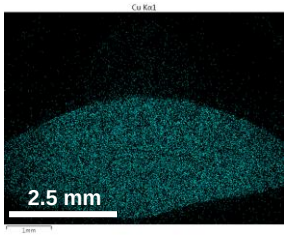	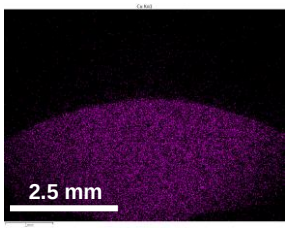	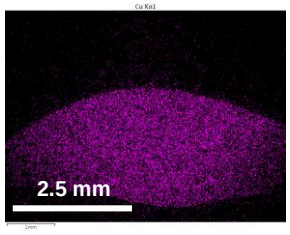	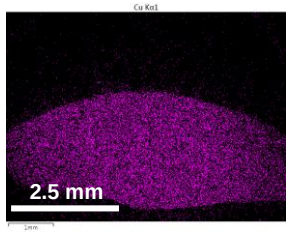
Fe			
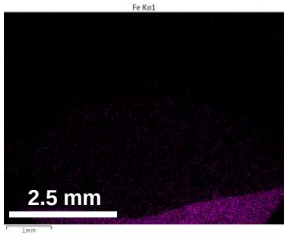	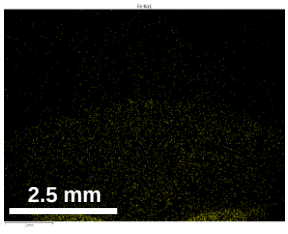	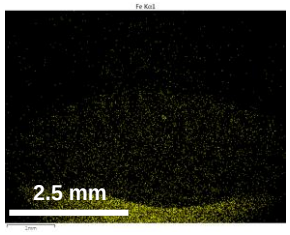	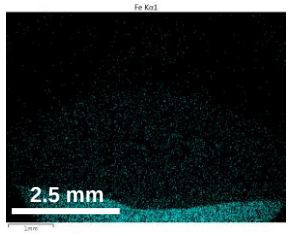

Welding wire			
AA2319 (AlCu)	AA4043 ($AlSi_5$)	AA4047 ($AlSi_{12}$)	AA5087 (AlMg)
HI (η=0.85), $J.mm^{-1}$			
120.1	117.5	118.2	108.0
Macro			
Si			
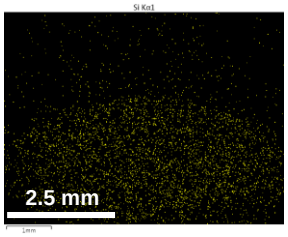	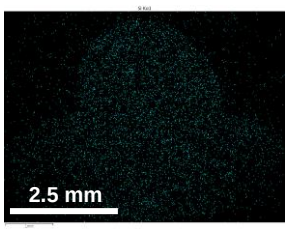	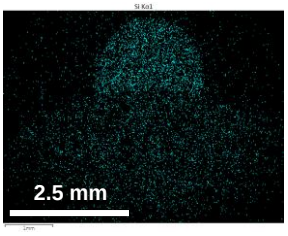	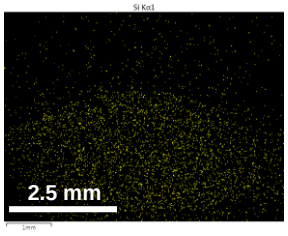
Mn			
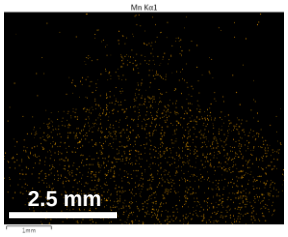	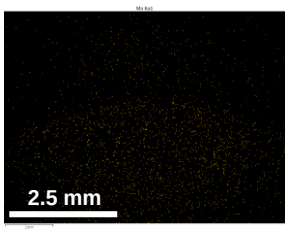	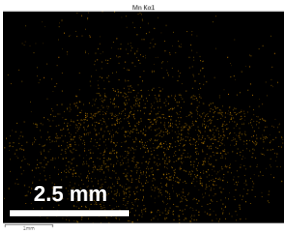	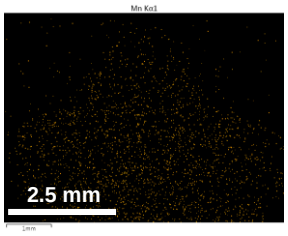
Mg			
-	-	-	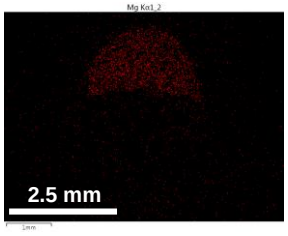

References

A.S.M American Society for Metals, Bulletin of binary phase diagrams, 1994. . ASM International, Materials Park, OH.

Abbasi, M., Karimi Taheri, a., Salehi, M.T., 2001. Growth rate of intermetallic compounds in Al/Cu bimetal produced by cold roll welding process. J. Alloys Compd. 319, 233–241. doi:10.1016/S0925-8388(01)00872-6

Abe, Y., Kato, T., Mori, K., 2009. Self-piercing riveting of high tensile strength steel and aluminium alloy sheets using conventional rivet and die. J. Mater. Process. Technol. 209, 3914–3922. doi:10.1016/j.jmatprotec.2008.09.007

Abe, Y., Mori, K., Kato, T., 2011. Joining of high strength steel and aluminium alloy sheets by mechanical clinching with dies for control of metal flow. J. Mater. Process. Technol. 212, 884–889. doi:10.1016/j.jmatprotec.2011.11.015

Acarer, M., Demir, B., 2008. An investigation of mechanical and metallurgical properties of explosive welded aluminum–dual phase steel. Mater. Lett. 62, 4158–4160. doi:10.1016/j.matlet.2008.05.060

Aerodynamic metals PTE Ltd, 2009. Triplate aluminium/Steel Transition Joint [WWW Document]. URL http://sg111447476.trustpass.alibaba.com/product/119936153-103226010/Triplate_aluminium_Steel_Transition_Joint.html (accessed 9.27.15).

Agudo, L., Eyidi, D., Schmaranzer, C.H., Arenholz, E., Jank, N., Bruckner, J., Pyzalla, A.R., 2007. Intermetallic Fe x Al y -phases in a steel/Al-alloy fusion weld. J. Mater. Sci. 42, 4205–4214. doi:10.1007/s10853-006-0644-0

Akdeniz, M. V, 1998. THE EFFECT OF SUBSTITUTIONAL IMPURITIES ON THE EVOLUTION OF Fe-Al DIFFUSION LAYER. Science (80-.). 46.

Aluminum: Properties and Physical Metallurgy, 1984. . ASM International.

Assuncao, E., 2012. Investigation of conduction to keyhole mode transition. Cranfield University.

Assuncao, E., Williams, S., Yapp, D., 2012. Interaction time and beam diameter effects on the conduction mode limit. Opt. Lasers Eng. 50, 823–828. doi:10.1016/j.optlaseng.2012.02.001

ASW, 1996. Tenform high-strength low-alloy steel properties [WWW Document]. URL https://app.aws.org/mwf/attachments/86/100386/hot_rolled_hsla.pdf

Avt, T.A., Joints, A., Group, E. a a W., 2002. Joining - Adhesive bonding, in: The Aluminium Automotive Manual. European aluminium association.

AWS, 1991. Welding Handbook, Welding Processes, Eighth. ed. AWS, Miami.

Azom, 2000. Pure aluminium properties.pdf [WWW Document]. Alum. - Specif. Prop. Classif. Classes, Supplier Data by Aalco. URL http://www.azom.com/article.aspx?ArticleID=2863#6

BOC, 2007. Aluminium welding [WWW Document]. Sect. 8 Consum. - Alum. Weld. doi:10.1533/9780857093264.83

Borrisutthekul, R., Yachi, T., Miyashita, Y., Mutoh, Y., 2007. Suppression of intermetallic reaction layer formation by controlling heat flow in dissimilar joining of steel and aluminum alloy. Mater. Sci. Eng. A 467, 108–113. doi:10.1016/j.msea.2007.03.049

Bouche, K., Barbier, F., Coulet, a, 1998. Intermetallic compound layer growth between solid iron and molten aluminium. Mater. Sci. Eng. A 249, 167–175. doi:10.1016/S0921-5093(98)00573-5

British Standard Instiurion, 2001. BS EN ISO 14273:2001 Specimen dimensions and procedure for shear testing resistance spot , seam and embossed projection welds. London.

Callister, W.D., 2006. Materials Science and Engineering: An Introduction, 7th ed. John Wiley & Sons, Inc.

Cheng, W.J., Wang, C.J., 2009. Growth of intermetallic layer in the aluminide mild steel during hot-dipping. Surf. Coatings Technol. 204, 824–828. doi:10.1016/j.surfcoat.2009.09.061

Cottrell, S.A., 1995. An Introduction to Metallurgy, 2nd ed. Maney Publishing.

Cozzolino, L., 2013. Finite element analysis of localised rolling to reduce residual stress and distortion. Cranfield University.

Dharmendra, C., Rao, K.P., Wilden, J., Reich, S., 2011. Study on laser welding–brazing of zinc coated steel to aluminum alloy with a zinc based filler. Mater. Sci. Eng. A 528, 1497–1503. doi:10.1016/j.msea.2010.10.050

Dong, H., Hu, W., Duan, Y., Wang, X., Dong, C., 2012. Dissimilar metal joining of aluminum alloy to galvanized steel with Al–Si, Al–Cu, Al–Si–Cu and Zn–Al filler wires. J. Mater. Process. Technol. 212, 458–464. doi:10.1016/j.jmatprotec.2011.10.009

E N British Standard, 2009. Welding — Recommendations for welding of metallic materials. Part I: General guidance for arc welding (BS EN 1011 - 1:2009). doi:978-0-580-58000-0

Engler, S., Ramsayer, R., Poprawe, R., 2011. Process Studies on Laser Welding of Copper with Brilliant Green and Infrared Lasers. Phys. Procedia 12, 339–346. doi:10.1016/j.phpro.2011.03.142

Fan, J., Thomy, C., Vollertsen, F., 2011. Effect of Thermal Cycle on the Formation of Intermetallic Compounds in Laser Welding of Aluminum-Steel Overlap Joints. Phys. Procedia 12, 134–141. doi:10.1016/j.phpro.2011.03.017

Feng, Ishihara, K.N., Shingu, P.H., 1991. The formation of metastable phases by mechanical alloying in the aluminium and copper system. Metall. Trans. A 22A, 2849–2854.

Findik, F., 2011. Recent developments in explosive welding. Mater. Des. 32, 1081–1093. doi:10.1016/j.matdes.2010.10.017

Fronius, 2013. Operating range extension for CMT weld process [WWW Document]. Keep. up-to-date. URL http://www.fronius.ca/cps/rde/xchg/SID-5E1398EC-95667169/fronius_canada/hs.xsl/32_4332_ENG_HTML.htm#.U8Ep8rHwomk (accessed 7.12.14).

Fronius, 2014. CMT: Three letters that stand for the stablest weld process anywhere in the world [WWW Document]. URL http://www.fronius.com/cps/rde/xchg/SID-B0C6E4CC-0B1EFADC/fronius_international/hs.xsl/79_23609_ENG_HTML.htm#.U8Kn-bHwolJ (accessed 7.13.14).

Graham, 2014. Audi TT Production: Weber Screwdriving Systems [WWW Document]. URL http://www.weberusa.com/industries/automotive/item/54-audi-tt-production (accessed 9.25.15).

Haddadi, F., Prangnell, P., 2013. Grain Structure Evolution in Aluminium To Steel, in: MS&T 2013. Montreal, pp. 1252–1259.

Hashemzadeh, M., Suder, W., Williams, S., Powell, J., Kaplan, A.F.H., Voisey, K.T., 2014. The application of specific point energy analysis to laser cutting with 1 µm laser radiation. pp. 1–9.

Hess, A., Schuster, R., Heider, A., Weber, R., Graf, T., 2011. Continuous Wave Laser Welding of Copper with Combined Beams at Wavelengths of 1030nm and of 515nm. Phys. Procedia 12, 88–94. doi:10.1016/j.phpro.2011.03.012

Heumann, T., Dittrich, N., 1959. Structure character of the Fe2Al5 intermetallic compound in hot-dip aluminizing process. Zeitschrift Fur Met. 50, 617–623.

International Standard, 2005. Lasers and laser-related equipment — Test methods for laser beam widths, divergence angles and beam propagation ratios — Part 1: Stigmatic and simple astigmatic beams. BSI. doi:11146-1:2005

Ion, J., 2005. Laser Processing of Engineering Materials: Principles, Procedure and Industrial Application, 1st editio. ed. Elsevier Butterworth-Heinemann, Oxford.

Kan, M.J., Kim, C.H., 2013. Cold-Metal-Transfer Arc Joining of Al 6K32 Alloy to Steel Sheets. Defect Diffus. Forum 334-335, 247–251.

Kang, M., Kim, C., 2015. Joining Al 5052 alloy to aluminized steel sheet using cold metal transfer process. Mater. Des. 81, 95–103. doi:10.1016/j.matdes.2015.05.035

Kastensson, Å., 2014. Developing lightweight concepts in the automotive industry: taking on the environmental challenge with the SåNätt project. J. Clean. Prod. 66, 337–346. doi:10.1016/j.jclepro.2013.11.007

Kim, D., Badarinarayan, H., Kim, J.H., Kim, C., Okamoto, K., Wagoner, R.H., Chung, K., 2010. Numerical simulation of friction stir butt welding process for AA5083-H18 sheets. Eur. J. Mech. - A/Solids 29, 204–215.

doi:10.1016/j.euromechsol.2009.10.006

Kim, H., Lee, J.Y., Paik, K., Koh, K., Won, J., Choe, S., Lee, J., Moon, J., Park, Y., 2003. Effects of Cu / Al Intermetallic Compound (IMC) on Copper Wire and Aluminum Pad Bondability 26, 367–374.

Klages, H., 2006. Laserstrahl-Mikroschweißen ungleicher Metalle durch Nahtschweißen mit gepulsten Nd : YAG-Lasern. RWTH Aachen.

Kobayashi, S., Yakou, T., 2002. Control of intermetallic compound layers at interface between steel and aluminum by diffusion-treatment. Mater. Sci. 338, 44–53.

Korte, M., Stirn, B., Laukant, H., Wallmann, C., Mu, M., Haldenwanger, H., Glatzel, U., 2005. Fluxless laser beam joining of aluminium with zinc coated steel. Sci. Technol. 10, 219–226. doi:10.1179/174329305X37051

Kouters, M.H.M., Gubbels, G.H.M., O'Halloran, O., Rongen, R., 2011. Characterization of intermetallic compounds in Cu-Al ball bonds : layer growth , mechanical properties and oxidation, in: Microelectronics and Packaging Conference (EMPC), 18th European. IEEE, pp. 1–7.

Kreimeyer, M., Wagner, F., Sepold, G., 2004. DEVELOPMENT OF A COMBINED JOINING-FORMING PROCESS FOR ALUMINUM-STEEL JOINTS Aluminum Aluminum, in: ICALEO 2004.

Laser Materials Processing (Google eBook), 1983. . Elsevier.

Lee, W., Schmuecker, M., Mercardo, U., Biallas, G., Jung, S., 2006. Interfacial reaction in steel–aluminum joints made by friction stir welding. Scr. Mater. 55, 355–358. doi:10.1016/j.scriptamat.2006.04.028

Liu, Z., Gao, W., Wang, F., 1998. OXIDATION BEHAVIOUR OF FeAl INTERMETALLIC COATINGS PRODUCED BY MAGNETRON SPUTTER DEPOSITION 39, 1497–1502.

Ltd., I.A., 2009. Tutorial to get started with the AxioVision Imaging System.

Ma, J., Harooni, M., Carlson, B., Kovacevic, R., 2014. Dissimilar joining of galvanized high-strength steel to aluminum alloy in a zero-gap lap joint configuration by two-pass laser welding. Mater. Des. 58, 390–401. doi:10.1016/j.matdes.2014.01.046

Mai, T. a., Spowage, a. C., 2004. Characterisation of dissimilar joints in laser welding of steel–kovar, copper–steel and copper–aluminium. Mater. Sci. Eng. A 374, 224–233. doi:10.1016/j.msea.2004.02.025

Martinsen, K., Hu, S.J., Carlson, B.E., 2015. Joining of dissimilar materials. CIRP Ann. - Manuf. Technol. 64, 679–699. doi:10.1016/j.cirp.2015.05.006

Massalski, T., 1986. Binary Alloy Phase Diagrams, American S. ed. Williams, Jr. W. Scott, Metals Park, Ohio.

Mathieu, A., Shabadi, R., Deschamps, A., Suery, M., Matteı, S., Grevey, D., Cicala, E., 2007. Dissimilar material joining using laser (aluminum to steel using zinc-based filler wire). Opt. Laser Technol. 39, 652–661.

doi:10.1016/j.optlastec.2005.08.014

Matweb, 1996. Iron, Fe - properties [WWW Document]. URL http://www.matweb.com/search/DataSheet.aspx?MatGUID=654ca9c358264b5392d43315d8535b7d&ckck=1

Meco, S., Ganguly, S., Williams, S., McPherson, N., 2014. Effect of Laser Processing Parameters on the Formation of Intermetallic Compounds in Fe-Al Dissimilar Welding. J. Mater. Eng. Perform. 23, 3361–3370. doi:10.1007/s11665-014-1106-5

Meco, S., Pardal, G., Ganguly, S., Williams, S., McPherson, N., 2015. Application of laser in seam welding of dissimilar steel to aluminium joints for thick structural components. Opt. Lasers Eng. 67, 22–30. doi:10.1016/j.optlaseng.2014.10.006

Metals Handbook, vol. 63, 10th ed, 1992. . ASM International.

Metalweb, 2013. Plate, sheet and strip typical physical properties - AA5083 H22 [WWW Document]. Alum. Roll. plate sheet. URL http://www.metalweb.co.uk/product/aluminium/aluminium-rolled-plate-sheet/ (accessed 1.1.15).

MetPrep Ltd, n.d. MetPrep Preparation Procedure – No 35 Extruded 5XXX Series Aluminium Alloy [WWW Document]. URL http://www.metprep.co.uk/pdfs/Prep35.pdf (accessed 8.29.15).

Mock, P., 2014. EU CO2 standards for passenger cars and light-commercial vehicles [WWW Document]. Policy Updat. URL http://www.theicct.org/eu-co2-standards-passenger-cars-and-lcvs

Mukherjee, S., Chakraborty, S., Galun, R., Estrin, Y., Manna, I., 2010. Transport phenomena in conduction mode laser beam welding of Fe–Al dissimilar couple with Ta diffusion barrier. Int. J. Heat Mass Transf. 53, 5274–5282. doi:10.1016/j.ijheatmasstransfer.2010.07.032

Nakamura, S., Sakurai, M., Kamimuki, K., 2000. Detection technique for transition between deep penetration mode and shallow penetration mode in CO2. J. Phys. D. Appl. Phys. 33, 2941–2948. doi:10.1088/0022-3727/33/22/311

Okamoto, H., 2000. Desk Handbook: Phase Diagrams for Binary Alloys, First. ed. ASM Internationall.

Olsen, F.O., 2009. Hybrid Laser Arc Welding, in: Hybrid Laser-Arc Welding. CRC Press, pp. 270–295.

Ozaki, H., Kutsuna, M., 2009. Laser-roll welding of a dissimilar metal joint of low carbon steel to aluminium alloy using 2 kW fibre laser. Weld. Int. 23, 345–352. doi:10.1080/09507110802542718

Padmanabham, G., Priya, Y.K., Prabhakar, K.V.P., Bathe, R.N., 2013. A comparison of interface characteristics and mechanical properties of aluminium-steel joints made by pulsed-MIG and Cold Metal Transfer (CMT) processes, in: DeRoy, T., David, S.A., Koseki, T., H Badsdeshia (Eds.), Trends in Welding Research 2012:

Proceedings of the 9th International Conference. ASM International, Chicago, pp. 227–234.

Pépe, B.N., Egerland, S., Colegrove, P.A., Yapp, D., 2011. Measuring the Process Efficiency of Controlled Gas Metal Arc Welding Processes 16, 412–417.

Peyre, P., Sierra, G., Deschauxbeaume, F., Stuart, D., Fras, G., 2007. Generation of aluminium–steel joints with laser-induced reactive wetting. Mater. Sci. Eng. A 444, 327–338. doi:10.1016/j.msea.2006.09.111

Pl, P., 1989. Explosion-Bonded Transition Joints for Structural Applications. Building 3, 64–72.

Plascencia, G., Utigard, T., Marín, T., 2005. The Oxidation Resistance of Copper-Aluminum Alloys at Temperatures up to 1 , 000 ° C. JOM 57, 80–84.

Prangnell, P., Haddadi, F., Chen, Y.C., 2011. Ultrasonic spot welding of aluminium to steel for automotive applications - microstructure and optimisation. Mater. Sci. Technol. 27, 617–624. doi:10.1179/026708310X520484

Qiu, R., Iwamoto, C., Satonaka, S., 2009a. Interfacial microstructure and strength of steel/aluminum alloy joints welded by resistance spot welding with cover plate. J. Mater. Process. Technol. 209, 4186–4193. doi:10.1016/j.jmatprotec.2008.11.003

Qiu, R., Iwamoto, C., Satonaka, S., 2009. The influence of reaction layer on the strength of aluminum/steel joint welded by resistance spot welding. Mater. Charact. 60, 156–159. doi:10.1016/j.matchar.2008.07.005

Qiu, R., Satonaka, S., Iwamoto, C., 2009b. Effect of interfacial reaction layer continuity on the tensile strength of resistance spot welded joints between aluminum alloy and steels. Mater. Des. 30, 3686–3689. doi:10.1016/j.matdes.2009.02.012

Qiu, R., Shi, H., Zhang, K., Tu, Y., Iwamoto, C., Satonaka, S., 2010. Interfacial characterization of joint between mild steel and aluminum alloy welded by resistance spot welding. Mater. Charact. 61, 684–688. doi:10.1016/j.matchar.2010.03.015

Quintino, L., Assuncao, E., 2013. Conduction laser welding, in: Katayama, S. (Ed.), Handbook of Laser Welding Technologies. Woodhead Publishing Limited, pp. 6–9. doi:10.1533/9780857098771.1.139

Rabkin, D.M., Ryabov, V.R., Lozovskaya, A. V., Dovzhenco, V.A., 1970. Preparation and properties of copper-aluminium intermetallic compounds. Sov. Powder Metall. Met. Ceram. 9, 695–700. doi:10.1007/BF00803820

Rathod, M., Kutsuna, M., 2004. Joining of Aluminum Alloy 5052 and Low-Carbon Steel by Laser Roll Welding. Weld. J. 16–26.

Richards, R.W., Jones, R.D., Clements, P.D., Clarke, H., 1994. Metallurgy of continuous hot dip aluminizing. Int. Mater. Rev. 39, 191–212. doi:10.1179/imr.1994.39.5.191

Rüttimann, C., Dürr, U., Ag, R., 2011. Efficient laser welding of copper. pp. 18–20.

Sánchez-Amaya, J.M., Delgado, T., De Damborenea, J.J., Lopez, V., Botana, F.J., 2009. Laser welding of AA 5083 samples by high power diode laser. Sci. Technol. Weld. Join. 14, 78–86. doi:10.1179/136217108X347629

Sánchez-Amaya, J.M., Delgado, T., González-Rovira, L., Botana, F.J., 2009. Laser welding of aluminium alloys 5083 and 6082 under conduction regime. Appl. Surf. Sci. 255, 9512–9521. doi:10.1016/j.apsusc.2009.07.081

Schubert, E., Zerner, D.I., Sepold, P.G., 1997. Laser Beam Joining of Material Combinations for Automotive Applications, in: SPIE 3097, Lasers in Material Processing. Munich, pp. 212–221. doi:10.1117/12.281079

Schwartz, M.M., 2003. Brazing (Google eBook), 2nd editio. ed. ASM International, Materials Park, OH 44073-0002.

Shahverdi, H.R., Ghomashchi, M.R., Shabestari, S., Hejazi, J., 2002. Microstructural analysis of interfacial reaction between molten aluminium and solid iron. J. Mater. Process. Technol. 124, 345–352.

Shen, C., Pan, Z., Ma, Y., Cuiuri, D., Li, H., 2015. Fabrication of iron-rich Fe–Al intermetallics using the wire-arc additive manufacturing process. Addit. Manuf. 7, 20–26. doi:10.1016/j.addma.2015.06.001

Shih, T., Tu, S., 2007. Interaction of steel with pure Al, Al–7Si and A356 alloys. Mater. Sci. Eng. A 454-455, 349–356. doi:10.1016/j.msea.2006.11.017

Sierra, G., Peyre, P., Beaume, F.D., Stuart, D., Fras, G., 2008. Steel to aluminium braze welding by laser process with Al–12Si filler wire. Sci. Technol. Weld. Join. 13, 430–437. doi:10.1179/174329308X341852

Sierra, G., Peyre, P., Deschauxbeaume, F., Stuart, D., Fras, G., 2007. Steel to aluminium key-hole laser welding. Mater. Sci. Eng. A 447, 197–208. doi:10.1016/j.msea.2006.10.106

Sierra, G., Peyre, P., Deschauxbeaume, F., Stuart, D., Fras, G., 2008. Galvanised steel to aluminium joining by laser and GTAW processes. Mater. Charact. 59, 1705–1715. doi:10.1016/j.matchar.2008.03.016

Springer, H., Kostka, a., Payton, E.J., Raabe, D., Kaysser-Pyzalla, a., Eggeler, G., 2011. On the formation and growth of intermetallic phases during interdiffusion between low-carbon steel and aluminum alloys. Acta Mater. 59, 1586–1600. doi:10.1016/j.actamat.2010.11.023

Suder, W.J., Williams, S., 2014. Power factor model for selection of welding parameters in CW laser welding. Opt. Laser Technol. 56, 223–229. doi:10.1016/j.optlastec.2013.08.016

Suder, W.J., Williams, S.W., 2012. Investigation of the effects of basic laser material interaction parameters in laser welding. J. Laser Appl. 24, 032009. doi:10.2351/1.4728136

Taban, E., Gould, J.E., Lippold, J.C., 2010. Dissimilar friction welding of 6061-T6 aluminum and AISI 1018 steel: Properties and microstructural characterization.

Mater. Des. 31, 2305–2311. doi:10.1016/j.matdes.2009.12.010

Thomy, C., Wagner, F., Vollertsen, F., Metschkow, B., 2007. Lasers in the shipyard - Industrial Laser Solutions Lasers in the shipyard - Industrial Laser Solutions [WWW Document]. Ind. Laser Solut. URL http://www.industrial-lasers.com/articles/2007/11/lasers-in-the-shipyard.html

Torkamany, M.J., Tahamtan, S., Sabbaghzadeh, J., 2010. Dissimilar welding of carbon steel to 5754 aluminum alloy by Nd:YAG pulsed laser. Mater. Des. 31, 458–465. doi:10.1016/j.matdes.2009.05.046

Transfer, C.M., 2012. Metallurgical arc-joining of steel and aluminium to make hybrid sheets 1–2.

Tricarico, L., Spina, R., 2010. Experimental investigation of laser beam welding of explosion-welded steel/aluminum structural transition joints. Mater. Des. 31, 1981–1992. doi:10.1016/j.matdes.2009.10.032

Tricarico, L., Spina, R., Sorgente, D., Brandizzi, M., 2009. Effects of heat treatments on mechanical properties of Fe/Al explosion-welded structural transition joints. Mater. Des. 30, 2693–2700. doi:10.1016/j.matdes.2008.10.010

Tsumarev, Y.A., Ignatova, Y.V., Tsumarev, Y.N., Latypova, Y.Y., 2014. Reducing the stress concentration in permanent T-joints. Weld. Int. 28, 406–408. doi:10.1080/09507116.2013.840026

TWI, n.d. What is explosive cladding? [WWW Document]. URL http://www.twi-global.com/technical-knowledge/faqs/process-faqs/faq-what-is-explosive-cladding/ (accessed 11.15.15).

Uzun, H., Dalle Donne, C., Argagnotto, A., Ghidini, T., Gambaro, C., 2005. Friction stir welding of dissimilar Al 6013-T4 To X5CrNi18-10 stainless steel. Mater. Des. 26, 41–46. doi:10.1016/j.matdes.2004.04.002

Villars, P., Prince, A., Okamoto, H., 1995. Handbook of Ternary Alloy Phase Diagrams, vol. 3. ASM International, Materials Park, OH.

Wang, X., Wood, J. V., Sui, Y., Lu, H., 1998. Formation of intermetallic compound in iron-aluminum alloys. J. Shanghai Univ. (English Ed. 2, 305–310. doi:10.1007/s11741-998-0045-5

Watanabe, T., Takayama, H., Yanagisawa, A., 2006. Joining of aluminum alloy to steel by friction stir welding. J. Mater. Process. Technol. 178, 342–349. doi:10.1016/j.jmatprotec.2006.04.117

Weigl, M., Albert, F., Schmidt, M., 2011. Enhancing the Ductility of Laser-Welded Copper-Aluminum Connections by using Adapted Filler Materials. Phys. Procedia 12, 332–338. doi:10.1016/j.phpro.2011.03.141

Wulff, F.W., Breach, C.D., Stephan, D., Saraswati, S., Dittmer, K.J., 2004. Characterisation of intermetallic growth in copper and gold ball bonds on aluminium metallization. Proc. 6th Electron. Packag. Technol. Conf. (EPTC 2004) (IEEE Cat. No.04EX971) 348–353. doi:10.1109/EPTC.2004.1396632

Yan, S., Hong, Z., Watanabe, T., Jingguo, T., 2010. CW/PW dual-beam YAG laser welding of steel/aluminum alloy sheets. Opt. Lasers Eng. 48, 732–736. doi:10.1016/j.optlaseng.2010.03.015

Yang, S., Zhang, J., Lian, J., Lei, Y., 2013. Welding of aluminum alloy to zinc coated steel by cold metal transfer. Mater. Des. 49, 602–612. doi:10.1016/j.matdes.2013.01.045

Yasui, T., Mizushima, H., Tsubaki, M., Fujita, T., Fukumoto, M., 2014. Influence of Tool Shape on Friction Stir Welded Joint of Aluminum and Steel with Circular Weld Line. Procedia Eng. 81, 2092–2097. doi:10.1016/j.proeng.2014.10.291

Yin, F., Zhao, M., Liu, Y., Han, W., Li, Z., 2013. Effect of Si on growth kinetics of intermetallic compounds during reaction between solid iron and molten aluminum. Trans. Nonferrous Met. Soc. China 23, 556–561. doi:10.1016/S1003-6326(13)62499-1

Yousaf, M., 2011. Variables Affecting Growth and Morphology of the Intermetallic Layer (Fe2Al5) of Steel Aluminized in Al-Cu Alloys. University of Engineering & Technology Lahore-Pakistan.

Zhang, H., Feng, J., He, P., Zhang, B., Chen, J., Wang, L., 2009. The arc characteristics and metal transfer behaviour of cold metal transfer and its use in joining aluminium to zinc-coated steel. Mater. Sci. Eng. A 499, 111–113. doi:10.1016/j.msea.2007.11.124